Title
Modeling Nonlinear Magneto-optical Effects in Atomic Vapors

Author
Rochester, Simon Michael

Publication Date
2010

Modeling Nonlinear Magneto-optical Effects in Atomic Vapors

by

Simon Michael Rochester

A dissertation submitted in partial satisfaction of the
requirements for the degree of
Doctor of Philosophy
in
Physics
in the
Graduate Division
of the
University of California, Berkeley

Committee in charge:

Professor Dmitry Budker, Chair
Professor Robert G. Littlejohn
Professor Alexei V. Filippenko

Fall 2010

Modeling Nonlinear Magneto-optical Effects in Atomic Vapors

Abstract

Modeling Nonlinear Magneto-optical Effects in Atomic Vapors

by

Simon Michael Rochester

Doctor of Philosophy in Physics

University of California, Berkeley

Professor Dmitry Budker, Chair

Nonlinear magneto-optical processes are a rich source of interesting and useful phenomena, with both practical and fundamental-physics applications. Theoretical modeling is helpful for understanding and visualizing the mechanisms for nonlinear magneto-optical effects (NMOE), and for analyzing and optimizing devices based on these effects. Part I of this Thesis describes Bloch-equation methods and visualization techniques that can be used to model a wide variety of NMOE in atomic vapors. Part II presents several applications of the methods, including the investigation and visualization of a specific effect involving radio-frequency fields, a study of the general consequences of hyperfine structure on NMOE, and modeling and optimization of systems for laser guide stars. Appendices present additional mathematical material and describe a *Mathematica* package used for density-matrix calculations.

Contents

Acknowledgments

I would like to thank my advisor, Prof. Dmitry Budker, and all of my co-authors both on the work described here and on all of the previous work done in my many years in the Budker group. I also acknowledge support from the NASA Earth and Space Science Fellowship Program. Finally, I would like to thank my friend Candace for hanging in there with me.

Chapter 1

Introduction

The term nonlinear magneto-optical effect (NMOE) describes a process occurring in atoms subject to optical and other electromagnetic fields, such that the optical properties of the atomic medium depend on the light field (Budker *et al.*, 2002a; Alexandrov *et al.*, 2005).[1] A system under these conditions can have rich and complex behavior, exhibiting phenomena such as electromagnetically induced transparency (Harris, 1997), electromagnetically induced absorption (Budker and Rochester, 2004), nonlinear magneto-optical rotation (Chapter 4 and Budker *et al.*, 2000b), self rotation (Rochester *et al.*, 2001), alignment-to-orientation conversion (Budker *et al.*, 2000a), double resonance (Chapter 8 and Zigdon *et al.*, 2010) , “fast” and “slow” light (Budker *et al.*, 1999a), Bennett-structure effects (Budker *et al.*, 2002b), synchronous-pumping resonances (Chapter 6 and Bell and Bloom, 1961; Budker *et al.*, 2002c; Malakyan *et al.*, 2004; Acosta *et al.*, 2006; Pustelny *et al.*, 2006a,b, 2007), and creation of high-order multipole moments (Yashchuk *et al.*, 2003; Pustelny *et al.*, 2006b; Acosta *et al.*, 2008). These processes are not so complicated that they cannot be described using intuitive physical language, however, and in many cases theoretical models and accompanying visualization techniques (Sec. 2.2 and Rochester and Budker, 2001) are vital in obtaining this understanding.

Techniques for preserving atomic polarization in vapor cells such as antirelaxation coatings (Balabas *et al.*, 2010) and the spin-exchange-relaxation-free (SERF) regime (Kominis *et al.*, 2003; Ledbetter *et al.*, 2008) now allow unprecedented sensitivity to NMOE. This translates to atomic magnetometers with magnetometric sensitivity on the order of that of superconducting quantum interference device (SQUID)-based magnetometers, which were previously leading in this area (Budker and Romalis,

---

[1] In *linear* magneto-optical effects, which generally occur in the limit of low light power, the optical properties of the medium are independent of the light field.

2007). This, along with the fact that atomic magnetometers—unlike SQUIDs—do not require cryogenics, makes a number of potential applications quite attractive, including detection in nuclear magnetic resonance (NMR, Ledbetter *et al.*, 2009) and magnetic-resonance imaging (MRI, Yashchuk *et al.*, 2004; Xu *et al.*, 2006a,b, 2008), dynamical measurements of biomagnetic fields (Bison *et al.*, 2003; Xia *et al.*, 2006), explosives and contraband detection (Lee *et al.*, 2006), space and geomagnetic measurements (Dougherty *et al.*, 2005, 2006), inertial rotation sensing (Kornack *et al.*, 2005), and fundamental physics measurements (Youdin *et al.*, 1996; Chin *et al.*, 2001; Budker *et al.*, 2006). These applications can benefit from theoretical models for the purposes of optimization and the analysis of systematic errors.

Finally, the theory of NMOE can also be helpful in somewhat unexpected ways—for example, in the design of systems for laser guide stars (Chapter 11 and Holzlöhner *et al.*, 2010), or in the description of the mechanism of NMR in a powder (Budker *et al.*, 2003).

Part I of this Thesis describes the methods used in the modeling of NMOE using the density-matrix evolution equations. Chapter 2 defines the density matrix and describes a visualization technique that can be used to illustrate the polarization dynamics. Chapter 3 describes the time evolution of the density matrix, including the effect of the external fields and various relaxation processes. Chapter 4 describes the effect of the atoms on the light and discusses some of the basic nonlinear magneto-optical effects. Chapter 5 describes approximate methods for the solution of the evolution equations. Chapter 6 describes methods for time-dependent fields, and Chapter 7 discusses methods for modeling coated cells and buffer gases, including the description of the atomic velocity distribution, atomic collisions, and multiple experimental regions.

Part II presents several applications of the methods described in Part I. Chapter 8 discusses nonlinear magneto-optical rotation in the presence of a radio-frequency (rf) field. It provides examples of the analytical solution of a low-angular-momentum system and the use of the methods for time-dependent fields. It also shows how the density-matrix visualization technique can be used to obtain physical insight into mechanisms for NMOE. Chapters 9 and 10 employ perturbative techniques to discuss the effect of hyperfine structure on NMOE in general and nonlinear Faraday rotation in particular. Lastly, Chapter 11 describes the use of numerical modeling and the methods of Chapter 7 to optimize the laser parameters for a laser guide star and to show how such a guide star can be employed to measure magnetic fields in the magnetosphere.

Appendices A through C give details of the algebra of rotations and angular momentum. Appendix D provides derivations of results used in Chapter 10. Finally,

Appendix E describes a package written for *Mathematica* to facilitate density-matrix calculations.

Chapters 2–5, Secs. 6.1 and 7.1, and Appendices A–E are largely taken from Auzinsh *et al.* (2010), with some revision, reorganization, deletions, and additions (in particular Secs. 2.3.1 and 5.2.3). Chapter 8 is taken from Zigdon *et al.* (2010), Chapters 9 and 10 are taken from Auzinsh *et al.* (2009a), Sec. 11.1 is excerpted from Holzlöhner *et al.* (2010), and Sec. 11.2 is excerpted from Higbie *et al.* (2009).

Part I

Methods

Chapter 2

The Density Matrix

2.1 Definition and properties

We consider experiments done on an ensemble of N atoms, for which the i-th atom can (in an idealized case, see below) be described by a particular wave function $|\psi_i\rangle$. Measurements are described by the average expectation value of an observable A for all of the atoms:

$$\overline{\langle A\rangle} = \frac{1}{N}\sum_{i=1}^{N} \langle\psi_i|A|\psi_i\rangle. \tag{2.1}$$

In a completely polarized ensemble, each atom has the same wave function (up to an overall phase), and the average expectation value reduces to the expectation value of this single wave function. It is straightforward to show, however, that in the general case there is no "average" wave function that correctly describes the ensemble. For example, the vector formed by the expectation values (S_x, S_y, S_z) for the wave function of a spin-1/2 system is always nonzero and points in a particular direction. However, for an unpolarized ensemble (e.g., one in which the wave functions are completely random) this vector must be zero by symmetry.

In principle, we could keep track of the wave function of every atom in the ensemble. However, aside from the computational difficulties involved, we have, in general, no way of measuring the individual atom wave functions. In order to describe the ensemble, then, we would like to find a generalization of the wave function as some sort of average over the atomic wave functions that can represent both polarized and unpolarized states.

To find such a representation, we can write the average expectation value of an observable as

$$\overline{\langle A\rangle} = \frac{1}{N}\sum_{i=1}^{N}\langle\psi_i|A|\psi_i\rangle = \sum_m \frac{1}{N}\sum_{i=1}^{N}\langle\psi_i|A|m\rangle\langle m|\psi_i\rangle = \sum_m \frac{1}{N}\sum_{i=1}^{N}\langle m|\psi_i\rangle\langle\psi_i|A|m\rangle. \tag{2.2}$$

Here we have inserted the identity operator

$$1 = \sum_m |m\rangle\langle m|, \tag{2.3}$$

where $\{|m\rangle\}$ is any complete set of basis states. Using the definition of the trace of an operator,

$$\mathrm{Tr}\,\mathcal{O} = \sum_m \langle m|\mathcal{O}|m\rangle, \tag{2.4}$$

we can write (2.2) as

$$\overline{\langle A\rangle} = \mathrm{Tr}\left(\frac{1}{N}\sum_{i=1}^{N}|\psi_i\rangle\langle\psi_i|A\right) = \mathrm{Tr}\left(\rho A\right), \tag{2.5}$$

where we have defined the new operator

$$\rho = \frac{1}{N}\sum_{i=1}^{N}|\psi_i\rangle\langle\psi_i|, \tag{2.6}$$

called the *density operator*. This operator is independent of A, and represents a kind of average over the atomic wave functions. The density operator evidently contains all of the information of interest about the average state of the ensemble, since the result of any possible physical measurement can be found by multiplying the corresponding operator by ρ and taking the trace.

The matrix elements of the density operator defined by Eq. (2.6) form the *density matrix*, and are given by

$$\rho_{mn} = \langle m|\rho|n\rangle = \frac{1}{N}\sum_{i=1}^{N}\langle m|\psi_i\rangle\langle\psi_i|n\rangle = \frac{1}{N}\sum_{i=1}^{N}c_m^{(i)}c_n^{(i)*}, \tag{2.7}$$

where $c_m^{(i)}$ is the m-th expansion coefficient for the i-th atom. In fact, we can regard Eq. (2.7) as an alternate definition of the density operator. A given system may require an infinite number of density-matrix elements to describe it completely; however, we will take the common approach of restricting the density matrix to a (finite) number of states of interest for a given problem. The diagonal elements of the density matrix are given by

$$\rho_{mm} = \frac{1}{N}\sum_{i=1}^{N} |c_m^{(i)}|^2, \tag{2.8}$$

and represent the average probability of finding an atom in the state $|m\rangle$ (the *population* of $|m\rangle$). Off-diagonal density-matrix elements ($m \neq n$) are referred to as *coherences*.

> We have introduced the concept of the density matrix starting with a model in which each atom in the ensemble is described by a wave function. While this is a convenient way to begin the exploration of the density-matrix apparatus, this model is unnecessarily restrictive. If the system under consideration is a part of a larger system consisting of interacting parts, it is generally impossible to assign wave functions to the individual parts (Landau and Lifshitz, 1977, Sec. 14). In this case, even a single atom may need to be described by a density matrix, rather than a wave function. An ensemble-averaged density matrix can be defined for this case by
>
> $$\rho = \sum_k |\psi_k\rangle P_k \langle\psi_k|, \tag{2.9}$$
>
> where P_k is the probability for the state $|\psi_k\rangle$ to exist in the ensemble. Note that the properties of the density matrix of the ensemble do not depend on whether this definition or Eq. (2.6) is used.
>
> A single-atom density matrix written in the basis of position eigenstates $[\rho(\mathbf{x}, \mathbf{x}')]$ is an analog of a single-particle distribution function. A multi-particle density matrix that accounts for correlations between atoms can be written. However, in the situations that we consider, there are generally no processes that generate coherences between different atoms. Thus we neglect such correlations in our treatment.

The density matrix has a number of useful properties. For a normalized density matrix, the total probability of being in any state must be unity. In other words, we have for the trace of the density matrix

$$\mathrm{Tr}\,\rho = \sum_n \frac{1}{N}\sum_{i=1}^{N} \langle n|\psi_i\rangle\langle\psi_i|n\rangle = \frac{1}{N}\sum_{i=1}^{N}\sum_n \langle\psi_i|n\rangle\langle n|\psi_i\rangle = \frac{1}{N}\sum_{i=1}^{N}\langle\psi_i|\psi_i\rangle = 1. \tag{2.10}$$

Also, by construction, the density matrix is *Hermitian*, meaning that it is equal to its conjugate transpose. There is a nice mathematical property that Hermiticity is a necessary and sufficient condition for a matrix to have real eigenvalues. The eigenvalues of the density matrix are the populations in the basis in which the density matrix has no coherences. Such a basis can always be found; in some cases it may simply require a rotation of the quantization axis (see Sec. 2.4). These populations must always be greater than or equal to zero—in other words, the density matrix is *nonnegative definite*.

In general, the matrix element ρ_{mn} depends on the magnitude of ρ_{mm} and ρ_{nn}, as well as on the correlation between the two states. We can define the normalized degree of coherence between states $|m\rangle$ and $|n\rangle$ by introducing the quantity

$$\zeta_{mn} = \frac{\rho_{mn}}{\sqrt{\rho_{mm}\rho_{nn}}}. \tag{2.11}$$

The absolute value of the complex parameter ζ_{mn} can be interpreted as the degree of coherence between the states $|m\rangle$ and $|n\rangle$:

$$|\zeta_{mn}| \leq 1. \tag{2.12}$$

This is similar to the approach used in statistics to obtain the normalized correlation matrix from an unnormalized covariance matrix—see, for example, Brandt (1999).

The density matrix can be used in place of a wave function in any situation, while the converse is true only for ensembles in a pure state. There is a simple test to determine whether a system is in a pure state (Stenholm, 2005). A quantum system is in a pure state if and only if it satisfies

$$\rho^2 = \rho, \tag{2.13}$$

as can be shown by diagonalizing ρ.

2.2 Angular-momentum probability surfaces

We now discuss a technique for visualizing the angular-momentum polarization state specified by the density matrix. Consider the density matrix corresponding to the manifold of Zeeman sublevels of a state with total angular momentum F. If we measure the projection of the angular momentum along some axis, the possible outcomes of the measurement, according to quantum mechanics, are the values $-F, -F+1\ldots, F$. The probability of measuring a given value m along the quantization axis is given by $\rho_{mm} = \langle Fm|\rho|Fm\rangle$. We will characterize the polarization state along the quantization axis by recording the probability $\rho_{FF} = \langle FF|\rho|FF\rangle$ of finding the maximum possible projection $m = F$. To find this quantity with respect to some other axis, we rotate the state $|FF\rangle$ using the rotation operator $\mathscr{D}(\phi, \theta, 0)$ (Appendix B), to obtain

$$|FF(\theta,\phi)\rangle = \mathscr{D}(\phi,\theta,0)|FF\rangle = \sum_{m'} D^{(F)}_{m'F}(\phi,\theta,0)|Fm'\rangle. \tag{2.14}$$

Thus the probability of finding the maximum projection of angular momentum along the (θ, ϕ) direction is given by

$$\begin{aligned}\rho_{FF}(\theta,\phi) &= \langle FF(\theta,\phi)|\rho|FF(\theta,\phi)\rangle \\ &= \sum_{mm'} D^{(F)*}_{mF}(\phi,\theta,0)\rho_{mm'}D^{(F)}_{m'F}(\phi,\theta,0).\end{aligned} \tag{2.15}$$

We can plot this probability as a function of the direction of the quantization axis to obtain a visual representation of the density matrix, the *angular-momentum probability surface* (AMPS, Auzinsh, 1997; Rochester and Budker, 2001).

As an example, consider atoms in a pure state with $F = 1$, $m = -1$, for which $|\psi\rangle = |1, -1\rangle$. The density matrix for this state is

$$\rho = \begin{pmatrix} 0 & 0 & 0 \\ 0 & 0 & 0 \\ 0 & 0 & 1 \end{pmatrix}. \tag{2.16}$$

Using the explicit form of the D-matrix (Appendix B), we obtain the following equation for the distance from the origin for the surface in a direction given by the angles θ and ϕ:

$$\rho_{FF}(\theta,\phi) = \sin^4(\theta/2). \tag{2.17}$$

This surface is plotted in Fig. 2.1, along with two of its cross-sections. Also shown is the surface for a copy of the density matrix that has been rotated by $\pi/4$ about the vector $\hat{\mathbf{n}} = \hat{\mathbf{x}} + \hat{\mathbf{y}}$. In fact, rotation of the polarization state as a whole is what occurs when a weak magnetic field is applied to the ensemble (Larmor precession). In Fig. 2.2 the probability surface for an unpolarized ensemble is drawn. The volume contained by the surface in Fig. 2.2 is smaller than that contained by the surfaces in Fig. 2.1, even though the normalization of the corresponding density matrices is the same. The volume of the probability surface is generally not the same for different polarization states of the ensemble. For example, if the polarized state shown in Fig. 2.1 gradually relaxes to the unpolarized state in Fig. 2.2, the volume as well as the shape changes in the process of relaxation, even though no atoms are lost from the ensemble.

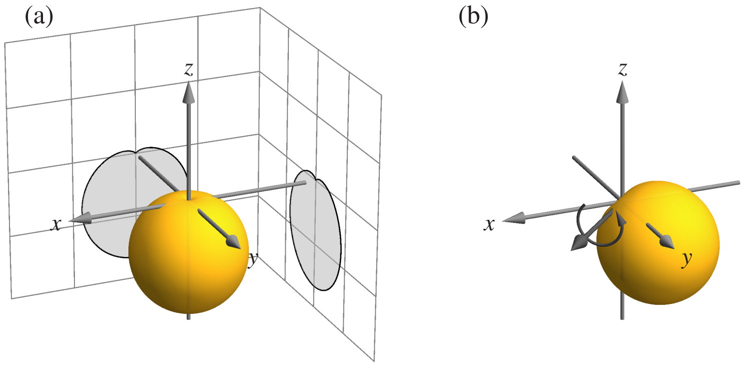

Figure 2.1: (a) Angular-momentum probability surfaces for the density matrix given in Eq. (2.16) and two of its cross-sections. The probability to measure the maximum projection of the angular momentum is equal to one in the $-\hat{\mathbf{z}}$-direction and zero in the $\hat{\mathbf{z}}$-direction (the “dimple” at the top of the surface). (b) The same density matrix rotated by $\pi/4$ around the vector $\hat{\mathbf{n}} = \hat{\mathbf{x}} + \hat{\mathbf{y}}$.

The immediate utility of the angular-momentum probability surfaces is that they illustrate the rotational symmetry properties of the density matrix. In the examples just given the unpolarized surface is spherically symmetric, because for an unpolarized density matrix there is no preferred direction. For the stretched state $|1,-1\rangle$ the quantization axis is the only preferred direction, while the other two directions are completely equivalent, as reflected by the axial symmetry of the probability surfaces shown in Fig. 2.1. Note that, as shown in Fig. 2.1, a physical rotation changes the symmetry axis, but does not affect the symmetry about that axis.

Why is it useful to know the symmetry of the state? We will see that the symmetry of the polarization state of atoms determines the kind of optical anisotropy they can have. For example, if the distribution is axially symmetric with respect to the direction of propagation of linearly polarized light, the optical properties of the ensemble, such as absorption coefficient or refractive index, will not depend on the direction of the light polarization.

Clearly, the probability surface contains significant information about the polarization of an atomic state, and hence about the corresponding density matrix. By looking at a probability surface, we can tell whether the state is polarized, what kind of po-

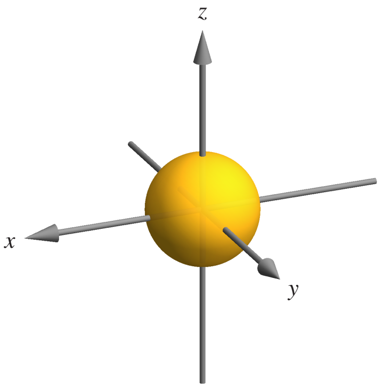

Figure 2.2: Angular-momentum probability surface for an unpolarized ensemble with $F = 1$. The surface is a sphere with radius 1/3, equal to the population in each Zeeman sublevel.

larization it has, what the preferred axes are, etc.
One might wonder, how complete is the knowledge of the density matrix that one can attain from the knowledge of the angular-momentum probability surface?

Remarkably, the probability surface contains as much information about the atoms as the density matrix. Thus, if the surface is known, the full density matrix can be recovered from it. To show this, we introduce in the next section another very useful representation of the density matrix: the expansion into multipole moments. We then use this property of the probability surface in Sec. 2.4 to demonstrate some relations between the symmetries of the probability surface and those of the density matrix.

2.3 Multipole moments

2.3.1 Definition

Consider the three density matrices for a $J = 1$ state

$$\rho_a = \frac{1}{3}\begin{pmatrix} 1 & 0 & 0 \\ 0 & 1 & 0 \\ 0 & 0 & 1 \end{pmatrix}, \quad \rho_b = \frac{1}{3}\begin{pmatrix} 0 & 0 & 0 \\ 0 & 1 & 0 \\ 0 & 0 & 2 \end{pmatrix}, \quad \rho_c = \frac{1}{2}\begin{pmatrix} 1 & 0 & 0 \\ 0 & 0 & 0 \\ 0 & 0 & 1 \end{pmatrix}, \tag{2.18}$$

whose angular-momentum probability surfaces are plotted in Fig. 2.3. From the figure, it is apparent that each of these density matrices have different symmetries, and thus different rotational properties. Specifically, ρ_a is spherically symmetric and so is unchanged by rotations (like a scalar), ρ_b has a preferred direction and rotates like a vector, and ρ_c has no preferred direction but a preferred axis—it rotates like a second-rank tensor. We describe these properties by saying that ρ_a represents *population* (atoms, but no polarization), ρ_b represents *orientation*, and ρ_c represents *alignment*.

> Note that ρ_b and ρ_c also have nonzero traces, as physically realistic density matrices must. Thus, strictly speaking, ρ_b and ρ_c represent population as well as orientation or alignment. We will generally consider this to be understood, and just refer to such density matrices as oriented or aligned.

The rotational properties of the surfaces in Fig. 2.3 correspond to those of particular spherical harmonics $Y_{lm}(\theta, \varphi)$. The spherical harmonics are functions of θ and φ, each with unique symmetry properties determined by l and m. The spherical harmonics Y_{00}, Y_{10}, and Y_{20} corresponding to the surfaces of Fig. 2.3 are plotted in Fig. 2.4. There is a difference in appearance between the AMPS and the plot of the Y_{lm}'s

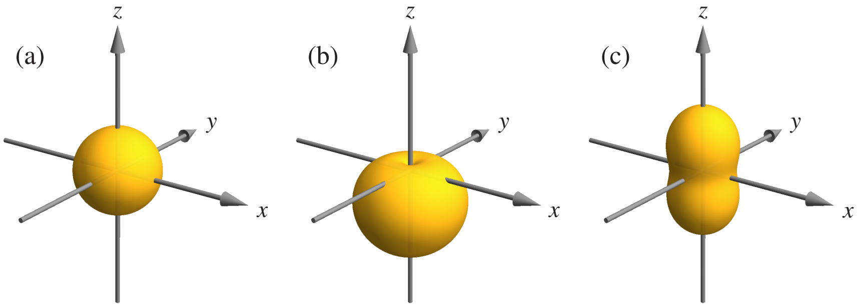

Figure 2.3: Plots of AMPS for the density matrices (a) ρ_a, (b) ρ_b, and (c) ρ_c of Eq. (2.18).

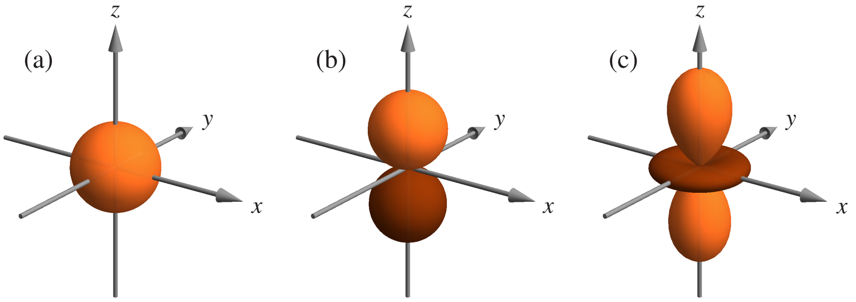

Figure 2.4: Plots of the spherical harmonics (a) Y_{00}, (b) Y_{10}, (c) Y_{20}. In (b) and (c) the darker shading indicates negative function values.

because Y_{10} and Y_{20} attain negative function values, whereas the AMPS contain a constant term corresponding to the population so that they are always positive. Nonetheless, we see that Y_{10} and Y_{20} have a preferred direction and a preferred axis, respectively, like the oriented and aligned states described in the previous section, while the Y_{00} state is isotropic, like the unpolarized state shown in Fig. 2.2.

Looking at Eq. (2.18), we can see that any $J = 1$ density matrix that has no coherences (i.e., has only diagonal elements) can be written as a linear combination of $\rho_{a,b,c}$. This means that, correspondingly, any AMPS for a $J = 1$ state that is symmetric about the z-axis can be decomposed into the surfaces shown in Fig. 2.3, which correspond to the Y_{lm}'s plotted in Fig. 2.4. In fact, any density matrix can be entirely decomposed into components (polarization moments) each of which exhibits symmetry corresponding to a particular spherical harmonic. Geometrically, this could be done by finding the linear combination of Y_{lm}'s that equals the angular-momentum probability surface for a particular state. However, it will often be more useful to us to think of the polarization moments in terms of a decomposition of the density matrix itself. We now describe how to go about this decomposition.

The density matrix ρ was introduced as an operator (Sec. 2.1). When we write the density operator as a density matrix, we are actually performing a decomposition of the density operator over a complete set of basis operators. For an atomic state with angular momentum F we write

$$\rho = \sum_{mm'} \rho_{mm'} |m\rangle\langle m'|, \tag{2.19}$$

where $\rho_{mm'}$ are the density-matrix elements, and $|m\rangle\langle m'|$ are the $(2F+1)\times(2F+1)$ basis operators. For example, the diagonal operators $|m\rangle\langle m|$ are the *projection operators* onto the states $|m\rangle$. As discussed in this chapter, this set of basis operators is of great physical importance, representing the populations of and coherences between the Zeeman sublevels. However, it does not always have the most desirable properties; for example, the same state can be described by a very different set of nonzero density-matrix elements depending on the choice of quantization axis, as in Fig. 2.5.

What is a more agreeable set of basis operators from the point of view of symmetry? In Appendix C we describe the irreducible tensor operators, which are operators that have the rotational symmetries of the spherical harmonics. Because the irreducible tensor operators are orthogonal, we also find that they form a complete basis: since a rank-κ operator has $2\kappa+1$ components $q = -\kappa, \dots, \kappa$, we see that the set of operators with rank $\kappa = 0, \dots, 2F$ have

$$\sum_{\kappa=0}^{2F} (2\kappa+1) = (2F+1)^2 \tag{2.20}$$

independent components, equal to the number of degrees of freedom of an operator on a state with angular momentum F. We therefore define a set of irreducible tensor operators $\mathcal{T}^{\kappa}_{q}$, called *polarization operators*, and expand the density matrix over this set:

$$\rho = \sum_{\kappa=0}^{2F} \sum_{q=-\kappa}^{\kappa} \rho^{\kappa q} \mathcal{T}^{\kappa}_{q}. \tag{2.21}$$

The *polarization moments* (PM; also known as *state multipoles*) of the density matrix are then defined as the coefficients $\rho^{\kappa q}$ in this expansion. (We will also use the term polarization moment to refer to a term $\rho^{\kappa q}\mathcal{T}^{\kappa}_{q}$ of the expansion.) We write ρ^{κ} to refer to the collection of components $\rho^{\kappa q}$ with $q = -\kappa, \dots, \kappa$.

The definition of an irreducible tensor, given in Appendix C, is quite restrictive, so that the properties of an irreducible tensor are essentially constrained up to an overall factor. We can therefore define the polarization operators by simply giving a normalization condition

$$\operatorname{Tr} \mathcal{T}^{\kappa}_{q} \mathcal{T}^{\kappa'\dagger}_{q'} = \delta_{\kappa\kappa'}\delta_{qq'} \tag{2.22}$$

and a phase convention

$$\mathcal{T}_q^{\kappa\dagger} = (-1)^q \mathcal{T}_{-q}^{\kappa} = \mathcal{T}^{\kappa q}. \tag{2.23}$$

Using the Wigner–Eckart theorem (Appendix C.2), we can then find the reduced matrix element of the polarization operators:

$$\begin{aligned} 1 &= \operatorname{Tr} \mathcal{T}_q^{\kappa} \mathcal{T}_q^{\kappa\dagger} \\ &= \sum_{mm'} \left(\mathcal{T}_q^{\kappa}\right)_{mm'} \left(\mathcal{T}_q^{\kappa}\right)^*_{mm'} \\ &= \sum_{mm'} \frac{1}{2F+1} \left|\langle F \| \mathcal{T}^{\kappa} \| F \rangle\right|^2 \langle F m' \kappa q | F m \rangle^2 \\ &= \frac{1}{2\kappa+1} \left|\langle F \| \mathcal{T}^{\kappa} \| F \rangle\right|^2 , \end{aligned} \tag{2.24}$$

giving

$$\langle F \| \mathcal{T}^{\kappa} \| F \rangle = \sqrt{2\kappa+1}, \tag{2.25}$$

where we have used the Clebsch–Gordan sum rule

$$\sum_{m_1 m_3} \langle F_1 m_1 F_2 m_2 | F_3 m_3 \rangle^2 = \frac{2F_3+1}{2F_2+1}, \tag{2.26}$$

and we know that the reduced matrix element is real because $\mathcal{T}_0^{\kappa\dagger} = \mathcal{T}_0^{\kappa}$ according to Eq. (2.23).

Now that we have the reduced matrix element, we can find the matrix elements of the polarization operators:

$$\langle F m' | \mathcal{T}_q^{\kappa} | F m \rangle = \sqrt{\frac{2\kappa+1}{2F+1}} \langle F m \kappa q | F m' \rangle = (-1)^{F-m} \langle F m' F, -m | \kappa q \rangle, \tag{2.27}$$

where we have used the Clebsch–Gordan identity

$$\langle F_1 m_1 F_2 m_2 | F_3 m_3 \rangle = (-1)^{F_1 - m_1} \sqrt{\frac{2F_3+1}{2F_2+1}} \langle F_3 m_3 F_1, -m_1 | F_2 m_2 \rangle. \tag{2.28}$$

To find the coefficients $\rho^{\kappa q}$ in the polarization-moment expansion, we multiply both sides of Eq. (2.21) by $\mathcal{T}_{q'}^{\kappa'\dagger}$, take the trace, and use the normalization condition:

$$\operatorname{Tr}\left(\rho \mathcal{T}_{q'}^{\kappa'\dagger}\right) = \sum_{\kappa q} \rho^{\kappa q} \operatorname{Tr}\left(\mathcal{T}_q^{\kappa} \mathcal{T}_{q'}^{\kappa'\dagger}\right) = \sum_{\kappa q} \rho^{\kappa q} \delta_{\kappa\kappa'} \delta_{qq'} = \rho^{\kappa' q'}. \tag{2.29}$$

Using Eq. (2.27) we can find a formula for the polarization moments in terms of the density-matrix elements:

$$\rho^{\kappa q} = \mathrm{Tr}\left(\rho \mathcal{T}_q^{\kappa \dagger}\right) = \sum_{mm'} \rho_{m'm} \left(\mathcal{T}_q^{\kappa}\right)_{m'm} = \sum_{mm'} (-1)^{F-m} \langle F m' F, -m | \kappa q \rangle \rho_{m'm}, \tag{2.30}$$

and the inverse formula

$$\rho_{m'm} = \sum_{\kappa q} \rho^{\kappa q} \left(\mathcal{T}_q^{\kappa}\right)_{m'm} = \sum_{\kappa q} (-1)^{F-m} \langle F m' F, -m | \kappa q \rangle \rho^{\kappa q}, \tag{2.31}$$

which allows reconstruction of the density-matrix elements if the polarization moments are known.

The coefficients $\rho^{\kappa q}$ are contravariant quantities. The corresponding covariant components ρ_q^{κ} are determined by

$$A = \sum_{\kappa=0}^{2F} \sum_{q=-\kappa}^{\kappa} \rho_q^{\kappa} \mathcal{T}^{\kappa q}, \tag{2.32}$$

and can be found as

$$\mathrm{Tr}\Big(\rho \mathcal{T}_{q'}^{\kappa'}\Big) = \sum_{\kappa q} \rho_q^{\kappa} \, \mathrm{Tr}\Big(\mathcal{T}^{\kappa q} \mathcal{T}_{q'}^{\kappa'}\Big) = \sum_{\kappa q} \rho_q^{\kappa} \delta_{\kappa \kappa'} \delta_{q q'} = \rho_{q'}^{\kappa'}. \tag{2.33}$$

Explicitly, we have

$$\rho_q^{\kappa} = \mathrm{Tr}\big(\rho \mathcal{T}_q^{\kappa}\big) = \sum_{mm'} \rho_{m'm} \left(\mathcal{T}_q^{\kappa}\right)_{mm'} = \sum_{mm'} (-1)^{F-m'} \langle F m F, -m' | \kappa q \rangle \rho_{m'm}, \tag{2.34}$$

and the inverse formula

$$\rho_{m'm} = \sum_{\kappa q} \rho_q^{\kappa} \left(\mathcal{T}_q^{\kappa \dagger}\right)_{m'm} = \sum_{\kappa q} (-1)^{F-m'} \langle F m F, -m' | \kappa q \rangle \rho_q^{\kappa}. \tag{2.35}$$

The polarization moments ρ^{κ} are given names by analogy with the expansion of a static electric field into multipole moments. In that case 2^{κ} point charges are required to produce a field configuration consisting of only a rank-κ moment. Thus we obtain the designations for the lowest-rank moments ρ^0—*monopole moment* (equal to the population divided by $\sqrt{2F+1}$), ρ^1—*dipole moment* or orientation, ρ^2—*quadrupole moment* or alignment, ρ^3—*octupole moment*, ρ^4—*hexadecapole moment*, ρ^5—*triacontadipole moment*, and ρ^6—*hexacontatetrapole moment*. (The utility of these terms diminishes rapidly as κ increases beyond this point.) Polarization moments as high as hexacontatetrapole have been created and detected (Pustelny *et al.*, 2006b).

It should be noted that there are other definitions of the terms "orientation" and "alignment" in the literature. For example, Zare (1988) identifies alignment with any of the even moments in atomic polarization (quadrupole, hexadecapole, etc.) and orientation with the odd moments (dipole, octupole, etc.). To add to the confusion, nuclear physicists often use the term "polarization" to specifically designate orientation, whereas in our convention, the term is used to describe an ensemble that has any moment with $\kappa > 0$.

2.3.2 Properties

We now discuss a few important properties of the polarization moments. Some physical intuition about them can be gained by examining their relation to the Zeeman populations and coherences (Sec. 2.1). This is found from the transformation equations (2.30) and (2.31), and the properties of the Clebsch–Gordan coefficients, in particular the requirement that $m' - m = q$ for the Clebsch–Gordan coefficients in the sums to be nonzero. For example, in Eq. (2.30), setting $q = 0$ implies that only terms with $m = m'$, i.e., the Zeeman-sublevel populations ρ_{mm}, contribute to the sum. Furthermore, setting $m = m'$ in Eq. (2.31) shows that the Zeeman populations can be expressed entirely in terms of the polarization moments with $q = 0$. Thus the polarization moments ρ_0^κ describe polarization along the quantization axis, i.e., *longitudinal polarization* characterizing to the distribution of Zeeman populations. Analogously, a nonzero PM with $q \neq 0$ means that $\rho_{mm'}$ coherences with $m' - m = q$ are nonzero. When there are coherences between the sublevels, $\rho_q^\kappa \neq 0$ for some $q \neq 0$, and the medium is said to have *transverse polarization.*.

The polarization moments are helpful in understanding the symmetry of the atomic polarization, as each moment has the symmetry of a particular spherical harmonic $Y_{\kappa q}(\theta, \phi)$. Note that the symmetry is an invariant of physical rotations of the system. An example is Larmor precession: the linear Zeeman effect causes polarization moments with the same rank κ and different q to transform into each other, but does not change the rank κ or the symmetry of the angular momentum, as discussed in Sec. 2.2. In the special case of rotations around $\hat{\mathbf{z}}$, no moments are mixed—components are merely altered by a phase factor.

In addition, the multipole expansion is useful in certain situations for reducing the complexity of the density matrix evolution equations, especially for states with large angular momentum. In molecular spectroscopy, one typically deals with states of much larger angular momenta (rotational quantum numbers $\simeq 100$) than for atoms.

In this case, the standard Liouville equations of motion form a large coupled system that can be difficult to solve. However, the equations of motion for the multipole expansion coefficients can be much simpler (Auzinsh and Ferber, 1991). This idea was introduced by Dyakonov (1964) and Ducloy (1976) and later applied to the analysis of a large variety of nonlinear magneto-optical effects in diatomic molecules (see the book by Auzinsh and Ferber, 1995, and references therein).

We can apply the idea of the polarization moments representing the symmetry of the system to the analysis of relaxation processes. Suppose there is some relaxation mechanism that is on average not associated with any specific directions in space, such as relaxation in atomic collisions. Because the index q describes spatial components, the relaxation rates for different polarization moments can depend on κ but not on q. It turns out, there are certain general inequalities that constrain possible relative values of the relaxation rates for different polarization moments (see, for example, Auzinsh and Ferber, 1995, Sec. 5.8).

2.3.3 Relation to the probability surfaces

We now find an expression for the angular-momentum probability surfaces in terms of the polarization moments. Expanding the density matrix in the definition of the AMPS (Eq. 2.15) in polarization moments, we have

$$\begin{aligned}\rho_{FF}(\theta,\phi) &= \sum_{\kappa=0}^{2F}\sum_{q=-\kappa}^{\kappa}\langle FF(\theta,\phi)|\rho^{\kappa q}\mathcal{T}_q^{\kappa}|FF(\theta,\phi)\rangle \\ &= \sum_{\kappa=0}^{2F}\sum_{q=-\kappa}^{\kappa}\rho^{\kappa q}\langle FF|\mathscr{D}^{\dagger}(\phi,\theta,0)\mathcal{T}_q^{\kappa}\mathscr{D}(\phi,\theta,0)|FF\rangle.\end{aligned} \tag{2.36}$$

Using the definition of an irreducible spherical tensor (Eq. C.12) and Eq. (2.27) for the matrix elements of the polarization operators, we can write Eq. (2.36) as

$$\begin{aligned}\rho_{FF}(\theta,\phi) &= \sum_{\kappa=0}^{2F}\sum_{q=-\kappa}^{\kappa}\rho^{\kappa q}\sum_{q'}\langle FF|D_{qq'}^{(\kappa)*}T_{q'}^{\kappa}|FF\rangle \\ &= \sum_{\kappa=0}^{2F}\sum_{q=-\kappa}^{\kappa}\rho^{\kappa q}\sqrt{\frac{2\kappa+1}{2F+1}}\langle FF\kappa 0|FF\rangle D_{q0}^{(\kappa)*}.\end{aligned} \tag{2.37}$$

In this special case, the Wigner D-function is given by a spherical harmonic (Varshalovich *et al.*, 1988, Eq. 4.17(1)):

$$D^{(\kappa)}_{q0}(\phi,\theta) = \sqrt{\frac{4\pi}{2\kappa+1}}Y^*_{\kappa q}(\theta,\phi), \tag{2.38}$$

giving the AMPS as an expansion in the spherical harmonics (Alexandrov *et al.*, 2005):

$$\rho_{FF}(\theta,\phi) = \sqrt{\frac{4\pi}{2F+1}}\sum_{\kappa=0}^{2F}\sum_{q=-\kappa}^{\kappa}\langle FF\kappa 0|FF\rangle\rho^{\kappa q}Y_{\kappa q}(\theta,\phi). \tag{2.39}$$

Given a probability distribution $\rho_{FF}(\theta,\phi)$, the polarization moments $\rho^{\kappa q}$ and thus the density matrix elements $\rho_{mm'}$ can be recovered using the orthonormality of the spherical harmonics, so all three are complete and equivalent descriptions of the ensemble-averaged polarization. All three descriptions can be useful in calculations, especially in the large-F limit, for which $\rho_{FF}(\theta,\phi)$ corresponds [apart from a normalization factor (Auzinsh and Ferber, 1995)] to the classical probability distribution of the angular momentum direction.

> Another way to visually represent angular-momentum states quite similar to the angular-momentum probability surfaces is to plot a spatial distribution related to the *Wigner function* for angular-momentum states (see, for instance, Dowling *et al.*, 1994). The Wigner function is defined with a formula much like Eq. (2.39):
>
> $$W(\theta,\phi) = \sum_{\kappa=0}^{2F}\sum_{q=-\kappa}^{\kappa}\rho^{\kappa q}Y_{\kappa q}(\theta,\phi), \tag{2.40}$$
>
> the essential difference being that the contributions of polarization moments of various ranks are weighted differently. This difference has consequences for the physical interpretation of the surfaces: the angular-momentum probability surfaces represent probability distributions and so are always positive, while the Wigner functions can be negative and cannot be interpreted as probability distributions. Wigner functions are sometimes plotted as positive distributions by defining
>
> $$f(\theta,\phi) = 1 + \frac{W(\theta,\phi)}{\sqrt{F(F+1)}}. \tag{2.41}$$

2.4 Symmetries of the probability surfaces

We have seen in the previous section that there is a one-to-one correspondence between the density matrix for the Zeeman sublevels of a state with total angular momentum F and the angular-momentum probability surface for the state.

Armed with this result, we can deepen our understanding of the symmetry properties of the polarization surfaces. Specifically, the symmetry of the angular-momentum probability surface can reveal, at a glance, important information about specific density-matrix elements. For example, the k-fold symmetry with respect to the quantization axis of the angular-momentum probability surface corresponds to the $|\Delta m| = k$ coherences in the density matrix.

This can be stated more precisely in the following way: The angular-momentum probability surface has k-fold symmetry about some axis if and only if the density matrix, when written with the quantization axis chosen to lie along this symmetry axis, only has nonzero coherences (i.e., off-diagonal matrix elements) with $\Delta m = kN$, where N is an integer.

To prove the general result regarding the connection between the coherences and the symmetry of the angular-momentum probability surface, we start by noting that, if the surface is invariant under a certain rotation, then, due to the one-to-one correspondence of the surface and the density matrix, the latter is also invariant under such rotation. Let us consider rotations about the quantization axis. Under a rotation by an angle φ, the $\rho_{mm'}$ element of the density matrix is multiplied by a phase factor $e^{i(m-m')\varphi}$ (Appendix B). If there is k-fold symmetry, under a rotation by an angle $\varphi = 2\pi/k$, the probability surface and thus the density matrix will remain unchanged. Thus

$$e^{i(m-m')2\pi/k}\rho_{mm'} = e^{iN2\pi}\rho_{mm'}, \tag{2.42}$$

where N is an integer, which requires that either $m - m' = kN$ or $\rho_{mm'} = 0$. The proof in the converse direction is similarly straightforward: the density matrix that only has $m - m' = kN$ coherences is invariant with respect to a rotation by $\varphi = 2\pi/k$, and so is the corresponding surface.

Consider a density matrix for $F = 2$:

$$\rho = \begin{pmatrix} \frac{7}{32} & 0 & -\frac{\sqrt{\frac{3}{2}}}{16} & 0 & \frac{7}{32} \\ 0 & \frac{1}{8} & 0 & \frac{1}{8} & 0 \\ -\frac{\sqrt{\frac{3}{2}}}{16} & 0 & \frac{5}{16} & 0 & -\frac{\sqrt{\frac{3}{2}}}{16} \\ 0 & \frac{1}{8} & 0 & \frac{1}{8} & 0 \\ \frac{7}{32} & 0 & -\frac{\sqrt{\frac{3}{2}}}{16} & 0 & \frac{7}{32} \end{pmatrix}. \tag{2.43}$$

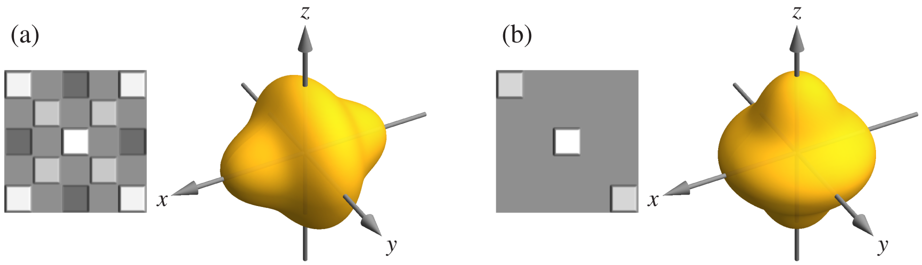

Figure 2.5: (a) The AMPS and density matrix (shown schematically) for ρ of Eq. (2.43). The density matrix has only coherences with $|\Delta m| = 2$ and 4 (zeros are represented by 50% gray, lighter shades are positive values, and darker shades are negative), corresponding to two-fold symmetry about the z-axis. (b) Rotating the surface by 90 degrees results in rotational symmetry about the z-axis; this implies that the density matrix has no coherences.

A schematic representation of the density matrix and the corresponding angular-momentum probability surface are shown in Fig. 2.5(a). We see that the only nonzero coherences are those with $|\Delta m| = 2$ and 4, and the probability surface is two-fold symmetric with respect to the quantization axis along z.

Looking at Fig. 2.5(a), it is clear that the surface has another symmetry, namely, that it is invariant with respect to rotations about the x-axis. (This may not be clear from just looking at the density matrix, however.) Suppose we therefore rotate the surface so that this symmetry axis is along the quantization axis (Fig. 2.5b). The surface is then k-fold symmetric about the quantization axis for arbitrary k. Suppose a coherence $\rho_{mm'}$ is nonzero for some $m \neq m'$. Then we must have $m - m' = kN$ for some integer N and every k. But if we choose $k > |m - m'|$ the equality cannot be satisfied. This means that if the surface is totally symmetric around an axis, the density matrix will have no coherences when written in the basis corresponding to that axis (Fig. 2.5b).

Thus if we have a surface with various axes of symmetry, in order to write the density matrix in the simplest form, we should choose the quantization axis along the axis of highest symmetry. While this axis may be difficult to determine directly from the density matrix, it can be found by simply looking at the angular-momentum probability surface.

Chapter 3

The Liouville Equation

The state of a system, whether it is described by a wave function or, more generally, by a density matrix, evolves in time. The evolution is governed by the initial conditions, the internal structure of the particles, as well as by external fields such as static electric and magnetic fields, or light fields. In addition, a system under study is generally not completely isolated from the environment, and the interactions with the environment must be modeled by including phenomenological terms into the evolution equations. These interactions generally lead to relaxation and repopulation—for example, radiative decay, collisions, and the departure and arrival of particles from and to the system (e.g., atoms flying into and out of the interaction region).

In this chapter, we derive the density-matrix evolution equation from the Schrödinger equation, and use it to describe polarized atoms evolving in a static electric field. We then discuss the inclusion of phenomenological terms describing relaxation and repopulation into the evolution equation, and obtain the steady-state solution for the density matrix in a simple case of a $F = 1 \to F = 0$ transition subject to linearly polarized light and a static magnetic field in the Faraday geometry.

3.1 Temporal evolution of the density matrix

3.1.1 Derivation of the Liouville equation

To derive an equation describing the evolution of a density matrix, we first take the time derivative of ρ, using the explicit definition in terms of the average of the individual atomic wave functions:

$$\begin{aligned} i\hbar\frac{d}{dt}\rho &= i\hbar\frac{1}{N}\sum_{i=1}^{N}\frac{d}{dt}|\psi_i\rangle\langle\psi_i| \\ &= \frac{1}{N}\sum_{i=1}^{N}\left[\left(i\hbar\frac{d}{dt}|\psi_i\rangle\right)\langle\psi_i| + |\psi_i\rangle\left(i\hbar\frac{d}{dt}\langle\psi_i|\right)\right]. \end{aligned} \tag{3.1}$$

The expression is now in terms of the evolution of the atomic wave functions, and so we can use the time-dependent Schrödinger equation

$$i\hbar\frac{d}{dt}|\psi\rangle = H|\psi\rangle \tag{3.2}$$

and its Hermitian conjugate

$$-i\hbar\frac{d}{dt}\langle\psi| = \langle\psi|H. \tag{3.3}$$

This gives

$$\begin{aligned} i\hbar\frac{d}{dt}\rho &= \frac{1}{N}\sum_{i=1}^{N}\left(H|\psi_i\rangle\langle\psi_i| - |\psi_i\rangle\langle\psi_i|H\right) \\ &= [H,\rho]. \end{aligned} \tag{3.4}$$

This equation is the *Liouville equation* for a density matrix.

3.1.2 Example: alignment-to-orientation conversion

Now that we have introduced the density matrix, the equations describing its evolution, and the polarization probability surfaces, let us consider an example showing how these can be applied in practice.

Consider $F = 1$ atoms prepared in the state described by the density matrix (2.16) and shown in Fig. 2.1(a). Suppose an electric field $\boldsymbol{\mathcal{E}}$ is applied along $\hat{\mathbf{x}}$. We will use the Liouville equation to find the evolution of the state and visualize the evolution with the angular-momentum probability surfaces.

The effective second-order Hamiltonian describing the interaction of the electric field with the atoms can be written in terms of scalar ($\kappa = 0$), vector ($\kappa = 1$), and tensor ($\kappa = 2$) parts, each given by a rank-κ tensor product between the electric field and its complex conjugate dotted with a rank-κ irreducible tensor operator $\hat{\alpha}^{\kappa}$:

$$H_{\text{eff}} = \sum_{\kappa=0}^{2}\{\mathcal{E}^{(1)} \otimes \mathcal{E}^{(1)*}\}^{\kappa} \cdot \hat{\alpha}^{\kappa}. \tag{3.5}$$

The reduced matrix element of $\hat{\alpha}^{\kappa}$ is given by the polarizability α_κ of the atomic state multiplied by a numerical coefficient set according to a convention:

$$\begin{aligned}\langle F\|\hat{\alpha}^{\kappa}\|F\rangle &= -\frac{\sqrt{2F+1}}{2\langle 1,\kappa \pmod 2, 1, -\kappa \pmod 2|\kappa,0\rangle\langle FF\kappa 0|FF\rangle}\alpha_\kappa \\ &= \begin{cases} \frac{\sqrt{3}}{2}\alpha_0\sqrt{2F+1} & \text{for } \kappa=0 \\ -\frac{1}{\sqrt{2}}\alpha_1\sqrt{2F+3+\frac{1}{F}} & \text{for } \kappa=1 \\ -\frac{\sqrt{3}}{2\sqrt{2}}\alpha_2\sqrt{2F+7-\frac{3}{F}+\frac{24}{2F-1}} & \text{for } \kappa=2\,. \end{cases}\end{aligned} \tag{3.6}$$

Neglecting the scalar polarizability, we find for the Hamiltonian in our example

$$H_{\text{eff}} = \begin{pmatrix} \frac{1}{4}\alpha_2\mathcal{E}_x^2 & 0 & -\frac{3}{4}\alpha_2\mathcal{E}_x^2 \\ 0 & -\frac{1}{2}\alpha_2\mathcal{E}_x^2 & 0 \\ -\frac{3}{4}\alpha_2\mathcal{E}_x^2 & 0 & \frac{1}{4}\alpha_2\mathcal{E}_x^2 \end{pmatrix}. \tag{3.7}$$

Using this Hamiltonian in the Liouville equation (3.4) we obtain the following set of differential equations for the density-matrix elements $\rho_{m,m'}$:

$$\dot{\rho}_{1,1} = i\frac{\omega_S}{2}\left(\rho_{-1,1}-\rho_{1,-1}\right), \tag{3.8a}$$

$$\dot{\rho}_{1,0} = i\frac{\omega_S}{2}\left(\rho_{-1,0}-\rho_{1,0}\right), \tag{3.8b}$$

$$\dot{\rho}_{1,-1} = i\frac{\omega_S}{2}\left(\rho_{-1,-1}-\rho_{1,1}\right), \tag{3.8c}$$

$$\dot{\rho}_{0,1} = i\frac{\omega_S}{2}\left(\rho_{0,1}-\rho_{0,-1}\right), \tag{3.8d}$$

$$\dot{\rho}_{0,0} = 0, \tag{3.8e}$$

$$\dot{\rho}_{0,-1} = i\frac{\omega_S}{2}\left(\rho_{0,-1}-\rho_{0,1}\right), \tag{3.8f}$$

$$\dot{\rho}_{-1,1} = i\frac{\omega_S}{2}\left(\rho_{1,1}-\rho_{-1,-1}\right), \tag{3.8g}$$

$$\dot{\rho}_{-1,0} = i\frac{\omega_S}{2}\alpha_2\left(\rho_{1,0}-\rho_{-1,0}\right), \tag{3.8h}$$

$$\dot{\rho}_{-1,-1} = i\frac{\omega_S}{2}\left(\rho_{1,-1}-\rho_{-1,1}\right), \tag{3.8i}$$

where

$$\omega_S = \frac{2\pi}{\tau_S} = \frac{3\alpha_2\mathcal{E}^2}{2\hbar} \tag{3.9}$$

is the Stark splitting, i.e., the energy difference between the eigenstates of the Hamiltonian. (For $F = 1$ there is only one such splitting.) Solving the differential equations, we find for the time-dependent density matrix

$$\rho(t) = \begin{pmatrix} \sin^2\left(\frac{\omega_S t}{2}\right) & 0 & \frac{i}{2}\sin\omega_S t \\ 0 & 0 & 0 \\ -\frac{i}{2}\sin\omega_S t & 0 & \cos^2\left(\frac{\omega_S t}{2}\right) \end{pmatrix}. \tag{3.10}$$

This formula explicitly shows periodic evolution of the density matrix at a frequency ω_S. Since this evolution is induced by Stark splitting, it is known as *Stark beats*, in analogy to the beating that one hears when two closely spaced audio-frequency tones are played simultaneously.

We can visualize the dynamic evolution of the atomic polarization using the probability surface. The radius vector describing the probability surface is (Eq. 2.15; see also Sec. B.2),

$$\rho_{FF}(\theta, \phi) = \frac{3}{8} + \frac{1}{8}\cos 2\theta - \frac{1}{2}\cos\theta\cos\omega_S t - \frac{1}{4}\sin 2\phi\,\sin^2\theta\sin\omega_S t. \tag{3.11}$$

This surface is plotted in Fig. 3.1 for several values of t. The surface exhibits the changing symmetry of the atomic polarization. Initially the ensemble has a preferred direction: the surface is symmetric about the z-axis, but not symmetric with respect to inversion of the z-axis—it "points," or has orientation, in the $-\hat{\mathbf{z}}$-direction. At $t = \tau_S/4$ the "doughnut"-shaped surface has a preferred axis (it is symmetric about $\hat{\mathbf{x}} + \hat{\mathbf{y}}$), but no preferred direction (it is the same in both the $\hat{\mathbf{x}} + \hat{\mathbf{y}}$ and $-(\hat{\mathbf{x}} + \hat{\mathbf{y}})$ directions; hence it is said to be aligned. The ensemble continues to oscillate between states that contain orientation and those that contain only alignment. Thus this type of evolution is known as alignment-to-orientation conversion, because it can be responsible for the appearance of orientation in systems in which only alignment was initially created (see Auzinsh and Ferber, 1992; Budker *et al.*, 2002a, and references therein).

3.2 Relaxation and repopulation

3.2.1 General discussion

The Liouville equation as derived from the Schrödinger equation only describes evolution that is governed by a Hamiltonian. If the atomic system of interest is interacting with the environment, i.e., degrees of freedom not taken into account in the density matrix, the evolution is in general not of this form. The terms

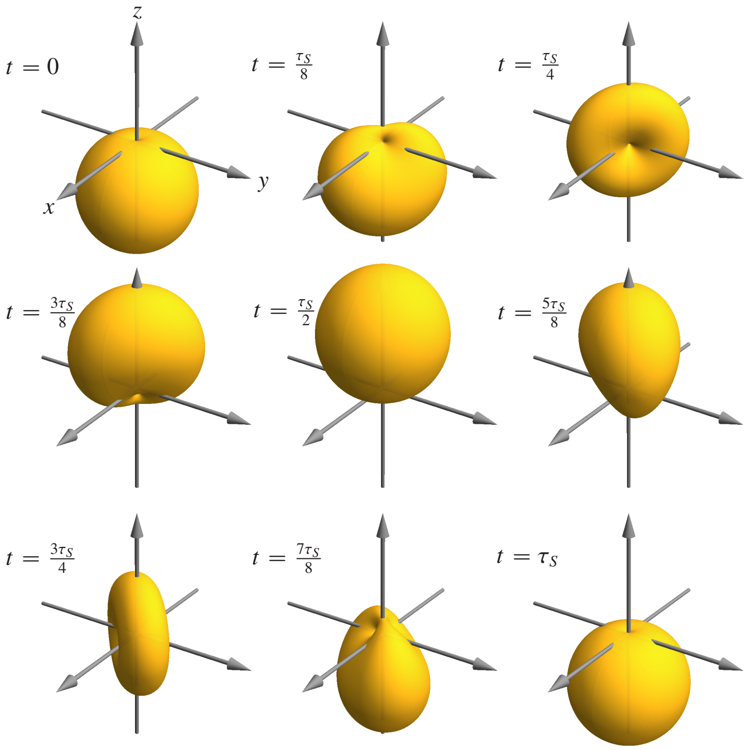

Figure 3.1: A sequence of AMPS representing a state with $F = 1$ evolving due to an electric field. The state is initially ($t = 0$) stretched along $-\hat{\mathbf{z}}$ and an electric field is applied along $\hat{\mathbf{y}}$, causing Stark beats with period τ_S. At $t = \tau_S/4$, the atoms are aligned along $\hat{\mathbf{x}} + \hat{\mathbf{y}}$. At $t = \tau_S/2$ the atoms have orientation in the $+\hat{\mathbf{z}}$-direction, at $t = 3\tau_S/4$ they are aligned along $\hat{\mathbf{x}} - \hat{\mathbf{y}}$, and, finally, at $t = \tau_S$ the polarization returns to its initial state.

describing the evolution due to interaction with the environment can often be written phenomenologically.

In fact, these phenomenological terms are often required even when the atoms in the system are not interacting with other atoms in the environment, e.g., the walls of a container. Each atom interacts with the quantum vacuum, which is the cause of spontaneous decay of excited states. In a calculation in which the fields are described quantum mechanically, the fluctuations of the quantum vacuum are included in the system. However, we typically employ the semiclassical approach, in which the atoms are treated quantum mechanically, but the fields are treated classically. In this case the quantum vacuum is outside the system and the effects due to it must be included "by hand."

The phenomenological terms can conveniently be divided into relaxation terms, which describe the decay of atomic populations and coherences, and repopulation terms, which describe the transfer of populations and coherences that occur along with the decay. If the relaxation of the amplitude of an atomic state $|n\rangle$ is assumed exponential with rate $\Gamma_n/2$, the rate of change of the population of this level due to relaxation is given by $\dot{\rho}_{nn} = -\Gamma_n \rho_{nn}$. Furthermore, the rate of change of a coherence

$\rho_{nn'}$ is given by the average of the decay rates: $\dot{\rho}_{nn'} = -(\Gamma_n + \Gamma_{n'})\rho_{nn'}/2$. (This is equivalent to the coherence decaying at the sum of the decay rates for the amplitudes in the wave function picture.) These terms can be conveniently included in the Liouville equation using the *relaxation matrix* $\widehat{\Gamma}$ as (Stenholm, 2005)

$$i\hbar\frac{d}{dt}\rho = [H, \rho] - i\hbar\frac{1}{2}(\widehat{\Gamma}\rho + \rho\widehat{\Gamma}). \tag{3.12}$$

Here $\widehat{\Gamma}$ is a diagonal matrix with the population decay rate of each state on the diagonal. These rates can include terms due to spontaneous emission and collisions, as well as atoms leaving the experimental volume (*transit relaxation*). For example, if an atomic system is subject to relaxation due to spontaneous decay and atomic transit, the diagonal matrix elements corresponding to ground states will be given by the transit rate γ, and those corresponding to excited states will be given by $\gamma + \Gamma$, where Γ is the excited-state decay rate.

As atomic states relax, populations and coherences are generally transferred, or repopulated, into other states (this must be true if the total number of atoms in the system is constant). For example, as atoms leave the region of interest, other atoms may be entering (transit repopulation). Depending on the situation, these "new" atoms may be polarized or unpolarized. For example, if the incoming atoms are unpolarized ground-state atoms with n sublevels in the ground state, the influx term in the Liouville equation is a diagonal matrix, which we will denote by Λ, with the ground-state terms equal to γ/n, where γ is the *transit rate*. This form of the influx term ensures a proper normalization of the density matrix as we can see from the trivial case of no external fields. Then the commutator term in the Liouville equation is zero (i.e., the Hamiltonian commutes with the density matrix), so the Liouville equation reduces to

$$i\hbar\frac{d}{dt}\rho = -i\hbar\frac{1}{2}(\widehat{\Gamma}\rho + \rho\widehat{\Gamma}) + i\hbar\Lambda = 0 \tag{3.13}$$

in the steady state. The upper-state and off-diagonal elements of the density matrix are zero; for the ground-state diagonal elements, the equation is written

$$-i\gamma\rho_{mm} + i\gamma/n = 0, \tag{3.14}$$

with solution $\rho_{mm} = 1/n$ for the n nonzero elements.

Another repopulation term describes atoms that spontaneously decay from the upper states and end up in one of the lower levels described by the density matrix, leading to the transfer of populations and possibly also coherences from the upper to the lower states. We will discuss the specific form of the repopulation matrix for this case in Sec. 3.2.2. Comprehensive discussion of the inclusion of relaxation in the density-matrix equations is given by, for example, Stenholm (2005), Blum (1996), and Shore (1990).

3.2.2 Repopulation via spontaneous decay

Barrat and Cohen-Tannoudji (1961) have shown that, given a density matrix ρ_{rs} in an upper state, the rate of change of the lower-state density matrix ρ_{mn} due to spontaneous emission is given by

$$\dot{\rho}_{mn} = \sum_{r,s} \frac{4\omega_{rm}^3}{3\hbar c^3} \mathbf{d}_{mr} \cdot \mathbf{d}_{sn} \rho_{rs} = \sum_{r,s} F_{mn}^{sr} \rho_{rs}, \tag{3.15}$$

where $F_{mn}^{sr}\rho_{rs}$, given by

$$F_{mn}^{sr} = \frac{4\omega_{rm}^3}{3\hbar c^3} \mathbf{d}_{mr} \cdot \mathbf{d}_{sn}, \tag{3.16}$$

is the *spontaneous-emission operator*. The sum over the upper pair of indices can also be written as a trace, which results in the compact form

$$\dot{\rho} = \mathrm{Tr}\, \rho F. \tag{3.17}$$

The rigorous derivation of this result requires quantum electrodynamics. As an alternative, let us present a heuristic explanation for the various factors in Eq. (3.15). A well-known classical electrodynamics formula tells us that the rate of emission of radiation from an oscillating dipole moment $\mathbf{d}(t) = \mathbf{d} \sin \omega t$ is

$$\mathcal{I} = \frac{2}{3c^3} \ddot{\mathbf{d}}(t)^2 = \frac{2\omega^4}{3c^3} \mathbf{d} \cdot \mathbf{d}. \tag{3.18}$$

To convert this expression into a rate for the emission of photons, we divide by the energy of a photon, $\hbar\omega$, to find

$$\frac{2\omega^3}{3\hbar c^3} \mathbf{d} \cdot \mathbf{d}. \tag{3.19}$$

This formula resembles Eq. (3.15), which can be considered its quantum-mechanical analog. In the quantum-mechanical case, a sum must be performed over all possible dipole moments that connect the upper state to a particular lower-state population or coherence.

Another way to justify these formulas comes from symmetry considerations. We have seen that the dipole transition rate induced by an optical field $\boldsymbol{\mathcal{E}}$ is given by

$(\mathbf{d}\cdot\boldsymbol{\mathcal{E}})^2$, i.e., the square of the transition matrix element. Just keeping the directional information from the electric field, we can write this in terms of the polarization vector $\hat{\boldsymbol{\varepsilon}}$: $(\mathbf{d}\cdot\hat{\boldsymbol{\varepsilon}})^2$. In spontaneous decay, the electric field inducing the transitions (produced by the quantum vacuum fluctuations) has all possible polarizations. The total transition probability is the sum over the probabilities for all these polarizations; since there is no particular polarization of the electric field, no polarization information can remain in the formula for the total spontaneous decay rate. In this case, the sum over the terms $(\mathbf{d}\cdot\hat{\boldsymbol{\varepsilon}})^2$ must not contain $\hat{\boldsymbol{\varepsilon}}$, but must still be a scalar that is quadratic in $\mathbf{d}$. The only possibility then is $\mathbf{d}\cdot\mathbf{d}$.

The rate for emission into a particular electromagnetic mode with polarization $\hat{\boldsymbol{\varepsilon}}$ while generating a particular ground-state coherence ρ_{mn} is

$$\frac{d\Phi}{d\Omega}=\frac{\omega^3}{2\pi\hbar c^3}\sum_{rs}\hat{\boldsymbol{\varepsilon}}^*\cdot\mathbf{d}_{mr}\rho_{rs}\mathbf{d}_{sn}\cdot\hat{\boldsymbol{\varepsilon}},\tag{3.20}$$

where $d\Omega$ is the differential solid angle in the propagation direction of the mode. Summing over two transverse polarizations and integrating over angles introduces a factor $8\pi/3$ and yields Eq. (3.15). If we take the trace over the ground state and multiply by $\hbar\omega$ to convert to intensity, on the other hand, we find the fluorescence intensity of a particular polarization emitted into a solid angle:

$$\frac{d\mathcal{I}}{d\Omega}=\frac{\omega^4}{2\pi c^3}\sum_{mrs}\hat{\boldsymbol{\varepsilon}}^*\cdot\mathbf{d}_{mr}\rho_{rs}\mathbf{d}_{sm}\cdot\hat{\boldsymbol{\varepsilon}}.\tag{3.21}$$

We now examine what kinds of atomic polarization can be transferred from the upper to the lower state. The explicit form of the spontaneous-emission operator (Eq. 3.15) tells us that, in general, coherences can be transferred from the upper to the lower state via spontaneous emission. This is not surprising, because we can quite easily create a situation in which it is clear that only populations should be transferred when viewed in one basis, but must involve coherences when the basis is rotated.

Consider a closed $J=1/2\rightarrow J'=1/2$ transition. Suppose that initially we have only the $m'=1/2$ sublevel populated, which can then decay to the ground state. The initial excited-state density matrix is

$$\rho'=\begin{pmatrix}1&0\\0&0\end{pmatrix}.\tag{3.22}$$

The final populations of the ground $m=1/2$ and $m=-1/2$ sublevel are proportional to the square of the corresponding $3j$ symbols (or Clebsch–Gordan coefficients) and

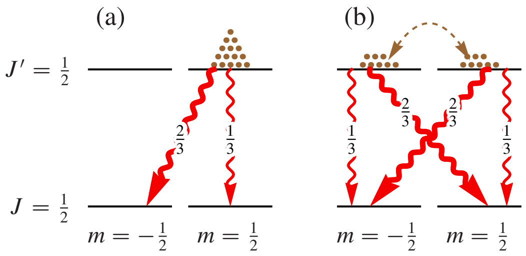

Figure 3.2: Spontaneous decay to a $J = 1/2$ ground state of (a) a $|J' = 1/2, m' = 1/2\rangle$ state and (b) the same state represented in a basis in which it is polarized along $\hat{\mathbf{x}}$. Arrows representing spontaneous decay transitions are labeled with the corresponding branching ratios; coherence between atomic states is indicated with a dashed arrow. In (a) only populations are transferred to the ground state; in (b) both populations and coherences are transferred.

are found to be 1/3 and 2/3, respectively (Fig. 3.2a). Since the initial state (spins "pointing" along $\hat{\mathbf{z}}$, in the quantum-mechanical sense) is symmetric about the z-axis, and the process of spontaneous decay has no preferred direction, the final state must also be symmetric about the z-axis. Therefore there can be no coherences in the final state ground-state density matrix, and it is given by

$$\rho = \begin{pmatrix} \frac{1}{3} & 0 \\ 0 & \frac{2}{3} \end{pmatrix}. \tag{3.23}$$

In this basis only populations have been transferred by spontaneous decay.

Now, suppose that we rotate the basis so that in the new basis the spins in the upper state "point" along $\hat{\mathbf{x}}$. By symmetry, a state that points along $\hat{\mathbf{x}}$ has equal projections on the $m' = \pm 1/2$ states, so the initial-state populations must be the same and equal to 1/2. Also, because the initial state is a pure state, the coherences between the two basis states must be maximal, i.e., their magnitudes must also be 1/2. It turns out that the coherences are real (real coherences are generally associated with polarization along x, while imaginary coherences are associated with polarization along y). This can be verified by actually performing the rotation using the Wigner matrices (Appendix B). Therefore, in this basis, the density matrix for the same initial state takes the form

$$\tilde{\rho}' = \frac{1}{2}\begin{pmatrix} 1 & 1 \\ 1 & 1 \end{pmatrix}. \tag{3.24}$$

Applying the same rotation to the ground-state density matrix ρ gives

$$\tilde{\rho} = \frac{1}{2}\begin{pmatrix} 1 & -\frac{1}{3} \\ -\frac{1}{3} & 1 \end{pmatrix}. \tag{3.25}$$

This leads us to the conclusion that coherences in the initial density matrix $\tilde{\rho}'$ have been transferred to the ground-state density matrix $\tilde{\rho}$ by spontaneous decay. The coherences have, however, been "diluted" somewhat—their magnitude is 1/3 of that found in the initial, fully polarized state. This corresponds to the dilution of the longitudinal polarization that occurs between Eqs. (3.22) and (3.23): ρ' has the maximum possible difference between the two upper-state populations, and in ρ the difference between the ground-state populations is smaller. It can also be understood by examining the diagram of the processes in Fig. 3.2(b). Since the different modes of the quantum vacuum fluctuations are uncorrelated, coherence between two atomic states can only be transferred to ground states if both of the states decay into the same mode, i.e., both transitions have the same Δm. Here, the only pair of transitions that satisfy this are the two $\Delta m = 0$ transitions. But these transitions have a branching ratio of 1/3, so only that fraction of the coherence is transferred.

> Note that not only is the polarization diluted upon transfer to the ground state, but it also changes direction—the excited state (3.22) is oriented in the positive $\hat{\mathbf{z}}$ direction, while the resulting ground state (3.23) has orientation along $-\hat{\mathbf{z}}$. Such a reversal of orientation direction in the decay of a stretched state is a feature of $J = 1/2 \to J' = 1/2$ transitions and does not occur for states with higher angular momenta. A more detailed discussion of the dilution of polarization in spontaneous emission can be found in Chapter 5 of the book by Auzinsh and Ferber (1995).

Using Eq. (3.15) and the Wigner–Eckart theorem (Eq. C.19), we can find the result directly in any basis. We expand the dot product in the spherical basis and use the relation $d_q^\dagger = (-1)^q d_{-q}$ to obtain for a $J \to J'$ transition

$$\begin{aligned} F_{m_1 m_2}^{m_1' m_2'} &= \frac{4\omega^3}{3\hbar c^3} \sum_q (-1)^q \langle J m_1 | d_q | J' m_2' \rangle \langle J' m_1' | d_{-q} | J m_2 \rangle \\ &= \frac{4\omega^3}{3\hbar c^3} \sum_q \langle J m_1 | d_q | J' m_2' \rangle \langle J m_2 | d_q | J' m_1' \rangle^* \\ &= (-1)^{2J - m_1 - m_2} (2J' + 1) \, \Gamma \sum_q \begin{pmatrix} J & 1 & J' \\ -m_1 & q & m_2' \end{pmatrix} \begin{pmatrix} J & 1 & J' \\ -m_2 & q & m_1' \end{pmatrix}, \end{aligned} \tag{3.26}$$

where in the last line we have used (Sobelman, 1992)

$$\frac{4\omega^3}{3\hbar c^3} \frac{1}{2J' + 1} \left| \langle J \| d \| J' \rangle \right|^2 = \Gamma, \tag{3.27}$$

where Γ is the spontaneous decay rate. Using this, we can write the matrix elements of the spontaneous-emission operator for the $J = 1/2 \to J' = 1/2$ system as

$$F = \begin{pmatrix} F_{1/2,1/2} = \Gamma \begin{pmatrix} \frac{1}{3} & 0 \\ 0 & \frac{2}{3} \end{pmatrix} & F_{1/2,-1/2} = \Gamma \begin{pmatrix} 0 & 0 \\ -\frac{1}{3} & 0 \end{pmatrix} \\ F_{-1/2,1/2} = \Gamma \begin{pmatrix} 0 & -\frac{1}{3} \\ 0 & 0 \end{pmatrix} & F_{-1/2,-1/2} = \Gamma \begin{pmatrix} \frac{2}{3} & 0 \\ 0 & \frac{1}{3} \end{pmatrix} \end{pmatrix}. \tag{3.28}$$

Here the outer matrix corresponds to the lower indices of F^{sr}_{mn} and is in the basis of the ground states; each of its matrix elements is a matrix in the basis of the upper state corresponding to the upper indices.

To obtain the rate of change of a ground-state density-matrix element ρ_{mn}, we take the trace $\mathrm{Tr}\, F_{mn}\rho'$. Performing this procedure with the initial states (3.22) and (3.24), we obtain

$$\dot{\rho} = \Gamma \begin{pmatrix} \frac{1}{3} & 0 \\ 0 & \frac{2}{3} \end{pmatrix} \qquad \text{and} \qquad \dot{\tilde{\rho}} = \frac{\Gamma}{2} \begin{pmatrix} 1 & -\frac{1}{3} \\ -\frac{1}{3} & 1 \end{pmatrix}, \tag{3.29}$$

as expected. These are the *initial* rates for the repopulation of the ground state—as the upper state populations and coherences exponentially decay at the rate Γ, the ground-state repopulation rate will decrease correspondingly.

3.3 Solving for the steady state: an example

In a system in which there are relaxation mechanisms, light fields are continuous wave (cw), and other external fields are held constant, the ensemble generally obtains a steady state. The steady state can be found by setting the derivatives in the Bloch equations to zero and solving the resulting system of algebraic equations.

In this section, we find the steady state density matrix in a simple case—that of linearly polarized light resonant with a $F = 1 \to F' = 0$ transition (Fig. 3.3). We choose the quantization axis to be along the light-propagation direction $\hat{\mathbf{z}}$ and the light-polarization axis to be along $\hat{\mathbf{x}}$; we also assume that there is a static magnetic field applied along $\hat{\mathbf{z}}$.

This system is the "canonical" system for our purposes, in that it is the simplest system in which nonlinear magneto-optical effects depending on ground-state alignment can occur. In Sec. 4.2 we will use the results obtained here to find the signals (e.g., optical rotation) observed in the transmitted light corresponding to various linear and nonlinear effects.

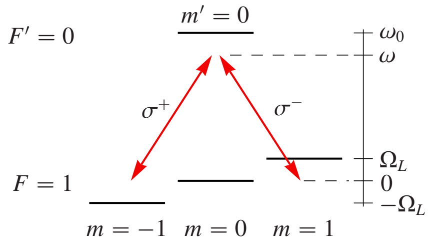

Figure 3.3: A $F = 1 \rightarrow F' = 0$ transition of frequency ω_0. The lower sublevels are split by an energy corresponding to the Larmor frequency Ω_L. The arrows indicate the interaction with light of frequency ω polarized perpendicular to the quantization axis. The upper state spontaneously decays at rate Γ.

Our eventual aim is to model an ensemble in which the atoms have a range of velocities—for example, thermally distributed atoms in a vapor cell (Fig. 3.4). The effect of atomic motion along the light-propagation direction is to Doppler-shift the light frequency in the reference frame of the atom; this leads to Doppler broadening of the observed signals. To approach this problem, we will initially neglect the motion along the z-axis, as if the atoms have been laser-cooled along this axis. The signals for this case can then be integrated over the Doppler shifts to find the result for the thermal ensemble. (Additional complications arise if the vapor cell is coated or contains buffer gas—this will be described in Chapter 7.)

We begin by finding the density-matrix evolution equation for the atoms in the laser beam. We assume that the atoms that leave the laser beam have their polarization destroyed before entering the beam again; thus only the atoms in the laser beam need be considered (this is the usual case for an uncoated, buffer-gas-free vapor cell). For simplicity, we will assume that the light-intensity profile is uniform, and will model the atoms' transit through the beam by assuming a uniform relaxation rate γ equal to the inverse of the average transit time (see Sec. 3.2.1).

Using the Hamiltonians for the magnetic-field–atom and light–atom interaction

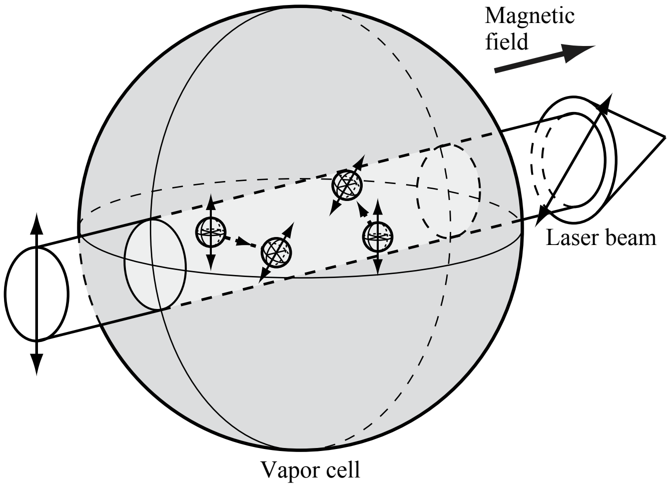

Figure 3.4: Atoms in a vapor cell subject to linearly polarized light and a static magnetic field. The atoms fly through the light beam at a rate γ. The interaction between the atoms and the light alters the light amplitude and polarization at the output.

(under the rotating-wave approximation, discussed in Sec. 3.3.2) we write the evolution equations for the density matrix describing both the lower and upper states. (This is in contrast to our discussion in earlier chapters, where we have mostly considered density matrices for only one state.) We then solve the equations in the steady-state condition.

3.3.1 The Hamiltonian

We use the basis states $|\xi F m\rangle$, where ξ represents additional quantum numbers, denoted by

$$|\xi F,1\rangle = \begin{pmatrix}1\\0\\0\\0\end{pmatrix}, \quad |\xi F,0\rangle = \begin{pmatrix}0\\1\\0\\0\end{pmatrix}, \quad |\xi F,-1\rangle = \begin{pmatrix}0\\0\\1\\0\end{pmatrix}, \quad |\xi' F',0\rangle = \begin{pmatrix}0\\0\\0\\1\end{pmatrix}. \tag{3.30}$$

In indices of density-matrix elements, we will refer to these states as simply m for the lower-state sublevels and m' for the upper-state sublevels. Thus, the density matrix takes the form

$$\rho = \begin{pmatrix} \rho_{1,1} & \rho_{1,0} & \rho_{1,-1} & \rho_{1,0'} \\ \rho_{0,1} & \rho_{0,0} & \rho_{0,-1} & \rho_{0,0'} \\ \rho_{-1,1} & \rho_{-1,0} & \rho_{-1,-1} & \rho_{-1,0'} \\ \rho_{0',1} & \rho_{0',0} & \rho_{0',-1} & \rho_{0',0'} \end{pmatrix}. \tag{3.31}$$

The total Hamiltonian H is the sum of the unperturbed Hamiltonian H_0, the light–atom-interaction Hamiltonian H_l, and the magnetic-field–atom-interaction Hamiltonian H_B. Taking the energy of the lower state to be zero, the unperturbed Hamiltonian H_0 is given by

$$H_0 = \begin{pmatrix} 0 & 0 & 0 & 0 \\ 0 & 0 & 0 & 0 \\ 0 & 0 & 0 & 0 \\ 0 & 0 & 0 & \hbar\omega_0 \end{pmatrix}, \tag{3.32}$$

where ω_0 is the transition frequency.

An x-polarized optical electric field $\boldsymbol{\mathcal{E}}$ is written

$$\boldsymbol{\mathcal{E}} = \mathcal{E}_0 \cos\omega t\, \hat{\mathbf{x}}, \tag{3.33}$$

where $\mathcal{E}_0$ is the electric field amplitude and ω is the light frequency. We assume that the atomic medium is optically thin, so that we can neglect the change in light polarization and intensity inside the medium when calculating the state of the medium. The light–atom interaction Hamiltonian is given by

$$\begin{aligned} H_l &= -\boldsymbol{\mathcal{E}} \cdot \mathbf{d} \\ &= -\mathcal{E}_0 \cos(\omega t)\, d_x \\ &= -\frac{1}{\sqrt{2}} \mathcal{E}_0 \cos(\omega t)\,(d_{-1} - d_{+1})\,, \end{aligned} \tag{3.34}$$

where $\mathbf{d}$ is the dipole operator. The matrix elements of d_{+1} and d_{-1} for this transition can be written using the Wigner–Eckart theorem (Appendix C.2) as

$$\langle \xi_1 F_1 m_1 | d_{\pm 1} | \xi_2 F_2 m_2 \rangle = (-1)^{F_1 - m_1} \langle \xi_1 F_1 \| d \| \xi_2 F_2 \rangle \begin{pmatrix} F_1 & 1 & F_2 \\ -m_1 & \pm 1 & m_2 \end{pmatrix}. \tag{3.35}$$

Reduced matrix elements with different ordering of states are related by (Eq. C.18):

$$\langle \xi_1 F_1 \| T^\kappa \| \xi_2 F_2 \rangle = (-1)^{F_1 - F_2} \langle \xi_2 F_2 \| T^\kappa \| \xi_1 F_1 \rangle^*, \tag{3.36}$$

and since the reduced dipole matrix element is real,

$$\langle \xi F \| d \| \xi' F' \rangle = -\langle \xi' F' \| d \| \xi F \rangle. \tag{3.37}$$

Using Eqs. (3.35) and (3.37), we have

$$d_{-1} = \frac{\langle \xi 1 \| d \| \xi' 0' \rangle}{\sqrt{3}} \begin{pmatrix} 0 & 0 & 0 & 0 \\ 0 & 0 & 0 & 0 \\ 0 & 0 & 0 & 1 \\ -1 & 0 & 0 & 0 \end{pmatrix}, \tag{3.38a}$$

$$d_{1} = \frac{\langle \xi 1 \| d \| \xi' 0' \rangle}{\sqrt{3}} \begin{pmatrix} 0 & 0 & 0 & 1 \\ 0 & 0 & 0 & 0 \\ 0 & 0 & 0 & 0 \\ 0 & 0 & -1 & 0 \end{pmatrix}. \tag{3.38b}$$

Thus H_l is given in matrix form by

$$H_l = \frac{\hbar \Omega_R \cos \omega t}{\sqrt{2}} \begin{pmatrix} 0 & 0 & 0 & 1 \\ 0 & 0 & 0 & 0 \\ 0 & 0 & 0 & -1 \\ 1 & 0 & -1 & 0 \end{pmatrix}, \tag{3.39}$$

where $\Omega_R = \langle \xi F \| d \| \xi' F' \rangle \mathcal{E}_0 / \left(\sqrt{3}\hbar\right)$ is the optical Rabi frequency.

The magnetic field interaction Hamiltonian H_B for a $\hat{\mathbf{z}}$-directed magnetic field $\mathbf{B}$ is given by

$$\begin{aligned} H_B &= -\boldsymbol{\mu}\cdot\mathbf{B} \\ &= g\mu_0\,\mathbf{F}\cdot\mathbf{B} \\ &= g\mu_0 F_z B \\ &= \hbar\Omega_L \begin{pmatrix} 1 & 0 & 0 & 0 \\ 0 & 0 & 0 & 0 \\ 0 & 0 & -1 & 0 \\ 0 & 0 & 0 & 0 \end{pmatrix}, \end{aligned} \tag{3.40}$$

where $\Omega_L = g\mu_0 B/\hbar$ is the Larmor frequency. Thus the total Hamiltonian is given by

$$\begin{aligned} H &= H_0 + H_l + H_B \\ &= \hbar \begin{pmatrix} \Omega_L & 0 & 0 & \frac{1}{\sqrt{2}}\Omega_R\cos\omega t \\ 0 & 0 & 0 & 0 \\ 0 & 0 & -\Omega_L & -\frac{1}{\sqrt{2}}\Omega_R\cos\omega t \\ \frac{1}{\sqrt{2}}\Omega_R\cos\omega t & 0 & -\frac{1}{\sqrt{2}}\Omega_R\cos\omega t & \omega_0 \end{pmatrix}. \end{aligned} \tag{3.41}$$

3.3.2 Rotating-wave approximation

We have now come up against the problem that the Hamiltonian has time dependence at the optical frequency. This oscillation is vital for the resonant behavior of the system to be observed. However, we would like to remove it from direct consideration if possible. Intuitively, it seems that it must be possible to avoid considering this time dependence, because its time scale is much shorter than any other time scale in the problem, and short enough so that any measurement will be an average over many cycles of the optical oscillation. To examine this, consider a two-state system with a Hamiltonian of the form

$$H = \hbar \begin{pmatrix} 0 & \Omega\sin\omega t \\ \Omega\sin\omega t & \omega_0 \end{pmatrix} = \hbar \begin{pmatrix} 0 & \frac{i\Omega}{2}\left(e^{-i\omega t} - e^{i\omega t}\right) \\ \frac{i\Omega}{2}\left(e^{-i\omega t} - e^{i\omega t}\right) & \omega_0 \end{pmatrix}. \tag{3.42}$$

The oscillating field with frequency ω and coupling strength $\hbar\Omega$ induces transitions between the two states with frequency splitting ω_0. The field can be written as the sum of two complex components with frequencies of opposite sign; in the case of a magnetic field coupling two Zeeman sublevels, one of these components corresponds to a magnetic field rotating with the Larmor precession and the other to a field rotating in the opposite direction. This Hamiltonian could also represent the coupling of two

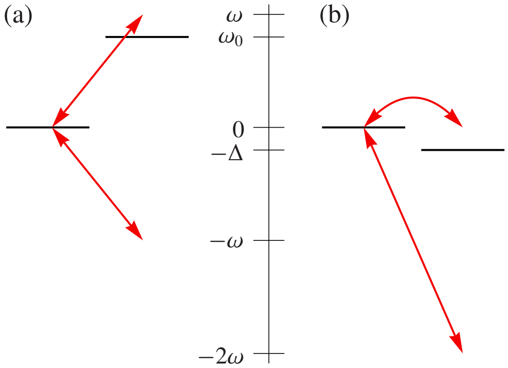

Figure 3.5: A two-level system subject to an oscillating external field. An energy scale in frequency units is shown. (a) In the laboratory frame, the atomic resonance frequency is ω_0 and the oscillation frequency is ω. One component of the oscillating field is detuned by $\Delta = \omega - \omega_0$ from the atomic resonance, while the other component is tuned 2ω below the first. (b) In the rotating frame, all oscillation and atomic resonance frequencies have been shifted by ω. The near-resonant component of the field is now at zero frequency, and the formerly upper state now lies Δ *below* the lower state, so that the relationship between the oscillation frequency and the resonance frequency remains intact. If the counter-rotating component at frequency -2ω is neglected, the problem is reduced to that of a static field coupling two close-lying levels. Note that as the frequency of the oscillating field is changed, the rotating frame must also be adjusted in order for the co-rotating component to remain static. The change in detuning is then reflected in the position of the "upper" state.

states by an electric field, in which case the physical interpretation of a rotation would not apply; however, the terminology of a "rotating wave" is still used by analogy. In any case, if $\omega \approx \omega_0$, one of the components (the "co-rotating") is near-resonant with the transition, while the second ("counter-rotating") is detuned from the first by 2ω (Fig. 3.5a). When the transition frequency is much greater than the linewidth of the transition (nearly always the case for optical transitions), the counter-rotating component can be considered far off-resonant and can be neglected.

The co-rotating component of the oscillating field can be rendered static by a suitable transformation into a new frame. For the magnetic-field case under consideration, this frame rotates around the z-axis along with the co-rotating component. According to Eq. (B.7) this transformation is produced by a rotation matrix of the form $D_{m'm} = e^{im\omega t}\delta_{m'm}$; we can multiply this matrix by an overall phase to obtain the transformation matrix

$$U = \begin{pmatrix} 1 & 0 \\ 0 & e^{-i\omega t} \end{pmatrix}. \tag{3.43}$$

This matrix, like any matrix that transforms one basis to another, is unitary, meaning that it satisfies $U^\dagger U = 1$. Since we are rotating the frame, this transformation is intended to act on the basis, so that its effect on a state vector is given by

$$|\widetilde{\psi}\rangle = U^\dagger|\psi\rangle. \tag{3.44}$$

What is the Hamiltonian in the rotating frame? Under a change of basis, an operator typically transforms as $\widetilde{\mathcal{O}} = U^\dagger \mathcal{O} U$. However, it is convenient to consider the Hamiltonian to transform slightly differently. The rotating frame, obtained using the time-dependent U, is not inertial, and so the evolution equation in this frame must be modified. This can be accounted for by defining a modified *effective Hamiltonian*

$$\widetilde{H}_{\text{eff}} = U^\dagger H U - i\hbar U^\dagger \frac{\partial U}{\partial t} \tag{3.45}$$

in the rotating frame. The first term on the right-hand side is the standard operator transformation, while the second term, independent of the Hamiltonian, corrects for the effect of the noninertial frame. It is analogous to a fictitious force in classical mechanics used to account for the modifications that Newton's laws undergo in an accelerating frame.

To derive the form (3.45) for the effective Hamiltonian, we start with the time-dependent Schrödinger equation in the laboratory frame:

$$H|\psi\rangle = i\hbar\frac{\partial}{\partial t}|\psi\rangle. \tag{3.46}$$

Multiplying both sides by $U^\dagger$ and inserting the identity operator $UU^\dagger$ in front of the state ket on each side, we obtain

$$U^\dagger H U U^\dagger|\psi\rangle = i\hbar U^\dagger \frac{\partial}{\partial t}\left(UU^\dagger|\psi\rangle\right). \tag{3.47}$$

Using Eq. (3.44), we find

$$\begin{aligned} U^\dagger H U|\widetilde{\psi}\rangle &= i\hbar U^\dagger \frac{\partial}{\partial t}\left(U|\widetilde{\psi}\rangle\right) \\ &= i\hbar U^\dagger\left[\left(\frac{\partial U}{\partial t}\right)|\widetilde{\psi}\rangle + U\frac{\partial}{\partial t}|\widetilde{\psi}\rangle\right]. \end{aligned} \tag{3.48}$$

This can be rearranged to form

$$\left(U^\dagger H U - i\hbar U^\dagger \frac{\partial U}{\partial t}\right)|\widetilde{\psi}\rangle = i\hbar\frac{\partial}{\partial t}|\widetilde{\psi}\rangle, \tag{3.49}$$

and comparison with Eq. (3.46) shows that the evolution in the rotating frame can be described by a Schrödinger equation with an effective Hamiltonian given by Eq. (3.45). From now on we will refer to this effective Hamiltonian simply as the rotating-frame Hamiltonian and denote it by $\widetilde{H}$.

For the two-level system described by the Hamiltonian (3.42), the rotating-frame Hamiltonian is found to be

$$\widetilde{H} = \hbar \begin{pmatrix} 0 & \frac{i\Omega}{2}\left(1 - e^{-2i\omega t}\right) \\ -\frac{i\Omega}{2}\left(1 - e^{2i\omega t}\right) & -\Delta \end{pmatrix}, \tag{3.50}$$

where $\Delta = \omega - \omega_0$ is the detuning from resonance. Insofar as Δ is much smaller than ω, we now have two nearly degenerate levels coupled by a static field and a far-off-resonant oscillating field (Fig. 3.5b). (In the magnetic-field case, from the point of view of the frame moving with the co-rotating component of the field, the counter-rotating component rotates at twice the oscillation frequency.) If ω is much greater than the linewidth of the transition, the effect of the oscillating field is negligible and can be ignored (the rotating-wave approximation), resulting in

$$\widetilde{H} \simeq \hbar \begin{pmatrix} 0 & \frac{i\Omega}{2} \\ -\frac{i\Omega}{2} & -\Delta \end{pmatrix}. \tag{3.51}$$

The Hamiltonian is now static; the factors of $1/2$ in the coupling terms have resulted from the fact that we have discarded half of the external field.

In the cases that we will consider, the unitary matrix U can always be written in the form

$$U = e^{-iAt}, \tag{3.52}$$

where A is a Hermitian matrix. For example, for the transformation matrix (3.43), we have

$$A = \begin{pmatrix} 0 & 0 \\ 0 & \omega \end{pmatrix}. \tag{3.53}$$

Using Eq. (3.52) in the definition of the rotating-frame Hamiltonian, we have

$$\widetilde{H} = U^{\dagger} H U - \hbar A. \tag{3.54}$$

This shows that the effect of the correction term in the rotating-wave Hamiltonian is to shift the atomic resonance frequencies by the same amount as the oscillating-field frequencies are shifted. We can also formulate a rule of thumb for choosing the transformation to go into the rotating frame: choose the diagonal elements of A so that when it is subtracted from the laboratory-frame Hamiltonian the atomic resonance frequencies are replaced by the oscillating field detunings. In the optical-field case, A will generally resemble the unperturbed Hamiltonian H_0 divided by $\hbar$, with optical frequencies in place of the atomic transition frequencies.

Following this procedure for the system described in Sec. 3.3.1, we choose the matrix

$$A = \begin{pmatrix} 0 & 0 & 0 & 0 \\ 0 & 0 & 0 & 0 \\ 0 & 0 & 0 & 0 \\ 0 & 0 & 0 & \omega \end{pmatrix}, \tag{3.55}$$

resulting in the static rotating-frame Hamiltonian

$$\widetilde{H} \simeq \hbar \begin{pmatrix} \Omega_L & 0 & 0 & \frac{1}{2\sqrt{2}}\Omega_R \\ 0 & 0 & 0 & 0 \\ 0 & 0 & -\Omega_L & -\frac{1}{2\sqrt{2}}\Omega_R \\ \frac{1}{2\sqrt{2}}\Omega_R & 0 & -\frac{1}{2\sqrt{2}}\Omega_R & -\Delta \end{pmatrix}. \tag{3.56}$$

Transforming the density matrix with the matrix U, we can find that the density matrix in the laboratory frame is given in terms of the rotating-frame density-matrix elements by

$$\rho = U\tilde{\rho}U^\dagger = \begin{pmatrix} \tilde{\rho}_{1,1} & \tilde{\rho}_{1,0} & \tilde{\rho}_{1,-1} & e^{i\omega t}\tilde{\rho}_{1,0'} \\ \tilde{\rho}_{0,1} & \tilde{\rho}_{0,0} & \tilde{\rho}_{0,-1} & e^{i\omega t}\tilde{\rho}_{0,0'} \\ \tilde{\rho}_{-1,1} & \tilde{\rho}_{-1,0} & \tilde{\rho}_{-1,-1} & e^{i\omega t}\tilde{\rho}_{-1,0'} \\ e^{-i\omega t}\tilde{\rho}_{0',1} & e^{-i\omega t}\tilde{\rho}_{0',0} & e^{-i\omega t}\tilde{\rho}_{0',-1} & \tilde{\rho}_{0',0'} \end{pmatrix}. \tag{3.57}$$

This formula will be useful when we need to interpret the results of the calculation of the rotating-frame density matrix. We see that the optical coherences in the laboratory and rotating frames differ by a phase factor oscillating at the optical frequency, while all other density-matrix elements are the same in the two frames.

3.3.3 Relaxation and repopulation

As discussed in Sec. 3.2.1, the effect of relaxation on the density-matrix evolution is not accounted for by the Hamiltonian and must be added "by hand." In the most easily described case, atoms in each basis state $|n\rangle$ relax at particular rates Γ_n, and there are no additional dephasing effects. Then the effect of relaxation can be written

$$\left.\frac{d\rho}{dt}\right|_{\text{relax}} = -\frac{1}{2}(\widehat{\Gamma}\rho + \rho\widehat{\Gamma}), \tag{3.58}$$

where the relaxation matrix $\widehat{\Gamma}$ is a diagonal matrix with the diagonal elements given by $\widehat{\Gamma}_{nn} = \Gamma_n$.

For the $F = 1 \rightarrow F' = 0$ transition under consideration, each sublevel undergoes relaxation at a rate γ due to the exit of atoms from the light beam. In addition, the upper state undergoes spontaneous decay at a rate Γ. The relaxation matrix is then given by

$$\widehat{\Gamma} = \begin{pmatrix} \gamma & 0 & 0 & 0 \\ 0 & \gamma & 0 & 0 \\ 0 & 0 & \gamma & 0 \\ 0 & 0 & 0 & \gamma + \Gamma \end{pmatrix}. \tag{3.59}$$

Note that this relaxation matrix is the same in the laboratory and rotating frames.

If the number of atoms in the system is conserved, there must be repopulation processes corresponding to the relaxation processes in order to replenish the atoms. These processes can be described by a repopulation matrix Λ, which may depend on ρ:

$$\left.\frac{d\rho}{dt}\right|_{\text{repop}} = \Lambda. \tag{3.60}$$

As atoms fly out of the beam, there are other atoms, assumed to be in the ground state but otherwise unpolarized, flying into the beam at the same rate. Since the atomic density is normalized to unity, atoms arrive in each of the three ground-state sublevels at a rate $\gamma/3$. Note that this is the simplest possible model for transit relaxation and repopulation. In this model, if the light is turned off and the system is left to relax via this mechanism, the ground-state population would return to its equilibrium state exponentially. This is not always the case experimentally. For a more in-depth discussion of transit relaxation, see, for example, the book by Auzinsh and Ferber (1995).

In addition, the atoms that spontaneously decay from the upper state also repopulate the ground state. In general, the transition rate between various pairs of upper- and lower-state sublevels can be different, and coherences as well as population can be transferred by spontaneous decay (Sec. 3.2.2). In this case, however, there is only one upper-state sublevel, so there are no coherences in the upper state and the spontaneous transition rates to all three lower-state sublevels are the same (i.e., the radiation is isotropic) and equal to $\Gamma\rho_{0'0'}/3$. Thus the repopulation matrix takes the form

$$\Lambda = (\gamma + \Gamma\rho_{0'0'}) \begin{pmatrix} \frac{1}{3} & 0 & 0 & 0 \\ 0 & \frac{1}{3} & 0 & 0 \\ 0 & 0 & \frac{1}{3} & 0 \\ 0 & 0 & 0 & 0 \end{pmatrix}. \tag{3.61}$$

This repopulation matrix is also the same in the laboratory and rotating frames.

3.3.4 Solution of the Liouville equation

The complete Liouville equation for the rotating-frame density matrix is written

$$i\hbar\frac{d}{dt}\tilde{\rho} = \left[\widetilde{H}, \tilde{\rho}\right] - i\hbar\frac{1}{2}(\widehat{\Gamma}\tilde{\rho} + \tilde{\rho}\widehat{\Gamma}) + i\hbar\Lambda. \tag{3.62}$$

Using the explicit matrices (3.56), (3.59), and (3.61), we find the evolution equations for the density-matrix elements in the rotating frame:

$$\dot{\tilde{\rho}}_{-1,-1} = -\gamma\tilde{\rho}_{-1,-1} + \frac{1}{3}\left(\gamma + \Gamma\tilde{\rho}_{0',0'}\right) + \frac{1}{\sqrt{2}}\Omega_R \operatorname{Im}\tilde{\rho}_{-1,0'}, \tag{3.63a}$$

$$\dot{\tilde{\rho}}_{0,0} = -\gamma\tilde{\rho}_{0,0} + \frac{1}{3}\left(\gamma + \Gamma\tilde{\rho}_{0',0'}\right), \tag{3.63b}$$

$$\dot{\tilde{\rho}}_{1,1} = -\gamma\tilde{\rho}_{1,1} + \frac{1}{3}\left(\gamma + \Gamma\tilde{\rho}_{0',0'}\right) - \frac{1}{\sqrt{2}}\Omega_R \operatorname{Im}\tilde{\rho}_{1,0'}, \tag{3.63c}$$

$$\dot{\tilde{\rho}}_{1,0} = \dot{\tilde{\rho}}^{*}_{0,1} = -\left(\gamma + i\Omega_L\right)\tilde{\rho}_{1,0} - \frac{i}{2\sqrt{2}}\Omega_R\tilde{\rho}_{0',0}, \tag{3.63d}$$

$$\dot{\tilde{\rho}}_{0,-1} = \dot{\tilde{\rho}}^{*}_{-1,0} = -\left(\gamma + i\Omega_L\right)\tilde{\rho}_{0,-1} - \frac{i}{2\sqrt{2}}\Omega_R\tilde{\rho}_{0,0'}, \tag{3.63e}$$

$$\dot{\tilde{\rho}}_{1,-1} = \dot{\tilde{\rho}}^{*}_{-1,1} = -\left(\gamma + 2i\Omega_L\right)\tilde{\rho}_{1,-1} - \frac{i}{2\sqrt{2}}\Omega_R\left(\tilde{\rho}_{1,0'} + \tilde{\rho}_{0',-1}\right), \tag{3.63f}$$

$$\begin{aligned}\dot{\tilde{\rho}}_{1,0'} = \dot{\tilde{\rho}}^{*}_{0',1} = &-\left(\gamma + \frac{1}{2}\Gamma + i\left(\Omega_L + \Delta\right)\right)\tilde{\rho}_{1,0'} \\ &- \frac{i}{2\sqrt{2}}\Omega_R\left(\tilde{\rho}_{0',0'} + \tilde{\rho}_{1,-1} - \tilde{\rho}_{1,1}\right),\end{aligned} \tag{3.63g}$$

$$\begin{aligned}\dot{\tilde{\rho}}_{-1,0'} = \dot{\tilde{\rho}}^{*}_{0',-1} = &-\left(\gamma + \frac{1}{2}\Gamma + i\left(\Delta - \Omega_L\right)\right)\tilde{\rho}_{-1,0'} \\ &- \frac{i}{2\sqrt{2}}\Omega_R\left(-\tilde{\rho}_{0',0'} + \tilde{\rho}_{-1,-1} - \tilde{\rho}_{-1,1}\right),\end{aligned} \tag{3.63h}$$

$$\dot{\tilde{\rho}}_{0,0'} = \dot{\tilde{\rho}}^{*}_{0',0} = -\left(\gamma + \frac{1}{2}\Gamma + i\Delta\right)\tilde{\rho}_{0,0'} - \frac{i}{2\sqrt{2}}\Omega_R\left(\tilde{\rho}_{0,-1} - \tilde{\rho}_{0,1}\right), \tag{3.63i}$$

$$\dot{\tilde{\rho}}_{0',0'} = -(\gamma + \Gamma)\tilde{\rho}_{0',0'} - \frac{1}{\sqrt{2}}\Omega_R\left(\operatorname{Im}\tilde{\rho}_{-1,0'} - \operatorname{Im}\tilde{\rho}_{1,0'}\right). \tag{3.63j}$$

Each term in these equations has a physical meaning that derives from our prior discussion of the Hamiltonian and the relaxation and repopulation matrices. For example, Eqs. (3.63a) and (3.63c) describe the rate of change of the population of the $m = -1$ and $m = 1$ sublevels of the ground state, respectively. The first term in each of these equations describes relaxation at a rate γ due to transit of the atoms out the beam, the second term describes repopulation due to transit and spontaneous decay, and the last term accounts for the interaction of the light field (proportional to the Rabi frequency Ω_R) and the electric-dipole moment that depends on the coherences between the $m = -1$ or $m = 1$ and the excited $m' = 0$ state. Because the density matrix is Hermitian, we have $\operatorname{Im} \rho_{m,m'} = (\rho_{mm'} - \rho^*_{mm'})/(2i) = (\rho_{mm'} - \rho_{m'm})/(2i)$. Note that Eqs. (3.63a) and (3.63c) are real, consistent with the mathematical fact that the diagonal elements of a Hermitian matrix are real and the physical fact that these elements represent populations.

To find the steady-state solution of Eqs. (3.63), we set the time derivatives on the left-hand side to zero, and solve the resulting system of linear equations. This would be a somewhat arduous task by hand, but it can be accomplished using a computer algebra system such as *Mathematica.* For experiments using allowed optical transitions, the transit rate γ is usually much slower than the upper-state spontaneous decay rate Γ. Using this as a simplifying assumption, the steady-state solution is given by

$$\begin{aligned}\tilde{\rho}_{-1,-1} = \frac{1}{D}\Big\{&8\gamma^2\Gamma^2\left[-4\Delta\kappa_2\Omega_L + 3\kappa_2^2\Omega_L^2 + \Delta^2(\kappa_2+2)(\kappa_2+4)\right]\\ &+ \gamma^2\Gamma^4(\kappa_2+2)^3 + 128\gamma^2\Delta^4 + 8\gamma\Gamma^3\Delta\kappa_2^2\Omega_L\\ &+ 16\Omega_L^2\left[4\left(\Delta-\Omega_L\right)^2+\Gamma^2\right]\left[8\left(\Omega_L+\Delta\right)^2+\Gamma^2(\kappa_2+2)\right]\Big\},\end{aligned} \tag{3.64a}$$

$$\begin{aligned}\tilde{\rho}_{0,0} = \frac{2}{D}\Big\{&4\Omega_L^2\left[16\Gamma^2(\kappa_2+2)\left(\Omega_L^2+\Delta^2\right) + 64\left(\Delta^2-\Omega_L^2\right)^2 + \Gamma^4(\kappa_2+2)^2\right]\\ &+ \gamma^2\left[\Gamma^2(\kappa_2+1)+4\Delta^2\right]\left[\Gamma^2(\kappa_2+2)^2+16\Delta^2\right]\Big\},\end{aligned} \tag{3.64b}$$

$$\begin{aligned}\tilde{\rho}_{1,1} = \frac{1}{D}\Big\{&8\gamma^2\Gamma^2\left[4\Delta\kappa_2\Omega_L + 3\kappa_2^2\Omega_L^2 + \Delta^2(\kappa_2+2)(\kappa_2+4)\right]\\ &+ \gamma^2\Gamma^4(\kappa_2+2)^3 + 128\gamma^2\Delta^4 - 8\gamma\Gamma^3\Delta\kappa_2^2\Omega_L\\ &+ 16\Omega_L^2\left[4\left(\Omega_L+\Delta\right)^2+\Gamma^2\right]\left[8\left(\Delta-\Omega_L\right)^2+\Gamma^2(\kappa_2+2)\right]\Big\},\end{aligned} \tag{3.64c}$$

$$\tilde{\rho}_{1,0} = \tilde{\rho}^*_{0,1} = 0, \tag{3.64d}$$

$$\tilde{\rho}_{0,-1} = \tilde{\rho}^*_{-1,0} = 0, \tag{3.64e}$$

$$\begin{aligned}\tilde{\rho}_{1,-1} = \tilde{\rho}^*_{-1,1} = \frac{\gamma\Gamma\kappa_2}{D}\big\{&\gamma\left[\Gamma^3(\kappa_2+2)^2+16\Gamma\Delta^2\right] - 4\Omega_L\left[2\Gamma^2(\kappa_2+2)\Omega_L\right.\\ &\left.+ 8i\Gamma\left(\Omega_L^2+\Delta^2\right) + 16\Omega_L\left(\Omega_L^2-\Delta^2\right) + i\Gamma^3(\kappa_2+2)\right]\big\},\end{aligned} \tag{3.64f}$$

$$\begin{aligned}\tilde{\rho}_{1,0'} = \tilde{\rho}^*_{0',1} = \frac{\sqrt{2\gamma\Gamma\kappa_2}}{D}\Big\{&8\Omega_L^2\left[2\left(\Omega_L+\Delta\right)+i\Gamma\right]\left[8\left(\Delta-\Omega_L\right)^2+\Gamma^2(\kappa_2+2)\right]\\ &-2\gamma\Gamma^2\kappa_2\Omega_L[\Gamma(\kappa_2+2)-4i\Delta]\\ &+\gamma^2(2\Delta+i\Gamma)\left[-8i\Gamma\Omega_L+16\Delta\left(\Delta-\Omega_L\right)+\Gamma^2(\kappa_2+2)^2\right]\Big\},\end{aligned} \tag{3.64g}$$

$$\begin{aligned}\tilde{\rho}_{-1,0'} = \tilde{\rho}^*_{0',-1} = \frac{\sqrt{2\gamma\Gamma\kappa_2}}{D}\Big\{&-2\gamma\Gamma^2\kappa_2\Omega_L[\Gamma(\kappa_2+2)-4i\Delta]\\ &-i\gamma^2(\Gamma-2i\Delta)\left[8i\Gamma\Omega_L+16\Delta\left(\Omega_L+\Delta\right)+\Gamma^2(\kappa_2+2)^2\right]\\ &+8\Omega_L^2\left(2\Omega_L-i\Gamma-2\Delta\right)\left[8\left(\Omega_L+\Delta\right)^2+\Gamma^2(\kappa_2+2)\right]\Big\},\end{aligned} \tag{3.64h}$$

$$\tilde{\rho}_{0,0'} = \tilde{\rho}^*_{0',0} = 0, \tag{3.64i}$$

$$\tilde{\rho}_{0',0'} = \frac{2\gamma\Gamma\kappa_2}{D}\left\{8\Omega_L^2\left[8\left(\Omega_L^2+\Delta^2\right)+\Gamma^2(\kappa_2+2)\right]+\gamma^2\left[\Gamma^2(\kappa_2+2)^2+16\Delta^2\right]\right\}, \tag{3.64j}$$

where the common denominator D is given by

$$\begin{aligned}D = 8\Omega_L^2&\left[32\Gamma^2(\kappa_2+3)\left(\Omega_L^2+\Delta^2\right)+192\left(\Delta^2-\Omega_L^2\right)^2+\Gamma^4(\kappa_2+2)(\kappa_2+6)\right]\\ &+2\gamma^2\left[\Gamma^2(\kappa_2+2)^2+16\Delta^2\right]\left[\Gamma^2(2\kappa_2+3)+12\Delta^2\right].\end{aligned} \tag{3.65}$$

Here $\kappa_2 = \Omega_R^2/(\Gamma\gamma)$ is the optical-pumping saturation parameter. We will analyze these results in various ways in the next chapter. It is interesting to note that the coherences involving the $m = 0$ ground-state sublevel vanish identically. Indeed, this is to be expected because this sublevel is not coupled to the upper state by light, nor is it coupled to the $m = \pm 1$ ground-state sublevels by the $\hat{\mathbf{z}}$-directed magnetic field. In fact, we could have excluded this sublevel from our consideration completely, and taken its effect into account by assuming that the upper state spontaneously decays into "unobserved states" with a branching fraction of 1/3.

Note that as the complexity of a system increases beyond that of the one considered here, the complexity of the analytical solutions grows extremely rapidly. For such systems, it is usually the most convenient to obtain numerical solutions, or to use one of the approximate methods discussed in Chapter 5.

Chapter 4

The Effect on Transmitted Light

In a wide class of experiments in nonlinear spectroscopy, polarized light (generally from a laser) is directed through an atomic medium, and the changes in the light field strength and polarization are observed in the transmitted light. In the previous chapter we have seen how the polarized light affects the atomic ensemble; in this chapter we determine how the atoms, in turn, affect the light.

We first find the propagation equation (Sec. 4.1) for the optical field in the medium. This equation can be used to relate the atomic density matrix to the changes in the light parameters. Using the result for the steady-state density matrix found in Sec. 3.3, we analyze the resulting predicted experimental signals in various regimes.

As we will see, light is directly affected by coherences between the lower and upper states of an atomic dipole transition. The lowest-order (linear) optical effects that are observed depend only on these coherences. Higher-order (nonlinear) effects result from the creation of other types of atomic polarization.

4.1 Derivation from the wave equation

We describe the electric field $\boldsymbol{\mathcal{E}}$ of a plane wave of frequency ω and wave vector $\mathbf{k}$ using the α–ϵ parametrization (Fig. 4.1):

$$\begin{aligned}\boldsymbol{\mathcal{E}}(\mathbf{r},t) = \operatorname{Re}\Big\{\mathcal{E}_0 e^{i(\mathbf{k}\cdot\mathbf{r}-\omega t+\varphi)}[(\cos\alpha\cos\epsilon - i\sin\alpha\sin\epsilon)\,\hat{\mathbf{e}}_1 \\ + (\sin\alpha\cos\epsilon + i\cos\alpha\sin\epsilon)\,\hat{\mathbf{e}}_2]\Big\},\end{aligned} \tag{4.1}$$

where $\hat{\mathbf{e}}_1$ and $\hat{\mathbf{e}}_2 = \hat{\mathbf{k}}\times\hat{\mathbf{e}}_1$ are two orthogonal unit vectors perpendicular to $\mathbf{k}$, $\mathcal{E}_0$ is the electric-field amplitude, φ is an overall phase, α is the polarization angle (*azimuth*)

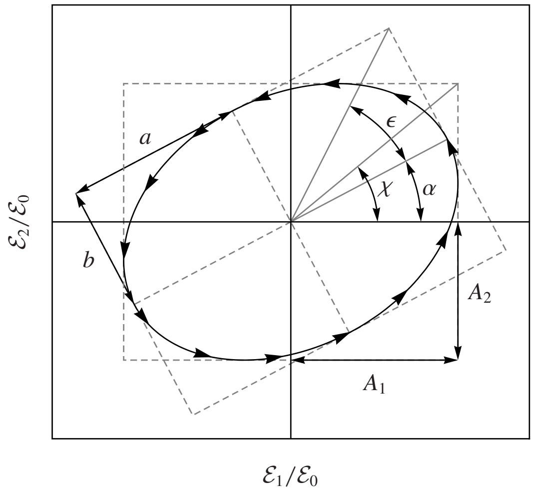

Figure 4.1: Elliptically polarized light. For a given value of the spatial coordinate $\mathbf{r}$, the electric-field vector $\boldsymbol{\mathcal{E}}(t) = \mathcal{E}_1(t)\hat{\mathbf{e}}_1 + \mathcal{E}_2(t)\hat{\mathbf{e}}_2$ of the light draws out an ellipse. Various parameters characterizing the ellipse are shown, including the polarization angle α and ellipticity ϵ described in the text. Other parameters are a and b, the normalized semimajor and semiminor axes of the ellipse, A_1 and A_2, the normalized amplitudes along the $\hat{\mathbf{e}}_1$ and $\hat{\mathbf{e}}_2$ axes, and $\chi = \arctan A_2/A_1$, which can be used in an alternative parameterization.

with respect to the $\hat{\mathbf{e}}_1$ axis, and ϵ is the ellipticity (equal up to a sign to the arctangent of the ratio of the minor to the major axis of the polarization ellipse).

The four real parameters $\mathcal{E}_0$, φ, α, and ϵ characterize the amplitude, phase, and polarization of the light field. As light propagates through a medium, the changes in the electric field can be described in terms of changes of these parameters: the change in the electric field amplitude $\Delta\mathcal{E}_0$ (related to the *absorption* or *gain* in the medium), the *phase shift* $\Delta\varphi$, the *polarization rotation* $\Delta\alpha$, and the *change in ellipticity* $\Delta\epsilon$. These changes are described by the wave equation in a medium, which governs the propagation of the optical field. Because the wave equation depends on the dipole polarization of the medium, which in turn depends on the atomic density matrix, we can use the wave equation to relate the changes in the optical parameters to the density matrix.

The wave equation follows directly from the Maxwell equations for electromagnetic fields in a medium:

$$\boldsymbol{\nabla} \cdot \mathbf{D} = 4\pi\varrho, \tag{4.2a}$$

$$\boldsymbol{\nabla} \times \boldsymbol{\mathcal{E}} = -\frac{1}{c}\frac{\partial \mathbf{B}}{\partial t}, \tag{4.2b}$$

$$\boldsymbol{\nabla} \cdot \mathbf{B} = 0, \tag{4.2c}$$

$$\boldsymbol{\nabla} \times \mathbf{H} = \frac{4\pi}{c}\mathbf{j} + \frac{1}{c}\frac{\partial \mathbf{D}}{\partial t}. \tag{4.2d}$$

We are interested in cases in which the free electric charge density ϱ and the free current density $\mathbf{j}$ are zero, and we will assume that the medium is nonmagnetic, which implies that $\mathbf{H}$ is equal to the magnetic field $\mathbf{B}$. The *electric displacement* $\mathbf{D}$ is given by

$$\mathbf{D} = \boldsymbol{\mathcal{E}} + 4\pi\mathbf{P}, \tag{4.3}$$

where $\mathbf{P}$ is the polarization of the medium, i.e., the dipole moment per unit volume. The dipole moment can be found from the density matrix as the expectation value of the dipole operator (Sec. 2.1): $\mathbf{P} = n\,\mathrm{Tr}\,\rho\mathbf{d}$, where n is the atomic density. With these assumptions we have

$$\boldsymbol{\nabla}\cdot\boldsymbol{\mathcal{E}} + 4\pi\boldsymbol{\nabla}\cdot\mathbf{P} = 0, \tag{4.4a}$$

$$\boldsymbol{\nabla}\times\boldsymbol{\mathcal{E}} = -\frac{1}{c}\frac{\partial\mathbf{B}}{\partial t}, \tag{4.4b}$$

$$\boldsymbol{\nabla}\cdot\mathbf{B} = 0, \tag{4.4c}$$

$$\boldsymbol{\nabla}\times\mathbf{B} = \frac{1}{c}\frac{\partial\boldsymbol{\mathcal{E}}}{\partial t} + \frac{4\pi}{c}\frac{\partial\mathbf{P}}{\partial t}. \tag{4.4d}$$

We then eliminate $\mathbf{B}$ by taking the curl of both sides of Eq. (4.4b) and substituting for $\boldsymbol{\nabla}\times\mathbf{B}$ with Eq. (4.4). This gives

$$\boldsymbol{\nabla}\times\boldsymbol{\nabla}\times\boldsymbol{\mathcal{E}} = -\frac{1}{c^2}\frac{\partial^2\boldsymbol{\mathcal{E}}}{\partial t^2} - \frac{4\pi}{c^2}\frac{\partial^2\mathbf{P}}{\partial t^2}. \tag{4.5}$$

We now use the vector identity

$$\boldsymbol{\nabla}\times\boldsymbol{\nabla}\times\boldsymbol{\mathcal{E}} = \boldsymbol{\nabla}\left(\boldsymbol{\nabla}\cdot\boldsymbol{\mathcal{E}}\right) - \nabla^2\boldsymbol{\mathcal{E}}. \tag{4.6}$$

In general, the divergence of $\boldsymbol{\mathcal{E}}$ is not zero for nonlinear media, but under the assumption that $\boldsymbol{\mathcal{E}}$ is a transverse plane wave, the field never points along the direction in which it varies, so $\boldsymbol{\nabla}\cdot\boldsymbol{\mathcal{E}} = 0$. With this we arrive at the wave equation:

$$\nabla^2\boldsymbol{\mathcal{E}} - \frac{1}{c^2}\frac{\partial^2\boldsymbol{\mathcal{E}}}{\partial t^2} = \frac{4\pi}{c^2}\frac{\partial^2\mathbf{P}}{\partial t^2}. \tag{4.7}$$

The medium polarization $\mathbf{P}$ is induced by the electric field of the light, so it oscillates at the light frequency. (We will show directly that that this is true below.) As with the light field, we can pull out the spatial and temporal dependence of the polarization and write the amplitude, directional, and phase information in terms of four real parameters:

$$\mathbf{P} = \mathrm{Re}\left\{e^{i(\mathbf{k}\cdot\mathbf{r}-\omega t+\varphi)}\left[\left(P_1 - iP_2\right)\hat{\mathbf{e}}_1 + \left(P_3 - iP_4\right)\hat{\mathbf{e}}_2\right]\right\}, \tag{4.8}$$

where the P_i are the *in-phase* and *quadrature components* of the polarization (not to be confused with the Stokes parameters designated with the same notation). Here we have chosen to reference the overall phase to that of the light in order to simplify the subsequent algebra; φ is not an independent parameter in this expression.

For a plane wave, the light-field parameters only vary along the propagation direction $\hat{\mathbf{k}}$. Using this fact and taking into account the time dependence of $\boldsymbol{\mathcal{E}}$ and $\mathbf{P}$ given by Eqs. (4.1) and (4.8), the wave equation reduces to

$$\frac{\partial^2 \boldsymbol{\mathcal{E}}}{\partial \ell^2} + k^2 \boldsymbol{\mathcal{E}} = -4\pi k^2 \mathbf{P}, \tag{4.9}$$

where ℓ is the distance along the light propagation direction (the optical path), and we have used $k = \omega/c$.

We now substitute the parametrized expressions for $\boldsymbol{\mathcal{E}}$ and $\mathbf{P}$ into Eq. (4.9). Taking the second derivative of the electric field with respect to ℓ results in many terms containing derivatives of the light-field parameters. There are second-order terms containing factors such as $d^2\alpha/d\ell^2$ or $(d\phi/d\ell)(d\alpha/d\ell)$, and first-order terms containing factors such as $k(d\alpha/d\ell)$. The first-order terms must each contain a factor of k in order for the units of the first-order and second-order terms to be the same. Comparing the general form of these terms, we see that if the first derivatives such as $d\alpha/d\ell$ are much smaller than k, i.e., if the fractional change of the light-field parameters is small over a distance equal to the wavelength of the light, the second-order terms can be neglected. Under this approximation, we can solve the wave equation to find expressions for the change of the light-field parameters per unit distance:

$$\frac{1}{\mathcal{E}_0}\frac{d\mathcal{E}_0}{d\ell} = \frac{2\pi\omega}{\mathcal{E}_0 c}\left[\sin\alpha\left(-P_1\sin\epsilon + P_4\cos\epsilon\right) + \cos\alpha\left(P_2\cos\epsilon + P_3\sin\epsilon\right)\right], \tag{4.10a}$$

$$\frac{d\varphi}{d\ell} = \frac{2\pi\omega}{\mathcal{E}_0 c}\sec 2\epsilon\left[\cos\alpha\left(P_1\cos\epsilon + P_4\sin\epsilon\right) + \sin\alpha\left(-P_2\sin\epsilon + P_3\cos\epsilon\right)\right], \tag{4.10b}$$

$$\frac{d\alpha}{d\ell} = \frac{2\pi\omega}{\mathcal{E}_0 c}\sec 2\epsilon\left[\cos\alpha\left(P_1\sin\epsilon + P_4\cos\epsilon\right) - \sin\alpha\left(P_2\cos\epsilon - P_3\sin\epsilon\right)\right], \tag{4.10c}$$

$$\frac{d\epsilon}{d\ell} = -\frac{2\pi\omega}{\mathcal{E}_0 c}\left[\sin\alpha\left(P_1\cos\epsilon + P_4\sin\epsilon\right) + \cos\alpha\left(P_2\sin\epsilon - P_3\cos\epsilon\right)\right]. \tag{4.10d}$$

As an example, let us consider light linearly polarized along $\hat{\mathbf{x}}$, propagating along $\hat{\mathbf{z}}$. Choosing $\hat{\mathbf{e}}_1 = \hat{\mathbf{x}}$, $\hat{\mathbf{e}}_2 = \hat{\mathbf{y}}$, the initial values of α and ϵ are zero, and we have

$$\frac{1}{\mathcal{E}_0}\frac{d\mathcal{E}_0}{dz} = \frac{2\pi\omega}{\mathcal{E}_0 c}P_2, \tag{4.11a}$$

$$\frac{d\varphi}{dz} = \frac{2\pi\omega}{\mathcal{E}_0 c}P_1, \tag{4.11b}$$

$$\frac{d\alpha}{dz} = \frac{2\pi\omega}{\mathcal{E}_0 c}P_4, \tag{4.11c}$$

$$\frac{d\epsilon}{dz} = \frac{2\pi\omega}{\mathcal{E}_0 c} P_3. \tag{4.11d}$$

We will calculate the polarization components P_i explicitly later in this chapter. Here we have assumed that the parameters $\mathcal{E}_0$, φ, α, ϵ do not change appreciably over the length of the medium (i.e., the medium is *optically thin*), so that they can be approximated by their initial values in the right-hand sides of Eqs. (4.10). In the *optically thick* case, we must solve the differential equations for these parameters as the light propagates through the medium. Since the density matrix itself depends on the light field, some complications in the analysis may arise, especially when atoms can travel between regions with different light parameters. Some of these issues will be discussed in Chapter 7.

From Eqs. (4.11), it is particularly apparent that, as one would expect, the polarization components along the electric field are responsible for absorption and phase shift, while the perpendicular components cause changes in polarization. However, it is less intuitive that the out-of-phase components of polarization P_2 and P_4 are responsible for absorption and rotation, which involve the change in amplitude of components of the in-phase field.

This can be made a little clearer by considering the case of a *linear medium*, for which the induced complex polarization is proportional to the complex electric field:

$$\widetilde{\mathbf{P}} = \overset{\leftrightarrow}{\boldsymbol{\chi}} \cdot \widetilde{\boldsymbol{\mathcal{E}}}, \tag{4.12}$$

where the *linear susceptibility tensor* $\overset{\leftrightarrow}{\boldsymbol{\chi}}$ is the complex proportionality constant. Here $\widetilde{\boldsymbol{\mathcal{E}}}$ and $\widetilde{\mathbf{P}}$ are defined as in Eqs. (4.1) and (4.8), respectively, but without dropping the imaginary parts of the expressions. The real part of $\overset{\leftrightarrow}{\boldsymbol{\chi}}$ describes the in-phase response of the medium, and the imaginary part describes polarization produced out of phase with the light field. For our case of a light field propagating along $\hat{\mathbf{z}}$ and linearly polarized along $\hat{\mathbf{x}}$, the χ_{xx} component (related to P_1 and P_2) describes the polarization induced in the direction of the electric field, and the χ_{yx} component (related to P_3 and P_4) describes polarization induced transverse to the electric field. It is clear from symmetry that if $\chi_{yx} = 0$, the light field will remain strictly polarized along $\hat{\mathbf{x}}$ and no optical rotation or change in ellipticity will occur. Taking this case for simplicity, the wave equation (4.9) for the x-component of the light field becomes

$$\frac{\partial^2 \widetilde{\mathcal{E}}_x}{\partial z^2} + k^2(1 + 4\pi\chi_{xx})\widetilde{\mathcal{E}}_x = 0. \tag{4.13}$$

If χ_{xx} is real, the result of the polarization is to change the effective value of k, i.e., to change the wavelength of light in the medium. This is equivalent to imposing a phase shift that is proportional to the distance traveled in the medium. This effect of the in-phase response of the medium is analogous to changing the spring constant k_s of a simple harmonic oscillator described by

$$m\ddot{x} + k_s x = 0, \tag{4.14}$$

where m is the mass of the particle acted on by the spring and x is the position. Here, changing the spring constant changes the frequency of oscillation and does not induce any damping. Similarly, changing the in-phase polarization response of the medium affects the "springiness" of the medium, leading to the effective change in the wave number k.

Now consider the case in which χ_{xx} is imaginary, so that the induced polarization is out of phase with the electric field. Because the first space derivative of $\mathcal{E}_x$, assuming slow variation of the light parameters, is given by $\partial\widetilde{\mathcal{E}}_x/\partial z = ik\widetilde{\mathcal{E}}_x$, we can rewrite the polarization term of Eq. (4.13) to obtain

$$\frac{\partial^2\widetilde{\mathcal{E}}_x}{\partial z^2} + 4\pi\,\mathrm{Im}\,(\chi_{xx})\,k\frac{\partial\widetilde{\mathcal{E}}_x}{\partial z} + k^2\widetilde{\mathcal{E}}_x = 0. \tag{4.15}$$

In this form we can see that this term is analogous to a retarding force $-b\dot{x}$ that opposes the motion of a damped harmonic oscillator:

$$m\ddot{x} - b\dot{x} + k_s x = 0. \tag{4.16}$$

This force continuously removes kinetic energy from the harmonic oscillator (or continuously adds it if the sign of b is negative). Likewise, the out-of-phase polarization always either opposes or enhances the rate of change of the electric field with respect to distance, causing either absorption or gain, depending on the sign of $\mathrm{Im}\,(\chi_{xx})$.

As noted above, the effect of a continuously changing phase is to change the wave number in the medium. Thus, the phase shift can alternatively be represented by an index of refraction n:

$$\mathcal{E}_0(z)e^{i[kz-\omega t+\varphi(z)]} = \mathcal{E}_0(z)e^{i(nkz-\omega t)}, \tag{4.17}$$

where we have taken z as the propagation axis. For a thin medium, $\varphi(z) = (d\varphi/dz)z$. Therefore $nkz = kz + (d\varphi/dz)z$, so

$$n = 1 + \frac{d\varphi}{k\,dz}. \tag{4.18}$$

If a complex index of refraction $\tilde{n}$ is used, it can account for both the phase shift and the attenuation:

$$\mathcal{E}_0 e^{i(\tilde{n}kz-\omega t)} = \mathcal{E}_0 e^{-\mathrm{Im}(\tilde{n})kz}\, e^{i[\mathrm{Re}(\tilde{n})kz-\omega t]}. \tag{4.19}$$

Taking the space derivative shows that we can define the imaginary part of $\tilde{n}$ by

$$\operatorname{Im}\tilde{n} = -\frac{1}{\mathcal{E}_0}\frac{d\mathcal{E}_0}{k\,dz}. \tag{4.20}$$

The real and imaginary parts of the complex index of refraction can be used along with the changes in the polarization angle and ellipticity as the four quantities measuring changes in the optical field. Another approach is to define the complex index of refraction for two complementary light polarizations (for example, left- and right-circular). These two complex quantities then characterize the modifications to the light field. For example, as will be discussed in Sec. 4.2, linear optical rotation can be interpreted as a phase shift between left- and right-circularly polarized light, i.e., the difference between the real part of the index of refraction for the two polarizations.

We will primarily discuss optical signals in terms of $\mathcal{E}_0$, φ, α, and ϵ, and refer to the index of refraction picture where appropriate.

4.2 Example of observed signals

The changes in the light parameters induced by propagation through a medium found in Sec. 4.1 are written in terms of the medium polarization in the laboratory frame, rather than the rotating frame. We can write one density matrix in terms of the other using Eq. (3.57). Calculating the expectation value of the optical polarization of the medium $\mathbf{P} = n\operatorname{Tr}\rho\mathbf{d}$ (where n is the atomic density), we find

$$\mathbf{P} = n\operatorname{Re}\left(\sqrt{\frac{2}{3}}\langle\xi 1\|d\|\xi' 0'\rangle e^{-i\omega t}\left[\left(\tilde{\rho}_{0',-1} - \tilde{\rho}_{0',1}\right)\hat{\mathbf{x}} + i\left(\tilde{\rho}_{0',-1} + \tilde{\rho}_{0',1}\right)\hat{\mathbf{y}} + \sqrt{2}\tilde{\rho}_{0',0}\hat{\mathbf{z}}\right]\right). \tag{4.21}$$

Because the light is propagating along $\hat{\mathbf{z}}$, the component of induced polarization in that direction must be zero. Consulting Eq. (3.64i) we see that this is indeed the case. We can thus write the medium polarization in terms of the parameters $P_{1,2,3,4}$ of Eq. (4.8) with $\hat{\mathbf{e}}_1 = \hat{\mathbf{x}}$ and $\hat{\mathbf{e}}_2 = \hat{\mathbf{y}}$. Comparing Eqs. (4.8) and (4.21), we find

$$P_1 = \sqrt{\frac{2}{3}}\langle\xi 1\|d\|\xi' 0'\rangle n\operatorname{Re}\left(\tilde{\rho}_{-1,0'} - \tilde{\rho}_{1,0'}\right), \tag{4.22a}$$

$$P_2 = \sqrt{\frac{2}{3}}\langle\xi 1\|d\|\xi' 0'\rangle n\operatorname{Im}\left(\tilde{\rho}_{-1,0'} - \tilde{\rho}_{1,0'}\right), \tag{4.22b}$$

$$P_3 = \sqrt{\frac{2}{3}}\langle\xi 1\|d\|\xi' 0'\rangle n\operatorname{Im}\left(\tilde{\rho}_{-1,0'} + \tilde{\rho}_{1,0'}\right), \tag{4.22c}$$

$$P_4 = -\sqrt{\frac{2}{3}}\langle\xi 1\|d\|\xi' 0'\rangle n \operatorname{Re}\left(\tilde{\rho}_{-1,0'} + \tilde{\rho}_{1,0'}\right). \tag{4.22d}$$

This is all we need in order to calculate the effect of the atomic medium on the light. The observables are found in terms of the rotating-frame density matrix by substituting Eq. (4.22) into Eqs. (4.11):

$$\frac{1}{\mathcal{E}_0}\frac{d\mathcal{E}_0}{d\ell} = \frac{n\Gamma\lambda^2 \operatorname{Im}\left(\tilde{\rho}_{-1,0'} - \tilde{\rho}_{1,0'}\right)}{4\sqrt{2}\pi\Omega_R}, \tag{4.23a}$$

$$\frac{d\varphi}{d\ell} = \frac{n\Gamma\lambda^2 \operatorname{Re}\left(\tilde{\rho}_{-1,0'} - \tilde{\rho}_{1,0'}\right)}{4\sqrt{2}\pi\Omega_R}, \tag{4.23b}$$

$$\frac{d\alpha}{d\ell} = -\frac{n\Gamma\lambda^2 \operatorname{Re}\left(\tilde{\rho}_{-1,0'} + \tilde{\rho}_{1,0'}\right)}{4\sqrt{2}\pi\Omega_R}, \tag{4.23c}$$

$$\frac{d\epsilon}{d\ell} = \frac{n\Gamma\lambda^2 \operatorname{Im}\left(\tilde{\rho}_{-1,0'} + \tilde{\rho}_{1,0'}\right)}{4\sqrt{2}\pi\Omega_R}, \tag{4.23d}$$

where we have used Eq. (3.27) to write the reduced matrix element of the dipole operator in terms of Γ.

Substituting the solution (3.64) for the density-matrix elements into Eq. (4.23), we find

$$\frac{\ell_0}{\mathcal{E}_0}\frac{d\mathcal{E}_0}{d\ell} = -\frac{3\Gamma^2}{D}\left\{8\Omega_L^2\left[8\Omega_L^2 + \Gamma^2(\kappa_2+2) + 8\Delta^2\right] + \gamma^2\left[\Gamma^2(\kappa_2+2)^2 + 16\Delta^2\right]\right\}, \tag{4.24a}$$

$$\ell_0\frac{d\varphi}{d\ell} = -\frac{6\Gamma\Delta}{D}\left\{8\Omega_L^2\left[-8\Omega_L^2 + \Gamma^2(\kappa_2+2) + 8\Delta^2\right] + \gamma^2\left[\Gamma^2(\kappa_2+2)^2 + 16\Delta^2\right]\right\}, \tag{4.24b}$$

$$\begin{aligned}\ell_0\frac{d\alpha}{d\ell} = -\frac{6\Gamma\Omega_L}{D}\Big\{&8\Omega_L^2\left[8\Omega_L^2 + \Gamma^2(\kappa_2+2) - 8\Delta^2\right] \\ &+ \gamma\left[4\gamma\left(\Gamma^2 - 4\Delta^2\right) - \Gamma^3\kappa_2(\kappa_2+2)\right]\Big\},\end{aligned} \tag{4.24c}$$

$$\ell_0\frac{d\epsilon}{d\ell} = \frac{24\Gamma^2\Delta\Omega_L}{D}\left[\gamma(\Gamma\kappa_2 - 4\gamma) - 16\Omega_L^2\right], \tag{4.24d}$$

where D is given by Eq. (3.65). We have written the results in terms of the *unsaturated absorption length* on resonance

$$\ell_0 = -\left(\frac{1}{\mathcal{I}}\frac{d\mathcal{I}}{d\ell}\right)^{-1} = -\left(\frac{2}{\mathcal{E}_0}\frac{d\mathcal{E}_0}{d\ell}\right)^{-1} = \frac{6\pi}{\lambda^2 n}, \tag{4.25}$$

found by setting κ_2, Ω_L, and Δ to zero.

The resonant absorption length can be written in terms of the *photon-absorption cross-section* σ according to

$$\ell_0 = \frac{1}{n\sigma}. \tag{4.26}$$

Equation (4.25) then tells us that

$$\sigma = \frac{1}{3}\frac{\lambda^2}{2\pi}, \tag{4.27}$$

i.e., that the absorption cross-section on resonance does not depend on anything except the wavelength of the transition and the ratio of the degeneracies of the initial and final state that determines the numerical coefficient, equal to 1/3 in this case. See, for example, the book by Budker *et al.* (2008, Prob. 3.5) for an alternative derivation and additional discussion.

4.2.1 Linear effects

Note that so far we have made no assumptions about the strength of the light field, i.e., the value of the saturation parameter κ_2. In order to make the distinction between linear and nonlinear processes, it is helpful to take the limit of vanishingly small light power, $\kappa_2 \to 0$. In this case, the nonlinear effects (which are first order in κ_2 for small κ_2) can be neglected, and the linear effects (which are independent of κ_2) remain.

To find the signals in the linear case, we can set $\kappa_2 = 0$ to obtain

$$\frac{\ell_0}{\mathcal{E}_0}\frac{d\mathcal{E}_0}{d\ell} = -\frac{1}{2}\frac{\Gamma^2\left(4\Delta^2+4\Omega_L^2+\Gamma^2\right)}{16\left(\Delta^2-\Omega_L^2\right)^2+8\Gamma^2\left(\Delta^2+\Omega_L^2\right)+\Gamma^4}, \tag{4.28a}$$

$$\ell_0\frac{d\varphi}{d\ell} = -\frac{\Gamma\Delta\left(4\Delta^2-4\Omega_L^2+\Gamma^2\right)}{16\left(\Delta^2-\Omega_L^2\right)^2+8\Gamma^2\left(\Delta^2+\Omega_L^2\right)+\Gamma^4}, \tag{4.28b}$$

$$\ell_0\frac{d\alpha}{d\ell} = -\frac{\Gamma\Omega_L\left(4\Omega_L^2-4\Delta^2+\Gamma^2\right)}{16\left(\Delta^2-\Omega_L^2\right)^2+8\Gamma^2\left(\Delta^2+\Omega_L^2\right)+\Gamma^4}, \tag{4.28c}$$

$$\ell_0\frac{d\epsilon}{d\ell} = -\frac{4\Gamma^2\Delta\Omega_L}{16\left(\Delta^2-\Omega_L^2\right)^2+8\Gamma^2\left(\Delta^2+\Omega_L^2\right)+\Gamma^4}. \tag{4.28d}$$

These solutions apply as long as $\kappa_2 \ll 1$; note that they are also independent of γ (under the assumption $\gamma \ll \Gamma$).

In experiments of the type under examination here, measurements are commonly carried out by varying either the magnetic field strength or the light frequency while holding all other parameters fixed. For the Doppler-free linear effects there is considerable symmetry between these two approaches, as is indicated by Eqs.

(4.28) and illustrated by Fig. 4.2. In both cases there is resonant behavior with a characteristic width given by the natural width Γ. In the left-hand column of Fig. 4.2, the Larmor frequency (proportional to the magnetic field strength) is fixed at $\Omega_L = 0.2\Gamma$ and the light detuning Δ is varied. In the right-hand column, the light frequency detuning from resonance is fixed at $\Delta = 0.2\Gamma$ and Ω_L is varied. The normalized optical signals are plotted. We see that the attenuation coefficient $d\mathcal{E}_0/d\ell$ (top row) and the change in ellipticity $d\epsilon/d\ell$ (bottom row) are unchanged under the exchange of Δ and Ω_L, while the phase shift $d\varphi/d\ell$ (second row) and optical rotation $d\alpha/d\ell$ (third row) are transformed into each other.

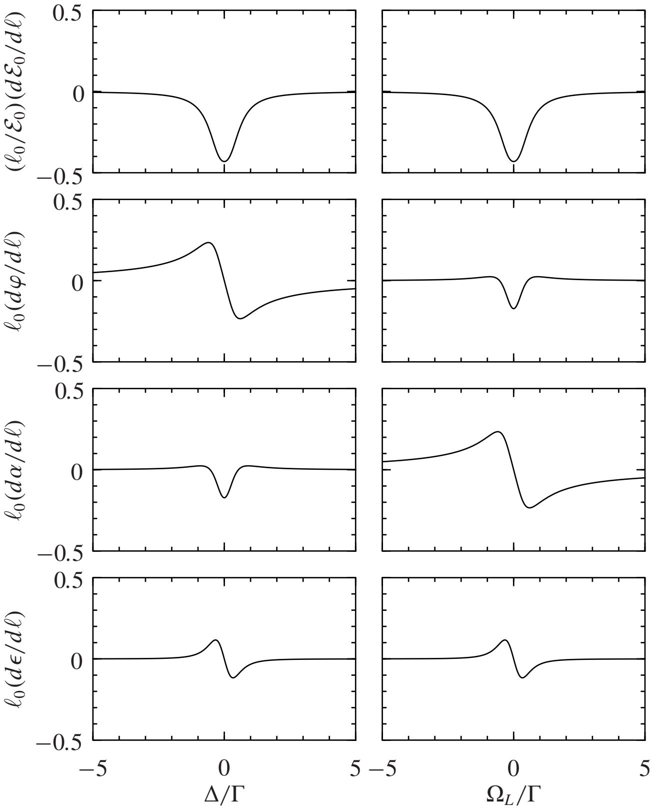

Figure 4.2: Signals observed in transmitted light resonant with a $F = 1 \rightarrow F' = 0$ atomic transition in the linear case (weak light power; $\kappa_2 = 0$). The parameters are $\Omega_L = 0.2\Gamma$ (left-hand plots), and $\Delta = 0.2\Gamma$ (right-hand plots).

The symmetry can be understood by considering the resonant behavior of the two transitions driven by the σ^+ and σ^- components of the light, respectively (Fig. 3.3). Each of these transitions induces absorption with a Lorentzian lineshape and a phase shift with a dispersive lineshape, as can be seen by setting $\Omega_L = 0$ in Eqs. (4.28):

$$\frac{\ell_0}{\mathcal{E}_0}\frac{d\mathcal{E}_0}{d\ell} = -\frac{1}{2}\frac{\Gamma^2}{\Gamma^2 + 4\Delta^2}, \tag{4.29a}$$

$$\ell_0\frac{d\varphi}{d\ell} = -\frac{\Gamma\Delta}{\Gamma^2 + 4\Delta^2}. \tag{4.29b}$$

(This dependence can in fact be obtained using a classical model of a damped harmonic oscillator.) These two lineshapes are close to those shown in the top two plots of the left-hand column of Fig. 4.2 (the difference arises because the magnetic field is not zero in the figure). Some important features of these lineshapes are as follows: they each have a characteristic width Γ; the absorptive curve is symmetric, while the dispersive curve is antisymmetric; the absorptive curve is maximum on resonance, while the dispersive curve is zero on resonance; at large detunings the absorptive curve falls off as Δ^{-2}, while the dispersive curve falls off as Δ^{-1}.

The signals in Fig. 4.2 are each proportional to either the sum or difference of the absorption or phase shift signals from the two transitions. As an example, we consider the optical-rotation signal. The optical rotation in the linear case is generated by *circular birefringence*—a phase shift between the two circular components of the light field upon traversal of the medium.[1] When two circular components are combined to create linearly polarized light, it is the phase relationship between the two components that determines the direction of linear polarization. If the relative phase changes, the polarization angle rotates. Therefore, the optical-rotation signal is given by the difference between the dispersive phase-shift lineshapes for the σ^+ and σ^- transitions. According to the discussion in Sec. 4.1, this quantity can also be written in terms of the difference between the real parts of the complex indices of refraction for left- and right-circularly polarized light:

$$\frac{d\alpha}{d\ell} = k\left(\mathrm{Re}\,\tilde{n}_+ - \mathrm{Re}\,\tilde{n}_-\right), \tag{4.30}$$

where $\tilde{n}_\pm$ are the refractive indices for the corresponding circular polarizations.[2]

> The general effect of polarization rotation upon light propagation in a medium in the presence of a longitudinal magnetic field was discovered by Michael Faraday and bears his name. However, it was the work of Italian physicists Macaluso and Corbino (1898) that uncovered the resonant character of the magneto-optical effect (as a function of light detuning from resonance) for an atomic vapor. The same authors also connected the phenomenon to the Zeeman effect (Macaluso and Corbino, 1899).

Changes in the Larmor frequency and in the light detuning can both be interpreted in terms of level shifts: the relative distance between the σ^+ and σ^- resonances is given by twice the Larmor frequency, whereas changing the light detuning effectively shifts the two resonances together. If the magnetic field is zero the two resonances overlap exactly and the difference between them is zero; there is no optical rotation in this case. If the magnetic field is nonzero, as in Fig. 4.3, the difference between the two curves gives the characteristic spectral shape of linear optical rotation. Note that although the optical-rotation lineshape is symmetric, as is an absorptive Lorentzian, the fact that it arises from the individual dispersive lineshapes means that the total area under the curve is zero. This is important when considering mechanisms such as

---

[1] We will see that optical rotation can also be induced by *linear dichroism*—a difference in absorption for two orthogonal linear polarizations.

[2] See also the detailed tutorial discussion of this given by Budker *et al.* (2008, Prob. 4.1).

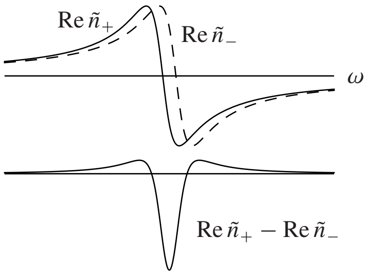

Figure 4.3: (Top) Real parts of the complex refractive indices as a function of light frequency for σ^+ and σ^- light. The curves are shifted with respect to one another due to the magnetic field. (Bottom) Linear optical rotation is proportional to the difference between $\mathrm{Re}\,\tilde{n}_+$ and $\mathrm{Re}\,\tilde{n}_-$.

Doppler broadening, which tends to “wash out” effects with this property. In fact, this is the case for all of the linear signals except for absorption (Fig. 4.2), for similar reasons.

Now we consider the magnetic-field dependence of optical rotation. From the point of view of the individual σ^+ and σ^- resonances, changing the magnetic field shifts the transition resonance frequency, producing the same effect as detuning the light. Thus each phase-shift resonance has a dispersive lineshape in a magnetic field, and the optical rotation signal is the difference between them, as before. However, the magnetic field shifts the resonances in opposite directions to each other, meaning that one of the dispersive curves must be flipped about the vertical axis. Since the dispersive curves are antisymmetric, this has the effect of changing its sign. In other words, we can find the magnetic-field dependence of the optical rotation signal by adding, rather than subtracting, the dispersive curves. This results in the dispersive shape shown in Fig. 4.2.

Note that the spectral dependence of the total phase shift $d\varphi/d\ell$ is the sum of the phase shifts due to the two resonances. Thus the detuning dependence of the phase shift should have the same shape as the magnetic-field dependence of optical rotation (Fig. 4.2), and vice versa, as can be shown with similar reasoning to that given above.

The total absorption signal depends on the sum of the σ^+ and σ^- absorptive resonances, while the change-of-ellipticity signal depends on their difference, i.e., the *circular dichroism* of the medium. (Linear polarization contains equal amounts of right- and left-circular polarization; if more of one is absorbed than the other, the polarization will no longer be linear.) The above line of reasoning can be continued to show that the absorption and change-of-ellipticity signals transform into themselves upon interchange of Δ and Ω_L.

The high degree of symmetry between the light-detuning and magnetic-field dependencies does not hold over to the nonlinear forms of the optical signals. While the linear effects are understood in terms of level shifts, the nonlinear effects that we will be concerned with are more properly understood in terms of the evolution of atomic polarization. For low light power, this evolution is the Larmor precession due

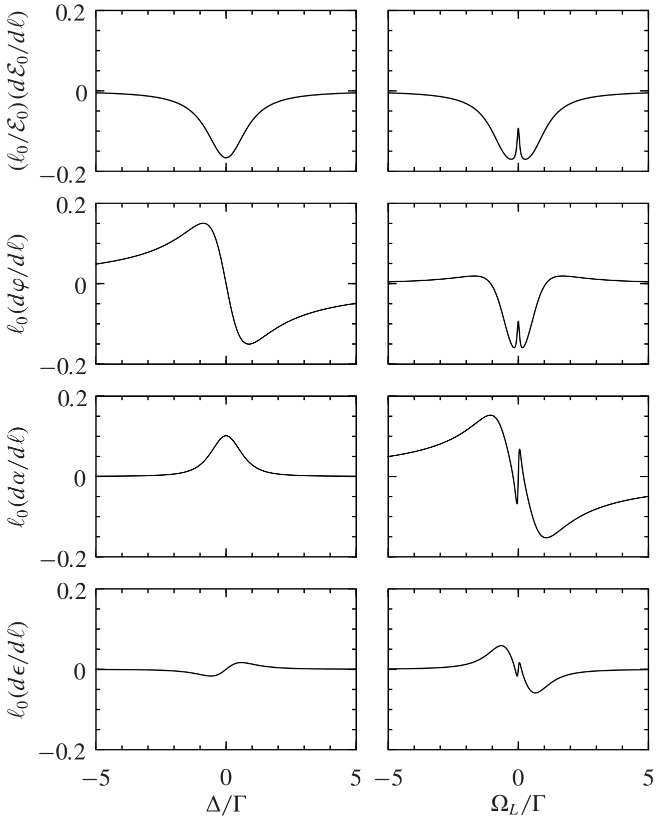

Figure 4.4: Signals observed in transmitted light resonant with a $F = 1 \rightarrow F' = 0$ atomic transition. Parameters are $\Delta = 0.5\,\Gamma$ (left-hand plots), $\Omega_L = 0.05\,\Gamma$ (right-hand plots), $\gamma = 0.05\,\Gamma$, and $\kappa_2 = 5$.

to the magnetic field. This means that the system has the potential to be much more sensitive to changes in the Larmor frequency than changes in the light frequency. We take up this case in the following section.

4.2.2 Nonlinear effects

We now turn our attention to higher light powers, for which nonlinear effects become prominent. Plotting Eqs. (4.24) with a nonzero saturation parameter ($\kappa_2 = 5$) yields some interesting developments (Fig. 4.4). In the right column, the magnetic resonances of width Γ due to the linear effect are still visible, but superimposed on them are much narrower resonances with widths on the order of the transit width $\gamma = 0.05\Gamma$. Evidently, these narrow resonances constitute the nonlinear signals. From Fig. 4.4 we see that, for a given light intensity, the magnetic field can be used to switch the system between the linear and nonlinear regimes. Keeping this in mind, in the left column a small magnetic field ($\Omega_L = \gamma$) is chosen, so that the optical spectra of the nonlinear effects can be examined. We see that no sharp features

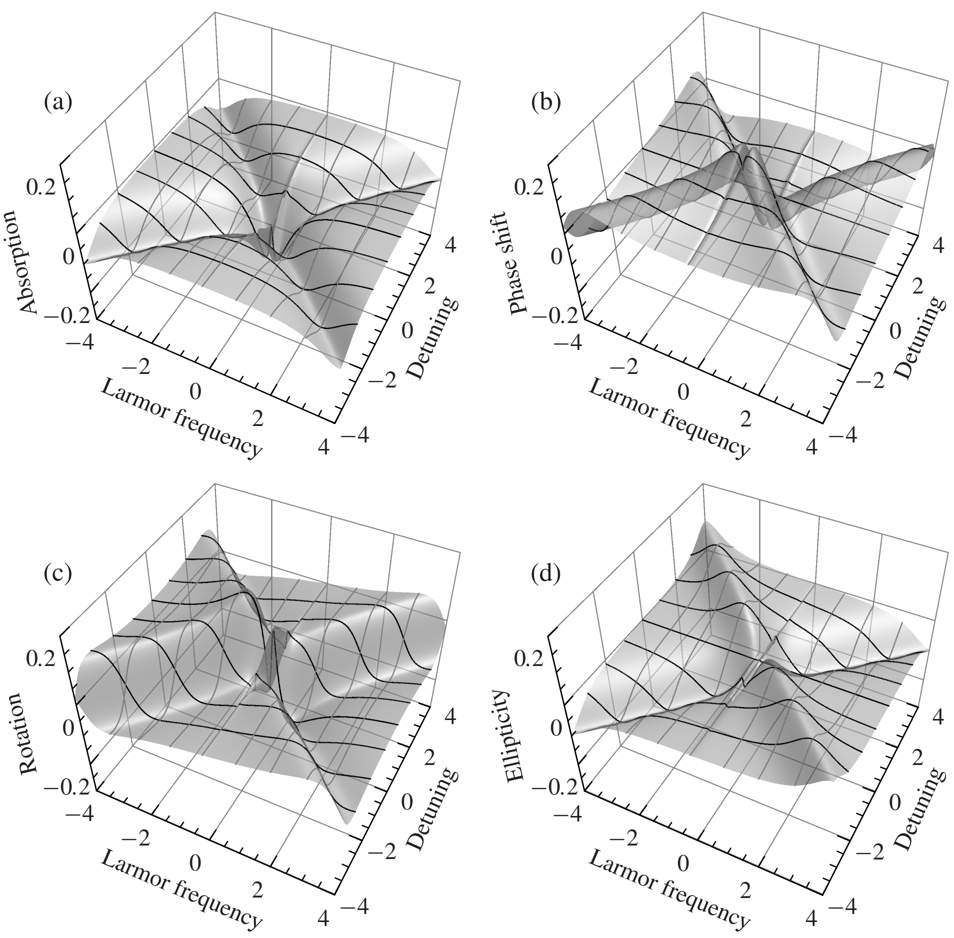

Figure 4.5: Normalized optical signals using the same parameters as in Fig. 4.4.

appear—the symmetry between the detuning and the magnetic-field dependencies is broken in the nonlinear case. (This can also be seen in Fig. 4.5, which shows 3D plots of the same signals as a function of both Δ and Ω_L.) The left column of Fig. 4.4 also shows that the absorption and dispersion spectra are largely the same as in the linear case. However, some differences arise in the spectra of magneto-optical rotation and induced ellipticity. The spectra have the opposite sign as for the linear effects; this is to be expected from comparing the signs of the linear and nonlinear magnetic-field resonances in the right column. In addition, the shapes of the resonances are somewhat different—in particular, the area under the optical-rotation curve is no longer zero. In the following, we discuss the mechanisms that result in these features.

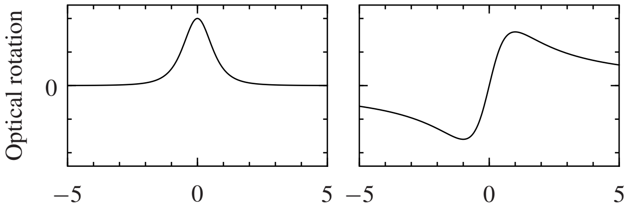

Figure 4.6: Lowest-order nonlinear magneto-optical rotation in arbitrary units (Eq. 4.32). Left-hand plot is the optical spectrum (square of an absorptive Lorentzian) with $u = 0.5$; right-hand plot is the magnetic-field dependence (dispersive Lorentzian) with $v = 0.5$.

Because the characteristic width of the resonances in the optical spectrum is Γ while the nonlinear magnetic-field resonances are of width γ, we define the dimensionless parameters $u = 2\Omega_L/\gamma$ and $v = 2\Delta/\Gamma$, which can be considered to have magnitudes on the order of unity or smaller. Let us concentrate on the optical-rotation signal. Using the assumption that $|u|$ and $|v|$ are not much greater than unity, and our previous assumption $\gamma \ll \Gamma$, we find from Eq. (4.24c),

$$\ell_0 \frac{d\alpha}{d\ell} = \frac{1}{8} \frac{u\kappa_2(\kappa_2+2)}{u^2\left(v^2+1+\frac{\kappa_2}{2}\right)\left(v^2+1+\frac{\kappa_2}{6}\right)+\left(v^2+1+\frac{2\kappa_2}{3}\right)\left[v^2+(1+\frac{\kappa_2}{2})^2\right]}. \tag{4.31}$$

Note that this signal is zero when κ_2 is zero, i.e., the linear effect (independent of κ_2) studied in the previous section is missing. This is because the assumption that $|\Omega_L|$ is on the order of γ means that $|\Omega_L| \ll \Gamma$, which—as can be seen in Fig. 4.4—means that the linear effect is very small compared to the nonlinear effect. (Of course, if κ_2 were set to zero, this assumption would not be valid, and the linear term would need to be included.)

The dependence of Eq. (4.31) on u shows that the *nonlinear magneto-optical rotation (NMOR)* signal is a dispersive Lorentzian in the magnetic field for any value of the saturation parameter or detuning. The dependence on v and κ_2 is, however, more complicated. To gain a basic understanding, we can expand the nonlinear signal to lowest order in the saturation parameter:

$$\ell_0 \frac{d\alpha}{d\ell} = \frac{u\kappa_2}{4\left(u^2+1\right)\left(v^2+1\right)^2} + O\left(\kappa_2^2\right). \tag{4.32}$$

The signal is first order in the saturation parameter (given that the linear effect has been neglected). To lowest order, the optical spectrum of the signal is the square of a Lorentzian (Fig. 4.6). As we will see, this is because two consecutive optical processes are required to produce the nonlinear signal, each of which have a Lorentzian spectrum. As noted above, this spectrum is qualitatively different from that for linear optical rotation.

> In the geometry considered here, with the magnetic field collinear with the propagation direction of linearly polarized light, NMOR is also known as the *nonlinear Faraday effect* or *nonlinear Faraday rotation.* There were several independent discoveries and rediscoveries of this effect, beginning with precursor observations in the 1970s (and even earlier). The story of these observations and the eventual understanding of them is related in a review paper by Budker *et al.* (2002a). The observation of the nested features in the magnetic-field dependence of the signal as in Fig. 4.4 played a crucial part in these developments. Nonlinear Faraday rotation experiments can now be found in undergraduate physics laboratories; a description of the one at Berkeley is given by Budker *et al.* (1999b).

To understand the nonlinear magneto-optical rotation, it is convenient to think of it as occurring in three stages. First, atoms are optically pumped by the x-polarized light. Atoms are removed from the state that absorbs x-polarized light, causing the ensemble to become dark (nonabsorbing) with respect to the pump light. However, this same state is still bright (absorbing) with respect to y-polarized light. In fact, the atoms will absorb y-polarized light even more strongly after optical pumping, because when atoms are pumped out of the bright state and into the dark state with respect to the x-polarized light, from the point of view of y-polarized light they are pumped from the dark into the bright state. This difference in absorption for light of orthogonal linear polarizations is called *linear dichroism.* The medium, which has been optically pumped into an aligned state, thus resembles a dichroic polarizer, e.g., a Polaroid film, absorbing one linear polarization and transmitting the other. In the second stage of the process, the atomic alignment precesses in the magnetic field, rotating the axis of dichroism. Now the dichroic axis is no longer along the initial light-polarization axis. Finally, in the third stage of the process, the light polarization is rotated by interaction with the dichroic atomic medium, which tends to rotate light toward its transmitting axis. The third, "probing," step does not require high light intensity, and can be performed either by a weak probe beam or by the same pump light present in the first step, as in our present example. This *rotating-polarizer model* was introduced by Kanorsky *et al.* (1993).

In the physical system that we are examining, the three stages described above happen simultaneously and continuously, rather than sequentially. Nevertheless, the rotating-polarizer model presents an accurate physical picture of the mechanism for the lowest-order NMOR. How does it account for the dispersive shape of the magnetic resonance? The optically pumped atoms relax after an average time $1/\gamma$. This time is one of the factors determining the angle by which the atomic alignment axis can precess. As the magnetic field is increased, the atoms precess farther in this time, increasing the angle of the polarizer and thus the optical-rotation angle. This means that for small fields, the NMOR signal is proportional to the magnetic field. When the magnetic field becomes high enough that the atoms can precess on the order of a full revolution before relaxing, on the other hand, the atomic polarization begins to average out, reducing the signal. The shape of the resonance is antisymmetric simply because when the magnetic field is reversed, the atoms precess in the opposite direction. The spectral lineshape is also described by the rotating-polarizer model: both the pumping and probing stages are absorptive processes, so the lineshape is the product of the two absorptive Lorentzians.

> In our discussion above, we associate nonlinear magneto-optical rotation with linear dichroism of the medium. Yet, in Eq. (4.23c) we see that the rotation is proportional to the real part of the sum of optical coherences corresponding to the two circular components. This form is suggestive of the difference in refractive indices for the two circular components (as for linear magneto-optical rotation). So do we have linear dichroism or circular birefringence in the nonlinear case? (This question, not too long ago, was a subject of debate among researchers.)
>
> Mathematically, the description of the system can be carried out in any complete basis, so on one hand both approaches are correct. On the other hand, in terms of the physical picture there is a clear distinction. The intuitive definition of the complex index of refraction is based on the idea that, when light of a particular polarization propagates through the medium, the medium induces changes in the amplitude and phase of the light. This concept only makes sense, however, if the polarization of the light in this mode does not change upon traversal of the medium, i.e., if this particular polarization is a *polarization eigenstate* of the medium. Otherwise, the index of refraction for this polarization mode will depend on the polarization of the total light field. This means that, in order to describe a process in a physically meaningful way, we must confine ourselves to considering the indices of refraction of the polarization eigenstates. The polarization eigenstates in the case of low-power NMOR are two orthogonal linear polarizations, and so the appropriate description is in terms of linear dichroism.

Despite the success of the rotating-polarizer model for low-power NMOR, it turns out that it fails at higher light powers. For $\kappa_2 \gtrsim 1$ the effect of the AC-Stark shifts due to the light in combination with the magnetic field can induce *alignment-to-orientation conversion (AOC)*, previously discussed in Sec. 3.1.2. Atomic orientation does not result in linear dichroism. However, it does produce circular birefringence, which, as we saw in Sec. 4.2.1, can also induce optical rotation. We note here that in certain situations rotation due to AOC can have very different characteristics than low-power rotation (Budker *et al.*, 2000a). In particular, for $F \to F' = F + 1$ transitions the sign of rotation due to AOC is opposite to that predicted by the rotating-polarizer model. For the $F = 1 \to F' = 0$ transition under consideration, however, the effect of AOC is not striking; the main effect of high light power is broadening of the spectral and magnetic resonances due to effective relaxation induced by optical pumping. We now analyze this effect, known as *power broadening*, for the $F = 1 \to F' = 0$ system.

When the optical pumping rate $\Gamma_p = \Omega_R^2/\Gamma$ is small, transit relaxation is the dominant ground-state relaxation mechanism, and the additional relaxation induced by the light itself can be ignored. However, when the optical pumping rate is comparable to or greater than the transit rate γ, i.e., when $\Gamma_p/\gamma = \kappa_2 \gtrsim 1$, polarized atoms may have their polarization destroyed by an additional optical pumping cycle before they have a chance to relax due to transit relaxation. This will only occur if the polarization of the atom is different than that produced by the light; otherwise optical pumping will have no apparent effect.

We can estimate the relaxation rate due to optical pumping as the pumping rate $\Gamma_p = \gamma\kappa_2$. If this relaxation were isotropic, as is transit relaxation (i.e., if it caused atoms to relax at the same rate no matter their polarization), we could add this relaxation rate to the transit rate to obtain the total relaxation rate $\gamma(1+\kappa_2)$. Because the width of the magnetic-field resonance in NMOR is given by the ground-state relaxation rate, this would then be the estimate of the power broadened width.

In fact, optical-pumping-induced relaxation is not isotropic, as noted above. In our case we can assume that the x-polarized light relaxes atomic polarization that is along the y-axis, but not that along x. This means that power broadening has a somewhat weaker dependence on κ_2. A simple rate-equation model that keeps track of atomic polarization along x and y, relaxation due to transit and the light, and the magnetic-field induced precession gives the power-broadened width as $\gamma\sqrt{1+\kappa_2}$. This is precisely the result obtained from the full density-matrix calculation for the case of an open system and with detuning set to zero. (An open system is slightly simpler than the closed system we have been considering, because there is only one optical pumping mechanism, depopulation pumping, rather than both depopulation and repopulation pumping.)

For the system considered in this section, we can obtain the power-broadened width of the NMOR resonance from formula (4.31), which is valid for arbitrary saturation parameter. First note that, according to this formula, the magnetic-field dependence of the optical rotation is a dispersive Lorentzian for any value of the saturation parameter, i.e., it takes the form

$$\frac{abu}{u^2 + b^2}, \tag{4.33}$$

where the peak-to-peak height is a, and the width measured between the two peaks is

$2b$. The slope at $u = 0$ is a/b. Comparing Eq. (4.31) with the functional form (4.33), we find that the peak-to-peak height is

$$\ell_0 \frac{d\alpha}{d\ell}\bigg|_{\text{p-p}} = \frac{\kappa_2(\kappa_2+2)}{8\sqrt{\left(v^2+1+\frac{\kappa_2}{2}\right)\left(v^2+1+\frac{\kappa_2}{6}\right)\left(v^2+1+\frac{2\kappa_2}{3}\right)\left[v^2+(1+\frac{\kappa_2}{2})^2\right]}}, \tag{4.34}$$

and the power-broadened width is

$$\Delta u\big|_{\text{p-p}} = 2\sqrt{\frac{\left(v^2+1+\frac{2\kappa_2}{3}\right)\left[v^2+(1+\frac{\kappa_2}{2})^2\right]}{\left(v^2+1+\frac{\kappa_2}{2}\right)\left(v^2+1+\frac{\kappa_2}{6}\right)}}\,. \tag{4.35}$$

These quantities are plotted for $v = 0$ in Fig. 4.7.

The sharp dependence of the nonlinear Faraday rotation signal on the magnetic field finds application in sensitive *atomic magnetometers.* To increase sensitivity to magnetic fields, it is generally desirable to maximize the slope of the signal as a function of magnetic field. For small fields near zero, the slope is given by

$$\frac{d}{du}\left(\ell_0 \frac{d\alpha}{d\ell}\right)_{u=0} = \frac{\kappa_2(\kappa_2+2)}{8\left(v^2+1+\frac{2\kappa_2}{3}\right)\left[v^2+(1+\frac{\kappa_2}{2})^2\right]}. \tag{4.36}$$

By maximizing with respect to κ_2, or by looking at Fig. 4.7, we see that to achieve the highest slope the saturation parameter should be of order unity.

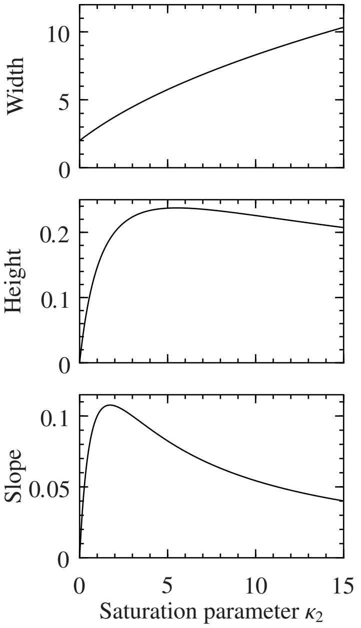

Figure 4.7: Peak-to-peak width $\Delta u|_{\text{p-p}}$, height $\ell_0 \frac{d\alpha}{d\ell}\big|_{\text{p-p}}$ and small-field slope $\frac{d}{du}\left(\ell_0 \frac{d\alpha}{d\ell}\right)_{u=0}$ of NMOR for zero detuning as a function of saturation parameter κ_2.

4.2.3 Doppler broadening

So far we have assumed that the atoms are motionless, or at least have no velocity component along the light-propagation direction. This will not be the case in a real experiment unless cooling and trapping techniques are employed. In a vapor cell, atomic velocities will be distributed according to the Maxwell–Boltzmann distribution, which, for a component v of the velocity, takes the form

$$f_v(v)dv = \left(\frac{m}{2\pi k_B T}\right)^{1/2} e^{-mv^2/(2k_BT)}dv, \tag{4.37}$$

where m is the atomic mass, k_B is the Boltzmann constant, and T is the temperature.

We now determine the effect of the atomic velocity on the optical signals. Suppose that an atom is stationary at position $z = z_0$, with the light propagating along the z-axis. The optical electric field viewed at the location of the atom has time dependence $\sin(\omega t - kz_0)$, neglecting an overall phase, where ω is the light frequency and k is the light wave number. This is the dependence used in our previous calculation, where we have set $z_0 = 0$. Now suppose the atom is not stationary, but rather moves with a constant velocity v, so that its longitudinal position is $z(t) = z_0 + vt$. The electric field of the light as viewed at the position of the atom now has time dependence $\sin[\omega t - kz(t)] = \sin[(\omega - kv)t - kz_0]$. This shows that the light frequency has been replaced by an effective light frequency $\omega - kv$.

The shift $\Delta_v = -kv$ is the *non-relativistic Doppler shift* due to the atomic velocity. The calculation of the optical signals for an atom of velocity v goes through exactly as for a stationary atom, with the replacement $\Delta \to \Delta + \Delta_v$. The Doppler-broadened signals can be found by integrating the Doppler-shifted signal over velocity, after weighting with the Maxwell–Boltzmann distribution. This procedure relies on the assumption that the vapor cell does not contain buffer gas and is not antirelaxation coated, so that atoms cannot change their velocity without losing their polarization. (Velocity-mixing effects are considered in Sec. 7.1.) In addition, we neglect subtle effects such as the correlation of transit rate with velocity.

It is convenient to write the Maxwell–Boltzmann distribution in terms of the Doppler shift. This gives

$$\begin{aligned} f_{\Delta_v}(\Delta_v)d\Delta_v &= \left(\frac{m}{2\pi k^2 k_B T}\right)^{1/2} e^{-m\Delta_v^2/(2k^2 k_B T)} d\Delta_v \\ &= \frac{1}{\Gamma_D\sqrt{\pi}} e^{-\Delta_v^2/\Gamma_D^2} d\Delta_v, \end{aligned} \tag{4.38}$$

where $\Gamma_D = k\sqrt{2k_B T/m}$ is the *Doppler width* (note that there are other definitions of the Doppler width that differ by numerical factors from this one). The Doppler width is the characteristic spectral width of optical signals for Doppler-broadened media.

If we designate one of the optical signals (4.24) by $S(\Delta)$, the Doppler-broadened signal is given by the integral

$$S_{\text{DB}}(\Delta) = \int_{-\infty}^{\infty} S(\Delta + \Delta_v) f_{\Delta_v}(\Delta_v) d\Delta_v, \tag{4.39}$$

i.e., the *convolution* of S and f_{Δ_v}. The procedure of convolution is illustrated for the case of linear absorption in Fig. 4.8. The magnetic field is set to zero, and the

Doppler width is assumed to be 10 times the natural width. The signal at each detuning Δ is the total absorption from atoms of all velocities (velocity groups). The contributions of a representative sample of velocity groups are shown as solid curves, and the integral is shown as a dashed line.

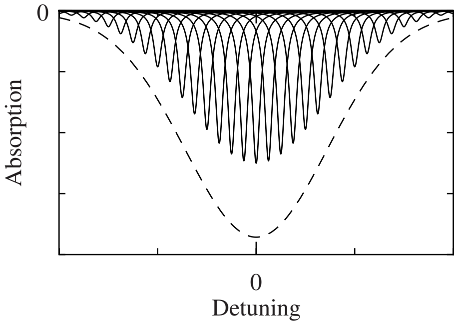

Figure 4.8: Convolution of the Doppler-free linear absorption spectrum with the Gaussian Doppler profile. The solid lines show the contributions of individual velocity groups to the Doppler-broadened spectrum (dashed line).

It is clear that the main effect of Doppler broadening is simply to increase the spectral linewidth from $\sim\Gamma$ to $\sim\Gamma_D$. There are some additional consequences of Doppler broadening for the linear effects, however. The reason for this can be illustrated by two-dimensional plots of the optical signals, such as those in Fig. 4.9, which compares magneto-optical rotation in the linear and nonlinear cases.

In Fig. 4.9(a), linear optical rotation as a function of detuning and Larmor frequency is displayed as a density plot, with white representing the largest positive signal and black the most negative signal. Because of the symmetry between detuning and the Larmor frequency for the linear effects discussed in Sec. 4.2.1, the signal peaks appear as diagonal features in the plot. Spectral convolution with the Doppler distribution will blur this plot in the vertical direction. However, because the features lie along a diagonal, blurring in the vertical direction will also effectively blur the features in the horizontal direction. As a result, not only is the spectral linewidth broadened, but the *magnetic* resonance linewidth is also broadened from Γ to Γ_D for the linear effect. This makes sense, as the original explanation for the

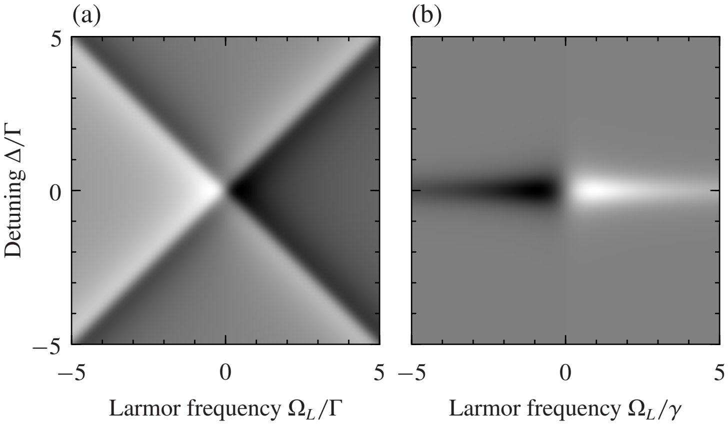

Figure 4.9: Density plots of the (a) linear (Eq. 4.28c) and (b) nonlinear (Eq. 4.31) Doppler-free magneto-optical rotation signals as a function of detuning and Larmor frequency. Note the different horizontal scales. In part (b), the saturation parameter has been chosen as $\kappa_2 = 2$.

linear effects involved splitting of the spectral resonances—if the spectral linewidths are broader, a larger magnetic field is needed in order to split them.

Another aspect of the linear signal plot to note is that there are positive (light) and negative (dark) signals along any given vertical axis. When blurring is performed along the vertical direction, the light and dark areas will overlap and cancel, reducing the magnitude of the signal. In general, if the integral of the Doppler-free spectrum is zero, the magnitude of the Doppler-broadened signal will be suppressed by Γ/Γ_D compared to a signal whose Doppler-free spectrum is all of one sign.

For comparison, nonlinear magneto-optical rotation is plotted in Fig. 4.9(b). In this case, the features lie along the horizontal and vertical axes, so that when the plot is blurred in the vertical direction, the magnetic-resonance feature in the horizontal direction is not broadened. In addition, each spectrum (along a vertical axis) contains only a positive or negative signal, so there is no cancelation induced by the blurring. This is one of the factors that makes NMOR an attractive measurement tool for thermal gases. Note, however, that in more complicated systems, such as those with hyperfine structure, there can be cancelations in the Doppler-broadened signal. The character of the Doppler-broadened spectrum can also be strongly affected by velocity-changing atomic collisions. These phenomena will be discussed in detail in Chapter 10.

Chapter 5

Perturbative and Approximate Methods

In this chapter, we use the perturbative method to solve the Liouville equation to second order in the optical electric field. This solution allows us to obtain lowest-order formulas for optical pumping (depopulation and repopulation), the excitation of atoms to the upper state (excitation matrix), and observable effects in transmitted light. These problems were solved in a general form in the 1960s, most notably, in the work of Barrat and Cohen-Tannoudji (1961), Cohen-Tannoudji (1962a,b), Dyakonov (1965), and Happer and Mathur (1967).

> Note that the terms in the density matrix responsible for the lowest-order nonlinear effects are actually *third* order in the electric field, as can be seen by examining the nonperturbative solution Eq. (3.64) for the density matrix. However, by considering pump-probe arrangements in which the interaction with each light field is second order or below, we can use the second-order perturbative solution to study higher-order effects.

We then discuss various forms of adiabatic elimination, by which the density-matrix evolution equations can be converted to rate equations under certain circumstances.

5.1 Perturbative solution of the steady-state density matrix

5.1.1 The general case

In Sec. 3.3 we solved the Liouville equation for a $F = 1 \to F' = 0$ system subject to light with arbitrarily large intensity. In this section we will find solutions for a general system in the limit of low light intensity.

We write the Liouville equation (Sec. 3.1) as before, except that we now separate from the repopulation matrix Λ the term describing repopulation due to spontaneous decay discussed in the previous section. This allows all of the dependence on ρ to be written explicitly:

$$\dot{\rho} = \frac{1}{i\hbar}\left[H,\rho\right] - \frac{1}{2}\{\widehat{\Gamma},\rho\} + \Lambda + \operatorname{Tr}\left(F\rho\right), \tag{5.1}$$

where H is the total Hamiltonian, $\widehat{\Gamma}$ is the relaxation matrix, Λ is the repopulation matrix, and F is the spontaneous emission operator. Here we have used the *anticommutator* $\{A,B\} = AB + BA$. If we neglect relaxation mechanisms, such as spin-exchange collisions, that depend on the density matrix, we can assume that Λ is independent of ρ.

We now take the total Hamiltonian to be composed of a diagonal part H_0 and a time-independent perturbation $\hbar V$, so that $H = H_0 + \hbar V$, where we write V in frequency units for notational convenience. The unperturbed Hamiltonian H_0 describes the level structure of the atom, and can also account for static external fields directed along the z-axis, so that their contribution to the Hamiltonian is diagonal. (The method is also applicable to a non-diagonal H_0 if it can first be diagonalized.) We will later take the perturbation V to be the Hamiltonian for light interaction under the rotating-wave approximation.

Taking the matrix element $\dot{\rho}_{mn} \equiv \langle m|\dot{\rho}|n\rangle$, where $|m\rangle$ and $|n\rangle$ are eigenstates of H_0 with eigenenergies E_m and E_n, we obtain

$$\begin{aligned}\dot{\rho}_{mn} &= -\frac{i}{\hbar}\langle m|[H_0,\rho]|n\rangle - i\langle m|[\hbar V,\rho]|n\rangle - \frac{1}{2}\langle m|\{\widehat{\Gamma},\rho\}|n\rangle \\ &\qquad + \langle m|\Lambda|n\rangle + \langle m|\operatorname{Tr}\left(F\rho\right)|n\rangle \\ &= -i\widetilde{\omega}_{mn}\rho_{mn} - i\sum_p\left[V_{mp}\rho_{pn} - \rho_{mp}V_{pn}\right] + \Lambda_{mn} + \sum_{rs}F^{sr}_{mn}\rho_{rs},\end{aligned} \tag{5.2}$$

where we define the complex frequency splitting $\widetilde{\omega}_{mn} = \left(E_m - E_n\right)/\hbar - i\left(\Gamma_m + \Gamma_n\right)/2$, with $\Gamma_m = \widehat{\Gamma}_{mm}$ ($\widehat{\Gamma}$ is assumed to be diagonal). If $\Gamma_m \neq 0$ for all m, the density matrix evolution is damped, and the density matrix reaches a steady state at large t. This means that we can set $\dot{\rho}_{mn} = 0$ on the left side of Eq. (5.2). We can then move the first term on the right side to the left to find an implicit steady-state solution for ρ_{mn}:

$$\rho_{mn} = \frac{1}{i\widetilde{\omega}_{mn}}\left(\Lambda_{mn} + \sum_{rs}F^{sr}_{mn}\rho_{rs} - i\sum_p\left(V_{mp}\rho_{pn} - \rho_{mp}V_{pn}\right)\right). \tag{5.3}$$

We can find a series expansion for ρ_{mn} by recursively substituting this expression into itself: every instance of a matrix element of ρ on the right side is replaced using the equality (5.3), and this procedure is repeated on the result. We assume that the atomic structure is such that there are no cascade decays, i.e., quantities such as $F^{pk}_{sr}F^{sr}_{mn}$ are zero. We also assume that Λ repopulates only the ground state, so that, for example, $F^{sr}_{mn}\Lambda_{rp}$ is zero (since $|r\rangle$ must be an excited state for F^{sr}_{mn} to be nonzero). If we drop all terms containing three or more factors of V, the process terminates, yielding

$$\begin{aligned}\rho_{mn} \approx \frac{1}{i\widetilde{\omega}_{mn}} \Bigg\{ & \Lambda_{mn} + \sum_p \left(\frac{\Lambda_{mp}V_{pn}}{\widetilde{\omega}_{mp}} - \frac{V_{mp}\Lambda_{pn}}{\widetilde{\omega}_{pn}} \right) \\ & + \sum_{pk} \left[\frac{\Lambda_{mp}V_{pk}V_{kn}}{\widetilde{\omega}_{mp}\widetilde{\omega}_{mk}} - \frac{V_{mp}\Lambda_{pk}V_{kn}}{\widetilde{\omega}_{pk}} \left(\frac{1}{\widetilde{\omega}_{mk}} + \frac{1}{\widetilde{\omega}_{pn}} \right) + \frac{V_{mp}V_{pk}\Lambda_{kn}}{\widetilde{\omega}_{pn}\widetilde{\omega}_{kn}} \right] \\ & + i \sum_{rs} \frac{F^{sr}_{mn}}{\widetilde{\omega}_{rs}} \sum_{pk} \frac{V_{rp}\Lambda_{pk}V_{ks}}{\widetilde{\omega}_{pk}} \left(\frac{1}{\widetilde{\omega}_{rk}} + \frac{1}{\widetilde{\omega}_{ps}} \right) \Bigg\}.\end{aligned} \tag{5.4}$$

This is the steady-state solution to the density matrix valid to second order. This expression can be simplified. In the case in which V represents the electric-dipole interaction Hamiltonian, it only mixes ground and excited states and does not mix ground states with each other. If we additionally assume that Λ represents initially unpolarized atoms and we restrict our attention to ground-state density-matrix elements ρ_{mn}, Eq. (5.4) reduces to

$$\begin{aligned}\rho_{mn} \approx \frac{\Lambda_{mm}}{i\widetilde{\omega}_{mn}} \Bigg[& \delta_{mn} + \sum_p V_{mp}V_{pn} \left(\frac{1}{\widetilde{\omega}_{mm}\widetilde{\omega}_{mp}} + \frac{1}{\widetilde{\omega}_{nn}\widetilde{\omega}_{pn}} \right) \\ & + i \sum_{rs} \frac{F^{sr}_{mn}}{\widetilde{\omega}_{rs}} \sum_k \frac{V_{rk}V_{ks}}{\widetilde{\omega}_{kk}} \left(\frac{1}{\widetilde{\omega}_{rk}} + \frac{1}{\widetilde{\omega}_{ks}} \right) \Bigg],\end{aligned} \tag{5.5}$$

where k runs over the ground states and p, r, and s run over the excited states. In Eq. (5.5) the first term in the square brackets represents the initial unpolarized ground state, the second term accounts for the loss of atoms that have been pumped out of the ground state, and the last term accounts for atoms that have returned to the ground state through spontaneous decay.

5.1.2 The optical-field case

We now choose the perturbation V to represent the interaction of the atoms with a light field. As we have seen previously, the light–atom interaction Hamiltonian in the dipole approximation is given by $H_l = -\mathbf{d} \cdot \boldsymbol{\mathcal{E}}$. Here we write the electric field $\boldsymbol{\mathcal{E}}$ in terms of a complex polarization vector $\hat{\boldsymbol{\varepsilon}}$ as

$$\boldsymbol{\mathcal{E}} = \mathcal{E}_0 \operatorname{Re} \hat{\boldsymbol{\varepsilon}} e^{i(\mathbf{k}\cdot\mathbf{r}-\omega t)}, \tag{5.6}$$

where ω is the light frequency, $\mathbf{k}$ is the wave vector, and $\mathcal{E}_0$ is the real electric field amplitude. We assume that a particular atom is in uniform motion, so that the position vector $\mathbf{r}$ is given by $\mathbf{r} = \mathbf{r}_0 + \mathbf{v}t$, where $\mathbf{r}_0$ is the initial position and $\mathbf{v}$ is the velocity of the atom.

We now employ the rotating-wave approximation to remove the optical-frequency time dependence from the Hamiltonian. We apply a unitary transformation via the diagonal matrix U with matrix elements

$$U_{pp} = e^{i[\mathbf{k}\cdot(\mathbf{r}_0+\mathbf{v}t)-\omega t]} \tag{5.7}$$

when $|p\rangle$ is an excited state, and $U_{pp} = 1$ when it is a ground state. Proceeding as in Sec. 3.3.2, we find that in the rotating frame (denoted here by a prime) the upper-state eigenenergies (diagonal terms of the Hamiltonian) are modified to

$$E'_p = E_p - \hbar\left(\omega - \mathbf{k}\cdot\mathbf{v}\right), \tag{5.8}$$

and the matrix elements of H_l become

$$\begin{aligned} (H'_l)_{pk} &= -\frac{1}{2}\mathcal{E}_0 \hat{\boldsymbol{\varepsilon}} \cdot \mathbf{d}_{pk} \\ (H'_l)_{kp} &= -\frac{1}{2}\mathcal{E}_0 \hat{\boldsymbol{\varepsilon}}^* \cdot \mathbf{d}_{kp} \end{aligned} \tag{5.9}$$

for $|p\rangle$ an excited state and $|k\rangle$ a ground state.

Thus Eq. (5.5) can be written in the rotating frame by setting $V = H'_l/\hbar$ and replacing transition frequencies ω_{pk} between the excited and ground states with

$$\omega'_{pk} = \omega_{pk} - \omega + \mathbf{k}\cdot\mathbf{v}. \tag{5.10}$$

This gives

$$\begin{aligned} \rho_{mn} \approx \frac{\Lambda_{mm}}{i\widetilde{\omega}_{mn}} \Bigg[&\delta_{mn} + \frac{\mathcal{E}_0^2}{4\hbar^2} \sum_p \hat{\boldsymbol{\varepsilon}}^* \cdot \mathbf{d}_{mp} \hat{\boldsymbol{\varepsilon}} \cdot \mathbf{d}_{pn} \left(\frac{1}{\widetilde{\omega}_{nn}\widetilde{\omega}'_{pn}} - \frac{1}{\widetilde{\omega}_{mm}(\widetilde{\omega}'_{pm})^*} \right) \\ &+ i\frac{\mathcal{E}_0^2}{4\hbar^2} \sum_{rs} \frac{F^{sr}_{mn}}{\widetilde{\omega}_{rs}} \sum_k \frac{\hat{\boldsymbol{\varepsilon}} \cdot \mathbf{d}_{rk} \hat{\boldsymbol{\varepsilon}}^* \cdot \mathbf{d}_{ks}}{\widetilde{\omega}_{kk}} \left(\frac{1}{\widetilde{\omega}'_{rk}} - \frac{1}{(\widetilde{\omega}'_{sk})^*} \right) \Bigg]. \end{aligned} \tag{5.11}$$

We assume that the excited states relax at a rate Γ and the ground states at a rate $\gamma \ll \Gamma$, so $\widetilde{\omega}_{mm} = \widetilde{\omega}_{nn} = -i\gamma$. A common situation, and the one that will be of interest to us in Chapter 9, is when coherences only develop between nearly degenerate ground or upper states, i.e., for which $\omega_{mn}, \omega_{rs} \ll \Gamma$. Note that this is the case for the nonlinear effects studied in Chapter 4. Making this assumption, we find

$$\rho_{mn} \approx \frac{\Lambda_{mm}}{i\widetilde{\omega}_{mn}}\left[\delta_{mn} - \frac{\mathcal{E}_0^2}{4\hbar^2}\frac{\Gamma}{\gamma}\left(\sum_p \frac{\hat{\boldsymbol{\varepsilon}}^* \cdot \mathbf{d}_{mp}\hat{\boldsymbol{\varepsilon}} \cdot \mathbf{d}_{pn}}{(\omega'_{pm})^2 + (\Gamma/2)^2} - \sum_{rs}\frac{F_{mn}^{sr}}{\Gamma}\sum_k \frac{\hat{\boldsymbol{\varepsilon}} \cdot \mathbf{d}_{rk}\hat{\boldsymbol{\varepsilon}}^* \cdot \mathbf{d}_{ks}}{(\omega'_{rk})^2 + (\Gamma/2)^2}\right)\right]. \tag{5.12}$$

The density matrix, as determined by Eq. (5.12), is a function of the atomic velocity $\mathbf{v}$ through the velocity dependence of the Doppler-shifted transition frequencies. Equation (5.12) can be applied directly to the individual velocity groups in a Doppler-broadened ensemble, assuming that the atomic velocities do not change during the polarization relaxation time. This is the case for the transit effect studied in Chapters 3 and 4. When a polarization-preserving technique like buffer gas or an antirelaxation coating is used, however, atoms undergo collisions that change their velocities without destroying their polarization. This means that we must account for atomic polarization in one velocity group that originated in another velocity group. In the limit in which the collision rate is much higher than the polarization relaxation rate, the polarization in all of the velocity groups becomes the same. This is the *complete-mixing* approximation.

We can find the mixed density matrix by taking a weighted average of the density matrices for each velocity group. The weighting function is the Maxwellian velocity distribution, written in frequency space as (Eq. 4.38)

$$f_{\Delta_v}(\Delta_v)d\Delta_v = \frac{1}{\Gamma_D\sqrt{\pi}}e^{-\Delta_v^2/\Gamma_D^2}d\Delta_v. \tag{5.13}$$

Assuming that the Doppler width Γ_D is much greater than Γ, performing the integral over atomic velocity amounts to replacing the Lorentzian spectrum with a Gaussian one, i.e., making the replacement

$$\frac{\Gamma}{(\omega_{rk} - \omega + \mathbf{k} \cdot \mathbf{v})^2 + (\Gamma/2)^2} \to \frac{2\sqrt{\pi}}{\Gamma_D}e^{-(\omega-\omega_{rk})^2/\Gamma_D^2}. \tag{5.14}$$

We then have for the velocity-averaged ground-state density matrix

$$\begin{aligned}\rho_{mn} \approx \frac{\Lambda_{mm}}{i\widetilde{\omega}_{mn}}\Bigg[\delta_{mn} - \frac{\sqrt{\pi}\mathcal{E}_0^2}{2\hbar^2\gamma\Gamma_D}\Bigg(&\sum_p \hat{\boldsymbol{\varepsilon}}^* \cdot \mathbf{d}_{mp}\hat{\boldsymbol{\varepsilon}} \cdot \mathbf{d}_{pn} e^{-(\omega-\omega_{pm})^2/\Gamma_D^2} \\ &- \sum_{krs} \frac{4\omega_{rm}^3}{3\hbar c^3\Gamma}\mathbf{d}_{mr} \cdot \mathbf{d}_{sn}\hat{\boldsymbol{\varepsilon}} \cdot \mathbf{d}_{rk}\hat{\boldsymbol{\varepsilon}}^* \cdot \mathbf{d}_{ks} e^{-(\omega-\omega_{rk})^2/\Gamma_D^2}\Bigg)\Bigg],\end{aligned} \tag{5.15}$$

where we have used the explicit form (3.16) of the spontaneous emission operator.

5.1.3 Repopulation and depopulation

The first term in Eqs. (5.12) and (5.15) describes the unperturbed ground-state density matrix, while the second term of each of these equations describes the perturbation induced by the light. There are two contributions—the first describes the effect of depopulation pumping, i.e., atoms that have been removed from the ground state by optical pumping. Defining $\Lambda_{mm} = \gamma/w$, where w is the multiplicity of the ground state, this contribution takes the form

$$\rho_{mn}^{(\text{depop.})} \approx -\frac{\pi}{2}\frac{\mathcal{E}_0^2}{w\hbar^2\left(i\omega_{mn}+\gamma\right)}\sum_p \hat{\boldsymbol{\varepsilon}}^* \cdot \mathbf{d}_{mp}\hat{\boldsymbol{\varepsilon}} \cdot \mathbf{d}_{pn} G(\omega'_{pm}), \tag{5.16}$$

where the lineshape function $G(\Delta)$ is given by

$$G(\Delta) = \frac{1}{\pi}\frac{\Gamma/2}{\Delta^2 + \left(\Gamma/2\right)^2} \tag{5.17}$$

when there is no velocity mixing, and

$$G(\Delta) = \frac{1}{\Gamma_D\sqrt{\pi}} e^{-\Delta^2/\Gamma_D^2} \tag{5.18}$$

when there is complete mixing. (In the case with no mixing, the argument to the lineshape function is the Doppler-shifted light detuning, while in the complete-mixing case it is the unshifted detuning.)

The second contribution describes repopulation pumping—atoms that have been returned to the ground state through spontaneous decay. It is given by

$$\rho_{mn}^{(\text{repop.})} \approx \frac{\pi}{2}\frac{\mathcal{E}_0^2}{w\hbar^2\left(i\omega_{mn}+\gamma\right)}\sum_{krs} \frac{4\omega_{rm}^3}{3\hbar c^3\Gamma}\mathbf{d}_{mr} \cdot \mathbf{d}_{sn}\hat{\boldsymbol{\varepsilon}} \cdot \mathbf{d}_{rk}\hat{\boldsymbol{\varepsilon}}^* \cdot \mathbf{d}_{ks} G(\omega'_{rk}). \tag{5.19}$$

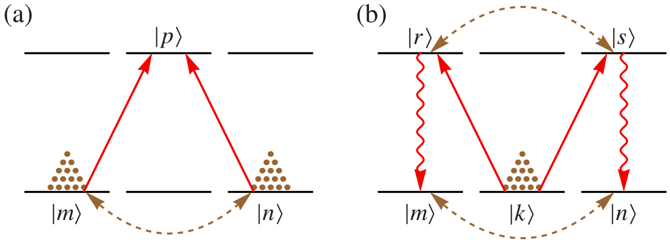

Figure 5.1: Generation of coherence in the ground state of an atomic transition. (a) Two ground-state sublevels $|m\rangle$, $|n\rangle$ connected to the same upper-state sublevel $|p\rangle$. (b) A ground-state sublevel $|k\rangle$ connected to two upper-state sublevels $|r\rangle$, $|s\rangle$, generating coherence between them. The coherence is then transferred to a pair of ground-state sublevels $|m\rangle$, $|n\rangle$ via spontaneous decay.

In a perturbative analysis, the various effects of the light can be assumed to be acting independently. Therefore, these terms can be considered separately in order to analyze the various processes occurring during light–atom interactions. We will do this in Chapter 9.

The terms describing depopulation and repopulation pumping can be converted into rates by noting that the characteristic time for the ground state to reach equilibrium is $1/\gamma$. Because Eqs. (5.16) and (5.19) give the steady-state value for each process, the rate of change for each process must be obtained by multiplying by γ:

$$\dot{\rho}_{mn}^{(\text{depop.})} \approx -\frac{\pi}{2}\frac{\gamma\mathcal{E}_0^2}{w\hbar^2\left(i\omega_{mn}+\gamma\right)}\sum_p \hat{\boldsymbol{\varepsilon}}^*\cdot\mathbf{d}_{mp}\hat{\boldsymbol{\varepsilon}}\cdot\mathbf{d}_{pn}G(\omega'_{pm}), \tag{5.20}$$

and

$$\dot{\rho}_{mn}^{(\text{repop.})} \approx \frac{\pi}{2}\frac{\gamma\mathcal{E}_0^2}{w\hbar^2\left(i\omega_{mn}+\gamma\right)}\sum_{krs}\frac{4\omega_{rm}^3}{3\hbar c^3\Gamma}\mathbf{d}_{mr}\cdot\mathbf{d}_{sn}\hat{\boldsymbol{\varepsilon}}\cdot\mathbf{d}_{rk}\hat{\boldsymbol{\varepsilon}}^*\cdot\mathbf{d}_{ks}G(\omega'_{rk}). \tag{5.21}$$

By examining the formulas for repopulation and depopulation pumping, we can see how coherences can be generated in the ground state by the light. The term for depopulation pumping on a coherence ρ_{mn} is nonzero only if $|m\rangle$ and $|n\rangle$ are both connected to a single upper state $|p\rangle$ (Fig. 5.1a). Coherence is created by repopulation pumping, on the other hand, when the light connects the states via the chain $|m\rangle \leftrightarrow |r\rangle \leftrightarrow |k\rangle \leftrightarrow |s\rangle \leftrightarrow |n\rangle$. The ground state $|k\rangle$ is connected to two upper states $|r\rangle$ and $|s\rangle$, generating coherence between them; the coherence is then transferred to the ground state by spontaneous decay (Fig. 5.1b). Note that if there is initially coherence in the ground state, it can be transferred to the upper state by the light, allowing for another path by which repopulation pumping can create coherence in the ground state (see Sec. 5.1.4).

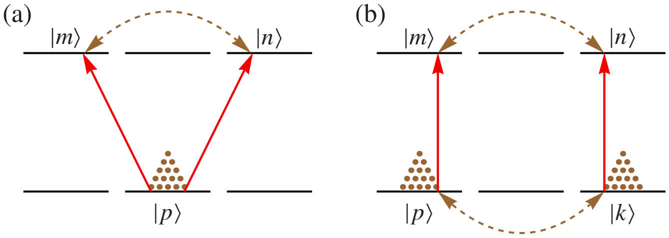

Figure 5.2: Generation by excitation light of coherence in the upper state of an atomic transition. (a) A ground-state sublevel connected to two upper-state sublevels. (b) A pair of ground-state sublevels with coherence between them connected to a pair of upper-state sublevels.

5.1.4 Optical excitation

We can also use Eq. (5.4) to examine the effect of excitation light on the upper state. Assuming now that $|m\rangle$ and $|n\rangle$ are upper states, Eq. (5.4) reduces to

$$\rho_{mn} \approx -\frac{1}{i\widetilde{\omega}_{mn}} \sum_{pk} \frac{V_{mp}\Lambda_{pk}V_{kn}}{\widetilde{\omega}_{pk}} \left(\frac{1}{\widetilde{\omega}_{mk}} + \frac{1}{\widetilde{\omega}_{pn}} \right), \tag{5.22}$$

where $|p\rangle$ and $|k\rangle$ now represent ground states. Under the assumption that ground- and upper-state coherences only develop between states that are split by much less than Γ, this formula becomes

$$\rho_{mn} \approx \sum_{pk} \frac{V_{mp}\Lambda_{pk}V_{kn}}{(i\omega_{pk} + \gamma)\left[\omega_{pn}^2 + (\Gamma/2)^2\right]}. \tag{5.23}$$

Equation (5.23) indicates the ways in which coherences can be produced in the upper state. If Λ is diagonal, as would be the case for an initially unpolarized ground state, then we must have $p = k$. In that case, the only way that an upper-state coherence ρ_{mn} can be nonzero is if V_{mp} and V_{pn} are both nonzero; i.e., the light connects $|p\rangle$ to both $|m\rangle$ and $|n\rangle$ (Fig. 5.2a). If Λ has off-diagonal elements Λ_{pk}, representing initial ground-state coherences ρ_{pk}, then ρ_{mn} can be nonzero if the light connects $|p\rangle$ to $|m\rangle$ and $|k\rangle$ to $|n\rangle$ (Fig. 5.2b).

Substituting the optical Hamiltonian into Eq. (5.23) and using $\Lambda = \gamma\rho^{(0)}$, we have

$$\begin{aligned} \rho_{mn} &\approx \frac{\mathcal{E}_0^2}{4\hbar^2} \sum_{pk} \frac{\gamma}{i\omega_{pk} + \gamma} \frac{\hat{\boldsymbol{\varepsilon}} \cdot \mathbf{d}_{mp}\rho_{pk}^{(0)}\hat{\boldsymbol{\varepsilon}}^* \cdot \mathbf{d}_{kn}}{(\omega'_{pn})^2 + (\Gamma/2)^2} \\ &= \frac{\pi\mathcal{E}_0^2}{2\Gamma\hbar^2} \sum_{pk} \hat{\boldsymbol{\varepsilon}} \cdot \mathbf{d}_{mp}\rho_{pk}^{(0)}\hat{\boldsymbol{\varepsilon}}^* \cdot \mathbf{d}_{kn} G\left(\omega'_{pn}\right), \end{aligned} \tag{5.24}$$

where in the last line we have assumed that $|p\rangle$ and $|k\rangle$ are degenerate.

> Additional discussion, including an examination of a set of monochromatic light fields of different frequencies and the transition to the broad-line approximation (Sec. 5.2.2), can be found in the book by Aleksandrov *et al.* (1993).

5.1.5 Absorption and optical rotation signals

In Sec. 4.1 we found expressions for optical signals by using the wave equation to relate the medium polarization to the changes in optical parameters. In that section we primarily used the α–ϵ parametrization of the light field—it will also be convenient to write these expressions using the complex polarization vector $\hat{\boldsymbol{\varepsilon}}$ to characterize the polarization of the light field. After obtaining these formulas, we will apply the perturbative solution of the density matrix to them. This will supply expressions for the optical signals in terms of the ground-state density matrix, valid to lowest order in the probe light field.

Equation (5.6) describes the electric field of the light. The complex polarization vector $\hat{\boldsymbol{\varepsilon}}$ is normalized so that $\hat{\boldsymbol{\varepsilon}}\cdot\hat{\boldsymbol{\varepsilon}}^* = 1$. We are free to choose a phase convention for $\hat{\boldsymbol{\varepsilon}}$; a convenient choice is to assume that $\hat{\boldsymbol{\varepsilon}}\cdot\hat{\boldsymbol{\varepsilon}}$ is real and nonnegative. Then $0 \le \hat{\boldsymbol{\varepsilon}}\cdot\hat{\boldsymbol{\varepsilon}} \le 1$, with $\hat{\boldsymbol{\varepsilon}}\cdot\hat{\boldsymbol{\varepsilon}} = 1$ for linear polarization and $\hat{\boldsymbol{\varepsilon}}\cdot\hat{\boldsymbol{\varepsilon}} = 0$ for circular polarization. The dot product between the real and imaginary parts of $\hat{\boldsymbol{\varepsilon}}$ is then given by

$$\begin{aligned}(\operatorname{Re}\hat{\boldsymbol{\varepsilon}})\cdot(\operatorname{Im}\hat{\boldsymbol{\varepsilon}}) &= -\frac{i}{4}\left(\hat{\boldsymbol{\varepsilon}}+\hat{\boldsymbol{\varepsilon}}^*\right)\cdot\left(\hat{\boldsymbol{\varepsilon}}-\hat{\boldsymbol{\varepsilon}}^*\right)\\ &= -\frac{i}{4}\left[\hat{\boldsymbol{\varepsilon}}\cdot\hat{\boldsymbol{\varepsilon}}-\left(\hat{\boldsymbol{\varepsilon}}\cdot\hat{\boldsymbol{\varepsilon}}\right)^*\right]\\ &= 0,\end{aligned} \tag{5.25}$$

so we can define a pair of orthogonal real unit vectors by

$$\hat{\mathbf{e}}_1 = \frac{\operatorname{Re}\hat{\boldsymbol{\varepsilon}}}{|\operatorname{Re}\hat{\boldsymbol{\varepsilon}}|}, \tag{5.26a}$$

$$\hat{\mathbf{e}}_2 = \hat{\mathbf{k}}\times\hat{\mathbf{e}}_1 = \pm\frac{\operatorname{Im}\hat{\boldsymbol{\varepsilon}}}{|\operatorname{Im}\hat{\boldsymbol{\varepsilon}}|}. \tag{5.26b}$$

The magnitudes of the real and imaginary parts of $\hat{\boldsymbol{\varepsilon}}$ are given by

$$|\operatorname{Re}\hat{\boldsymbol{\varepsilon}}| = \frac{1}{2}\left|\hat{\boldsymbol{\varepsilon}}^*+\hat{\boldsymbol{\varepsilon}}\right| = \sqrt{\frac{1+\hat{\boldsymbol{\varepsilon}}\cdot\hat{\boldsymbol{\varepsilon}}}{2}}, \tag{5.27a}$$

$$|\operatorname{Im}\hat{\boldsymbol{\varepsilon}}| = \frac{1}{2}\left|i\left(\hat{\boldsymbol{\varepsilon}}^*-\hat{\boldsymbol{\varepsilon}}\right)\right| = \sqrt{\frac{1-\hat{\boldsymbol{\varepsilon}}\cdot\hat{\boldsymbol{\varepsilon}}}{2}}. \tag{5.27b}$$

We can rewrite the optical electric field (5.6) in terms of $\hat{\mathbf{e}}_1$ and $\hat{\mathbf{e}}_2$ as

$$\boldsymbol{\mathcal{E}} = \mathcal{E}_0 \operatorname{Re}\left(e^{i(\mathbf{k}\cdot\mathbf{r}-\omega t+\varphi)}\left(|\operatorname{Re}\hat{\boldsymbol{\varepsilon}}|\,\hat{\mathbf{e}}_1 \pm i\,|\operatorname{Im}\hat{\boldsymbol{\varepsilon}}|\,\hat{\mathbf{e}}_2\right)\right). \tag{5.28}$$

We can also parametrize the optical field as we have done previously, in terms of the rotation angle φ and ellipticity ϵ:

$$\boldsymbol{\mathcal{E}} = \operatorname{Re}\left\{\mathcal{E}_0 e^{i(\mathbf{k}\cdot\mathbf{r}-\omega t+\varphi)}\left[(\cos\alpha\cos\epsilon - i\sin\alpha\sin\epsilon)\,\hat{\mathbf{e}}_1 + (\sin\alpha\cos\epsilon + i\cos\alpha\sin\epsilon)\,\hat{\mathbf{e}}_2\right]\right\}. \tag{5.29}$$

With the basis vectors defined in terms of the polarization vector by Eq. (5.26), we can compare Eqs. (5.28) and (5.29) to see that $\alpha = 0$. In addition, using Eq. (5.27), we can relate ϵ to $\hat{\boldsymbol{\varepsilon}}$:

$$\cos\epsilon = \sqrt{\frac{1+\hat{\boldsymbol{\varepsilon}}\cdot\hat{\boldsymbol{\varepsilon}}}{2}}, \tag{5.30a}$$

$$\sin\epsilon = \pm\sqrt{\frac{1-\hat{\boldsymbol{\varepsilon}}\cdot\hat{\boldsymbol{\varepsilon}}}{2}}, \tag{5.30b}$$

which gives

$$\epsilon = \pm\arctan\sqrt{\frac{1-\hat{\boldsymbol{\varepsilon}}\cdot\hat{\boldsymbol{\varepsilon}}}{1+\hat{\boldsymbol{\varepsilon}}\cdot\hat{\boldsymbol{\varepsilon}}}}. \tag{5.31}$$

In Sec. 4.1, we found that the change in the optical parameters over an infinitesimal path length $d\ell$ is given by (assuming $\alpha = 0$)

$$\frac{1}{\mathcal{E}_0}\frac{d\mathcal{E}_0}{d\ell} = \frac{d\ln\mathcal{E}_0}{d\ell} = \frac{2\pi\omega}{\mathcal{E}_0 c}\left(P_2\cos\epsilon + P_3\sin\epsilon\right), \tag{5.32a}$$

$$\frac{d\varphi}{d\ell} = \frac{2\pi\omega}{\mathcal{E}_0 c}\sec 2\epsilon\left(P_1\cos\epsilon + P_4\sin\epsilon\right), \tag{5.32b}$$

$$\frac{d\alpha}{d\ell} = \frac{2\pi\omega}{\mathcal{E}_0 c}\sec 2\epsilon\left(P_1\sin\epsilon + P_4\cos\epsilon\right), \tag{5.32c}$$

$$\frac{d\epsilon}{d\ell} = -\frac{2\pi\omega}{\mathcal{E}_0 c}\left(P_2\sin\epsilon - P_3\cos\epsilon\right). \tag{5.32d}$$

Here the components P_i of the medium polarization $\mathbf{P} = n\langle\mathbf{d}\rangle$ are defined by

$$\mathbf{P} = \operatorname{Re}\left\{e^{i(\mathbf{k}\cdot\mathbf{r}-\omega t+\varphi)}\left[(P_1 - iP_2)\,\hat{\mathbf{e}}_1 + (P_3 - iP_4)\,\hat{\mathbf{e}}_2\right]\right\}. \tag{5.33}$$

Evaluating the trace to find the medium polarization, we find

$$\begin{aligned}\mathbf{P} &= n\,\mathrm{Tr}\,\rho\mathbf{d}\\ &= n\sum_{mp} 2\,\mathrm{Re}\left(\rho_{pm}\mathbf{d}_{mp}\right)\\ &= n\sum_{mp} 2\,\mathrm{Re}\left(\rho'_{pm}\mathbf{d}_{mp}e^{i(\mathbf{k}\cdot\mathbf{r}-\omega t+\varphi)}\right),\end{aligned} \tag{5.34}$$

where m runs over ground states, and p runs over excited states. In the last step we have written $\mathbf{P}$ in terms of the density matrix in the rotating frame, using $\rho = U\rho' U^\dagger$.

Comparing Eqs. (5.33) and (5.34), we find for the components of $\mathbf{P}$,

$$P_1 = 2n\sum \mathrm{Re}\left[\rho'_{pm}\mathbf{d}_{mp}\cdot\hat{\mathbf{e}}_1\right], \tag{5.35a}$$

$$P_2 = -2n\sum \mathrm{Im}\left[\rho'_{pm}\mathbf{d}_{mp}\cdot\hat{\mathbf{e}}_1\right], \tag{5.35b}$$

$$P_3 = 2n\sum \mathrm{Re}\left[\rho'_{pm}\mathbf{d}_{mp}\cdot\hat{\mathbf{e}}_2\right], \tag{5.35c}$$

$$P_4 = -2n\sum \mathrm{Im}\left[\rho'_{pm}\mathbf{d}_{mp}\cdot\hat{\mathbf{e}}_2\right]. \tag{5.35d}$$

We can write Eqs. (5.32) in terms of $\hat{\boldsymbol{\varepsilon}}$ and ρ' using Eqs. (5.26), (5.27), and (5.35). We find that we can write for an observable $\mathcal{O}$,

$$\frac{d\mathcal{O}}{d\ell} = -\frac{4\pi\omega n}{\mathcal{E}_0 c}\sum \mathrm{Im}\left[\rho'_{pm}\mathbf{d}_{mp}\cdot\mathbf{u}_{\mathcal{O}}\right], \tag{5.36}$$

where

$$\mathbf{u}_{\ln(\mathcal{E}_0)} = \hat{\boldsymbol{\varepsilon}}^*, \tag{5.37a}$$

$$\mathbf{u}_\varphi = -i\frac{\hat{\boldsymbol{\varepsilon}}^*}{|\hat{\boldsymbol{\varepsilon}}\cdot\hat{\boldsymbol{\varepsilon}}|}, \tag{5.37b}$$

$$\mathbf{u}_\alpha = \hat{\mathbf{k}}\times\frac{\mathrm{Re}\,\hat{\boldsymbol{\varepsilon}}}{|\hat{\boldsymbol{\varepsilon}}\cdot\hat{\boldsymbol{\varepsilon}}|} - i\frac{\mathrm{Re}\,\hat{\boldsymbol{\varepsilon}}}{|\hat{\boldsymbol{\varepsilon}}\cdot\hat{\boldsymbol{\varepsilon}}|}\sqrt{\frac{1-\hat{\boldsymbol{\varepsilon}}\cdot\hat{\boldsymbol{\varepsilon}}}{1+\hat{\boldsymbol{\varepsilon}}\cdot\hat{\boldsymbol{\varepsilon}}}}, \tag{5.37c}$$

$$\mathbf{u}_\epsilon = -i\left(\hat{\mathbf{k}}\times\mathrm{Re}\,\hat{\boldsymbol{\varepsilon}} \mp i\,\mathrm{Re}\,\hat{\boldsymbol{\varepsilon}}\sqrt{\frac{1-\hat{\boldsymbol{\varepsilon}}\cdot\hat{\boldsymbol{\varepsilon}}}{1+\hat{\boldsymbol{\varepsilon}}\cdot\hat{\boldsymbol{\varepsilon}}}}\right). \tag{5.37d}$$

For linear polarization, this reduces to

$$\mathbf{u}_{\ln(\mathcal{E}_0)} = \hat{\boldsymbol{\varepsilon}}, \tag{5.38a}$$

$$\mathbf{u}_\varphi = -i\hat{\boldsymbol{\varepsilon}}, \tag{5.38b}$$

$$\mathbf{u}_\alpha = \hat{\mathbf{k}}\times\hat{\boldsymbol{\varepsilon}}, \tag{5.38c}$$

$$\mathbf{u}_\epsilon = -i\hat{\mathbf{k}}\times\hat{\boldsymbol{\varepsilon}}. \tag{5.38d}$$

We can use the perturbation expansion obtained in Sec. 5.1 to find a lowest-order expression for Eq. (5.36) in terms of the ground-state density matrix elements. Optical polarization appears at first order in the expansion in the electric field. From Eq. (5.4) we have for the first-order optical coherences

$$\rho'_{pm} \approx \sum_n \frac{iV_{pn}\Lambda_{nm}}{\widetilde{\omega}'_{pm}\widetilde{\omega}_{mn}}. \tag{5.39}$$

We assume here that Λ represents the influx of ground-state atoms that have been polarized by some prior pump-light interaction. If these atoms have density matrix $\rho^{(0)}$, then $\Lambda_{nm} = \gamma\rho^{(0)}_{nm}$ and we have

$$\rho'_{pm} \approx -\frac{i}{2}\frac{\gamma\mathcal{E}_0}{\hbar}\sum_n \frac{\hat{\boldsymbol{\varepsilon}}\cdot\mathbf{d}_{pn}\rho^{(0)}_{nm}}{\widetilde{\omega}'_{pm}\widetilde{\omega}_{mn}}. \tag{5.40}$$

Substituting this expression into Eq. (5.36), we find

$$\frac{d\mathcal{O}}{d\ell} = \frac{2\pi\omega\gamma n}{\hbar c}\sum_{pmn}\mathrm{Re}\left[\frac{\hat{\boldsymbol{\varepsilon}}\cdot\mathbf{d}_{pn}\rho^{(0)}_{nm}\mathbf{d}_{mp}\cdot\mathbf{u}_{\mathcal{O}}}{\widetilde{\omega}'_{pm}\widetilde{\omega}_{mn}}\right]. \tag{5.41}$$

Neglecting coherences between nondegenerate ground states, we find

$$\begin{aligned}\frac{d\mathcal{O}}{d\ell} &= -\frac{2\pi\omega n}{\hbar c}\sum_{pmn}\mathrm{Im}\left[\frac{\hat{\boldsymbol{\varepsilon}}\cdot\mathbf{d}_{pn}\rho^{(0)}_{nm}\mathbf{d}_{mp}\cdot\mathbf{u}_{\mathcal{O}}}{\widetilde{\omega}'_{pm}}\right]\\ &= -\frac{2\pi\omega n}{\hbar c}\,\mathrm{Im}\left[\hat{\boldsymbol{\varepsilon}}\cdot\overset{\leftrightarrow}{\boldsymbol{\beta}}\cdot\mathbf{u}_{\mathcal{O}}\right],\end{aligned} \tag{5.42}$$

where we have defined

$$\overset{\leftrightarrow}{\boldsymbol{\beta}} = \sum_{pmn}\frac{\mathbf{d}_{pn}\rho^{(0)}_{nm}\mathbf{d}_{mp}}{\widetilde{\omega}'_{pm}}. \tag{5.43}$$

In Chapter 9 we calculate the light absorption under the assumption that $\rho^{(0)}_{nm}$ is independent of $\mathbf{v}$ (complete-mixing approximation). From Eqs. (5.10), (5.37a), and (5.42) we obtain

$$\begin{aligned}\frac{1}{\mathcal{E}_0}\frac{d\mathcal{E}_0}{d\ell} &= -\frac{2\pi\omega n}{\hbar c}\sum_{pmn}\mathrm{Im}\left(\frac{\hat{\boldsymbol{\varepsilon}}\cdot\mathbf{d}_{pn}\rho^{(0)}_{nm}\mathbf{d}_{mp}\cdot\hat{\boldsymbol{\varepsilon}}^*}{\omega_{pm}-\omega+\mathbf{k}\cdot\mathbf{v}-i\Gamma/2}\right)\\ &= -\frac{\pi\omega n\Gamma}{\hbar c}\sum_{pmn}\frac{\hat{\boldsymbol{\varepsilon}}\cdot\mathbf{d}_{pn}\rho^{(0)}_{nm}\mathbf{d}_{mp}\cdot\hat{\boldsymbol{\varepsilon}}^*}{(\omega_{pm}-\omega+\mathbf{k}\cdot\mathbf{v})^2+(\Gamma/2)^2}.\end{aligned} \tag{5.44}$$

The total light absorption is given by the average of Eq. (5.44) over atomic velocities. Weighting by a Maxwellian Doppler distribution and integrating as in Sec. 5.1, we find for the fractional change in electric field

$$\frac{1}{\mathcal{E}_0}\frac{d\mathcal{E}_0}{d\ell} = -\frac{2\pi^2\omega n}{\hbar c}\sum_{pmn}\hat{\boldsymbol{\varepsilon}}\cdot\mathbf{d}_{pn}\rho^{(0)}_{nm}\mathbf{d}_{mp}\cdot\hat{\boldsymbol{\varepsilon}}^{*}G\left(\omega_{pm}\right), \tag{5.45}$$

where the lineshape function G is as defined in Eq. (5.18).

5.2 Adiabatic elimination

Even when nonperturbative solutions to the density-matrix evolution equations are desired, it may be possible to simplify the equations using other approximations. In certain cases in which the relaxation time scales in a problem are widely separated, a simplifying procedure known as *adiabatic elimination* can be employed. In this approximation, discussed in this section, certain elements of the density matrix are considered to be dependent, rather than independent variables, and can be eliminated from the evolution equations.

We first take a detour and describe how, when solving for the steady-state density matrix, the optical coherences can be removed from the equations without making any approximations. We then show how this approach can be extended to the time-dependent evolution equations when either the laser line width or the natural line width is very broad.

5.2.1 Reduction of steady-state density-matrix equations

Consider the Liouville equation written in the form (5.2):

$$\dot{\rho}_{mn} = -i\widetilde{\omega}_{mn}\rho_{mn} + \Lambda_{mn} + \sum_{rs}F^{sr}_{mn}\rho_{rs} - i\sum_{p}\left[V_{mp}\rho_{pn} - \rho_{mp}V_{pn}\right]. \tag{5.46}$$

Here V describes an interaction that connects lower and upper states. Previously in this chapter we assumed that this interaction was weak, but in this section we take it to have arbitrary strength, so that the analysis is nonperturbative. We will consider the optical-field case under the rotating-wave approximation, in which V is given by (Eq. 5.9)

$$V_{pk} = -\frac{\mathcal{E}_0}{2\hbar}\hat{\boldsymbol{\varepsilon}}\cdot\mathbf{d}_{pk}, \tag{5.47a}$$

$$V_{kp} = -\frac{\mathcal{E}_0}{2\hbar}\hat{\boldsymbol{\varepsilon}}^{*}\cdot\mathbf{d}_{kp}, \tag{5.47b}$$

for $|p\rangle$ an excited state and $|k\rangle$ a ground state. Also, the complex frequency splitting $\widetilde{\omega}$ is given for the optical transitions by (Eq. 5.10)

$$\widetilde{\omega}_{pk} = \omega_{pk} - \omega + \mathbf{k}\cdot\mathbf{v} - \frac{i}{2}\left(\Gamma+\gamma\right), \tag{5.48a}$$

$$\widetilde{\omega}_{kp} = -\left(\omega_{pk} - \omega + \mathbf{k}\cdot\mathbf{v}\right) - \frac{i}{2}\left(\Gamma+\gamma\right), \tag{5.48b}$$

where we omit the prime previously used to indicate the rotating basis.

In the steady-state condition, the time derivatives are zero, and we can solve the Liouville equation implicitly as in Eq. (5.3). Now consider an optical coherence ρ_{mp}, where m is a ground state and p is an excited state, or vice versa. Such a coherence is not replenished by atomic transit or spontaneous decay, so Eq. (5.3) reduces to

$$\rho_{mp} = \frac{1}{\widetilde{\omega}_{mp}}\sum_r\left(\rho_{mr}V_{rp} - V_{mr}\rho_{rp}\right), \tag{5.49}$$

Note that the right-hand side of Eq. (5.49) is free of optical coherences—ρ_{mr} and ρ_{rp} are either ground- or excited-state density-matrix elements. We can therefore substitute Eq. (5.49) back into the steady-state version of (5.46) to eliminate the optical coherences:

$$\begin{aligned}0 = &-i\widetilde{\omega}_{mn}\rho_{mn} + \Lambda_{mn} + \sum_{rs}F_{mn}^{sr}\rho_{rs}\\ &-i\sum_{pr}\left[\left(\frac{1}{\widetilde{\omega}_{pn}}+\frac{1}{\widetilde{\omega}_{mr}}\right)V_{mp}\rho_{pr}V_{rn} - \frac{V_{mp}V_{pr}\rho_{rn}}{\widetilde{\omega}_{pn}} - \frac{\rho_{mp}V_{pr}V_{rn}}{\widetilde{\omega}_{mr}}\right],\end{aligned} \tag{5.50}$$

where m and n are now either both lower states or both upper states. This is now a complete set of equations for the lower- and upper-state density-matrix elements, a much smaller set of variables than the full system including the optical coherences.

Equation (5.50) also has the advantage over the full set of equations for the density matrix that it manifestly displays the resonant character of the interaction. Assuming for simplicity that both the lower states and the upper states are nearly degenerate, we can write the Doppler-shifted light detuning of Eq. (5.48) as $-\left(\omega_{pk}-\omega+\mathbf{k}\cdot\mathbf{v}\right)=\Delta$, giving

$$\frac{1}{\widetilde{\omega}_{pn}} = -\frac{1}{\pm\Delta+\frac{i}{2}\left(\Gamma+\gamma\right)} = i\left(\frac{\frac{1}{2}\left(\Gamma+\gamma\right)}{\Delta^2+\frac{1}{4}\left(\Gamma+\gamma\right)^2} \pm \frac{i\Delta}{\Delta^2+\frac{1}{4}\left(\Gamma+\gamma\right)^2}\right), \tag{5.51}$$

where we take the plus sign if $|n\rangle$ is an upper state, and the minus sign if it is a lower state. Each of the terms in the parentheses are resonant lineshape factors, the first term describing atomic transitions, and the second describing AC Stark shifts due to the light field. The terms in the square brackets in Eq. (5.50) can also be assigned physical meanings: for a lower state, the first term describes transitions from the upper states due to stimulated emission, while the second and third terms describe transfer of atoms between the lower states (optical pumping) as well as Stark shifts; for an upper state, the first term describes transitions from the ground state, while the second and third describe transfer between the upper states.

Note that we have not used any approximations in deriving Eq. (5.50). The derivation does, however, depend crucially on the steady-state condition—otherwise, we would not be able to solve for the optical coherences to obtain Eq. (5.49). We now see how in certain cases a quasi-steady-state condition can be assumed, under which it is possible to perform this step even when solving the time-dependent equations.

5.2.2 Broad-band light

One situation in which adiabatic elimination can be employed is when the incident light has a broad spectral profile. Under the *broad-line approximation* (BLA), this broad linewidth is assumed to be the result of fast phase fluctuations of the light field, corresponding to a short coherence lifetime and fast relaxation of optical coherences, faster than the other relaxation rates and pumping rates in the problem. Under this approximation, the optical coherences can be eliminated from the time-dependent density-matrix-evolution equations, producing a smaller set of rate equations for the ground- and excited-state populations and coherences.

At first glance, it would seem that this is an approximation that would best describe spectroscopic experiments of the past, when narrow-band lasers were not available, and physicists had to contend with using spectrally broad light sources such as discharge lamps. While this is certainly the case (the broad-line approximation was introduced in the 1960s; see the original paper reprinted in the book by Cohen-Tannoudji, 1994), this approximation remains a useful tool. For example, it can be applied to short pulses, and can be valuable in some situations with broadened laser light (Auzinsh *et al.*, 2009b). It can also be useful for theoretical analysis of a system, as rate equations are often more intuitive than the complete Liouville equation.

Although the broad-line approximation for light–atom interactions can be introduced into the density-matrix formalism phenomenologically (Cohen-Tannoudji, 1994), a more systematic approach allows a derivation beginning from the Liouville equation. We first give some physical justification for the technique, and then outline a rigorous method.

As mentioned above, the condition for the broad-line approximation is that the spectral width of the light is broader than any other relaxation or transition rate in the problem. Because spectrally broad light can be viewed as radiation with rapidly and chaotically fluctuating phase, this means that the coherence lifetime τ_l of the light is much shorter than any other relaxation time. This light generates optical coherences, which are subject to the same relaxation lifetime τ_l. Now consider a time period that is longer than τ_l, but shorter than any other relaxation lifetime, so that the lower- and upper-state density-matrix elements are essentially constant over this time. The optical coherences will quickly relax to the steady state determined by the other density-matrix elements.[1] Subsequent light-phase fluctuations will alter the optical coherences, but the new values will quickly relax also. Thus the optical coherences will fluctuate, but their mean values will be those of the steady state. If we neglect the fluctuations, we can set the time derivatives of the optical coherences to zero in the Liouville equation, allowing adiabatic elimination of the optical coherences (Stenholm, 2005). Note that taking this step means that the equations are valid only over timescales long enough that the fluctuations can be averaged over. On even longer timescales, we see that the mean values of the optical coherences depend on the current values of the other density-matrix elements, but not on the history of the optical coherences themselves, due to the randomization caused by the fluctuations. In other words, from the point of view of solving the system of differential equations for the density-matrix evolution, the optical coherences are now dependent variables, rather than independent variables, and can be eliminated from the equations, as was done in the previous section under steady-state conditions. This provides a set of rate equations for the density-matrix elements, identical to those obtained in Sec. 5.2.1, except that the time derivatives for the ground- and excited-state density-matrix elements have not been set to zero:

$$\begin{aligned}\dot{\rho}_{mn} = & -i\widetilde{\omega}_{mn}\rho_{mn} + \Lambda_{mn} + \sum_{rs} F^{sr}_{mn}\rho_{rs} \\ & - i\sum_{pr}\left[\left(\frac{1}{\widetilde{\omega}_{pn}} + \frac{1}{\widetilde{\omega}_{mr}}\right)V_{mp}\rho_{pr}V_{rn} - \frac{V_{mp}V_{pr}\rho_{rn}}{\widetilde{\omega}_{pn}} - \frac{\rho_{mp}V_{pr}V_{rn}}{\widetilde{\omega}_{mr}}\right].\end{aligned} \tag{5.52}$$

This is the set of approximate equations we have set out to obtain, describing the evolution of the density matrix in the presence of broad-band light. However, our derivation has not been completely mathematically justified. In particular, we have retained the information about the mean values of the optical coherences, but discarded the effects of fluctuations about the mean. A more rigorous derivation of

---

[1] Here we consider the density matrix under the rotating-wave approximation, in which the optical coherences are constant in the steady state.

the rate equations under the broad-line approximation was obtained by Blushs and Auzinsh (2004), using a procedure called *decoherence analysis*. In this derivation, the fluctuating phase of the light field is represented explicitly as a time-dependent light phase $\varphi(t)$. There are two models commonly used to describe the phase instabilities of the light, in which the phase either randomly jumps or undergoes random continuous drift (*phase diffusion*). Each of these models results in a light-frequency distribution with a Lorentzian spectral profile, and to our level of approximation, they each lead to the same set of evolution equations.

To find the desired rate equations by decoherence analysis, the differential equations for the optical coherences obtained from the Liouville equation are converted to integral form, and an average is taken over all possible fluctuations of $\varphi(t)$. Using one of the above models for the light-phase fluctuations, and employing the *decorrelation approximation*, in which the correlations between the fluctuations of the ground- and excited-state density-matrix elements and the optical coherences are neglected, the averages can be evaluated to find evolution equations for the mean values of the density-matrix elements. This gives solutions for the optical coherences that can be substituted back into the Liouville equation, as before. The result is equations for the evolution of the average values of the density-matrix elements that are identical to Eq. (5.52) except for a modification made to the effective linewidth of the transition. Equation (5.51) becomes

$$\begin{aligned}\frac{1}{\widetilde{\omega}_{pn}} &= -\frac{1}{\pm\Delta + \frac{i}{2}\left(\Gamma+\gamma+\Delta\omega\right)}\\ &= i\left(\frac{\frac{1}{2}\left(\Gamma+\gamma+\Delta\omega\right)}{\Delta^2+\frac{1}{4}\left(\Gamma+\gamma+\Delta\omega\right)^2} \pm \frac{i\Delta}{\Delta^2+\frac{1}{4}\left(\Gamma+\gamma+\Delta\omega\right)^2}\right),\end{aligned} \tag{5.53}$$

where $\Delta\omega$ is the full width at half-maximum intensity of the light spectral profile, and Δ is now the Doppler-shifted detuning of the center of the laser line from resonance. Thus, the effective linewidth of the transition is broadened by the laser linewidth, as one would expect on physical grounds.

5.2.3 Broad natural width

Another condition under which adiabatic elimination can be used is when the spontaneous decay rate of the upper state is much greater than the other rates in the problem, in particular the ground-state relaxation rate and the optical-pumping rate. Thus we assume $\gamma \ll \Gamma$ and $\kappa_1 \ll 1$, where $\kappa_1 = \Omega_R^2/\Gamma^2$ is the upper-state optical-pumping parameter, but we make no assumption about the ground-state optical-pumping parameter $\kappa_2 = \Omega_R^2/(\gamma\Gamma)$. Thus the light is weak enough so that the upper-state population is small, even though strong optical pumping may occur. Here we return to our assumption of narrow-band light.

In this case the upper-state populations and coherences, as well as the optical coherences, relax quickly compared to the other evolution timescales, so that they adiabatically follow the ground-state matrix elements. Setting the time derivatives of the optical coherences to zero, we obtain equations for the upper- and lower-state density-matrix elements that are identical to Eq. (5.52) for the case of broad-band light.

In the current case of widely separated upper- and lower-state relaxation rates, however, we can go further. We can set the time derivatives of the upper-state populations and coherences to zero, and in addition assume that the upper-state population is small, because of the assumption $\kappa_1 \ll 1$. Thus for upper-state density-matrix elements ρ_{mn}, Eq. (5.52) reduces to

$$\rho_{mn} = -\frac{1}{\widetilde{\omega}_{mn}} \sum_{pr} \left(\frac{1}{\widetilde{\omega}_{pn}} + \frac{1}{\widetilde{\omega}_{mr}} \right) V_{mp} \rho_{pr} V_{rn}, \tag{5.54}$$

where the right-hand side contains only ground-state density-matrix elements. Substituting into Eq. (5.52), we obtain a closed set of equations for the ground-state matrix elements:

$$\begin{aligned} \dot{\rho}_{mn} = & - i\widetilde{\omega}_{mn}\rho_{mn} + \Lambda_{mn} + i \sum_{pr} \left[\frac{V_{mp} V_{pr} \rho_{rn}}{\widetilde{\omega}_{pn}} + \frac{\rho_{mp} V_{pr} V_{rn}}{\widetilde{\omega}_{mr}} \right] \\ & - \sum_{pqrs} F_{mn}^{sr} \frac{1}{\widetilde{\omega}_{rs}} \left(\frac{1}{\widetilde{\omega}_{ps}} + \frac{1}{\widetilde{\omega}_{rq}} \right) V_{rp} \rho_{pq} V_{qs}, \end{aligned} \tag{5.55}$$

where m and n now represent ground states.

Chapter 6

Time-dependent Fields

In the systems subject to static external fields considered so far, the effects of relaxation generally lead to a steady state, which can be solved for by setting the time derivatives in the evolution equation to zero. In many cases of interest, however, the external fields are time dependent. An important example is NMOR with modulated light, discussed in Sec. 6.1.

In the most general case, the evolution equations must be numerically integrated in time to find the time-dependent response of the system. However, when modulated fields are employed, we are generally interested in periodic solutions, i.e., the behavior of the system after the transients have died away. In this case, methods of solution can be employed that avoid the need to integrate in time until the response has settled into a periodic condition. In Sec. 6.2 a solution by expansion of the density matrix into a Fourier series is discussed, while in Sec. 6.3 a method for square-wave (piecewise constant) pulses is described.

6.1 Nonlinear magneto-optical rotation with modulated light

In each of the magneto-optical effects discussed in Chapter 4, the magnetic-field dependence of optical rotation is either a dispersive Lorentzian or is qualitatively similar to one: the rotation angle is linear in magnetic field at low fields and drops off with the field once the Larmor frequency exceeds a characteristic rate or width. For the linear effect in a Doppler-broadened medium the nominal width is the Doppler width, for Bennett-structure effects (Bennett, 1962; Budker *et al.*, 2002b) it is the natural width, and for the polarization-dependent effects it is the polarization relaxation rate.

From a practical point of view, this behavior means that there is a trade-off between the sensitivity and *dynamic range* of magnetometers based on these effects—narrower widths mean steeper slopes and higher sensitivity, but smaller cut-off fields above which the rotation goes rapidly to zero, narrowing the range of fields over which the magnetometer is sensitive.

The polarization-dependent nonlinear magneto-optical rotation effects, having the narrowest widths, exhibit this problem most strongly. For example, as discussed in Sec. 7.1, the wall-induced Ramsey effect occurring in antirelaxation-coated vapor cells has a typical width of 1 µG, so that magnetometers based on this effect are sensitive only to magnetic fields of this strength or weaker. It turns out, however, that a simple modification of the setup—adding modulation to the pump light and detecting optical rotation synchronously with modulation—can create additional resonances with comparably small widths, but centered at nonzero values of the magnetic field, as opposed to the "zero-field" resonances discussed above. These resonances can extend the dynamic range of magnetometers while maintaining high sensitivity. Below, we briefly describe nonlinear optical rotation with amplitude- and frequency-modulated light. A discussion of other types of modulation in the context of nonlinear magneto-optics along with an extensive bibliography can be found in a review by Alexandrov *et al.* (2005).

6.1.1 Amplitude modulation

Consider a group of atoms polarized by a short pulse of linearly polarized pump light. If the atoms are in a magnetic field they will begin to precess, and may induce optical rotation in a probe light beam. Contrary to the case with cw pump light in which steady-state signals are observed, here we observe a time-dependent, transient signal: the optical rotation oscillates as the polarization performs complete revolutions, and the signal dies away as the polarization relaxes (Fig. 6.1a). We will assume the Faraday geometry, in which the pump light and the probe light both propagate along the magnetic-field direction. Note that linearly polarized light produces polarization (a component of rank-two alignment with $q = 2$) with two-fold symmetry about the light propagation direction (as in Fig. 6.2 with $\kappa = |q| = 2$). This means that it takes one-half of a Larmor period for the polarization to return to its original state, i.e., the quantum-beat frequency is twice the Larmor frequency. Consequently, the oscillation frequency of the rotation signal is also twice the Larmor frequency Ω_L. In general, a polarization moment ρ^{κ}_{q} has q-fold symmetry about the reference axis (Fig. 6.2), and so would produce optical rotation that oscillates at $q\Omega_L$.

In order to optically pump more atoms, we may wish to use more pulses. If a train of light pulses is used with some arbitrary repetition rate, the atoms polarized in each pulse will, in general, precess out of phase with the atoms polarized in the previous pulses, tending to wash out the medium polarization and the time-dependent signal (Fig. 6.1b). However, if the pump pulses are synchronized with the oscillation period of the signal, the signal due to each successive group of polarized atoms will reinforce the signal due to the previously pumped atoms, producing a larger time-dependent aggregate signal (Fig. 6.1c). Thus we see that a resonance is achieved when the signal oscillation frequency $2\Omega_L$ is equal to the pulse repetition frequency Ω_m.

Actually, reinforcement of the signal occurs when a pulse occurs every two oscillation periods, as well (Fig. 6.1d). In fact, we can see that a resonance condition is achieved whenever $2\Omega_L = n\Omega_m$, where n is an integer (i.e., whenever twice the Larmor frequency is a harmonic of the pulse repetition rate). Furthermore, it is not necessary to use short pump pulses—any modulation of the light amplitude at the frequency Ω_m will produce a similar result.

Under resonance conditions, the polarization produced by successive pumping cycles adds constructively, producing net rotating polarization in the medium. This effect, introduced by Bell and Bloom (1961), is known as *synchronous optical pumping* or *optically driven spin precession*. This is a particular case of a general class of phenomena known as *beat resonances* exhibited when a parameter of the pump light or external field is modulated, as discussed below. In nonlinear magneto-optical experiments, such resonances are generally observed using *lock-in detection* of the transmission or polarization signal of the probe light, at a harmonic of the modulation frequency.

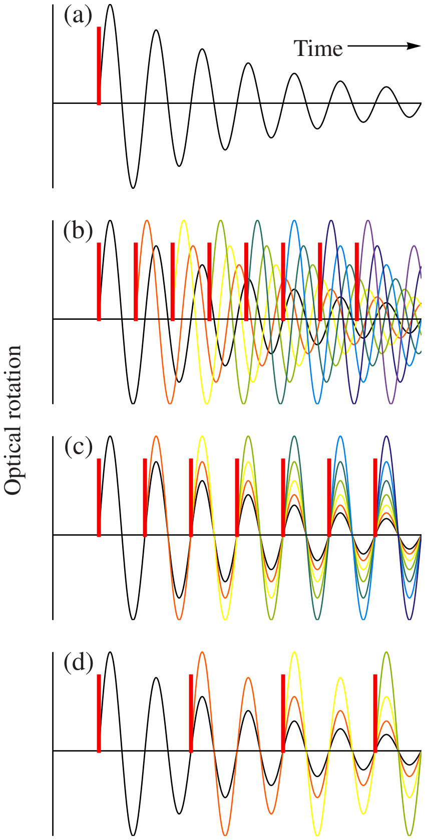

Figure 6.1: Optical rotation signal in response to (a) a single pump pulse (vertical bar), (b) a train of pulses, (c) pulses at twice the Larmor frequency, (d) pulses at the Larmor frequency. In (c) and (d) the response to successive pulses is additive, resulting in a resonance in the oscillating signal.

> It is very common in experimental practice that some experimental parameter is modulated (for example, sinusoidally), and a signal is detected either at the frequency of the modulation or its harmonic. Typically, *phase sensitive detection* is performed with a

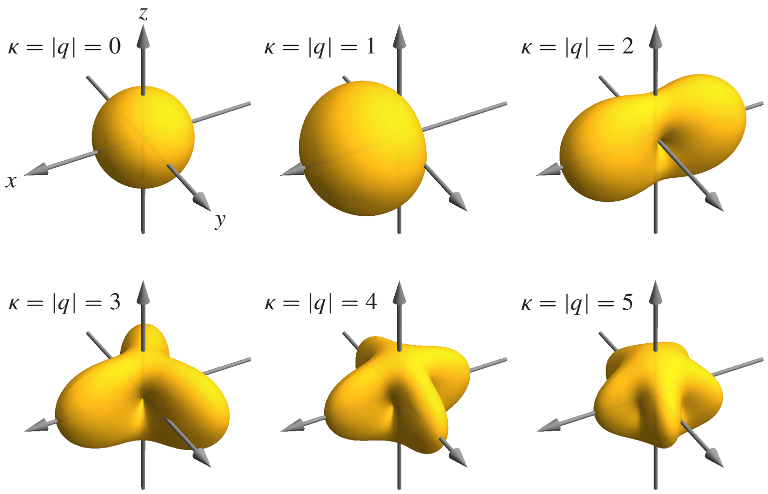

Figure 6.2: Angular-momentum polarization surfaces for $F = 4$ states composed only of population (ρ_0^0) and the maximum possible values of the components $\rho_{\pm\kappa}^{\kappa}$ for a particular κ. $\kappa = 0$: monopole moment (isotropic state with population only); $\kappa = 1$: dipole moment (oriented state); $\kappa = 2$: quadrupole moment (aligned state); $\kappa = 3$: octupole moment; $\kappa = 4$: hexadecapole moment; $\kappa = 5$: triakontadipole moment. Polarization moments with index q have $|q|$-fold symmetry about the z-axis.

device known as *lock-in amplifier* or *lock-in detector*, which has two inputs: "signal" and "reference."

Let us say that the parameter that is modulated goes as $\cos\Omega_m t$, where Ω_m is the modulation frequency. The reference should be fixed-amplitude signal oscillating at the frequency of the signal that we would like to detect (i.e., a harmonic of Ω_m). The phase of the reference can be chosen as desired; let us say, that the reference is in phase with the modulation. Given an input signal $S(t)$ that, generally, contains noise in addition to the useful signal we are looking for, a lock-in detector multiplies $S(t)$ by the reference signal and integrates the resulting signal with a time constant τ. It also does the same with the reference shifted by $\pi/2$. This provides the in-phase and quadrature signals:

$$\text{In-phase output}(t) \propto \int_{-\infty}^{t} S(t') \cos n\Omega_m t' e^{-(t-t')/\tau} dt', \tag{6.1}$$

$$\text{Quadrature output}(t) \propto \int_{-\infty}^{t} S(t') \sin n\Omega_m t' e^{-(t-t')/\tau} dt'. \tag{6.2}$$

Here it is assumed that the n-th harmonic is detected. If τ is much longer than the modulation period, this procedure averages out all the contributions to $S(t)$, except those at the "correct" frequency and phase.

> Lock-in detection is extremely helpful for discriminating the useful signal from noise and other spurious signals occurring at different frequency and/or not phased with the reference. It can be thought of phase-sensitive spectral filtering of the signal with the central frequency $n\Omega_m$ and the bandwidth given by $1/\tau$.

6.1.2 Frequency modulation

Frequency (rather than amplitude) modulation of the pump light can be used to produce an effect similar to that discussed in Sec. 6.1.1. Here, the optical pumping rate is modulated as a result of its frequency dependence. One example of this is *nonlinear magneto-optical (Faraday) rotation with frequency-modulated light (FM NMOR)* (Budker *et al.*, 2002c). In this technique, linearly polarized light near-resonant with an atomic transition is directed parallel to the magnetic field. The frequency of the light is modulated, moving it closer and farther from resonance. This causes the rates of optical pumping and probing to acquire a periodic time dependence. Similarly to the case of amplitude modulation, a resonance occurs when the quantum-beat frequency $q\Omega_L$ for a polarization moment ρ^{κ}_{q} equals a harmonic of the modulation frequency $n\Omega_m$ (the lowest-order polarization moment here has $\kappa = 2$, $q = 2$; the case of higher κ, which can support higher q is discussed in Yashchuk *et al.*, 2003). The atomic sample is pumped into a macroscopic rotating polarized state that causes a periodic modulation of the plane of light polarization at the output of the medium. The amplitude of time-dependent optical rotation at various harmonics of Ω_m can be measured with a phase-sensitive lock-in detector (Fig. 6.3).

Consider Fig. 6.3(a,b), which show the in-phase and quadrature signals detected at the first harmonic. At the center of the in-phase plot is the zero-field resonance, the same feature seen in nonlinear Faraday rotation with cw light. Near zero magnetic field, the modulation frequency is much larger than the Larmor frequency, so the fact that the light is modulated does not significantly affect the optical pumping. Thus the medium polarization reaches a steady state, as it would for cw light (Sec. 4.2.2), with its alignment axis tilted with respect to the light polarization. Considering the light now as a probe, the atomic alignment induces optical rotation, with the amount of rotation depending on how close the probe light is to optical resonance. Thus, as the probe frequency is modulated, the optical rotation signal acquires time dependence at harmonics of the modulation frequency, resulting in the zero-field resonance. If we define the beginning of the light modulation cycle to be the point in the cycle at which the light interacts most strongly with the atoms, the zero-field optical rotation signal will be in phase with the light modulation, and thus is largely suppressed in the quadrature component of the signal (Fig. 6.3b).

At $\Omega_L = 500$ Hz, the $2\Omega_L = \Omega_m$ resonance discussed above is seen. Precisely on resonance, a large rotating polarization is set up in the medium; this results in a peak in the quadrature component of the signal. The reason that this signal appears in the quadrature component is that the atomic polarization must rotate away from the light polarization axis in order for it to induce optical rotation—the maximum rotation is produced at an angle $\pi/4$. This results in a phase lag between optical pumping and the detection of optical rotation. As the magnetic field is moved out of the resonance condition, the net atomic polarization begins to wash out, as discussed above. This reduces the signal in the quadrature component. However, at the same time, an effective phase shift is introduced between pumping and probing, due to the difference between the modulation frequency and the quantum-beat frequency. This allows the signal to appear in the in-phase component as a dispersive-Lorentzian-shaped feature.

At $\Omega_L = 500$ Hz, very small features corresponding to the $2\Omega_L = 2\Omega_m$ resonance can be observed. The background slope seen in the in-phase component of the signal is due to the zero-field resonance for the transit effect (Sec. 7.1).

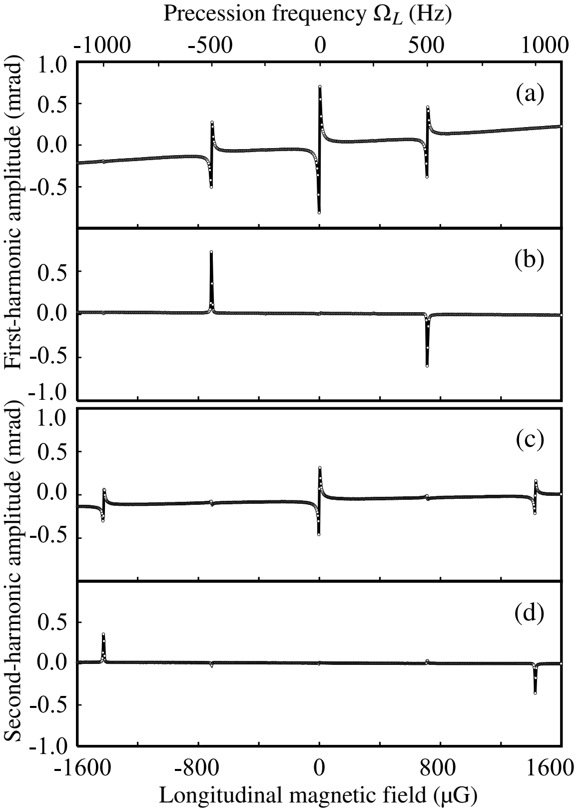

Figure 6.3: (From Budker *et al.* 2002c.) Signals detected at the first harmonic (a,b) and second harmonic (c,d) of Ω_m as a function of longitudinal magnetic field. This experiment employed buffer-gas-free, paraffin-coated vapor cells containing isotopically enriched ^{87}Rb. The laser was tuned near the D_1 line, laser power was 15 μW, beam diameter ~2 mm, $\Omega_m = 1$ kHz, and the modulation amplitude $\Delta\omega_m = 220$ MHz. Traces (a,c) and (b,d) correspond to the in-phase and the quadrature outputs of the signals from the lock-in detector, respectively.

The FM NMOR technique is useful for increasing the dynamic range of NMOR-based magnetometers. The beat resonances have width comparable to that of the zero-field resonance (since the dominant relaxation mechanisms are the same), but in principle can be centered at any desired magnetic field.

6.2 Fourier expansion technique for periodic excitation

6.2.1 Sinusoidal modulation

We consider an atomic transition with resonance frequency ω_0 subject to a frequency-modulated light field. If the modulation is sinusoidal, the detuning from resonance $\Delta = \omega_{\text{light}} - \omega_0$ is given by $\Delta = \Delta_0 + \Delta_m \cos \Omega_m t$, where Δ_m is the modulation depth, Ω_m is the modulation frequency, and Δ_0 is the central light frequency. The time evolution of the density matrix ρ is given by the Liouville equation (3.62). Under the rotating wave approximation, the time dependence of the Hamiltonian H is entirely due to the time dependence of Δ. The system of evolution equations can then be written in matrix form as

$$\begin{aligned} \frac{d\rho(t)}{dt} &= A\rho(t) + 2A'\rho(t)\cos\Omega_m t + b \\ &= A\rho(t) + A'\rho(t)\left(e^{i\Omega_m t} + e^{-i\Omega_m t}\right) + b, \end{aligned} \tag{6.3}$$

where $\rho(t)$ is now considered to be a vector of the density-matrix elements, A and A' are time-independent matrices, and b is a time-independent vector.

If the light, rather than being frequency modulated, is instead harmonically amplitude modulated so that the optical electric field amplitude is given by $\mathcal{E} = \mathcal{E}_0(1 + f\cos\Omega_m t)$, where f is the modulation depth, the density-matrix evolution equations can be written in the same form (6.3); all of the following discussion applies equally to this case.

We are interested in solutions of Eq. (6.3) that are periodic in time. Thus we expand $\rho(t)$ in a Fourier series in harmonics of the modulation frequency Ω_m,

$$\rho(t) = \sum a_n e^{in\Omega_m t}, \tag{6.4}$$

with constant coefficients a_n. It is convenient to write the equations in terms of the real and imaginary parts of the density matrix; then $\rho(t)$ is real, and consequently $a_{-n} = a_n^*$. Substituting (6.4) into Eq. (6.3), we have

$$\sum in\Omega_m a_n e^{in\Omega_m t} = A\sum a_n e^{in\Omega_m t} + A'\sum a_n\left(e^{i(n+1)\Omega_m t} + e^{i(n-1)\Omega_m t}\right) + b, \tag{6.5}$$

or

$$\sum\left[Aa_n - in\Omega_m a_n + A'\left(a_{n-1} + a_{n+1}\right)\right]e^{in\Omega_m t} = -b, \tag{6.6}$$

resulting in the recursion relation

$$C_n^{-1} a_{n-1} + C_n^0 a_n + C_n^1 a_{n+1} = -b\delta_{n,0}, \tag{6.7}$$

where $C_n^0 = A - in\Omega_m \mathbb{1}$ ($\mathbb{1}$ is the identity matrix), and we have generalized the relation by writing $C_n^{\pm 1} = A'$. The following discussion applies to the case in which C_n^1 and C_n^{-1} can differ [in general $C_n^{-1} = (C_n^1)^*$] and can each depend on n.

If a finite number of harmonics is kept, Eq. (6.7) forms a simultaneous system of equations for the coefficients a_n, which can be solved as a large system of linear equations. To avoid solving the entire system at once, an alterative method can be used, known as the *matrix continued fraction* method (Allegrini *et al.*, 1977).

To solve Eq. (6.7), we look for a series of "ladder" matrices S_n, for $n > 0$, that produce successive a_n:

$$a_n = S_n a_{n-1}. \tag{6.8}$$

Substituting into (6.7), we have, for $n > 0$,

$$\begin{aligned} 0 &= C_n^{-1} a_{n-1} + C_n^0 S_n a_{n-1} + C_n^1 S_{n+1} S_n a_{n-1} \\ &= \left(C_n^{-1} + C_n^0 S_n + C_n^1 S_{n+1} S_n \right) a_{n-1}, \end{aligned} \tag{6.9}$$

or, for nonzero a_{n-1},

$$S_n = -\left(C_n^0 + C_n^1 S_{n+1} \right)^{-1} C_n^{-1}. \tag{6.10}$$

This formula can be expanded out as a continued fraction,

$$S_n = -\frac{C_n^{-1}}{C_n^0 - \frac{C_n^1 C_{n+1}^{-1}}{C_{n+1}^0 - \frac{C_{n+1}^1 C_{n+2}^{-1}}{C_{n+2}^0 - \cdots}}}. \tag{6.11}$$

If S_m is set to zero for some appropriately high harmonic m, the matrices $S_{m-1}, \ldots, S_1$ can be found using Eq. (6.10). To fix a_0, we use Eq. (6.7) with $n = 0$:

$$\begin{aligned} -c &= C_0^{-1} a_1^* + C_0^0 a_0 + C_0^1 a_1 \\ &= C_0^{1\,*} S_1^* a_0^* + C_0^0 a_0 + C_0^1 S_1 a_0. \end{aligned} \tag{6.12}$$

Since a_0 is real,

$$a_0 = -\left(C_0^0 + 2\,\mathrm{Re}\, C_0^1 S_1 \right)^{-1} c. \tag{6.13}$$

The remaining a_n can be found using Eq. (6.8) and the known S_n.

Experimental signals such as optical rotation can be found in terms of the Fourier coefficients. The optical rotation $d\varphi$ induced in the pump light polarization per path length $d\ell$ in the medium is given by an equation of the form

$$\frac{d\varphi}{d\ell} = D\rho(t), \tag{6.14}$$

where D is a time-independent matrix. Experimentally, one measures the in-phase and quadrature components

$$\frac{d\overline{\varphi}_j^{\text{in}}}{d\ell} = \Omega_m \int_0^{2\pi/\Omega_m} \frac{d\varphi_j}{d\ell} \cos j\Omega_m t\, dt \tag{6.15}$$

$$\frac{d\overline{\varphi}_j^{\text{quad}}}{d\ell} = \Omega_m \int_0^{2\pi/\Omega_m} \frac{d\varphi_j}{d\ell} \sin j\Omega_m t\, dt. \tag{6.16}$$

at various harmonics j. Using the Fourier expansion for $\rho(t)$, we have

$$\frac{d\overline{\varphi}_j^{\text{in}}}{d\ell} = D\left(a_{-j} + a_j\right)/2 = D\,\mathrm{Re}\,a_j \tag{6.17}$$

$$\frac{d\overline{\varphi}_j^{\text{quad}}}{d\ell} = D\left(a_{-j} - a_j\right)/2 = D\,\mathrm{Im}\,a_j. \tag{6.18}$$

6.2.2 Multi-harmonic modulation

We can approximate the case of non-sinusoidal modulation (for example, pulsed amplitude modulation), by simultaneously modulating at a set of harmonics. In this case the system of density-matrix equations can be written

$$\begin{aligned}\frac{d\rho(t)}{dt} &= A\rho(t) + 2\sum_{k=1}^{\ell} A'_k\rho(t)\cos k\Omega_m t + b \\ &= A\rho(t) + \sum_{k=1}^{\ell} A'_k\rho(t)\left(e^{ik\Omega_m t} + e^{-ik\Omega_m t}\right) + b,\end{aligned} \tag{6.19}$$

where the modulation is described by a set of ℓ harmonics of the fundamental modulation frequency Ω_m, Expanding $\rho(t)$ in a Fourier series and substituting into Eq. (6.19), we have

$$\begin{aligned}\sum_n in\Omega_m a_n e^{in\Omega_m t} &= A\sum_n a_n e^{in\Omega_m t} \\ &\quad + \sum_{n,k} A'_k a_n\left(e^{i(n+k)\Omega_m t} + e^{i(n-k)\Omega_m t}\right) + b,\end{aligned} \tag{6.20}$$

or

$$\sum_n \left[A a_n - in\Omega_m a_n + \sum_k A'_k \left(a_{n-k} + a_{n+k} \right) \right] e^{in\Omega_m t} = -b, \tag{6.21}$$

resulting in the recursion relation

$$\sum_{k=-\ell}^{\ell} C_n^k a_{n+k} = -b\delta_{n,0}, \tag{6.22}$$

where we have generalized by defining $C_n^0 = A - in\Omega_m \mathbb{1}$ and $C_n^k = A'_{|k|}$.

In order to solve Eq. (6.22), we reduce it to the form of Eq. (6.7) using the method of Risken and Vollmer (1980). To illustrate how this is done, we consider the case $\ell = 3$. Assuming $m > 0$, we can write Eq. (6.22) for the cases $n = 3m-1, 3m, 3m+1$, combining them into one matrix equation, as

$$\begin{aligned}
\begin{pmatrix} 0 \\ 0 \\ 0 \end{pmatrix} &= \begin{pmatrix} C_{3m-1}^{-3} & C_{3m-1}^{-2} & C_{3m-1}^{-1} \\ 0 & C_{3m}^{-3} & C_{3m}^{-2} \\ 0 & 0 & C_{3m+1}^{-3} \end{pmatrix} \begin{pmatrix} a_{3m-4} \\ a_{3m-3} \\ a_{3m-2} \end{pmatrix} + \begin{pmatrix} C_{3m-1}^{0} & C_{3m-1}^{1} & C_{3m-1}^{2} \\ C_{3m}^{-1} & C_{3m}^{0} & C_{3m}^{1} \\ C_{3m+1}^{-2} & C_{3m+1}^{-1} & C_{3m+1}^{0} \end{pmatrix} \begin{pmatrix} a_{3m-1} \\ a_{3m} \\ a_{3m+1} \end{pmatrix} \\
&\quad + \begin{pmatrix} C_{3m-1}^{3} & 0 & 0 \\ C_{3m}^{2} & C_{3m}^{3} & 0 \\ C_{3m+1}^{1} & C_{3m+1}^{2} & C_{3m+1}^{3} \end{pmatrix} \begin{pmatrix} a_{3m+2} \\ a_{3m+3} \\ a_{3m+4} \end{pmatrix} \\
&= \hat{C}_m^{-1} \hat{a}_{m-1} + \hat{C}_m^{0} \hat{a}_m + \hat{C}_m^{1} \hat{a}_{m+1},
\end{aligned} \tag{6.23}$$

where we define new vectors, written for arbitrary odd ℓ, as

$$\hat{a}_n = \begin{pmatrix} a_{n\ell-(\ell-1)/2} \\ a_{n\ell-(\ell-1)/2+1} \\ \vdots \\ a_{n\ell+(\ell-1)/2} \end{pmatrix} \tag{6.24}$$

with ℓ times as many elements as the original a_n vectors, and new, larger matrices, defined by

$$\left[\hat{C}_n^k \right]_{q,r} = C_{n\ell+q}^{k\ell-q+r} \tag{6.25}$$

for $k = -1, 0, 1$, where q and r run from $-(\ell-1)/2$ to $(\ell-1)/2$ and C_n^j is taken to be zero for $|j| > \ell$. The recursion relation in terms of $\hat{C}_n^k$ and $\hat{a}_n$ is of the form of Eq. (6.7), and we can solve for ladder matrices defined by

$$\hat{a}_n = \hat{S}_n \hat{a}_{n-1}. \tag{6.26}$$

in the manner described in Sec. 6.2.1.

To fix $\hat{a}_0$, we note that $\hat{a}_{-n} = \widetilde{\hat{a}}_n$, where we define the tilde operator as complex conjugation in conjunction with reversal of the order in which the ℓ component vectors of $\hat{a}_n$ are written. For example, for $\ell = 3$,

$$\hat{a}_{-1} = \begin{pmatrix} a_{-4} \\ a_{-3} \\ a_{-2} \end{pmatrix} = \begin{pmatrix} a_4^* \\ a_3^* \\ a_2^* \end{pmatrix} = \widetilde{\begin{pmatrix} a_2 \\ a_3 \\ a_4 \end{pmatrix}} = \widetilde{\hat{a}}_1. \tag{6.27}$$

Then using Eq. (6.26), we can write

$$\hat{a}_{-n} = \widetilde{\hat{a}}_n = \widetilde{\hat{S}_n \hat{a}_{n-1}} = \widetilde{\hat{S}}_n \widetilde{\hat{a}}_{n-1} = \widetilde{\hat{S}}_n \hat{a}_{-n+1}, \tag{6.28}$$

where we define the tilde operation for a matrix as reversal of the order of both the ℓ rows and ℓ columns of its submatrices, along with complex conjugation. We again illustrate the procedure using the example $\ell = 3$. Writing Eq. (6.22) for $n = -1, 0, 1$, we have

$$\begin{aligned} \begin{pmatrix} 0 \\ -b \\ 0 \end{pmatrix} &= \begin{pmatrix} C_{-1}^{-3} & C_{-1}^{-2} & C_{-1}^{-1} \\ 0 & C_0^{-3} & C_0^{-2} \\ 0 & 0 & C_1^{-3} \end{pmatrix} \begin{pmatrix} a_{-4} \\ a_{-3} \\ a_{-2} \end{pmatrix} + \begin{pmatrix} C_{-1}^{0} & C_{-1}^{1} & C_{-1}^{2} \\ C_0^{-1} & C_0^{0} & C_0^{1} \\ C_1^{-2} & C_1^{-1} & C_1^{0} \end{pmatrix} \begin{pmatrix} a_{-1} \\ a_0 \\ a_1 \end{pmatrix} \\ &\quad + \begin{pmatrix} C_{-1}^{3} & 0 & 0 \\ C_0^{2} & C_0^{3} & 0 \\ C_1^{1} & C_1^{2} & C_1^{3} \end{pmatrix} \begin{pmatrix} a_2 \\ a_3 \\ a_4 \end{pmatrix} \\ &= \hat{C}_0^{-1} \hat{a}_{-1} + \hat{C}_0^{0} \hat{a}_0 + \hat{C}_0^{1} \hat{a}_1 \\ &= \hat{C}_0^{-1} \widetilde{\hat{S}}_1 \hat{a}_0 + \hat{C}_0^{0} \hat{a}_0 + \hat{C}_0^{1} \hat{S}_1 \hat{a}_0, \end{aligned} \tag{6.29}$$

so defining

$$\hat{b} = \begin{pmatrix} \vdots \\ 0 \\ b \\ 0 \\ \vdots \end{pmatrix}, \tag{6.30}$$

we have

$$\hat{a}_0 = -\left(\hat{C}_0^{-1} \widetilde{\hat{S}}_1 + \hat{C}_0^{0} + \hat{C}_0^{1} \hat{S}_1 \right)^{-1} \hat{b}. \tag{6.31}$$

This formula reduces to Eq. (6.13) for $\ell = 1$.

6.3 Method for square-wave pulses

A complementary case to that of sinusoidal modulation is that of square-wave pulses. In this case, we can make use of the fact that the system parameters are piecewise constant, and solve for the periodic condition. This method requires the diagonalization of the matrix describing the evolution of the system. (This may be unfeasible for large systems, in which case alternative numerical methods must be employed.) When the external parameters are held constant, the density-matrix evolution equations can be written

$$\dot{\rho} = A\rho + b, \tag{6.32}$$

where A and b are constant. Let λ and S be the vector of eigenvalues and associated matrix of eigenvectors of A, such that

$$S^{-1}AS = \Lambda, \tag{6.33}$$

where Λ is a diagonal matrix with the eigenvalues λ on the diagonal. Then, writing $\rho = S\rho'$, we have

$$\begin{aligned} \dot{\rho}' &= S^{-1}AS\rho' + S^{-1}b \\ &= \Lambda\rho' + b'. \end{aligned} \tag{6.34}$$

If ρ has the initial value $\rho(0)$, ρ' takes the initial value $\rho'(0) = S^{-1}\rho(0)$. Then ρ' has the solution

$$\rho'(t) = e^{\lambda t}\rho'(0) + \frac{b'}{\lambda}\left(e^{\lambda t} - 1\right), \tag{6.35}$$

or in matrix notation,

$$\rho'(t) = E(t)\rho'(0) + \Lambda^{-1}\left[E(t) - I\right]b', \tag{6.36}$$

where $E(t)$ is a diagonal matrix with diagonal elements given by $e^{\lambda t}$. Then

$$\begin{aligned} \rho(t) &= SE(t)S^{-1}\rho(0) + S\Lambda^{-1}\left[E(t) - I\right]S^{-1}b \\ &= M(t)\rho(0) + g(t), \end{aligned} \tag{6.37}$$

with $M(t) = SE(t)S^{-1}$ and $g(t) = S\Lambda^{-1}\left[E(t) - I\right]S^{-1}b$.

Now we assume that some parameter is square-wave modulated with period τ so that the matrix A is given by

$$A(t) = \begin{cases} A_1 & \text{for } n\tau \le t < n\tau + \tau_1 \\ A_2 & \text{for } n\tau + \tau_1 \le t < n\tau + \tau_1 + \tau_2 \end{cases}, \tag{6.38}$$

with integer n and $\tau = \tau_1 + \tau_2$. The vector b may also change in the same manner. In the steady state, we have $\rho((n+1)\tau) = \rho(n\tau)$, so

$$\begin{aligned}\rho(n\tau) &= M_2(\tau_2)\rho(n\tau + \tau_1) + g_2(\tau_2) \\ &= M_2(\tau_2)\left[M_1(\tau_1)\rho(n\tau) + g_1(\tau_1)\right] + g_2(\tau_2) \\ &= M_2(\tau_2)M_1(\tau_1)\rho(n\tau) + M_2(\tau_2)g_1(\tau_1) + g_2(\tau_2).\end{aligned} \tag{6.39}$$

Solving for $\rho(n\tau)$ gives

$$\rho(n\tau) = \left[I - M_2(\tau_2)M_1(\tau_1)\right]^{-1}\left[M_2(\tau_2)g_1(\tau_1) + g_2(\tau_2)\right], \tag{6.40}$$

and the density matrix during the period of oscillation can be found using Eq. (6.37).

Chapter 7

Antirelaxation-coated Vapor Cells and Multi-region Calculations

So far we have considered situations in which atoms with different velocities or positions in space can be considered separately. If, due to atomic motion, atoms travel between different experimental regions, or undergo velocity-changing collisions, the density matrices describing the atoms under different sets of conditions become coupled, and must be solved for simultaneously. This can occur with vapor cells that have an antirelaxation coating, or with atoms in the presence of a buffer gas. Both of these situations are considered in this chapter.

Atomic collisions also cause polarization relaxation and the exchange of polarization between atoms. These mechanisms are discussed. Finally, we also describe the effect of atomic recoil, which can transfer atoms between velocity groups.

7.1 Antirelaxation-coated cells

When an alkali atom strikes the glass wall of a vapor cell and then returns to the interior of the cell, its polarization state is essentially completely randomized. This means that for a dilute alkali vapor contained in a buffer-gas-free cell, the ground-state polarization lifetime is given by the average time of flight of an atom across the cell. If the interaction region (light beam) takes up only a fraction of the cell, the useful polarization lifetime is even shorter, because an atom is unlikely to leave the interaction region and then return to it before making contact with the cell walls.

There are surfaces that are much more gentle to the polarization of alkali atoms than glass. In particular, if the inner walls of the vapor cell are coated with a

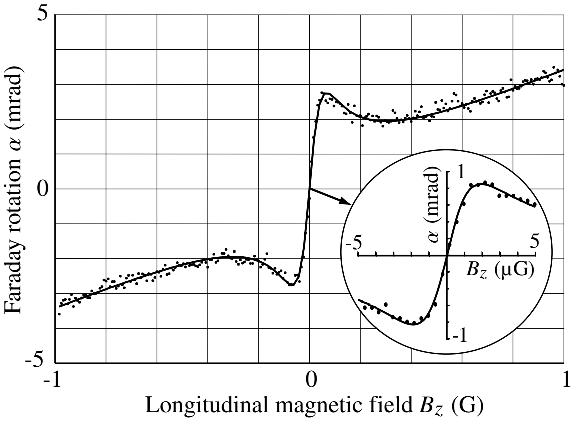

Figure 7.1: Longitudinal magnetic-field dependence of optical rotation in a paraffin-coated ^{85}Rb vapor cell (Budker *et al.*, 1998). The background slope is due to the Bennett-structure effect. The dispersion-like structure is due to the transit effect. The inset shows the near-zero B_z-field behavior at a 2×10^5 magnification of the magnetic-field scale. Light intensity is ∼100 μW/cm^2. The laser is tuned ∼150 MHz to the high frequency side of the $F = 3 \to F'$ absorption peak.

chemically inert substance like paraffin (chemical formula C_nH_{2n+2}), collisions with the cell walls have a much reduced effect on the atomic polarization. In fact, with specialized paraffin coatings the atoms can make up to 10^4 collisions with the cell walls before depolarizing (Bouchiat and Brossel, 1966; Alexandrov and Bonch-Bruevich, 1992; Alexandrov *et al.*, 1996). Other materials recently discovered to be effective as antirelaxation coatings can allow as many as 10^6 collisions (Balabas *et al.*, 2010).

Atomic polarization, then, can have a much longer lifetime in a coated than an uncoated cell, leading to much narrower features due to nonlinear magneto-optical effects. Figure 7.1 shows a measurement of NMOR in a coated cell as a function of magnetic field. The widest feature, seen here as a background slope, is due to the Bennett-structure effect (Budker *et al.*, 2002b). A narrower feature, with width on the order of 0.1 G, is due to the polarization evolution effect (precession of alignment or AOC). The width of this feature is determined by the transit rate of atoms through the light beam, so this effect is often called the *transit effect*. Both the Bennett-structure effect and the transit effect occur in uncoated cells. However, in measurements using coated cells, there is another feature hiding in the center of the plot.

If the magnetic-field range around zero is magnified by several orders of magnitude, a new effect can be observed with width on the order of 1 μG. The mechanism for this effect is also polarization evolution, but evolution over a much longer time scale. Rather than being optically pumped and then probed in one transit through the light beam, in this case the atoms responsible for the effect are pumped and then fly out of the light beam, collide with the cell walls numerous times, and then fly through the beam again, where they induce optical rotation. The time over which this process may occur is the ground-state polarization lifetime, so the polarization relaxation rate determines the width of the feature due to this effect.

This coated-cell effect involves a mechanism quite similar to that found in *Ramsey's*

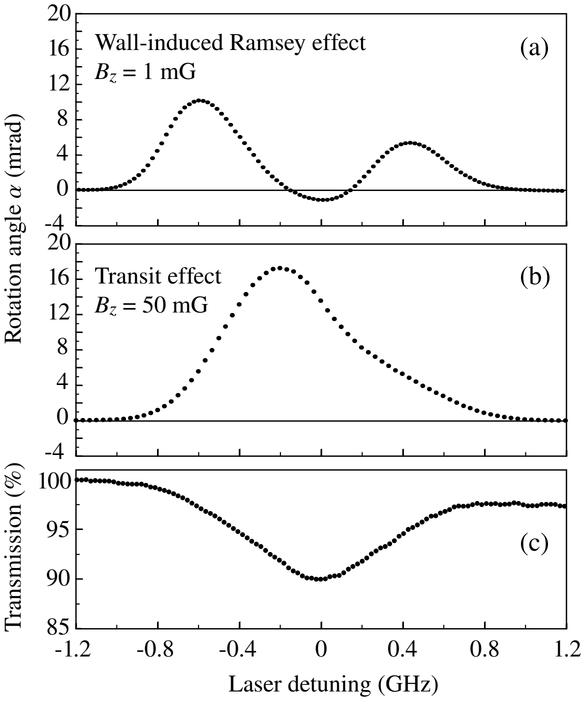

Figure 7.2: (a) Wall-induced Ramsey rotation spectrum for the $F = 3 \rightarrow F'$ component of the D_1 line of ^{85}Rb obtained by Budker *et al.* (2000b) for light intensity 1.2 mW/cm^2 and beam diameter $\sim$ 3 mm. (b) Transit effect rotation spectrum, for light intensity 0.6 mW/cm^2. (c) Light transmission spectrum for light intensity 1.2 mW/cm^2. The background slope in light transmission is due to the change in incident laser power during the frequency scan.

method of separated oscillatory fields. Norman Ramsey received the Nobel prize for the invention of this method, which involves separated fields used to prepare and then detect polarization in a molecular beam. The separation between the fields allows the accumulation of precession angle due to a static magnetic field—the farther apart the two fields, the longer the polarization can precess. In the coated vapor-cell case, optically pumped atoms return to the light field due to wall collisions rather than linear motion, so the effect is sometimes known as the *wall-induced Ramsey effect*, or just as the "wall effect."

> It is interesting to note that Ramsey himself (Kleppner, Ramsey and Fjelstadt, 1958), in order to decrease the resonance widths in experiments with separated oscillatory fields, constructed a "storage box" with Teflon-coated walls in which atoms would bounce around for a period of time before emerging to pass through the second oscillatory field. Teflon worked very well with hydrogen atoms, but is incompatible with the chemically aggressive alkali vapors. On the other hand, paraffin coating—which works wonders with the alkalis—does not work with hydrogen.

The NMOR spectra for the wall-induced Ramsey effect can be quite different from those for the transit effect (Fig. 7.2). In the wall-induced Ramsey effect, atoms undergo many velocity-changing collisions between pump and probe interactions, causing velocity mixing. This means that the Doppler shift for an atom during pumping may be entirely different than that during probing. If there are hyperfine transitions whose frequency separation is smaller than then Doppler width, it is possible that the light could be resonant with one hyperfine transition when the atom is pumped, and then, due to a different Doppler shift, be resonant with another transition when it is probed. Both the ground-state polarization produced by optical pumping and the effect on the light of the atomic polarization that has evolved in the magnetic field depend on the nature of the transition. For the $F = 3 \rightarrow F' = 2, 3$ component of the ^{85}Rb D$_1$ line, the contribution to optical rotation from atoms pumped and probed on different transitions has opposite sign to that from atoms pumped and probed on the same transition. Thus, when the laser is tuned near resonance with one of the transitions, atoms will tend to be pumped and probed on that same resonance, and produce rotation of one sign. On the other hand, when the laser is tuned between the two resonances, atoms are equally likely to be pumped and probed on either the same or different resonances, and so there are two contributions of the opposite sign which cancel. Therefore, the wall-induced Ramsey NMOR spectrum consists of two peaks, as seen in Fig. 7.2(a). In the transit effect for buffer-gas-free cells, in contrast, atoms remain in a particular velocity group during both optical pumping and probing. The transit-effect spectrum has a single peak because for each atom light is resonant with the same transition during both pumping and probing (Fig. 7.2b).

The cancelation of the optical rotation signal when Doppler-broadened hyperfine transitions overlap may also be thought of in terms of the polarization moments that may be created in the ground state. When there is overlap of the hyperfine resonances and atomic velocity mixing, the effect of the hyperfine structure on optical pumping may be effectively negated. This means that light may only create polarization moments that can be supported by the electronic angular momentum, regardless of the nuclear spin. In the case of the alkali atoms, the ground-state electronic angular momentum is $J = 1/2$, so, as discussed in Sec. 2.3, the highest-rank multipole moment that can be supported is $\kappa = 1$ (i.e., orientation). Because the NMOR effect requires the creation of alignment ($\kappa = 2$) in the ground state, the signal is suppressed. This discussion will be returned to in more detail in Chapters 9 and 10.

In order to extend the theoretical treatment of Chapters 3 and 4 to describe antirelaxation-coated cells, the velocity-mixing mechanism must be taken into account. In the low-light-power limit, this can be done by modifying the convolution procedure for Doppler broadening presented in Sec. 4.2.3. That procedure, as originally presented, assumes that the atomic velocities do not change, as for the transit effect. Then the signal due to each velocity group can be found independently and all velocity groups integrated over. If we assume, rather, that there is complete velocity mixing between pumping and probing, we must integrate over the density matrix found for each velocity group after optical pumping. Assuming that the atoms in each velocity group possess this aggregate density matrix, we can then integrate the optical rotation over atomic velocity to find the observed signal. This approach will be taken in Chapters 9 and 10.

As the light power is increased, it becomes important that, in general, only part of the vapor cell is illuminated. This means that the density matrices for atoms inside and outside the laser beam must be kept track of separately. Furthermore, atoms usually do not undergo complete velocity mixing while they are inside the laser beam, so density matrices for each atomic velocity group inside the beam must be considered. These density matrices are all coupled by the transfer of atoms into and out of the light beam, and the evolution equations for each must be solved simultaneously.

An additional complication in the treatment of antirelaxation-coated cells is that the polarization lifetime is long enough so that the effects of collisions between alkali atoms become significant. Alkali-alkali collisions can relax atomic polarization and also transfer it between the colliding atoms. These so-called *spin-exchange collisions* thus represent a relaxation mechanism with a more complex character than that of the normally isotropic relaxation due to collisions with the walls (in fact, due to the conservation of total angular momentum, the relaxation itself can be nonlinear).

> The following references provide further reading.
>
> In their early work on optical pumping, Robinson *et al.* (1958) showed that paraffin coatings could reduce the relaxation of atomic polarization due to wall collisions. Later on, working with a paraffin-coated Cs vapor cell, Kanorskii *et al.* (1995) discovered a narrow feature (of width ∼1 mG) in the magnetic-field dependence of Faraday rotation. Kanorskii *et al.* (1995) described the feature as a Ramsey resonance induced by multiple wall collisions. Bouchiat and Brossel (1966), Alexandrov and Bonch-Bruevich (1992), and Alexandrov *et al.* (1996) investigated the properties of paraffin coatings. Budker *et al.* (1998) performed an investigation of the wall-induced Ramsey effect in NMOR using Rb atoms contained in paraffin-coated cells and observed magnetic resonances of width ∼1 µG (Fig. 7.1). Coatings leading to longer lifetimes are being developed by Balabas *et al.* (2010).
>
> Ramsey's method is discussed in his Nobel lecture (Ramsey, 1990). Skalla and Waeckerle (1997) studied the wall-induced Ramsey effect in cells with various geometries (cylindrical, spherical, and toroidal), and used spatially separated pump and probe fields to measure *Berry's topological phase* (Berry, 1984). Pustelny *et al.* (2006b) investigated the possibilities of applying the separated optical field method to improve the sensitivity of NMOR-based magnetometers.

7.2 Multiple-region calculations

In an experimental volume containing regions under different experimental conditions and atoms of different velocities, the density matrix for the atoms must be a function of position and velocity. The dependences on position and velocity can be discretized into individual experimental regions and velocity groups, and a density matrix written for each combination. In situations in which atoms can undergo collisions without losing their polarization, the different density matrices can become coupled together in a way that requires them to be solved simultaneously.

For example, in a vapor cell, the volume can usually be divided into the region illuminated by the light beam and the unilluminated region. If there is an antirelaxation coating or a buffer gas, atoms will be able to travel back and forth between these two regions, and between different velocity groups, while retaining at least some of their polarization.

We first consider the example of an antirelaxation-coated vapor cell in more detail. If the atomic density is low and the light beam illuminates only a small portion of the vapor cell, we can neglect collisions while the atoms are in the light beam. Thus the density matrices describing the different velocity groups in the illuminated region are not directly coupled to each other. The atoms in the different velocity groups experience different experimental conditions, due to their different Doppler shifts.

Upon traveling from the illuminated region into the dark region, the atomic velocities are soon completely randomized due to (polarization-preserving) collisions with the cell wall. This is the complete-velocity-mixing regime; some consequences of this condition are discussed in Chapters 9 and 10. Because in the absence of light the experimental conditions do not depend on the velocity of the atoms, we can conclude that the density matrix for each velocity group is the same. Thus only one density matrix needs to be written for the dark region. It is coupled to each of the velocity groups in the illuminated region due to atomic motion into and out of the light beam.

While in the dark region, atoms will occasionally undergo a polarization-destroying collision with the cell wall. This is represented by uniform relaxation at a particular rate and repopulation of the dark region by unpolarized atoms at the same rate.

It is convenient to normalize the density matrices so that the total population of all of the velocity groups in each region is unity. Here we write the evolution equations due to these transport processes for the density-matrix elements of the dark region, $\rho_{mn}^{(d)}$, and of the various velocity groups v in the region illuminated by the light beam, $\rho_{mn}^{(b,v)}$ (m and n refer to arbitrary states). For the evolution of $\rho^{(b,v)}$, the terms describing the transit to and from the dark region of the cell give

$$\dot{\rho}_{mn}^{(b,v)} = -\gamma_b \rho_{mn}^{(b,v)} + \gamma_b \mathcal{G}_v \rho_{mn}^{(d)}, \tag{7.1}$$

where γ_b is the transit rate of atoms through the light beam, and $\mathcal{G}_v$ is the fraction of the atoms in the velocity group v under conditions of thermal equilibrium [the integral of Eq. (4.37) over the velocity range of the group v]. For the dark region, the terms describing the effect of depolarizing collisions and transit to and from the illuminated region give

$$\dot{\rho}^{(d)}_{mn} = -(\gamma_w + \gamma_d)\rho^{(d)}_{mn} + \delta^{\text{gr.}}_{mn}\frac{\gamma_w}{n_g} + \gamma_d \sum_v \rho^{(b,v)}_{mn}, \tag{7.2}$$

where γ_w is the rate of depolarizing collisions with the cell wall, ρ_d is the rate for atoms in the dark region to return to the light beam, and $\delta^{\text{gr.}}_{mn}$ is 1 if m and n are equal and represent a ground state, and 0 otherwise.

We can see that these equations enforce the correct normalization by summing the equations over all $m = n$ and setting the time derivatives to zero. We then find for the steady-state solution

$$\operatorname{Tr}\rho^{(d)} = 1, \qquad \operatorname{Tr}\rho^{(b,v)} = \mathcal{G}_v, \tag{7.3}$$

where we have used $\sum_v \mathcal{G}_v = 1$.

7.3 Spin-exchange and spin-randomization collisions

The rates of spontaneous decay of the upper states of allowed transitions are typically much faster than the relaxation rates due to collisions in dilute atomic vapors. Thus spontaneous decay is normally the dominant contributor to upper-state relaxation. Ground states, on the other hand, have no intrinsic relaxation mechanisms, and so their relaxation may have important contributions from various sources.

In an experiment with an uncoated vapor cell, the effective ground-state relaxation rate is generally determined by the transit rate of atoms through the light beam (after the atoms exit the light beam, they can no longer be observed, and they will be completely depolarized before returning to the light beam again). This rate is higher than the collision rate in a dilute gas, and so collisional relaxation can be neglected.

In an experiment with a coated cell, however, collisions with gaseous atoms and molecules, as well as residual spin-relaxing collisions with the cell wall, can all contribute to relaxation. A coated alkali vapor cell generally has a reservoir of the element in metallic form; if a polarized atom makes contact with this reservoir, its polarization is completely destroyed. Thus relaxation on the wall is often modeled as uniform relaxation at a rate γ_w.

Relaxation due to collisions between alkali atoms, and between alkali atoms and background or buffer gases, causes more complicated evolution. The duration of a binary atomic collision is typically on the order of the Bohr radius divided by the speed of sound, $\sim 10^{-12}$ seconds, which is much shorter than the time scale of the hyperfine interactions, characterized by the inverse of the hyperfine splitting. Thus the nuclear spin can be thought of as a spectator during the collision, and only the electronic spin is affected. After the collision, the electronic and nuclear spins recouple.

At low magnetic fields, the primary mechanism for alkali-atom spin relaxation arising from collisions with a buffer gas atom or molecule is the spin-rotation interaction (Happer *et al.*, 2010), which couples the spin $\mathbf{S}$ of the electron to the relative angular momentum $\mathbf{N}$ of the two particles. The relative angular momentum is generally large enough for it to be treated as a classical vector, and so it can be seen to induce a phase depending on the relative orientation of $\mathbf{S}$ and $\mathbf{N}$. Averaging over all directions of $\mathbf{N}$, the evolution due to this mechanism is found to be (Happer and Van Wijngaarden, 1987)

$$\dot{\rho} = -\gamma_{\text{sr}} \left[S(S+1)\rho - \mathbf{S} \cdot \rho \mathbf{S} \right], \tag{7.4}$$

where ρ_{sr} is the rate of relaxation due to the spin-rotation interaction (or spin randomization). Under the secular approximation (Bouchiat, 1963a,b; Grossetête, 1964), the fast-oscillating terms involving hyperfine coherences are dropped, and only those containing populations and Zeeman coherences are retained.

In considering alkali-atom–buffer-gas collisions, we have neglected the conservation of angular momentum under the assumption that the polarization of the buffer gas is negligible. The evolution due to binary collisions between alkali atoms is more complicated, because these collisions must conserve the angular momentum of the ensemble of alkali atoms. The collisions thus act to exchange spin between the atoms.

The potentials involved in alkali–alkali spin exchange are too large for a semiclassical approach like that used above to be appropriate. A partial-wave analysis yields for the evolution of an alkali species i due to spin-exchange collisions with an alkali species j (Happer *et al.*, 2010):

$$\begin{aligned} \dot{\rho}^{(i)} = -\,\gamma_{\text{se}}^{(i)} \Big\{ & \left|\mathbf{S}_i\right|^2 \rho^{(i)} - \mathbf{S}_i \cdot \rho^{(i)} \mathbf{S}_i \\ & - \langle \mathbf{S}_j \rangle \cdot \left(\left\{ \rho^{(i)}, \mathbf{S}_i \right\} - 2i \mathbf{S}_i \times \rho^{(i)} \mathbf{S}_i \right) - 2i\kappa_s \left[\langle \mathbf{S}_j \rangle \cdot \mathbf{S}_i, \rho^{(i)} \right] \Big\}. \end{aligned} \tag{7.5}$$

Here the spin-exchange rate γ_{se} is given by $\gamma_{\text{se}} = N^{(j)} v \sigma'$, and the frequency-shift parameter κ_s is given by $\kappa_s = \sigma''/\sigma'$, where $N^{(j)}$ is the number density of the species

j, v is the average relative velocity, and σ' and σ'' are the real and imaginary parts of the spin-exchange collision cross-section, respectively. This formula describes collisions between two different atomic species (for example, ^{87}Rb–^{85}Rb collisions, or ^{85}Rb–Cs collisions), as well as collisions between atoms of the same species (setting $j = i$). Terms involving the hyperfine coherences are again dropped under the secular approximation.

Note that if the atoms of species j have no average spin, ($\mathbf{S}_j = 0$), Eq. (7.5) reduces to Eq. (7.4), demonstrating that conservation of angular momentum does not play a role in this case. Equations analogous to Eqs. (7.5) and (7.4) also describe the effect on the alkali atoms of spin-exchange collisions with (polarized or unpolarized) noble buffer gas atoms. In this case spin is exchanged with the nuclei of the noble gas atoms; this is an important method for the production of spin-polarized ^{3}He and ^{129}Xe (Happer *et al.*, 1984).

The spin-exchange equation (7.5) is nonlinear, so that numerical methods are required to obtain solutions.

> Equations describing density-matrix evolution due to spin-exchange in alkali–alkali collisions have also been obtained by Okunevich (1994, 1995) and Vallés and Alvarez (1994, 1996), following work of Grossetête (1964, 1968) and Omont (1965).

7.4 Velocity-changing collisions

In the example of an antirelaxation-coated vapor cell discussed above, the complete-velocity-mixing condition is assumed; i.e., the atomic velocities are quickly randomized after the atoms leave the illuminated region of the cell. Effects that result from this condition are considered in Chapters 9 and 10. In other situations, however, the rate of velocity-changing collisions is slower compared to that of other processes, and the dynamics of the velocity-mixing process may be important.

For example, consider the case of mesospheric sodium, discussed in Chapter 11. In this case, the sodium atoms remain in the large diameter (on the order of one meter) light beam for times on the order of milliseconds, undergoing collisions with the background gases (e.g., N_2, O_2, and O). At high light intensities the rate of velocity-changing collisions [$\gamma_{\text{vcc}} \approx (35\ \mu\text{s})^{-1}$] is slower than the rate of optical pumping and the rate of velocity redistribution by atomic recoil, discussed in the next section. Therefore, the complete-mixing approximation cannot be used.

To address this situation, terms are added to the density-matrix evolution equations that couple the different velocity groups, in the same way that the transit terms discussed in Sec. 7.2 couple different regions in space. The collisions remove atoms from each velocity group $\rho^{(v)}$ at a rate γ_{vcc}. (Atoms are considered lost when they exit the light beam, so that there is no density matrix representing the dark region.) The rate that atoms are transferred into each velocity group depends on the model used for the velocity-changing collisions. If a hard collision model is used, in which velocities are completely randomized by one collision, the rate at which atoms are returned to each velocity group is given by the fraction of atoms in that group according to the equilibrium Maxwell velocity distribution. This gives for the evolution of the density-matrix elements due to velocity-changing collisions

$$\dot{\rho}_{mn}^{(v)} = -\gamma_{\text{vcc}}\rho_{mn}^{(v)} + \gamma_{\text{vcc}}\mathcal{G}_v \sum_{v'} \rho_{mn}^{(v')}, \tag{7.6}$$

where $\mathcal{G}_v$ is as defined in Sec. 7.2. According to this equation, an initial velocity distribution will evolve toward a Maxwellian distribution: $\operatorname{Tr}\rho^{(v)} = \mathcal{G}_v$.

In the case of soft collisions, which do not totally randomize an atom's velocity in a single collision, the rate of transfer between velocity groups depends on both the initial v' and final v velocities. We then write in the general case

$$\dot{\rho}_{mn}^{(v)} = -\gamma_{\text{vcc}}\rho_{mn}^{(v)} + \gamma_{\text{vcc}} \sum_{v'} f_{v'\to v}\rho_{mn}^{(v')}, \tag{7.7}$$

where $f_{v'\to v}$ is the probability for an atom with initial velocity v' to be transferred to the velocity group $\rho^{(v)}$ following a collision. Models such as the Keilson–Storer model (Keilson and Storer, 1952) can be used to determine a specific form for $f_{v'\to v}$. For more discussion, see, for example, Okunevich (2005), as well as Morgan and Happer (2010).

7.5 Atomic recoil

Another mechanism that can change the velocity of an atom is recoil due to absorption of a photon. When a photon is absorbed, the atom's velocity changes by the recoil velocity $v_r = \hbar k/m$, where m is the atomic mass and k is the wavenumber of the light. This mechanism is important for the analysis of sodium laser guide stars (Chapter 11); for the sodium D_2 line $v_r = 2.9461$ cm/s. If the atom is subsequently de-excited by stimulated emission due to the same traveling light field, the emitted photon has the momentum of the initial photon, and the atom regains its initial velocity. However, if the de-excitation occurs due to spontaneous emission, the direction of emission is random, and, on average, this step has no effect. Thus the average effect of an absorption–spontaneous emission cycle is the change of the atomic velocity by v_r. The corresponding change in the Doppler shift is $\Delta\omega_r = \hbar k^2/m$, equal to $2\pi \times 50.004$ kHz for the sodium D_2 line.

Due to the effect of recoil, the excitation light induces coherence between the ground state of atoms with a particular longitudinal velocity v and the excited state of atoms with velocity $v + v_r$. Thus, a complete description of atomic recoil would require keeping track of coherences between different velocity groups. To avoid this, different models for atomic recoil can be used, such as a model in which a fraction of the atoms undergoing spontaneous decay is diverted into the next higher velocity group. The width $\Delta\omega_v$ of a velocity group in frequency space is typically on the order of or larger than the natural width of the transition, Γ. Because the recoil shift $\Delta\omega_r$ is typically much smaller than this, a reasonable approximation can be obtained by letting a fraction $\Delta\omega_r/\Delta\omega_v$ of the upper-state atoms in each velocity group decay to the next higher velocity group.

Part II

Applications

Chapter 8

Nonlinear Magneto-optical Effects with Radio-frequency Fields

8.1 Introduction

This chapter presents work described by Zigdon *et al.* (2010). It gives an example of the solution of the density-matrix evolution equations discussed in Chapter 3, and the use of a technique for time-dependent fields discussed in Chapter 6. It also illustrates how the use of the angular-momentum probability surfaces can provide physical insight into the evolution of the atomic polarization.

The dynamics of atomic spin polarization in the presence of radio-frequency (rf) fields has been extensively studied (see, for example Kastler, 1950; Cohen-Tannoudji, 1994; Walker and Happer, 1997; Okunevich, 2004). Recently, it has been demonstrated that nonlinear magneto-optical rotation is a sensitive probe of atomic spin dynamics (Jackson Kimball *et al.*, 2009; Budker *et al.*, 2000b, 2002a), and can in fact be used to selectively create and probe different multipole moments of the atomic spin polarization (Yashchuk *et al.*, 2003; Pustelny *et al.*, 2006b; Acosta *et al.*, 2008). There are numerous practical applications for the use of NMOR to detect the response of atomic spins to rf fields: for example, in nuclear magnetic resonance (NMR) (Xu *et al.*, 2006a), nuclear quadruple resonance (NQR) (Garroway *et al.*, 2001), and magnetic resonance imaging (MRI) (Xu *et al.*, 2006b) experiments. One can also use such methods in tests of fundamental physics (Bradley *et al.*, 2003). In our previous research, we built an alkali-vapor magnetometer for the detection of rf fields (Ledbetter *et al.*, 2007). Recent work by researchers using a similar experimental setup is described by Wasilewski *et al.* (2010) and Chalupczak *et al.* (2010). The experiment by Ledbetter *et al.* (2007) demonstrated a sensitivity to oscillating magnetic fields of 100 pG/$\sqrt{\text{Hz}}$. The line shapes observed in the magnetometry experiment in the limit of low rf power are well understood. However, when higher-strength rf fields are applied, nontrivial line shapes are seen, with similarities to those of the of the "Majorana-Brossel effect" in double-resonance spectroscopy (Brossel and Bitter, 1952). Such signals were subsequently studied in work such as that of Friedmann and Wilson-Gordon (1987), Chakmakjian *et al.* (1988), and references therein. We have conducted experimental and theoretical investigations to explain the mechanism that produces these line shapes.

Experimental and theoretical analysis of double-resonance spectroscopy measured in transmission with a cesium paraffin-coated vapor cell was carried out by Di Domenico *et al.* (2006) and Weis *et al.* (2006). Good agreement was obtained between experimental data and the theoretical model.

The work described here employs the D_2 line of ^{87}Rb atoms contained in an paraffin-coated vapor cell, and optical rotation is detected. The signals are primarily due to interaction with the $F_g = 2 \to F_e = 1$ transition (the subscripts g and e indicate the ground and excited states, respectively). At low rf powers, the signals agree with the theoretical model, of the same form as that obtained by Di Domenico *et al.* (2006) and Weis *et al.* (2006). At higher rf powers, however, additional effects are observed which are described by a more general numerical model. We also present a qualitative explanation for the line shapes in terms of the underlying atomic spin dynamics of the system. An atomic polarization visualization technique (Sec. 2.2) is used to illustrate the mechanisms and their relationship to the detected NMOR signals. The character of the observed line shapes is found to be different depending on the value of the Rabi frequency for the rf field, Ω_{rf}, relative to the ground-state atomic-polarization relaxation rate γ_t and the magnetic resonance frequency Ω_L. This work is motivated by an ongoing project aimed at measuring collisional transfer of alignment in collisions between different ground-state alkali atoms (Jackson Kimball *et al.*, 2010).

8.2 Description of the experiment and theory

8.2.1 Description of experiment

The experiment employs a spherical paraffin-coated glass vapor cell (diameter = 10 cm) filled with a natural isotopic mixture of rubidium. The cell coating allows polarization of ground-state alkali atoms to survive several thousand wall collisions (Bouchiat and Brossel, 1966; Budker *et al.*, 1998), thereby extending the lifetime of atomic polarization. The cell is heated by a constant air stream from a heat exchanger.

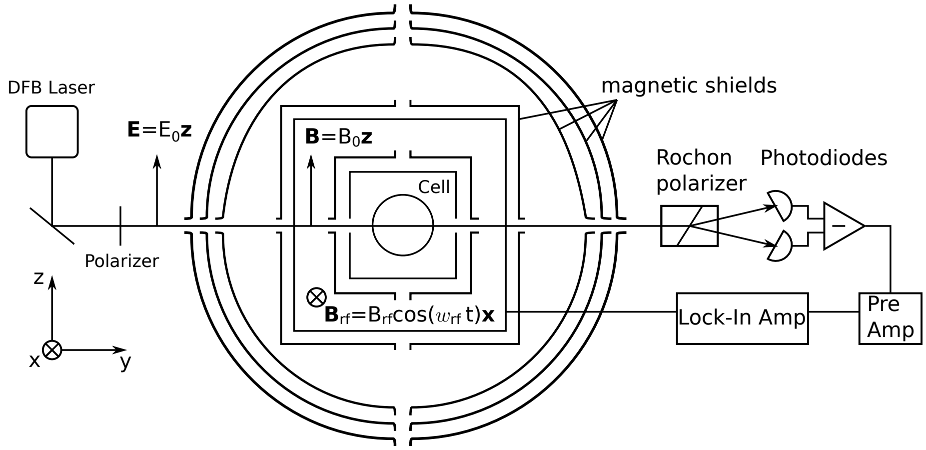

Figure 8.1: A laser beam linearly polarized along the z axis propagates through a paraffin-coated vapor cell, producing ground-state alignment in the ^{87}Rb atoms. A constant magnetic field $\mathbf{B}_0$ and an oscillating rf magnetic field $\mathbf{B}_{\mathrm{rf}}$ are applied within the magnetic shield that surrounds the cell. A balanced polarimeter and lock-in amplifier are used to analyze polarization rotation of the light induced by the atoms. A resonance is observed when the rf frequency is equal to the ground-state Larmor frequency of the atoms.

During all measurements in this work the temperature of the cell is stabilized at $\sim$41°C, resulting in a Rb vapor density of $7.2(7) \times 10^{10}$ atoms per cm^3. The density was extracted from fitting a low-light power (~ 8 µW) transmission spectrum for the Rb D_2 line to a calculated spectrum assuming linear absorption. Under these experimental conditions the longitudinal relaxation rate of ground-state alignment of the isotope ^{87}Rb was measured to be $31.7(7)$ s^{-1}. The value represents the effective relaxation rate of alignment polarization due to diverse types of atomic collisions occurring in the vapor cell, e.g., electron-randomization collisions with the wall, uniform relaxation due to the reservoir effect, and spin-exchange collisions among Rb atoms (Graf *et al.*, 2005). A four-layer µ-metal magnetic shield (see Fig. 8.1) surrounds the vapor cell and reduces the external magnetic field by a factor of $\sim 10^6$ (Budker *et al.*, 1998). Additionally, three orthogonal solenoidal coils placed inside the innermost shield are used to compensate residual magnetic fields to below 1 µG and to create additional static and oscillating fields. For our measurements we apply a static magnetic field $\mathbf{B}_0$ in the $\hat{\mathbf{z}}$ direction (typical strength $B_0 = 0.8$ mG) and an oscillating magnetic field $\mathbf{B}_{\mathrm{rf}} = B_{\mathrm{rf}}\hat{\mathbf{x}} \cos \omega_{\mathrm{rf}} t$ along the x-axis (typical amplitude up to $B_{\mathrm{rf}} = 0.25$ mG) using the sine wave output of a lock-in amplifier.

A laser beam, initially polarized along the z-axis, propagates through the vapor cell in the $\hat{\mathbf{y}}$ direction. The beam is generated by a distributed feedback (DFB) laser, which is tuned near the $F_g = 2 \rightarrow F_e = 1$ transition in the 780 nm D_2 line of ^{87}Rb, on the red-detuned slope of the Doppler-broadened absorption line, in order to maximize the optical rotation signal. The wavelength is locked using a dichroic atomic vapor laser lock (Corwin *et al.*, 1998; Yashchuk *et al.*, 2000). The light intensity is 10 µW throughout the measurements and the beam diameter is ∼2 mm. Linear dichroism of the atomic medium induces changes in the light polarization. [For high light power, the medium can also acquire circular birefringence (Budker *et al.*, 2000a).] After transmission through the vapor cell the polarization of the light beam is analyzed using a balanced polarimeter setup, consisting of a polarizing beam splitter (Rochon crystal) and two photodiodes detecting the intensities of the two beams exiting the crystal. The component of the difference signal that oscillates at the frequency of the rf field is then extracted by the lock-in amplifier.

Experimental signals as a function of rf frequency, along with predictions of the theory described in Sec. 8.2.2, are given in Fig. 8.2 for different amplitudes of the rf field. At the lowest amplitudes, the observed line shapes are Lorentzians, while for higher amplitudes, additional features are seen.

8.2.2 Description of theory

The experimental signal is primarily due to interaction with the $F_g = 2 \rightarrow F_e = 1$ transition of the D_2 line of ^{87}Rb, although there are also contributions from the $F_g = 2 \rightarrow F_e = 2$ and $F_g = 2 \rightarrow F_e = 3$ transitions. Theoretical modeling shows that signals produced on each of these transitions have similar line shapes, although the signal from a $F_g = 2 \rightarrow F_e = 3$ transition is of the opposite sign. In fact, the effects that we describe here are present for any transition with ground-state angular momentum $F_g \geq 1$. For the theoretical treatment presented here, we therefore consider the simplest case of a $F_g = 1 \rightarrow F_e = 0$ transition, for which analytical solutions are readily obtained. The model for this system gives results in reasonable agreement with the experimental data, indicating that the effects are not strongly dependent on the angular momenta characterizing the transition.

The atoms are subject to a $\hat{\mathbf{z}}$-directed field $\mathbf{B}_0 = B_0\hat{\mathbf{z}}$, corresponding to the Larmor frequency $\Omega_L = g\mu_B B_0$, where μ_B is the Bohr magneton and g is the Landé factor (we set $\hbar = 1$). Linearly polarized light propagating in the $\hat{\mathbf{y}}$ direction with polarization in the $\hat{\mathbf{z}}$ direction optically pumps the system and creates an aligned state. An oscillating rf magnetic field is applied in the $\hat{\mathbf{x}}$ direction, $\mathbf{B}_{\mathrm{rf}} = B_{\mathrm{rf}}\hat{\mathbf{x}}\cos\omega_{\mathrm{rf}}t$, corresponding to the rf Rabi frequency $\Omega_{\mathrm{rf}} = g\mu_B B_{\mathrm{rf}}$. The dependence on Ω_{rf} of the rf line shape of the optical rotation signal is studied. An analytic solution can be obtained in the case in which the rf power is low enough that the rf power-broadened

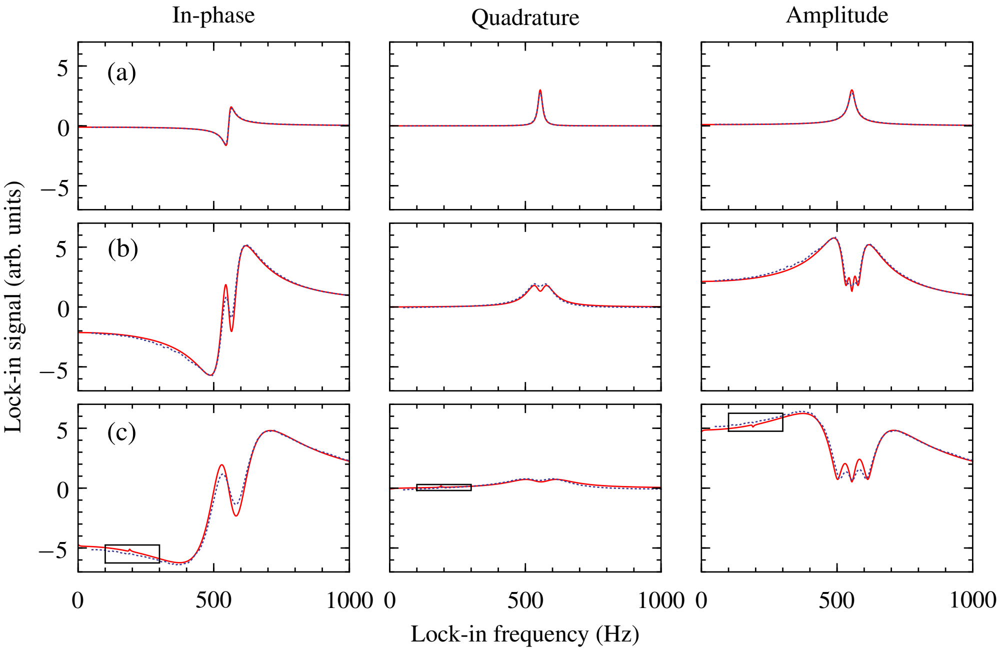

Figure 8.2: Experimental spectra (dotted lines) and theoretical predictions (solid lines) for three different values of the rf field amplitude. The experimental values (obtained from calibrated measurements of the coil current) in terms of the Rabi frequency $\Omega_{\rm rf}$ are (a) $\Omega_{\rm rf}/(2\pi) = 3$ Hz, (b) $\Omega_{\rm rf}/(2\pi) = 63$ Hz, (c) $\Omega_{\rm rf}/(2\pi) = 158$ Hz. These values are used in the theory, along with the values of natural width $\Gamma = 38\ \mu\text{s}^{-1} = 2\pi \times (6.1\ \text{MHz})$ (chosen equal to the natural width of the Rb D_2 transition), light power 5 μW, ground-state relaxation rate $\gamma_t = 50\ \text{s}^{-1} = 2\pi \times (8\ \text{Hz})$, and bias-field Larmor frequency $\Omega_L/(2\pi) = 554.75$ Hz. These last three parameters are chosen for optimal agreement with the data—they are reasonably close to the experimental values. The value for light power is applied to the theoretical model using the method described in Sec. 8.2.2. At low rf-field strengths, as in row (a), the spectra are Lorentzians. An additional central feature appears in the resonances when $\Omega_{\rm rf}$ exceeds γ_t, as in rows (b) and (c). Boxes in row (c) indicate regions plotted on expanded scales in Fig. 8.3.

line width is much smaller than Ω_L and $\omega_{\rm rf}$. Numerical solutions are obtained in the general case.

The experiment is performed using a vapor cell with an antirelaxation coating. In such a cell, atoms can be optically pumped in the light beam and then exit and return to the beam after undergoing collisions with the cell walls, without the polarization relaxing. Thus a complete theoretical description must take into account the different conditions—and the different state of the atoms—inside and outside the beam. If the light power is low enough so that saturation effects do not occur in the beam, however, the system can be modeled by considering the average state of the atoms over the entire cell. This amounts to mapping the case of a coated cell onto that of an uncoated cell (i.e., one in which atomic polarization completely relaxes between exiting and reentering the light beam). The light beam in the uncoated cell is taken to have an intensity equal to the average intensity over the entire cross-section of the coated cell, and the atomic transit rate through the beam is taken to be equal to the ground-state polarization relaxation rate in the coated cell. (This "effective" uncoated cell must be very large, in order to account for the slow ground-state relaxation of the coated cell.) This is the case that we will consider.

Another complication arising in a complete model of an atomic vapor cell is the velocity dependence of the atomic state due to Doppler broadening and collisional velocity mixing effects. These effects tend to change the dependence of a signal on the light frequency. Since we hold the light frequency fixed in this experiment, the main effect is the introduction of an overall scaling factor. Therefore, we neglect the velocity dependence in our model.

The atomic system is written in the Zeeman basis as in Sec. 3.3. The total time-dependent Hamiltonian H of the Doppler-free system under the optical rotating-wave approximation is

$$H = \begin{pmatrix} \Omega_L & \frac{\Omega_{\mathrm{rf}}}{2\sqrt{2}}\left(e^{i\omega_{\mathrm{rf}}t} + e^{-i\omega_{\mathrm{rf}}t}\right) & 0 & 0 \\ \frac{\Omega_{\mathrm{rf}}}{2\sqrt{2}}\left(e^{i\omega_{\mathrm{rf}}t} + e^{-i\omega_{\mathrm{rf}}t}\right) & 0 & \frac{\Omega_{\mathrm{rf}}}{2\sqrt{2}}\left(e^{i\omega_{\mathrm{rf}}t} + e^{-i\omega_{\mathrm{rf}}t}\right) & -\frac{\Omega_R}{2\sqrt{3}} \\ 0 & \frac{\Omega_{\mathrm{rf}}}{2\sqrt{2}}\left(e^{i\omega_{\mathrm{rf}}t} + e^{-i\omega_{\mathrm{rf}}t}\right) & -\Omega_L & 0 \\ 0 & -\frac{\Omega_R}{2\sqrt{3}} & 0 & -\Delta \end{pmatrix}, \tag{8.1}$$

where Ω_R is the Rabi frequency of the optical transition induced by the linearly polarized light and $\Delta = \omega - \omega_0$ is the optical detuning; ω is the frequency of the light and ω_0 is the frequency of the ground to excited state transition in the absence of a magnetic field. For the case in which the ground-state relaxation rate and Ω_{rf} are both much smaller than Ω_L and ω_{rf}, we can also perform the rotating-wave approximation on the rf field, in order to remove the Larmor-frequency time dependence from the Hamiltonian. In the rotating frame obtained using the unitary transformation

$$U(t) = \begin{pmatrix} e^{-i\omega_{\mathrm{rf}}t} & 0 & 0 & 0 \\ 0 & 1 & 0 & 0 \\ 0 & 0 & e^{i\omega_{\mathrm{rf}}t} & 0 \\ 0 & 0 & 0 & 1 \end{pmatrix}, \tag{8.2}$$

the density-matrix evolution can be written in terms of an effective Hamiltonian

$H' = U^{-1}HU - iU^{-1}\frac{dU}{dt}$. After dropping fast-oscillating, off-resonant terms, we have

$$H' = \begin{pmatrix} -\Delta_{\rm rf} & \frac{\Omega_{\rm rf}}{2\sqrt{2}} & 0 & 0 \\ \frac{\Omega_{\rm rf}}{2\sqrt{2}} & 0 & \frac{\Omega_{\rm rf}}{2\sqrt{2}} & -\frac{\Omega_R}{2\sqrt{3}} \\ 0 & \frac{\Omega_{\rm rf}}{2\sqrt{2}} & \Delta_{\rm rf} & 0 \\ 0 & -\frac{\Omega_R}{2\sqrt{3}} & 0 & -\Delta \end{pmatrix}, \tag{8.3}$$

where $\Delta_{\rm rf} = \omega_{\rm rf} - \Omega_L$ is the rf detuning. The evolution of the density matrix ρ (normalized so that $\operatorname{Tr}\rho = 1$) is described by the Liouville equation

$$\dot{\rho} = -i[H', \rho] - \frac{1}{2}\{\zeta, \rho\} + \Lambda, \tag{8.4}$$

where [ ] denotes the commutator and { } the anticommutator. The relaxation of the system is given by the matrix

$$\zeta = \begin{pmatrix} \gamma_t & 0 & 0 & 0 \\ 0 & \gamma_t & 0 & 0 \\ 0 & 0 & \gamma_t & 0 \\ 0 & 0 & 0 & \Gamma + \gamma_t \end{pmatrix}, \tag{8.5}$$

where the excited state decays spontaneously with a rate Γ and the ground and excited states relax with a rate γ_t due to the exit of atoms from the light beam. The matrix Λ describes repopulation of the ground state due to atoms entering the beam and spontaneous decay from the upper state, and is given by

$$\Lambda = \begin{pmatrix} \frac{\gamma_t}{3} + \frac{\Gamma}{3}\rho_{e_0e_0} & 0 & 0 & 0 \\ 0 & \frac{\gamma_t}{3} + \frac{\Gamma}{3}\rho_{e_0e_0} & 0 & 0 \\ 0 & 0 & \frac{\gamma_t}{3} + \frac{\Gamma}{3}\rho_{e_0e_0} & 0 \\ 0 & 0 & 0 & 0 \end{pmatrix}, \tag{8.6}$$

where the Zeeman ground and excited sublevels are denoted as g_{m_g} and e_{m_e}, and $\rho_{e_0e_0}$ is the population in the excited state.

Under the rotating-wave approximation for the rf field described above, the evolution equations for the rotating-frame density matrix contain no explicit time dependence. We can therefore set the time derivatives to zero and solve the resulting system of linear equations for the steady state. Taking the case of low light power, we solve the equations to third order in the optical Rabi frequency, which is the lowest order at which nonlinear optical rotation signals appear. Using the inverse transformation U^{-1}, we transform back to the laboratory frame to find the time-dependent density matrix.

The expectation value of the medium polarization is found from the laboratory-frame density matrix. By substituting this value into the wave equation, we can calculate the optical-rotation signal measured in the laboratory frame in terms of the rotating-frame density-matrix elements. After multiplying by the reference signal and averaging over time, we find the in-phase and quadrature (out-of-phase) signals per unit length $d\ell$ of the medium to be

$$\frac{\partial\varphi^{\mathrm{in}}}{\partial\ell} = -\frac{\sqrt{\frac{3}{2}}N\Gamma\lambda^2}{4\pi\Omega_R}\mathrm{Im}(\rho_{e_0g_{-1}} - \rho_{e_0g_1}), \tag{8.7}$$

$$\frac{\partial\varphi^{\mathrm{out}}}{\partial\ell} = \frac{\sqrt{\frac{3}{2}}N\Gamma\lambda^2}{4\pi\Omega_R}\mathrm{Re}(\rho_{e_0g_{-1}} + \rho_{e_0g_1}), \tag{8.8}$$

where λ is the transition wavelength, N is the atomic density, and $\rho_{e_0g_{-1}}$ and $\rho_{e_0g_1}$ are the optical coherences between the excited state and the ground g_{-1} and g_1 Zeeman sublevels, respectively. The magnitude of the optical-rotation signal is given by

$$\begin{aligned}\frac{\partial\varphi^{\mathrm{abs}}}{\partial\ell} &= \sqrt{\left(\frac{\partial\varphi^{\mathrm{in}}}{\partial\ell}\right)^2 + \left(\frac{\partial\varphi^{\mathrm{out}}}{\partial\ell}\right)^2} \\ &= \frac{\sqrt{\frac{3}{2}}N\Gamma\lambda^2}{4\pi\Omega_R}\{[\mathrm{Im}(\rho_{e_0g_{-1}} - \rho_{e_0g_1})]^2 + [\mathrm{Re}(\rho_{e_0g_{-1}} + \rho_{e_0g_1})]^2\}^{1/2}.\end{aligned} \tag{8.9}$$

The expressions obtained after substituting in the solution for the density matrix are complicated; to simplify the presentation we assume that the light field is on resonance and that Γ is much greater than all other rates in the problem. This gives

$$\frac{\partial\varphi^{\mathrm{in}}}{\partial\ell} = \frac{N\Delta_{\mathrm{rf}}\lambda^2\Omega_{\mathrm{rf}}(2\gamma_t{}^2 + 8\Delta_{\mathrm{rf}}^2 - \Omega_{\mathrm{rf}}^2)\Omega_R^2}{36\pi\Gamma\gamma_t(\gamma_t^2 + 4\Delta_{\mathrm{rf}}^2 + \Omega_{\mathrm{rf}}^2)[4(\gamma_t^2 + \Delta_{\mathrm{rf}}^2) + \Omega_{\mathrm{rf}}^2]}, \tag{8.10}$$

$$\frac{\partial\varphi^{\mathrm{out}}}{\partial\ell} = \frac{N\lambda^2\Omega_{\mathrm{rf}}(4\gamma_t^2 + 16\Delta_{\mathrm{rf}}^2 + \Omega_{\mathrm{rf}}^2)\Omega_R^2}{72\pi\Gamma(\gamma_t^2 + 4\Delta_{\mathrm{rf}}^2 + \Omega_{\mathrm{rf}}^2)[4(\gamma_t^2 + \Delta_{\mathrm{rf}}^2) + \Omega_{\mathrm{rf}}^2]}, \tag{8.11}$$

where we have neglected the contribution to optical rotation that is independent of the light power. These formulas are in agreement with Eqs. (16a) and (16b) of Weis *et al.* (2006). Expanding these expressions in a power series in Ω_{rf}, we obtain

$$\frac{\partial\varphi^{\mathrm{in}}}{\partial\ell} = \frac{N\Delta_{\mathrm{rf}}\lambda^2\Omega_R^2}{72\pi\Gamma\gamma_t(\gamma_t^2 + \Delta_{\mathrm{rf}}^2)}\Omega_{\mathrm{rf}} - \frac{N\Delta_{\mathrm{rf}}\lambda^2\Omega_R^2(7\gamma_t^2 + 10\Delta_{\mathrm{rf}}^2)}{288\pi\Gamma\gamma_t(\gamma_t^2 + \Delta_{\mathrm{rf}}^2)^2(\gamma_t^2 + 4\Delta_{\mathrm{rf}}^2)}\Omega_{\mathrm{rf}}^3 + O[\Omega_{\mathrm{rf}}]^5, \tag{8.12}$$

$$\frac{\partial\varphi^{\text{out}}}{\partial\ell}=\frac{N\lambda^2\Omega_R^2}{72\pi\Gamma(\gamma_t^2+\Delta_{\text{rf}}^2)}\Omega_{\text{rf}}-\frac{N\lambda^2\Omega_R^2(4\gamma_t^2+7\Delta_{\text{rf}}^2)}{288\pi\Gamma(\gamma_t^2+\Delta_{\text{rf}}^2)^2(\gamma_t^2+4\Delta_{\text{rf}}^2)}\Omega_{\text{rf}}^3+O[\Omega_{\text{rf}}]^5, \quad (8.13)$$

$$\frac{\partial\varphi^{\text{abs}}}{\partial\ell}=\frac{N\lambda^2\Omega_R^2\Omega_{\text{rf}}}{144\pi\Gamma\gamma_t\sqrt{\gamma_t^2+\Delta_{\text{rf}}^2}}-\frac{N\lambda^2\left(2\gamma_t^2+5\Delta_{\text{rf}}^2\right)\Omega_R^2\Omega_{\text{rf}}^3}{288\pi\Gamma\gamma_t\left(\gamma_t^2+\Delta_{\text{rf}}^2\right)^{3/2}\left(\gamma_t^2+4\Delta_{\text{rf}}^2\right)}+O[\Omega_{\text{rf}}]^5. \quad (8.14)$$

These expressions describe resonances in Δ_{rf} centered at $\Delta_{\text{rf}}=0$. To lowest order in Ω_{rf}, they are proportional to the real part, imaginary part, and absolute value, respectively, of a complex Lorentzian. Additional features appear at higher orders, as discussed in the next section.

When Ω_{rf} becomes of the same order as or exceeds Ω_L, the rotating-wave approximation for the rf field is no longer valid. In this case we use the Hamiltonian H of Eq. (8.1) and proceed in the laboratory frame. The Liouville equation now has explicit time dependence, and the density matrix $\rho(t)$ is a function of time. We then treat the system using the method of Fourier expansion discussed in Sec. 6.2.1. This method provides a linear system of time-independent equations that can be solved numerically for the Fourier coefficients in the expansion. The observed optical rotation signals can then be found as before.

8.3 Discussion

The predictions of the density-matrix calculation described in Sec. 8.2.2 are compared to the experimental data in Fig. 8.2. For each value of the rf field strength (characterized by the rf Rabi frequency Ω_{rf}), the in-phase and quadrature components and the magnitude of the optical-rotation signal as a function of the rf frequency ω_{rf} are shown. The version of the theoretical treatment valid for arbitrary rf-field strength discussed in Sec. 8.2.2 is used to generate the theoretical predictions, although for the lowest rf power, the signal is well described by the lowest-order terms of the expansions (8.12)–(8.14). Three regimes in the dependence on Ω_{rf} can be identified. At the lowest field strengths, $\Omega_{\text{rf}}<\gamma_t$, the in-phase and quadrature resonances in rf frequency take the form of dispersive and absorptive Lorentzians of characteristic width γ_t (Fig. 8.2a). At intermediate field strengths, $\gamma_t<\Omega_{\text{rf}}<|\Omega_L|$ (we assume $\gamma_t\ll|\Omega_L|$), the Lorentzians broaden and additional narrow features are seen at the center of the resonances (Fig. 8.2b), the result of polarization-averaging effects discussed below.

For higher fields, $\Omega_{\text{rf}}>|\Omega_L|$, effects due to ac Zeeman shifts and far-off-resonant fields are predicted to become important. We did not perform measurements in this regime, but the beginning of these effects can be seen in the data (Fig. 8.2c). The negative-frequency component of the rf field results in a resonance at $\omega_{\text{rf}}=-\Omega_L$

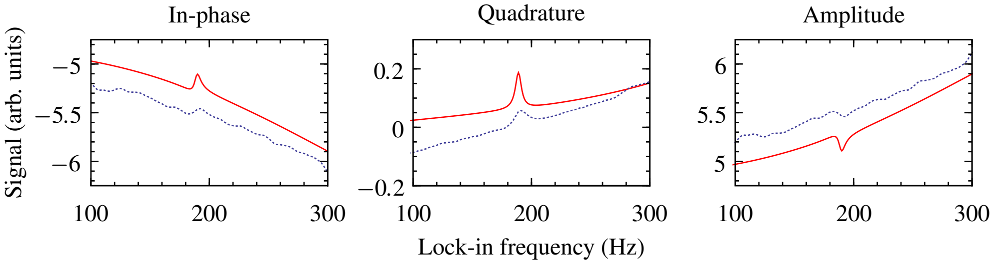

Figure 8.3: Row (c) of Fig. 8.2 (boxed regions) plotted on expanded scales. (The vertical scale is different for each plot.) A resonance due to high-field effects can be seen near $\omega_{\rm rf}/(2\pi) = \frac{1}{3}\Omega_L/(2\pi) \approx$ 185 Hz.

symmetric to the one at $\omega_{\rm rf} = \Omega_L$. In Fig. 8.2(b) and (c), the off-resonant tail of this negative-frequency resonance produces an overall slope in the in-phase component of the positive-frequency signal. Calculations for values of $\omega_{\rm rf}$ of the same order as Ω_L predict higher-order resonances at odd fractions (1/3, 1/5, etc.) of Ω_L. When the experimental data presented in Fig. 8.2(c) are plotted on expanded scales, as in Fig. 8.3, a higher-order resonance can be observed at one third the frequency of the main resonance, in agreement with theoretical predictions.

8.3.1 Low-field regime

We first consider the low-rf-field regime, $\Omega_{\rm rf} < \gamma_t$. This case was discussed by Ledbetter *et al.* (2007). An example of experimental data taken in this regime compared to theoretical predictions is shown in Fig. 8.2(a). As described by Eqs. (8.12)–(8.14), the resonance observed in the in-phase component, quadrature component, and magnitude of the optical-rotation signal takes the form of the real (dispersive) part, imaginary (absorptive) part, and the magnitude of a complex Lorentzian, respectively. The absolute value of a complex Lorentzian has the line shape of the square root of the absorptive part. Near resonance the quadrature component is the primary contributor to the magnitude, while farther from resonance, the in-phase component provides the main contribution. The characteristic width of the observed resonances is determined by the ground-state relaxation rate.

Optical pumping by the light field removes atoms from the $m_g = 0$ sublevel, leaving an incoherent mixture of atoms in the $m_g = \pm 1$ sublevels. The atomic polarization can be illustrated using the AMPS (Auzinsh, 1997; Rochester and Budker, 2001; Auzinsh *et al.*, 2010), whose radius in a given direction is determined by the probability of measuring the maximum possible angular-momentum projection in that direction. This provides the quantum-mechanical analog of the classical angular-momentum

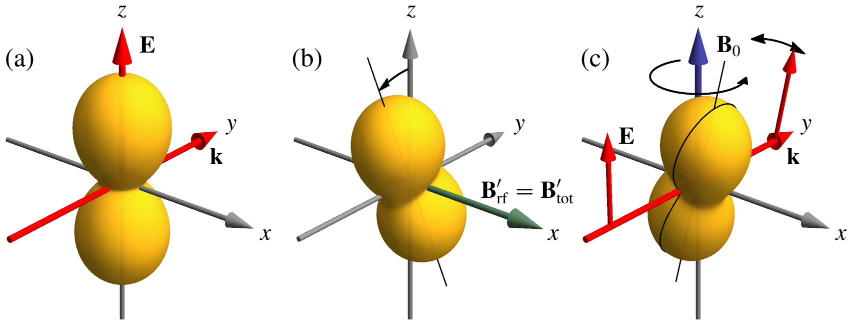

Figure 8.4: Angular-momentum-probability surfaces illustrating the behavior of the system with a resonant ($\Delta_{\rm rf} = 0$), weak rf field. (a) The light, with electric field $\mathbf{E}$, produces atomic alignment along the z-axis. (b) In the rotating frame, the atoms precess around the x-axis. Due to relaxation, a steady state is reached. (c) In the laboratory frame, the atoms precess around the z-axis, with the linear dichroism of the ensemble inducing oscillating optical rotation in the z-polarized, $\hat{\mathbf{y}}$-propagating light field. (An animation of the precession and optical rotation as a function of time can be viewed at `http://budker.berkeley.edu/ADM/media1_fig4c.mov`.) The transmission axis of the polarized ensemble, in this case parallel to the atomic alignment axis, is indicated with a line drawn on the surface.

probability distribution. The optically pumped distribution corresponds to atomic alignment along the z-axis with a "peanut"-shaped probability distribution (Fig. 8.4a). [All of the AMPS shown here are obtained directly from the density-matrix calculation. A quantity of the lowest-rank, isotropic polarization moment is subtracted from each figure so that the anisotropic polarization can be more clearly seen (Auzinsh *et al.*, 2010).] Because the $m_g = 0$ sublevel has been depleted, the atomic medium transmits z-polarized light, while tending to absorb orthogonally polarized light—i.e., the atoms function as a polarizing filter with transmission axis along the atomic alignment axis (Kanorsky *et al.*, 1993). This linear dichroism can induce rotation of the light polarization if the transmission axis is tilted away from the light polarization axis.

The observed signals in the low- and intermediate-field regimes can be most readily understood in terms of Larmor precession of the atomic alignment in the combined static and rf magnetic field. In the rotating frame, under the rotating-wave approximation for the rf field, the effect of the magnetic fields $\mathbf{B}_0$ and $\mathbf{B}_{\rm rf}$ can be described in terms of fictitious static fields $\mathbf{B}'_0$ and $\mathbf{B}'_{\rm rf}$. These fields can be determined by examining the rotating-frame Hamiltonian (8.3). The bias field in the rotating frame, $\mathbf{B}'_0$, points along $\mathbf{B}_0$, while its field strength is such that it produces a Larmor frequency given by the detuning of the rf field from resonance: $\Omega'_L = -\Delta_{\rm rf} = -\omega_{\rm rf} + \Omega_L$. The rf field $\mathbf{B}_{\rm rf}$ becomes a static field $\mathbf{B}'_{\rm rf}$ in the xy plane with associated Larmor frequency $\Omega'_{\rm rf} = \Omega_{\rm rf}/2$. The direction of this field in the xy

plane depends on the arbitrary phase chosen for the rotating frame; in our convention $\mathbf{B}'_{\rm rf}$ points along $\hat{\mathbf{x}}$. Thus the resultant field $\mathbf{B}'_{\rm tot} = \mathbf{B}'_0 + \mathbf{B}'_{\rm rf}$ lies in the xz plane.

The atomic polarization evolves in the rotating frame under the action of $\mathbf{B}'_{\rm tot}$. For low field strengths, this evolution is Larmor precession, so that the polarization continues to correspond to alignment. Because all of the external fields are static in the rotating frame, the effect of relaxation leads to a steady state for the atomic polarization. First consider the case in which the rf field is exactly on resonance ($\Delta_{\rm rf} = 0$). Then $\mathbf{B}'_{\rm tot}$ is equal to $\mathbf{B}'_{\rm rf}$ and points in the $\hat{\mathbf{x}}$ direction (Fig. 8.4b), and the atomic alignment precesses in the yz plane. Under the assumption $\Omega_{\rm rf} \ll \gamma_t$, the precession frequency is much less than the relaxation rate, so that each atom precesses through a small angle before relaxing. The rotating-frame steady-state ensemble polarization thus consists of alignment at a small angle to the z-axis in the yz plane (Fig. 8.4b).

In the laboratory frame, the alignment precesses about the z-axis (Fig. 8.4c). At the instant that the alignment is in the yz plane, it does not induce any polarization rotation in the $\hat{\mathbf{y}}$-propagating light field. On the other hand, whenever the alignment axis is tilted away from the initial light polarization axis (the z-axis) in the plane transverse to the light propagation direction (the xz plane), the atoms can induce optical rotation. Because of the precession of the alignment, the optical-rotation signal oscillates. The amplitude of the signal is determined by the amount of the alignment and the angle between the alignment axis and the z-axis (zenith angle). The phase of the oscillating signal is determined by the angle of the alignment axis about the z-axis in the rotating frame (azimuthal angle). The direction of the alignment axis in the rotating frame corresponds to its direction in the laboratory frame when the rf field is maximum. Only the component in the xz plane will induce optical rotation in y-propagating light, so an alignment axis in the xz plane in the rotating frame produces a signal in phase with the rf field oscillation, while the component in the yz plane produces a quadrature component in the signal. In the case of Fig. 8.4 the optical-rotation signal is entirely in the quadrature component.

As the rf field is tuned away from resonance, the total field in the rotating frame begins to point away from the x-axis and toward the z-axis. Precession about this field then takes the alignment in the rotating frame out of the yz plane (Fig. 8.5a). This tends to reduce the angle that the steady-state alignment makes with the z-axis, reducing the amplitude of the laboratory-frame optical rotation signal. On the other hand, because the alignment now has a component in the xy plane in the rotating frame, the oscillating rotation signal gains an in-phase component. When the rf field is tuned far enough away from resonance so that $|\Delta_{\rm rf}| > \gamma_t$, the precession frequency in the rotating frame becomes large enough that the atoms undergo an entire precession

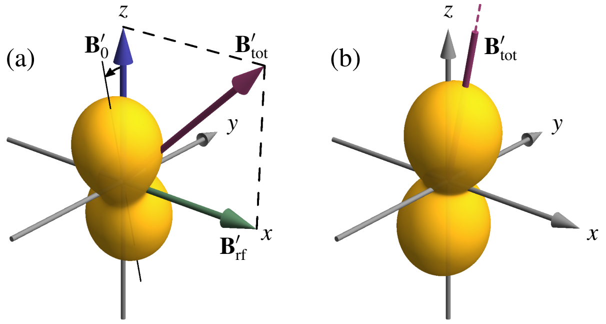

Figure 8.5: As Fig. 8.4, but with an off-resonant rf field. (a) In the rotating frame, the atoms precess around the total effective field, which lies in the xz plane. As a result, the polarization is no longer entirely in the yz plane. (b) Far off resonance, the effective magnetic field is large enough that the polarization is completely averaged about the magnetic-field direction. (The arrow representing $\mathbf{B}'_{\mathrm{tot}}$ is truncated, as it is too long to fit entirely on the plot.) An animation of the polarization, along with the in-phase component of the optical-rotation signal, as the rf-field detuning is swept through resonant and off-resonant conditions, can be viewed at `http://budker.berkeley.edu/ADM/media2_fig5.mov`.

cycle before relaxing. The ensemble polarization is then averaged about the direction of the total magnetic field (Fig. 8.5b). Because $\mathbf{B}'_{\mathrm{tot}}$ lies in the xz plane, the signal is now predominately in phase with the rf field, and the quadrature component is strongly suppressed. As the detuning becomes large, the average polarization points more and more along the z-axis, and the signal amplitude drops to zero.

The preceding description is seen to correspond to the signals shown in Fig. 8.2(a)—the dispersive (in-phase) and absorptive (quadrature) components and the magnitude of a Lorentzian with characteristic width γ_t—as well as to the lowest order terms of Eqs. (8.12)–(8.14).

8.3.2 Intermediate-field regime

When the rf field is large enough that $\gamma_t < \Omega_{\mathrm{rf}} < |\Omega_L|$, the rotating-frame precession frequency is high even at zero detuning. This causes averaging of the atomic polarization about the magnetic-field axis. For $\Delta_{\mathrm{rf}} = 0$ this is the x-axis: polarization transverse to the x-axis is averaged out. However, the polarization along the x-axis is preserved, so that the x-axis becomes the preferred axis for the polarization (Fig. 8.6a). The "doughnut"-shaped probability distribution seen in Fig. 8.6(a) is obtained from the initially pumped "peanut"-shaped distribution (Fig. 8.4a) when copies of the peanut distribution rotated by arbitrary angles about the x-axis are averaged together. Another way to explain the doughnut shape is to transform

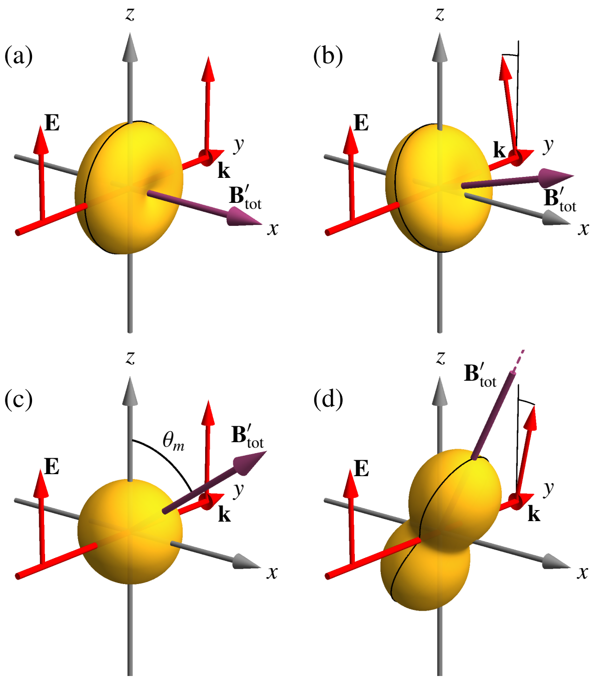

Figure 8.6: Rotating-frame AMPS for intermediate rf field strength, in the ideal case in which $\gamma_t \ll \Omega_{\rm rf} \ll |\Omega_L|$. Optical rotation is indicated for the instant in which the rotating frame coincides with the laboratory frame—this means that the generation of the in-phase component of the signal is shown. (a) When the rf field is on resonance, the atomic polarization (created along the z-axis) is averaged about the x-axis. The resulting polarization is a "doughnut" aligned along the x-axis. The transmission axis, perpendicular to the alignment axis, is marked with a line on the surface. (b) For small detunings, the alignment axis follows the effective magnetic field direction. (c) When the effective magnetic field is at the magic angle $\theta_m = \arccos(1/\sqrt{3})$ to the light polarization direction, the atomic polarization is completely averaged out due to precession. (d) For larger detunings, the polarization regains its original "peanut" shape, and the transmission axis is along the alignment axis. An animation of the atomic polarization and in-phase optical rotation as the rf-field detuning is swept through resonance can be viewed at `http://budker.berkeley.edu/ADM/media3_fig6.mov`.

to the basis in which the quantization axis is along $\hat{\mathbf{x}}$. In this basis, the excitation light is σ polarized, so that it pumps atoms out of the bright state consisting of a superposition of the $m_g = \pm 1$ sublevels, and leaves them in the dark state made up of the opposite superposition, as well as in the $m_g = 0$ sublevel. However, due to the precession induced by the $\hat{\mathbf{x}}$ directed magnetic field, atoms oscillate between the bright and dark superpositions, so that the pump light removes atoms from the $m_g = \pm 1$ sublevels incoherently. The atoms are then left in the $m_g = 0$ sublevel, i.e., the atoms have no angular-momentum projection on the x-axis and are symmetric about the x-axis, as seen in Fig. 8.6(a).

Polarization along the x-axis remains in the xy plane as it precesses around the z-axis in the laboratory frame and so does not induce any optical rotation. However, when the rf field is tuned slightly away from resonance, $\mathbf{B}'_{\rm tot}$ points away from the x-axis, and so also does the averaged atomic polarization (Fig. 8.6b). The polarization then causes optical rotation. As the polarization in the rotating frame is in the xz

plane, the signal in the laboratory frame is in phase with the rf field. (The plots in Fig. 8.6 are shown for the instant at which the rotating frame coincides with the laboratory frame, so that the in-phase component of the optical rotation is shown.)

To understand the generation of optical rotation in this case, it is important to note the effect of the different character of the ensemble polarization. In the low-field case, the angular-momentum probability distribution has maxima along the ensemble polarization axis (a peanut), while in the current case, the distribution has minima (a doughnut). (This result depends on the particular type of transition considered—for a $F_g \rightarrow F_e = F_g$ transition the situation is reversed.) We can think of the doughnut shape as an unpolarized distribution (sphere) with a peanut shape removed. From this viewpoint, it is reasonable that this "negative polarization" produces rotation of the opposite sign. More concretely, we can note that, as described above, in a doughnut distribution atoms are concentrated in the $m_g = 0$ sublevel with the quantization axis along the alignment axis. The state then preferentially absorbs light that is polarized along the alignment axis. In the analogy with a polarizing filter, the transmission axis of the doughnut-shaped probability distribution is transverse to, rather than along, the alignment axis. This explains the sign of the rotation shown in Fig. 8.6(b) when $\mathbf{B}'_{\text{tot}}$ points away from the x-axis. (The transmission axis of each polarization state is marked with a line on the surfaces plotted in Fig. 8.6.)

As the rf field is tuned farther from resonance, $\mathbf{B}'_{\text{tot}}$ points farther away from the x-axis, bringing the averaged alignment axis with it. This larger angle produces a larger optical rotation signal. However, another trend eventually takes over: because of the shape of the initially pumped polarization distribution, the amount of polarization that lies along the magnetic-field direction decreases. As a result, the amount of averaged polarization is reduced, tending to reduce the signal. In order to analyze this, we can plot just the aligned part of the initially pumped density matrix (the rank $\kappa = 2$, $q = 0$ polarization moment), neglecting the isotropic part that is included in Fig. 8.4(a). The surface corresponding to this moment is described by the spherical harmonic $Y_{2,0}(\theta, \phi) \propto 3\cos^2\theta - 1$, plotted in cross section in Fig. 8.7. Negative values of the function are indicated by dashed lines. There are maximum positive values along z ($\theta = 0$), and maximum negative values in the xy plane ($\theta = \pi/2$). As θ moves away from either of these values, the magnitude of the polarization is reduced. At a particular angle $\theta_m = \arccos(1/\sqrt{3})$, analogous to the magic angle observed in nuclear magnetic resonance experiments, the polarization moment goes to zero. This means that if $\mathbf{B}'_{\text{tot}}$ is at this angle to the z-axis, the averaged polarization completely cancels, sending the optical rotation signal to zero (Fig. 8.6c). This condition corresponds to the additional zero crossings seen in the in-phase component of Fig. 8.2(b,c) above and below the center of the resonance. The direction of the effective magnetic field in the rotating frame depends on the rf field strength and the detuning from resonance—as the field strength is increased, the detuning required to achieve the magic angle also increases.

When the detuning is even larger, there is once again residual polarization after averaging about the magnetic-field direction. However, now the magnetic-field direction is close enough to the initial alignment axis that the polarization resulting from averaging resembles the peanut shape of the initially pumped polarization (Fig. 8.6d). Thus, the optical-rotation signal in this case is opposite in sign to that for small detuning and has the same sign as that for the low-power case.

As the detuning continues to increase, $\mathbf{B}'_{\text{tot}}$ and the averaged atomic alignment point more toward the z-axis, reducing the optical-rotation signal.

The preceding discussion describes the in-phase signal shown in Fig. 8.2(b) and (c): a power-broadened Lorentzian with a narrower feature of the opposite sign in the center. If the discussion is strictly interpreted, there should be no quadrature signal in this regime, as the polarization in the rotating frame is always in the xz plane. Figure 8.2 does display (strongly suppressed) quadrature signals, which are a remnant of the low-field regime.

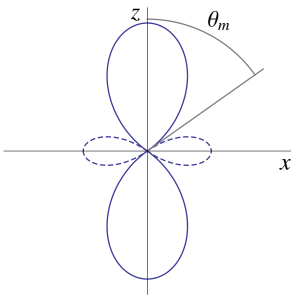

Figure 8.7: Cross section of the AMPS for pure alignment along the z-axis, described by $Y_{2,0}(\theta,\phi) \propto 3\cos^2\theta - 1$. Positive function values are shown as solid lines, negative function values as dashed lines. The magic angle $\theta_m = \arccos(1/\sqrt{3})$ is indicated.

8.3.3 High-field regime

As Ω_{rf} becomes of the same order as Ω_L or exceeds it, various higher-order effects appear in the data and the full theory that cannot be described under the rotating-wave approximation for the rf field. In particular, a resonance near $\Omega_L/3$ is seen, as shown in Fig. 8.3. This can be explained as due to ac Zeeman shifts, which produce evenly spaced sidebands that result in resonances at odd subharmonics of the lowest-order resonance. The additional features can also be interpreted as arising from higher-order resonances between the Larmor precession and the rf frequency, similar to those seen in nonlinear magneto-optical rotation with frequency-modulated light (Alexandrov *et al.*, 2005). As the rf field strength increases, many additional resonances are predicted by the theory.

Chapter 9

Polarization Effects in Transitions with Partially Resolved Hyperfine Structure

Atomic polarization, created in a medium by polarized light, can modify the optical response of the medium, affecting the light field. As we have already mentioned, the absorption of light of a particular polarization by atoms in a polarized state can be reduced [*electromagnetically induced transparency* (Fleischhauer *et al.*, 2005)] or increased [*electromagnetically induced absorption* (Lezama *et al.*, 1999)] compared to that for an unpolarized state. *Coherent population trapping* (Nasyrov *et al.*, 2006) is a closely related phenomenon, the study of which led to the discovery of an interesting effect that is also a powerful tool for the manipulation of atomic states: coherent population transfer between atomic states, known as *STIRAP* [*stimulated Raman adiabatic passage* (Bergmann *et al.*, 1998)]. *"Lasing without inversion"* (Kocharovskaya and Khanin Ya, 1988; Scully *et al.*, 1989) is another related effect.

Additional effects are encountered when atoms interact with coherent light in the presence of a magnetic field (Budker *et al.*, 2002a; Alexandrov *et al.*, 2005).[1] These magneto-optical effects—especially those involving magnetic-field-induced evolution of long-lived ground-state polarization—can be used to perform sensitive magnetometery (Budker and Romalis, 2007).

---

[1] Budker and Rochester (2004) discuss a relationship between these effects and electromagnetically induced absorption.

> These effects are also often referred to as "coherence effects," although this is something of a misnomer, as in some cases the effects can be described using a basis in which there are no ground-state coherences (Kanorsky *et al.*, 1993).

The atomic polarization responsible for specific effects, such as NMOR, can be described in terms of the polarization moments (PM) in the multipole expansion of the density matrix (Sec. 2.3). The lowest-rank multipole moments correspond to population, described by a rank $\kappa = 0$ tensor, orientation, described by a rank $\kappa = 1$ tensor, and alignment, described by a rank $\kappa = 2$ tensor. It is these three lowest-rank multipole moments that can directly affect light absorption and laser-induced fluorescence (Dyakonov, 1965; Auzinsh and Ferber, 1995), and thus can be created and detected through single-photon interactions. An atomic state with total angular momentum F can support multipole moments with rank up to $\kappa = 2F$; multi-photon interactions and multipole transitions higher than dipole allow the higher-order moments to be created and detected. Magneto-optical techniques can be used to selectively address individual high-rank multipoles as discussed by Yashchuk *et al.* (2003), Pustelny *et al.* (2006b), and Acosta *et al.* (2008).

Magneto-optical coherence effects that involve linearly polarized light generally require the production and detection of polarization corresponding to atomic alignment. [There are multi-field, high-light-power effects in which alignment is converted to orientation, which is then detected (Budker *et al.*, 2000a); these effects still depend on the creation of alignment by the light]. Thus, for ground-state coherence effects, the ground state in question must have angular momentum of at least $F = 1$ in order to support a rank-two polarization moment. The alkali atoms K, Rb, and Cs—commonly used for magneto-optical experiments—each have ground-state hyperfine sublevels with $F \geq 1$. If light is tuned to a suitable transition between a ground-state and an excited-state hyperfine sublevel, alignment can be created and detected in the ground state.

The situation changes, however, if the hyperfine structure is not resolved. If the hyperfine transitions are completely unresolved (as was the case in early work that used broad-band light sources such as electrodeless discharge lamps to excite atoms), then it is the fine-structure transition that is effectively excited—the D_1 line ($n^2S_{1/2} \to n^2P_{1/2}$) or the D_2 line ($n^2S_{1/2} \to n^2P_{3/2}$). In this case, the effects related to the excitation of a particular hyperfine transition are averaged out when all transitions are summed over. Thus the effect of the nuclear spin is removed, and the states have effective total angular momentum $J = 1/2$ for the ground state and $J = 1/2$ or $3/2$ for the excited state. In this case the highest rank multipole moment that can be supported by the ground state is orientation ($\kappa = 2J = 1$), and effects depending on atomic ground-state alignment will not be apparent.

In practical experiments with alkali atoms in vapor cells, even when narrow-band laser excitation is used, the hyperfine structure is in general only partially resolved, due to Doppler broadening. At room temperature, the Doppler widths of the atomic transitions in K, Rb, and Cs range from 463 MHz for K to 226 MHz for Cs. The ground-state hyperfine splittings, ranging from 462 MHz for K to 9.192 GHz for Cs, are on the order of or greater than the Doppler widths, while the excited-state hyperfine splittings, ranging from 8 MHz to 1.167 GHz, are generally on the order of or smaller than the Doppler width. Thus the question arises: how do coherence effects depend on the ground- and excited-state hyperfine splitting when the hyperfine structure is neither completely resolved nor completely unresolved?

In this chapter we present work by Auzinsh *et al.* (2009a). We discuss transitions for which one or the other of the excited- or ground-state hyperfine structure (hfs) is completely unresolved. We determine which polarization moments can be created in the ground state via single-photon interactions, and which moments can be detected through their influence on light absorption. We find that the two contributions to the ground-state polarization—absorption and polarization transfer through spontaneous decay—depend differently on the ground- and excited-state hyperfine structure.

In Chapter 10, we choose a particular system and investigate the detailed dependence of NMOR signals on the excited- and ground-state hyperfine splitting. We consider three cases: systems in which the atomic Doppler distribution can be neglected, and systems in which the Doppler distribution is broad compared to the natural linewidth and in which the rate of velocity-changing collisions is either much slower than or much faster than the ground-state polarization relaxation rate.

Throughout the discussion we use the low-light-intensity approximation in order to simplify the calculations and obtain analytic results. It can be shown, using higher-order perturbation theory and numerical calculations, that the essential results presented here hold for arbitrary light intensity, as well. Previous work that discusses the dependence of optical pumping on whether or not hyperfine structure (hfs) is resolved includes that of Happer and Mathur (1967), Happer (1972), and Lehmann (1967).

In this section, we discuss the creation and detection of atomic polarization in systems for which either the ground- or excited-state hyperfine structure is unresolved. This section deals with systems that can be described using the complete-mixing approximation, i.e., the assumption that atomic velocities are completely rethermalized in between optical pumping and probing. This is the case for experiments using buffer-gas or antirelaxation-coated vapor cells, in which atoms undergo frequent velocity-changing collisions during the ground-state polarization lifetime.

9.1 Depopulation pumping

We consider an ensemble of atoms with nuclear spin I, a ground state with electronic angular momentum J_g, and an excited state with angular momentum J_e. The various ground- and excited-state hyperfine levels are labeled by F_g and F_e, respectively. The atoms are subject to weak monochromatic light with complex polarization vector $\hat{\boldsymbol{\varepsilon}}$ and frequency ω, near-resonant with the atomic transition frequency $\omega_{J_gJ_e}$. We assume that the atoms undergo collisions that mix different components of the Doppler distribution. We also neglect coherences between different ground-state or different excited-state hyperfine levels (these coherences will not develop for low light power as long as the hyperfine splittings are larger than the natural width of the excited state). We first consider polarization produced in the ground state due to atoms absorbing light and being transferred to the excited state (depopulation pumping). The general form of the contribution to the ground-state density matrix due to this effect was found in Chapter 5:

$$\rho_{mn}^{(depop)} \propto \sum_r \hat{\boldsymbol{\varepsilon}}^* \cdot \mathbf{d}_{mr} \hat{\boldsymbol{\varepsilon}} \cdot \mathbf{d}_{rn} G(\omega - \omega_{rn}), \tag{9.1}$$

where m and n are degenerate ground states, r is an excited state, ω_{rn} is the transition frequency between r and n, and G is a function describing the spectral lineshape. If the natural width of the excited state is much smaller than the Doppler width Γ_D, G is approximately a Gaussian of the Doppler width. For the system described above, this takes the form

$$\begin{aligned}\rho_{F_gm,F_gm'}^{(depop)} \propto & \sum_{F_em''} \langle F_gm|\hat{\boldsymbol{\varepsilon}}^* \cdot \mathbf{d}|F_em''\rangle \\ & \times \langle F_em''|\hat{\boldsymbol{\varepsilon}} \cdot \mathbf{d}|F_gm'\rangle \, G(\omega - \omega_{F_eF_g}).\end{aligned} \tag{9.2}$$

Now suppose that the light frequency is tuned so that it is close, compared with the Doppler width, to an unresolved group of transition frequencies, and far from every other transition frequency (Fig. 9.1). We employ the simplest approximation that $G(\omega - \omega_{F_eF_g})$ takes the same value for each transition in the unresolved group, and is zero for all other transitions. With these approximations, Eq. (9.2) becomes

$$\rho_{F_gm,F_gm'}^{(depop)} \propto \sum_{F_em''} \langle F_gm|\hat{\boldsymbol{\varepsilon}}^* \cdot \mathbf{d}|F_em''\rangle\langle F_em''|\hat{\boldsymbol{\varepsilon}} \cdot \mathbf{d}|F_gm'\rangle, \tag{9.3}$$

where the sum now runs over only those excited states F_e that connect via one of the unresolved resonant transitions to the ground state F_g in question.

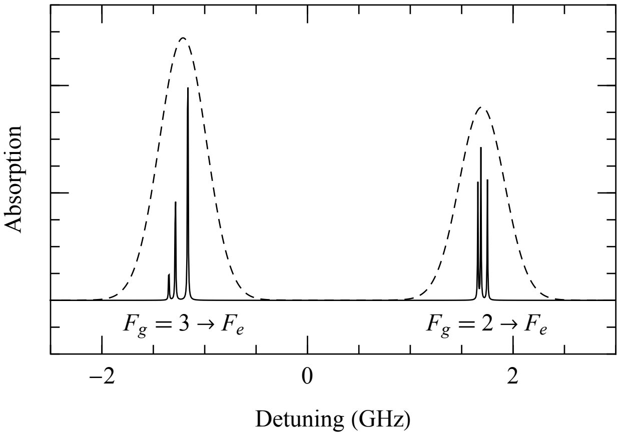

Figure 9.1: Doppler-free (solid line) and Doppler-broadened (dashed line) absorption spectra for the ^{85}Rb D_2 line. A Maxwellian velocity distribution at room temperature is assumed. If the incident light frequency is tuned near the center of the $F_g = 2 \to F_e$ transition group, the condition discussed in the text is fulfilled. Namely, the light detuning from each resonance frequency is either much less than or much greater than the Doppler width. The condition holds somewhat less rigorously for light tuned to the center of the $F_g = 3 \to F_e$ transition group.

We now investigate which coherences can be created in the ground state by the light. As we will see, this will determine which polarization moments can be created. Suppose first that the excited-state hfs is entirely unresolved. Then the sum over $|F_e m''\rangle\langle F_e m''|$ in Eq. (9.3) runs over all excited states, so that it is equivalent to the identity. We replace this sum with the sum over the eigenstates in the uncoupled basis $\sum_{m_I'' m_J''} |I m_I'' J_e m_J''\rangle\langle I m_I'' J_e m_J''|$. Further, we insert additional sums to expand the ground-state coupled-basis eigenstates in terms of the uncoupled basis. We also expand $\hat{\boldsymbol{\varepsilon}}$ and $\mathbf{d}$ in terms of their spherical components. Equation (9.3) becomes

$$\begin{aligned} \rho^{(depop)}_{F_g m, F_g m'} &\propto \sum (-1)^{q'+q''} (\varepsilon^*)_{q'} \varepsilon_{q''} \langle F_g m | I m_I J_g m_J\rangle \langle I m_I J_g m_J | d_{-q'} | I m_I'' J_e m_J''\rangle \\ &\quad \times \langle I m_I'' J_e m_J'' | d_{-q''} | I m_I' J_g m_J'\rangle \langle I m_I' J_g m_J' | F_g m'\rangle \\ &= \sum (-1)^{q'+q''} (\varepsilon^*)_{q'} \varepsilon_{q''} \langle F_g m | I m_I J_g m_J\rangle \langle J_g m_J | d_{-q'} | J_e m_J''\rangle \\ &\quad \times \langle J_e m_J'' | d_{-q''} | J_g m_J'\rangle \langle I m_I J_g m_J' | F_g m'\rangle, \end{aligned} \tag{9.4}$$

where the inner products $\langle \cdots | \cdots \rangle$ are given by the Clebsch–Gordan coefficients, with

$$\langle J_3 m_3 | J_1 m_1 J_2 m_2\rangle = \langle J_1 m_1 J_2 m_2 | J_3 m_3\rangle. \tag{9.5}$$

In the second line of Eq. (9.4) we have used the fact that the electric-dipole operator is diagonal in the nuclear-spin states.

We now use the Clebsch–Gordan condition $m_1 + m_2 = m_3$, as well as the related electric-dipole selection rule

$$\langle J_1 m_1 | d_q | J_2 m_2\rangle = 0 \text{ unless } m_1 = m_2 + q, \tag{9.6}$$

to determine which coherences $\rho^{(depop)}_{F_g m, F_g m'}$ can be nonzero in Eq. (9.4). Traversing the factors in the last line of Eq. (9.4) from left to right, we find that a term in the sum is zero unless

$$\begin{aligned} m = m_I + m_J,\ m''_J = m_J + q', \\ m'_J = m''_J + q'',\ m' = m_I + m'_J. \end{aligned} \tag{9.7}$$

From this we find that

$$|m' - m| = |q' + q''| \leq 2. \tag{9.8}$$

We can translate a limit on $|\Delta m|$ directly into a limit on the rank κ of PMs that can be created as follows. The PMs are the coefficients of the expansion of the density matrix into a sum of irreducible tensor operators (a set of operators with the rotational symmetries of the spherical harmonics). A PM of rank κ has $2\kappa + 1$ components with projections $q = -\kappa, \ldots, \kappa$, which are related to the Zeeman-basis density-matrix elements by (Eq. 2.34)

$$\rho^\kappa_q = \sum_{mm'} (-1)^{F-m'} \langle FmF, -m'|\kappa q\rangle \rho_{m'm}, \tag{9.9}$$

From Eq. (9.9), a ground-state PM ρ^κ_q with a given value of $|q|$ can exist if and only if there is a $|\Delta m| = |q|$ coherence in the ground-state density matrix. A limit on $|q|$ is not by itself a limit on κ, because any PM with rank $\kappa \geq |q|$ can have a component with projection q. However, if such a high-rank moment exists, we can always find a rotated basis such that the component with projection q in the original basis manifests itself as a component with projection κ in the rotated basis. Because Eq. (9.4) holds for arbitrary light polarization, it holds in the rotated basis, so we can conclude that no PM ρ^κ_q with rank κ greater than the limit on $|\Delta m|$ can be created, regardless of the value of q.

For the case under consideration, this analysis reveals that only PMs with $\kappa \leq 2$ are present. This is a consequence of the fact that we are considering the lowest-order contribution to optical pumping (namely, second order in the incident light field), so that multi-photon effects are not taken into account. A single photon is a spin-one particle, so it can support PMs up to $\kappa_\gamma = 2$. For a PM (PM) of rank κ to be created, the unpolarized (rank 0) density matrix must be coupled to a rank-κ PM by the rank $\kappa_\gamma \leq 2$ photon. The triangle condition for tensor products implies that $\kappa \leq \kappa_\gamma + 0 \leq 2$.

An additional condition on $|\Delta m|$ can be found from Eq. (9.7), using the fact that m_J and m'_J are projections of the ground-state electronic angular momentum, so that their absolute values are less than or equal to J_g. From the first and last conditions of Eq. (9.7) we find

$$|m' - m| = |m'_J - m_J| \leq 2J_g. \tag{9.10}$$

Thus the coherences that can be created within a ground-state hyperfine level F_g are limited to twice the ground-state electronic angular momentum J_g, even if $F_g > J_g$. As a consequence, PMs in the ground state are limited to rank $\kappa \leq 2J_g$. We can understand this restriction by examining Eq. (9.4). Because the excited-state hyperfine shifts have been eliminated from the expression and the electric-dipole operator does not act on the nuclear spin space, all traces of the hyperfine interaction in the excited state have been removed from Eq. (9.4). This is indicated by the fact that, in the last line of the equation, the nuclear spin does not appear in the state vectors describing excited states. Thus the excited state only couples to the electronic spin of the ground state, so that there is no mechanism for coupling two ground-state nuclear spin states. This means that any PM present in the ground state must be supported by the electronic spin only.

Considering now the case in which the excited-state hfs is resolved and the ground-state hfs is unresolved, opposite to the case considered so far, we find no similar restriction. It is clear from Eq. (9.3) that the polarization produced in a ground-state hyperfine level is independent of all of the other ground-state levels—only one ground-state level F_g appears in the equation. If the excited-state hfs is resolved, then likewise only one excited-state level F_e appears. Thus pumping on a transition $F_g \to F_e$ produces the same polarization in the level F_g as pumping on a completely isolated $F_g \to F_e$ transition, regardless of any nearby (unresolved) ground-state hyperfine levels. Any PM up to rank $\kappa = 2F_g$ can be produced, subject to the restriction $\kappa \leq 2$ in the lowest-order approximation.

In fact, these results can be obtained without the need for any calculations. It is clear that if all the hyperfine splittings are set to zero, the nuclear spin is effectively noninteracting, and can be ignored. In this case, only PMs that can be supported by the electronic spin J_g can be produced in the ground state. In particular, if we consider polarization of a given (degenerate) ground-state hyperfine level, we must have $\kappa \leq 2J_g$. If the ground-state hyperfine splitting is increased, this conclusion must remain unchanged, because the light only couples the ground states to the excited states; to lowest order it does not make any difference what is going on in the other ground-state hyperfine levels. If the excited-state hyperfine splitting is then increased, the various $F_g \to F_e$ hyperfine transitions become isolated; for an isolated transition the limit on the ground-state PMs is $\kappa \leq 2F_g$. Thus we see that the limit $\kappa \leq 2J_g$ on the ground-state PMs occurs when the excited-state hfs is unresolved, and this limit does not depend on whether or not the ground-state hfs is resolved.

The total angular momentum F_g can be significantly larger than J_g. For example, Cs has $I = 7/2$ and $J_g = 1/2$, so that the maximum value of F_g is 4. Thus PMs up to rank eight can be produced in the ground state by depopulation pumping if the

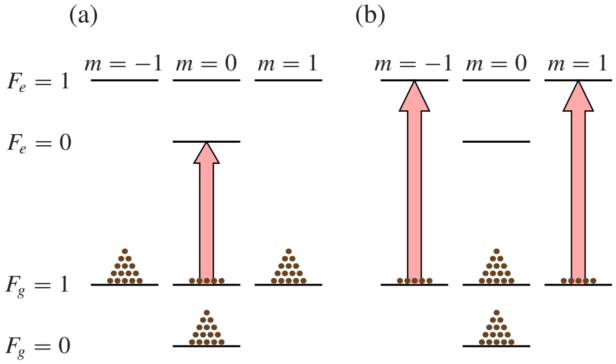

Figure 9.2: Excitation with z-polarized light on the (a) $1 \to 0$ and (b) $1 \to 1$ transitions of a totally resolved $J_g = 1/2 \to J_e = 1/2$ transition with $I = 1/2$. Alignment is produced in the $F_g = 1$ hyperfine level in both cases. Relative atomic populations are indicated by the number of dots displayed above each ground-state level. Relative transition strengths are indicated by the widths of the arrows—here the transition strengths are all the same.

excited-state hfs is resolved, but only up to rank one if it is unresolved. To second order in the light field the ground-state polarization that can be created is limited to at most rank two in any case. However, the question of whether rank-two polarization can be created is an important one: ground-state alignment is crucial for nonlinear magneto-optical effects with linearly polarized light, as we discuss in Chapter 10.

This situation is illustrated for linearly polarized light resonant with an alkali D_1 line ($J_g = J_e = 1/2$) in Figs. 9.2 and 9.3. We choose $I = 1/2$ for simplicity, and the quantization axis is taken along the direction of the light polarization. In Fig. 9.2 the hfs is completely resolved. Part (a) of the figure shows light resonant with the $F_g = 1 \to F_e = 0$ transition. Atoms are pumped out of the $|F_g = 1, m = 0\rangle$ sublevel, producing alignment in the $F_g = 1$ state. (Linearly polarized light in the absence of other fields can only produce even-rank moments, and an $F = 1$ state can only support PMs up to rank two; therefore, the anisotropy shown in Fig. 9.2 must correspond to alignment.)

If light is resonant with the $F_g = 1 \to F_e = 1$ transition, as in part (b), the $m = \pm 1$ sublevels of the $F_g = 1$ state are depleted, producing alignment with sign opposite to that in Fig. 9.2(a). This can be contrasted with

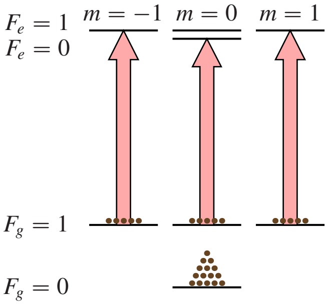

Figure 9.3: As in Fig. 9.2 but with excited-state hfs unresolved; light is resonant with the $F_g = 1 \to F_e$ transition group. No alignment is produced in the $F_g = 1$ ground state.

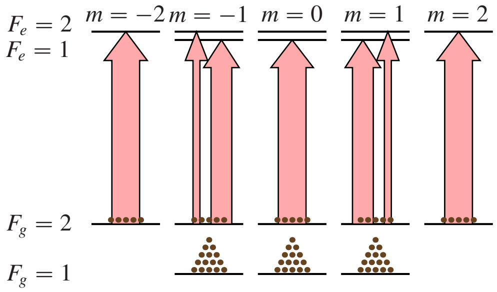

Figure 9.4: Excitation with z-polarized light on the $F_g = 2 \to F_e$ transition group of a D_1 transition with unresolved excited-state hfs. The nuclear spin is $I = 3/2$. No alignment is produced in the $F_g = 2$ hyperfine level. The width of each arrow represents the relative transition strength, which can be obtained from terms of the sum in Eq. (9.3).

the case in which the excited-state hyperfine structure is completely unresolved, shown in Fig. 9.3. Here, all the Zeeman sublevels of the $F_g = 1$ state are pumped out equally—the $|F_g = 1, m = 0\rangle$ sublevel on the $F_g = 1 \to F_e = 0$ transition, and the $|F_g = 1, m = \pm 1\rangle$ sublevels on the $F_g = 1 \to F_e = 1$ transition. [The relative pumping rates, which can be found from terms of the sum in Eq. (9.3), are all the same.] Thus no imbalance is created in the $F_g = 1$ sublevel populations, and no polarization is created in this state.

The same principle is illustrated for nuclear spin $I = 3/2$ in Fig. 9.4. The excited-state hfs is unresolved, and light is resonant with the $F_g = 2 \to F_e$ transitions. In this case, the $m = \pm 1$ ground-state sublevels are pumped on two different transitions. The total transition strength connecting each $F_g = 2$ sublevel to the excited state is the same, and so no polarization is produced in the $F_g = 2$ state.

The conclusions of this section must be modified when polarization produced in the ground state by spontaneous emission from the excited state is taken into account. We now consider the effect of this mechanism on the ground-state polarization (Sec. 9.2).

9.2 Excited state and repopulation pumping

Through second order in the incident light field (first order in light intensity), there is one additional contribution to the ground-state polarization besides the one considered in Sec. 9.1: that due to atoms being pumped to the excited state and then returning to the ground state via spontaneous emission (repopulation pumping). We first consider polarization produced in the excited state. The general form of the excited-state density matrix is (Happer, 1972)

$$\rho_{rs} \propto \sum_k \hat{\boldsymbol{\varepsilon}} \cdot \mathbf{d}_{rk} \hat{\boldsymbol{\varepsilon}}^* \cdot \mathbf{d}_{ks} G'(\omega - \omega_{rk}), \tag{9.11}$$

where r and s are excited states and k is a ground state. Unlike the ground-state polarization, that of the excited state generally decays before it can be mixed by collisions. Thus, the lineshape function $G'(\omega - \omega_{rk})$ in this case describes a feature with a width equal to the (possibly power-broadened) natural width of the transition. Comparing this expression to the formula for ground-state depopulation pumping (Eq. 9.1), we find that, as one would expect, the roles of the ground-state and excited state have been reversed. This means that the results of Sec. 9.1, with F_g and F_e interchanged, can be applied to the excited-state polarization. In this case, there is a limit $\kappa \leq 2J_e$ on the PMs that can be produced in the excited state, that occurs only when the *ground state* hfs is unresolved. The restriction does not depend on whether or not the excited-state hfs is resolved. There is the additional limit $\kappa \leq 2$ for low light power.

When the polarized atoms in the exited state decay due to spontaneous emission, the polarization can be transferred to the ground state. This contribution to the ground-state density matrix is given by (Eq. 5.24)

$$\rho_{mn}^{(repop)} \propto \sum_{sr} \mathbf{d}_{mr} \cdot \mathbf{d}_{sn} \rho_{rs}, \tag{9.12}$$

with ρ_{rs} as given above. (Note that after the atomic polarization is transferred to the ground state, it is averaged over velocity groups by collisions, so that the lineshape again has the Doppler width.) The fact that this formula has no reference to individual transition frequencies leads us to expect that the polarization transfer should be independent of the hyperfine splittings. Indeed, writing this expression out for the case under consideration gives

$$\begin{aligned} \rho_{F_g m, F_g m'}^{(repop)} \propto \sum (-1)^p \langle F_g m | d_p | F_e m'' \rangle \langle F_e m'' | \rho | F_e m''' \rangle \\ \times \langle F_e m''' | d_{-p} | F_g m' \rangle, \end{aligned} \tag{9.13}$$

and the only restriction to be obtained is $m' - m = m''' - m''$ (excited-state Δm equals ground-state Δm), while transforming to the uncoupled basis does not result in any additional limits. In other words, if the PM can be supported in the ground state, it can be transferred from the excited state via spontaneous emission.

Combining these results, we see that there is a similar restriction on polarization created in the ground state by repopulation pumping as the one on polarization created by depopulation pumping. However, the restriction occurs in the opposite case. When the ground state is unresolved the polarization produced by repopulation pumping must have $\kappa \leq 2J_e$. This limit does not depend on whether the excited-state hfs is resolved.

We now illustrate the foregoing for a system with $J_g = J_e = I = 1/2$ pumped with linearly polarized light. In Fig. 9.5 both the ground- and excited-state hfs is

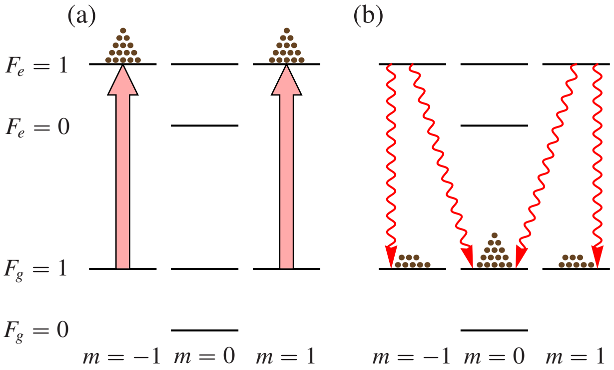

Figure 9.5: Level diagram for an D_1 transition with resolved hfs for an atom with $I = 1/2$ showing (a) optical excitation and (b) spontaneous decay with linearly polarized light resonant with the $F_g = 1 \to F_e = 1$ transition. The branching ratio for each allowed decay is the same, leading to an excess of atoms in the $|F_g = 1, m = 0\rangle$ sublevels over the populations of the $|F_g = 1, m = \pm 1\rangle$ sublevels by a ratio of 2:1.

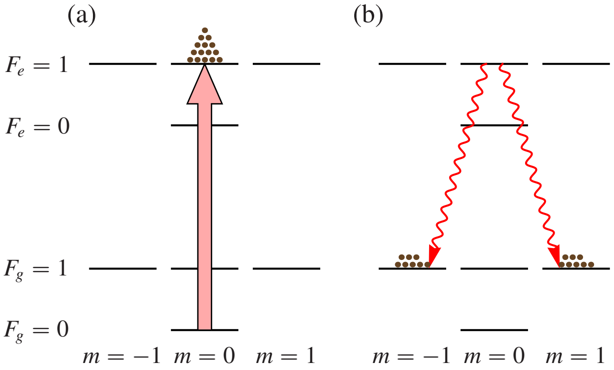

Figure 9.6: As in Fig. 9.5, but with light tuned to the $F_g = 0 \to F_e = 1$ transition. In this case an excess of atoms results in the $m = \pm 1$ states, so that the polarization has the opposite sign to that in Fig. 9.5.

resolved, and light is tuned to the $F_g = 1 \to F_e = 1$ transition. In part (a) of the figure, the pump light produces polarization in the $F_e = 1$ excited state. In part (b) the excited atoms spontaneously decay. This creates polarization in the $F_g = 1$ ground state, because more atoms are transferred to the $|F_g = 1, m = 0\rangle$ sublevel than to the $|F_g = 1, m = \pm 1\rangle$ sublevels. (In this and the following two figures, we do not show the atoms that decay to the $F_g = 0$ state.) Figure 9.6 is the same but with light tuned to the $F_g = 0 \to F_e = 1$ transition; polarization is also created in the $F_g = 1$ ground state in this case.

In Fig. 9.7 the ground-state hfs is now unresolved, while the excited-state hfs remains resolved. In this case, both ground-state hyperfine levels are pumped by the light, and equal populations are produced in the sublevels of the $F_e = 1$ state, as shown in part (a) of the figure. As seen in part (b), the excited-state atoms spontaneously decay in equal numbers to the $F_g = 1$ sublevels, so that no polarization is produced in the $F_g = 1$ state.

Note that in the opposite case, with unresolved excited-state hfs and resolved ground-state hfs, spontaneous decay is not prevented from producing polarization in the $F_g = 1$ ground state. In this case, atoms are pumped into the $F_e = 0$ state, as well

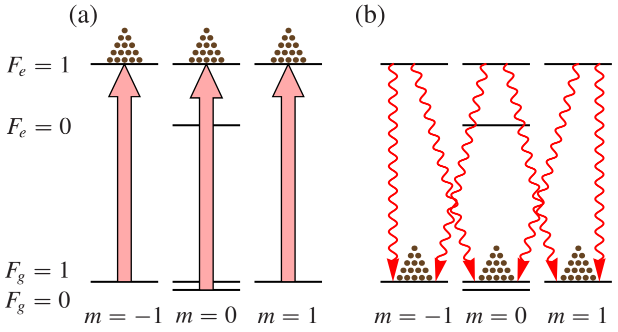

Figure 9.7: As in Fig. 9.5 but with unresolved ground-state hfs; light is tuned to the $F_g \to F_e = 1$ transition group. The contributions to the ground-state polarization illustrated in Figs. 9.5 and 9.6 cancel, so that no ground-state polarization is produced.

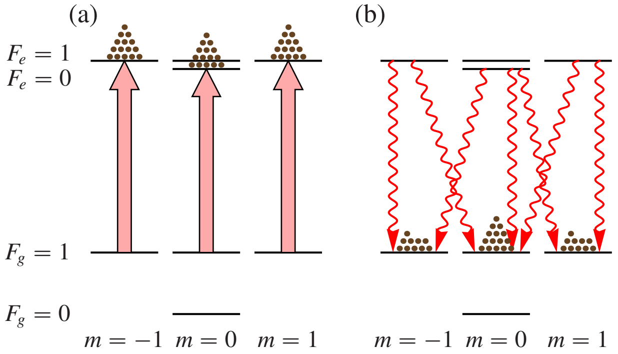

Figure 9.8: As in Fig. 9.5 but with unresolved excited-state hfs; light is tuned to the $F_g = 1 \to F_e$ transition group. Three decay channels transfer atoms to the $|F_g = 1, m = 0\rangle$ sublevel, while the $|F_g = 1, m = \pm 1\rangle$ sublevels are each fed by two decay channels. Since all the branching ratios are the same, the resulting population imbalance is 3:2.

as the $F_e = 1$ state, as shown in Fig. 9.8(a). Since the $|F_e = 0, m = 0\rangle$ state decays isotropically, the decay from this state does not cancel out the polarization created by decay from the $F_g = 1$ state (Fig. 9.8b). Thus we see that it is the ground-state hfs, and not the excited-state hfs, that needs to be resolved in order for polarization to be produced in the ground state due to spontaneous decay.

To summarize the results obtained so far, to lowest order in the excitation light, polarization can be either produced in the ground state directly through absorption, or transferred to the ground state by spontaneous emission. To this order, PMs due to both of these mechanisms must have rank $\kappa \le 2$. In addition, if the excited-state hfs is unresolved, there is a limit $\kappa \le 2J_g$ on the ground-state polarization due to depopulation, but no additional limit on the polarization due to repopulation. On the other hand, if the ground-state hfs is unresolved, there is a limit $\kappa \le 2J_e$ on the ground-state polarization due to repopulation, but no additional limit on polarization due to depopulation. Thus, unless both the excited-state and ground-state hyperfine structure is unresolved, one or the other of the mechanisms is capable of producing polarization of all ranks $\kappa \le 2$.

9.3 Absorption

The absorption $\mathcal{A}$ of a weak probe light beam is given in terms of the ground-state density matrix by (Eq. 5.45)

$$\mathcal{A} \propto \sum_{mnr} \hat{\boldsymbol{\varepsilon}} \cdot \mathbf{d}_{rm} \rho_{mn} \hat{\boldsymbol{\varepsilon}}^* \cdot \mathbf{d}_{nr} G(\omega - \omega_{rm}), \tag{9.14}$$

or

$$\mathcal{A} \propto \sum \langle F_e m | \hat{\boldsymbol{\varepsilon}} \cdot \mathbf{d} | F_g m' \rangle \langle F_g m' | \rho | F_g m'' \rangle \langle F_g m'' | \mathbf{d} \cdot \hat{\boldsymbol{\varepsilon}}^* | F_e m \rangle G(\omega - \omega_{F_e F_g}), \tag{9.15}$$

where all quantities are as defined above. Using the approximation, as in Secs. 9.1 and 9.2, that the light is resonant with an unresolved transition group and far detuned from all other transitions, this formula reduces to

$$\mathcal{A} \propto \sum \langle F_e m | \hat{\boldsymbol{\varepsilon}} \cdot \mathbf{d} | F_g m' \rangle \langle F_g m' | \rho | F_g m'' \rangle \langle F_g m'' | \mathbf{d} \cdot \hat{\boldsymbol{\varepsilon}}^* | F_e m \rangle, \tag{9.16}$$

where the sum over F_g and F_e includes only those combinations that are in the unresolved resonant transition group.

We now investigate the dependence of the absorption on the ground-state polarization in various cases. Consider the case in which the ground-state hfs is completely resolved, and the excited-state structure is unresolved. The light is tuned to an unresolved transition group consisting of transitions between one ground-state hyperfine level F_g and all of the excited-state levels. The sum in Eq. (9.16) over the excited states is then a closure relation, and can be replaced with a sum over any complete basis for the excited state, in particular, the uncoupled basis. We also insert closure relations to expand the ground states $\langle F_g m'' |$ and $| F_g m' \rangle$ in the uncoupled basis. We obtain

$$\begin{aligned} \mathcal{A} \propto & \sum (-1)^{q'+q''} \varepsilon_{q'} (\varepsilon^*)_{q''} \langle I m_I J_e m_J | d_{-q'} | I m'_I J_g m'_J \rangle \langle I m'_I J_g m'_J | F_g m' \rangle \\ & \qquad \times \langle F_g m' | \rho | F_g m'' \rangle \langle F_g m'' | I m''_I J_g m''_J \rangle \langle I m''_I J_g m''_J | d_{-q''} | I m_I J_e m_J \rangle \\ = & \sum (-1)^{q'+q''} \varepsilon_{q'} (\varepsilon^*)_{q''} \langle J_e m_J | d_{-q'} | J_g m'_J \rangle \langle I m_I J_g m'_J | F_g m' \rangle \langle F_g m' | \rho | F_g m'' \rangle \\ & \qquad \times \langle F_g m'' | I m_I J_g m''_J \rangle \langle J_g m''_J | d_{-q''} | J_e m_J \rangle, \end{aligned} \tag{9.17}$$

where only one nuclear-spin summation variable remains in the last line. The dipole matrix element selection rules and Clebsch–Gordan conditions require that

$$\begin{aligned} m' &= m_I + m'_J, \;\; m'_J = m_J + q', \\ m'' &= m_I + m''_J, \;\; m_J = m''_J + q'' \end{aligned} \tag{9.18}$$

must be satisfied in order for a term in the sum to contribute to the absorption. These conditions can be combined to yield $|m' - m''| = |q' + q''| \leq 2$. Thus only coherences with $|\Delta m| \leq 2$ (and PMs with $\kappa \leq 2$) can affect the lowest-order absorption signal. The reason for this is analogous to the reason that PMs of maximum rank two can be created with a lowest-order interaction with the light. As discussed in Chapter 5, absorption occurs when an atom is transferred to the excited state, i.e., when population (rank zero polarization) is created in the excited state. Thus, to be observed in the signal, a ground-state atomic PM must be coupled to a $\kappa = 0$ excited-state PM by a spin-one photon, which can support PMs up to rank two. The triangle condition for tensor products then implies that the rank of the atomic PM must be no greater than two.

Another restriction on the coherences that can affect absorption can be found from Eq. (9.18) by using the fact that $|m'_J| \leq J_g$ and $|m''_J| \leq J_g$. We find

$$|m' - m''| = \left|m'_J - m''_J\right| \leq 2J_g. \tag{9.19}$$

In other words, only PMs with $\kappa \leq 2J_g$ can affect the absorption signal, regardless of the value of F_g. Evidently, it is the excited-state hfs that determines which ground-state PMs can be detected in absorption, whether or not the ground-state hfs is resolved.

Considering the case in which both the excited- and ground-state hfs is entirely unresolved can lend some insight into this result. In this case, every combination of F_g and F_e enters in the sum in Eq. (9.16). If the ground-state hyperfine splitting is sent to zero, the sum must be extended to include matrix elements of ρ between different hyperfine levels. This means that all of the sums in Eq. (9.16) can be replaced with sums over uncoupled basis states, giving

$$\begin{aligned}\mathcal{A} \propto &\sum (-1)^{q'+q''} \varepsilon_{q'} (\varepsilon^*)_{q''} \langle I m_I J_e m_J | d_{-q'} | I m'_I J_g m'_J \rangle \\ &\qquad\qquad \times \langle I m'_I J_g m'_J | \rho | I m''_I J_g m''_J \rangle \langle I m''_I J_g m''_J | d_{-q''} | I m_I J_e m_J \rangle \\ = &\sum (-1)^{q'+q''} \varepsilon_{q'} (\varepsilon^*)_{q''} \langle J_e m_J | d_{-q'} | J_g m'_J \rangle \langle I m_I J_g m'_J | \rho | I m_I J_g m''_J \rangle \\ &\qquad\qquad \times \langle J_g m''_J | d_{-q''} | J_e m_J \rangle.\end{aligned} \tag{9.20}$$

Since the hyperfine interaction has been effectively eliminated, the absorption no longer depends on the nuclear spin: the complete density matrix does not enter, but rather the reduced density matrix

$$\rho^{(J)}_{m'_J m''_J} = \sum_{m_I} \rho_{m_I m'_J, m_I m''_J} \tag{9.21}$$

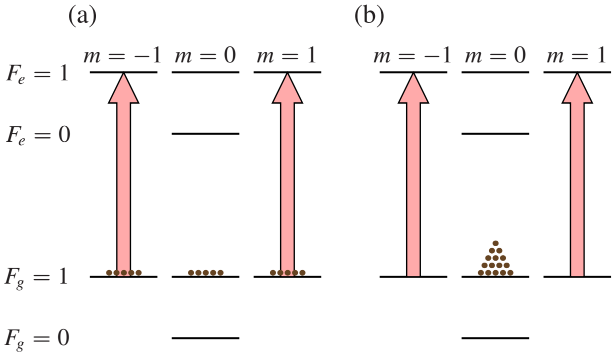

Figure 9.9: D_1 transition for an atom with $I = 1/2$ subject to linearly polarized light resonant with the $F_g = 1 \to F_e = 1$ transition. In part (a) the $F_g = 1$ ground state is unpolarized and there is light absorption. In part (b) the $F_g = 1$ state has the same total population, but is aligned, and there is no absorption.

that is averaged over the nuclear spin m_I. The reduced density matrix can only support PMs up to rank $\kappa = 2J_g$, so any PM in ρ with higher rank cannot affect the absorption. Considering a density matrix that is nonzero only within one ground-state hyperfine level F_g, we see that PMs with rank greater than two will not contribute to the signal. Since the other ground-state hyperfine levels are unoccupied, it makes no difference what the ground-state hyperfine splitting is, so we regain the result that, even if the ground-state hfs is resolved, only PMs with $\kappa \leq 2J_g$ can affect the absorption of light if the excited-state hfs is unresolved.

There is no corresponding restriction on the PMs that can affect absorption when the ground-state hfs is unresolved and the excited-state hfs is resolved. Indeed, we can consider the case in which only one ground-state hyperfine level F_g is populated: the absorption is then exactly as if the transition $F_g \to F_e$ were completely isolated. For such an isolated transition, the only limit on detectable PMs is $\kappa \leq 2$ for the low-power case.

As in the previous subsections, we illustrate this result for a D_1 transition for an atom with $I = 1/2$ subject to linearly polarized light. In Fig. 9.9 both the ground- and excited-state hfs is resolved, and the light is resonant with the $F_g = 1 \to F_e = 1$ transition. In part (a) there is no polarization in the $F_g = 1$ ground state: atoms are equally distributed among the Zeeman sublevels. Light is absorbed by atoms in the $|F_g = 1, m = \pm 1\rangle$ sublevels. In part (b) there are the same total number of atoms in the $F_g = 1$ state, but they are collected in the $m = 0$ sublevel. The population is the same, but the $F_g = 1$ state now also has alignment. In this particular case there is no absorption, because the atoms are all in the $m = 0$ dark state. Thus, in this

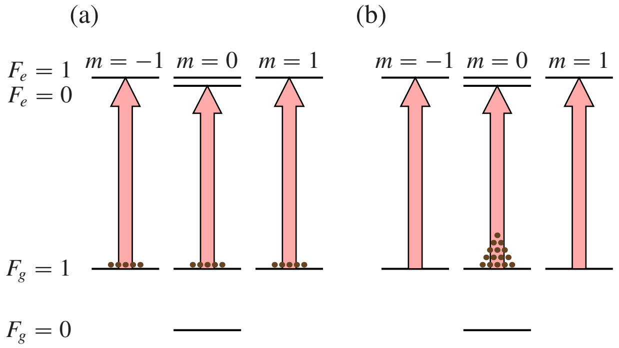

Figure 9.10: As in Fig. 9.9, but with unresolved excited-state hfs. In this case there is no difference in the absorption seen for an (a) unpolarized and (b) aligned $F_g = 1$ ground state.

situation, the rank-two PM has a strong effect on the absorption signal.

Figure 9.10 shows the same system, but with unresolved excited-state hfs. In this case there is no dark state; all of the atoms interact with the light. The distribution of the atoms among the Zeeman sublevels does not affect the light absorption, and so the rank-two PM is not detectable in the absorption signal.

9.4 Fluorescence

Finally, we consider which excited-state PMs can be observed in fluorescence. Assuming broad-band detection, the intensity of fluorescence into a particular polarization $\hat{\boldsymbol{\varepsilon}}$ is given in terms of the excited-state density matrix by (Eq. 3.21)

$$\mathcal{I} \propto \sum_{rsm} \hat{\boldsymbol{\varepsilon}}^* \cdot \mathbf{d}_{mr} \rho_{rs} \hat{\boldsymbol{\varepsilon}} \cdot \mathbf{d}_{sm}. \tag{9.22}$$

Because the sums in r and s go over all excited states, and m runs over all ground states, we can write Eq. (9.22) for our case in terms of the uncoupled-basis states. This gives

$$\begin{aligned} \mathcal{I} \propto \sum (-1)^{q'+q''} (\varepsilon^*)_{q'} \varepsilon_{q''} &\langle I m_I J_g m_J | d_{-q'} | I m_I' J_e m_J' \rangle \\ &\times \langle I m_I' J_e m_J' | \rho | I m_I'' J_e m_J'' \rangle \langle I m_I'' J_e m_J'' | d_{-q''} | I m_I J_g m_J \rangle, \end{aligned} \tag{9.23}$$

resulting in the restrictions

$$m_J'' = -q'' + m_J,\ m_J = -q' + m_J',\ m_I = m_I' = m_I'', \tag{9.24}$$

on the terms that can contribute to the fluorescence. This indicates that the nuclear polarization cannot affect the fluorescence signal, and so only the electronic excited-state polarization of rank $\kappa \leq 2J_e$ can be observed. In addition, only coherences

Table 9.1: Summary of the results of this chapter. For each quantity, the restriction on the rank κ of the polarization that can be created or detected is given in the fourth column. The restriction holds when the ground- or excited-state hfs, as given in the second column, is unresolved with respect to the width given in the third column. For fluorescence with broad-band detection the restriction holds regardless of whether the hfs is resolved.

	unresolved	w.r.t.	maximum κ
Ground-state pol. (depop.)	excited hfs	Doppler	$2J_g$
Ground-state pol. (repop.)	ground hfs	Doppler	$2J_e$
Excited-state pol.	ground hfs	Doppler-free	$2J_e$
Absorption	excited hfs	Doppler	$2J_g$
Fluorescence	—	—	$2J_e$

with $|m''_J - m'_J| = |q' + q''| \leq 2$ can be observed. This rule has appeared earlier as a consequence of the low-light-power assumption; because spontaneous decay is not induced by an incident light field, in this case the rule is exact. This means that no matter the value of J_e, and what PMs exist in the excited state, only polarization of rank $\kappa \leq 2$ can be observed in fluorescence.

9.5 Comparison of different cases

In this chapter, we have shown that, when the ground- or excited-state hfs is unresolved, there are restrictions on the rank of the PMs that can be created or detected by light. Some of these restrictions may at first seem counter-intuitive, but they can be obtained from very basic considerations. For example, the two facts that nuclear spin can be ignored if the hfs is completely unresolved and that lowest-order depopulation pumping of a given hyperfine level does not depend on ground-state hyperfine splitting lead directly to the result that PMs produced by depopulation pumping are subject to a limit of $\kappa \leq 2J_g$ when the excited-state hfs is unresolved. Various processes of creation and detection of polarization are subject to different restrictions (Table 9.1).

In particular, the two processes that can create ground-state polarization, namely, depopulation and repopulation pumping, are subject to restrictions under different conditions. Consequently, unless the hfs is entirely unresolved, there is always a mechanism for producing polarization limited in rank only by the total angular momentum, rather than the electronic angular momentum.

Chapter 10

The Effect of Hyperfine Splitting on Nonlinear Magneto-optical Rotation

Now let us examine the more general case of *partially* resolved hyperfine transitions, also discussed by Auzinsh *et al.* (2009a). For this study, we will look at the quantitative dependence on hyperfine splitting of nonlinear optical rotation—rotation of light polarization due to interaction with a $J_g \rightarrow J_e$ transition group in the presence of a magnetic field. In this case, the effect of ground-state atomic polarization is brought into starker relief: in the experimental situation that we consider, both the creation and detection of ground-state polarization is required in order to see any signal whatsoever. When linearly polarized light is used, as is supposed here, the lowest-order effect depends on rank-two atomic alignment. Thus, for the alkali atoms, the question of the dependence of the effect on hyperfine structure arises, because, as discussed in the previous section, both the creation and the detection of alignment in the $J_g = 1/2$ ground state can be suppressed due to unresolved hfs. [In fact, a higher-order effect can occur wherein alignment is created, the alignment is converted to orientation, and the orientation is detected (Auzinsh and Ferber, 1992; Budker *et al.*, 2000a; Auzinsh *et al.*, 2006). However, the conversion of alignment to orientation is an effect of tensor AC-Stark shifts, which can be shown by arguments similar to those in Chapter 9 to suffer suppression due to unresolved hfs in the same way as does the direct detection of alignment.]

In the Faraday geometry, linearly polarized light propagates in the direction of an applied magnetic field, and the rotation of the light polarization direction is measured. As discussed by Budker *et al.* (2002a), a number of magneto-optical effects can contribute to the optical rotation, including the linear Faraday effect, the Bennett-structure effect, and various effects depending on atomic polarization ("coherence effects"). Here we are concerned with optical rotation due to several different forms of the ground-state coherence effect, in which the atomic velocities are treated in three different ways. First we consider the atoms to have no velocity spread, and analyze the Doppler-free "transit effect," as for an atomic beam with negligible transverse velocity distribution (Schuh *et al.*, 1993). We then consider the case in which atoms have a Maxwellian distribution, but do not change their velocities in between pumping and probing—this corresponds to the transit effect for buffer-gas-free, dilute atomic vapors (Kanorsky *et al.*, 1993). Finally, we treat the case in which atoms undergo velocity-changing collisions between pumping and probing, as for buffer-gas cells (Novikova *et al.*, 2001) or the wall-induced Ramsey effect ("wall effect") in antirelaxation-coated vapor cells (Kanorskii *et al.*, 1995). We examine the dependence of these effects on the size of the hyperfine splittings as they vary from much smaller than the natural width to much greater than the Doppler width.

Throughout this chapter we consider formulas for the optical rotation signal valid to lowest order in light power, under the assumption that the ground-state relaxation rate γ is much smaller than both the excited-state natural width Γ and the hyperfine splittings. For the Doppler-free case a single analytic formula can be applied to both resolved and unresolved hfs (i.e., no assumption need be made about the relative size of the hyperfine splittings and the natural width). For the Doppler-broadened cases, analytic results can be obtained in various limits, which together describe the signal over the entire range of hyperfine splittings.

We first focus on the simplest case: the D$_1$ line ($J_g = J_e = 1/2$) for an atom with $I = 1/2$. This is a somewhat special case, because one of the two ground-state hyperfine levels has $F_g = 0$, and consequently can neither support atomic alignment nor produce optical rotation. We then consider the differences that arise when considering higher nuclear spin and also the D$_2$ line ($J_g = 1/2$ and $J_e = 3/2$). Some details of the calculation and general formulas for arbitrary J_g, J_e, and I are presented in Appendix D. These formulas are generalizations of those first given by Kanorsky *et al.* (1993).

10.1 Doppler-free transit effect

We consider nonlinear Faraday rotation on a $J_g \rightarrow J_e$ atomic transition for an atom with nuclear spin I. We can limit our attention to the ground-state coherence effects by using a "three-stage" model for Faraday rotation (Kanorsky *et al.*, 1993), in which optical pumping, atomic precession, and optical probing take place sequentially, and the light and magnetic fields are never present at the same time. In this case, the linear and Bennett-structure effects, which require the simultaneous application of light and magnetic fields, do not occur. Such a model can be realized in an atomic-beam experiment, but it is also a good approximation to a vapor-cell experiment that uses low light power and small enough magnetic fields so that the coherence effects are dominant.

The calculation is performed using second-order perturbation theory in the basis of the PMs $\rho^{(\kappa q)}(F_1F_2)$ of the density matrix (Appendix D.1). The three stages of the calculation are as follows. In stage (a), an x-directed light beam linearly polarized along z is applied, and we calculate optical pumping through second order in the optical Rabi frequency. In stage (b), the light field is removed, and a x-directed magnetic field is applied. We calculate the effect of this field on the atomic polarization. Finally, in stage (c), the magnetic field is turned off, and the light field is applied once more to probe the atomic polarization. The nonlinear optical rotation is found to lowest order in the probe-light Rabi frequency (Appendix D.2).

Because the magnetic field is neglected during the optical pumping stage, the atomic ground-state polarization that is produced in this stage is entirely along the light polarization direction, i.e., it has polarization component $q = 0$. Since linearly polarized light has a preferred axis, but no preferred direction, it cannot, in the absence of other fields, produce atomic polarization with a preferred direction, i.e., polarization with odd rank κ. Also, we have seen in Chapter 9 that, to lowest order in the light power, optical pumping cannot produce PMs with $\kappa > 2$. Thus the only ground-state PM with rank greater than zero that is produced at lowest order has $\kappa = 2$ and $q = 0$. We first consider the D$_1$ line ($J_g = J_e = 1/2$) for an atom with $I = 1/2$. In this case, the only ground-state hyperfine level that can support the $\rho^{(20)}(F_gF_g)$ moment has $F_g = 1$. (Due to the assumption that the hyperfine splittings are much greater than the ground-state relaxation rate, we can ignore ground-state hyperfine coherences throughout the discussion.) From Eq. (D.12), the value of this moment is found to be

$$\rho^{(20)}(11) = \frac{\tilde{\kappa}_2}{12\sqrt{6}}\Big(\left[L(\omega'_{0,1}) - L(\omega'_{1,1})\right] + \frac{R}{3}\left[L(\omega'_{1,0}) - L(\omega'_{1,1})\right] \Big), \tag{10.1}$$

where $\tilde{\kappa}_2 = \langle J_g \| d \| J_e \rangle^2 \mathcal{E}_0^2/(\Gamma\gamma)$ is the reduced optical-pumping saturation parameter ($\mathcal{E}_0$ is the optical electric field amplitude), R is the branching ratio for the transition $J_e \to J_g$, and $\omega'_{F_eF_g}$ is the transition frequency between excited-state and ground-state hyperfine levels in the frame "rotating" at the Doppler-shifted light frequency ω: $\omega'_{F_eF_g} = \omega_{F_eF_g} - \omega + \mathbf{k}\cdot\mathbf{v}$, where $\omega_{F_eF_g}$ is the transition frequency in the lab frame,

ω is the light frequency, $\mathbf{k}$ is the wave vector, and $\mathbf{v}$ is the atomic velocity. We also write $\omega'_{F_eF_g} = -\Delta_{F_eF_g} + \mathbf{k}\cdot\mathbf{v}$, where $\Delta_{F_eF_g}$ is the light detuning from resonance. We have defined the Lorentzian line profile

$$L(\omega') = \frac{(\Gamma/2)^2}{(\Gamma/2)^2 + \omega'^2}. \tag{10.2}$$

Equation (10.1) is written as the sum of two terms, each surrounded by square brackets. The first term is the contribution to the polarization due to depopulation pumping discussed in Sec. 9.1. This term is itself a sum of contributions due to pumping on the $F_g = 1 \to F_e = 0$ transition and the $F_g = 1 \to F_e = 1$ transition. These two contributions are of opposite sign, as illustrated in Fig. 9.2. Pumping on either transition produces alignment in the $F_g = 1$ ground state; the sign of the corresponding PM depends on whether there is more population in the $m = 0$ sublevel or the $m = \pm 1$ sublevels. We saw in the discussion of Sec. 9.1 that when the excited-state hfs is unresolved, polarization with rank $\kappa > 2J_g$ cannot be created by depopulation pumping (Fig. 9.3). We see here that as $\omega_{0,1}$ approaches $\omega_{1,1}$, i.e., as the excited-state hyperfine splitting goes to zero, the contributions from the two transitions cancel and this term goes to zero. For the Doppler-broadened atomic ensemble discussed in Chapter 9, the hfs was considered unresolved when the hyperfine splittings were smaller than the Doppler width. Since Eq. (10.1) describes a single velocity group, the relevant width here is the natural width Γ.

The second term of Eq. (10.1) is the contribution to the ground-state polarization due to repopulation pumping discussed in Sec. 9.2. This term is also composed of two contributions of opposite sign: one due to pumping on the $F_g = 1 \to F_e = 1$ transition and one due to pumping on the $F_g = 0 \to F_e = 1$ transition. The two contributions are illustrated in Figs. 9.5 and 9.6, which show the origin of the opposite signs. In Sec. 9.2 we found that depopulation pumping cannot create PMs with rank $\kappa > 2J_e$ when the ground-state hfs is unresolved (Fig. 9.7). We see here that this term of Eq. (10.1) goes to zero when $\omega_{1,0}$ approaches $\omega_{1,1}$, i.e., as the ground-state hyperfine splitting goes to zero.

In the second and third stages of the model of the coherence effect, the ground-state polarization precesses in a magnetic field and is probed by light with the same polarization as the pump light considered in the first stage. From Eq. (D.19) we find that the normalized optical rotation $d\alpha$ per path length $d\ell$ is proportional to the polarization produced in the first stage and is given by

$$\ell_0 \frac{d\alpha}{d\ell} = \frac{1}{4}\sqrt{\frac{3}{2}} \left[L(\omega'_{0,1}) - L(\omega'_{1,1})\right] x_1 \rho^{(20)}(11), \tag{10.3}$$

where

$$x_{F_g} = \frac{(\gamma/2)\Omega_{F_g}}{(\gamma/2)^2 + \Omega_{F_g}^2} \tag{10.4}$$

is the magnetic-resonance lineshape parameter, with $\Omega_{F_g} = g_{F_g}\mu_B B$ the Larmor frequency for the ground-state hyperfine level F_g (g_{F_g} is the Landé factor for the ground state F_g, and μ_B is the Bohr magneton), and

$$\ell_0 = -\left(\frac{1}{\mathcal{I}}\frac{d\mathcal{I}}{d\ell}\right)^{-1} = \frac{2\pi}{Rn\lambda^2}\frac{(2J_g+1)}{(2J_e+1)} \tag{10.5}$$

is the unsaturated resonant absorption length assuming totally unresolved hyperfine structure, where $\mathcal{I}$ is the light intensity, n is the atomic density, and λ is the light wavelength. The branching ratio R enters here because it factors into the transition strength.

The contributions to the optical rotation signal from the $F_g = 1 \rightarrow F_e = 0$ transition and the $F_g = 1 \rightarrow F_e = 1$ transition have opposite signs. To understand this, it is helpful to think of the optically polarized medium as a polarizing filter (Kanorsky *et al.*, 1993). When pumping on a $1 \rightarrow 0$ or $1 \rightarrow 1$ transition, the medium is pumped into a dark (nonabsorbing) state for that transition (Fig. 9.2), corresponding to a polarizing filter with its transmission axis along the input light polarization axis $\hat{\boldsymbol{\varepsilon}}$ (Fig. 10.1a). The Larmor precession induced by the magnetic field causes the transmission axis of the filter to rotate, so that it is no longer along $\hat{\boldsymbol{\varepsilon}}$. This in turn causes the output light polarization axis $\hat{\boldsymbol{\varepsilon}}'$ to rotate. The polarization of light passing through a polarizing filter tends to rotate toward the transmission axis, so that in this case the optical rotation is in the same sense as the Larmor precession (Fig. 10.1b). Now, compare the polarization produced when pumping on a $1 \rightarrow 0$ or $1 \rightarrow 1$ transition, as shown in Fig. 9.2. We see that the dark state for each transition is a bright (absorbing) state for the other. This means that if we choose one or the other of these states, it will function as just described for one of the transitions, but will function as a polarizing filter with its transmission axis *perpendicular* to $\hat{\boldsymbol{\varepsilon}}$ for the other transition (Fig. 10.1c). When the axis of the filter rotates in this case, the fact that the output light polarization tends to rotate toward the transmission axis means that here the optical rotation is in the other direction, in the opposite sense to the Larmor precession (Fig. 10.1d). In other words, for a particular sign of the rank-two PM, the optical rotation will have one sign when probed on one transition, and the opposite sign when probed on the other, as indicated by Eq. (10.3). Because the observation of optical rotation requires the detection of rank-two PMs, we might expect, analogously to the discussion in Sec. 9.3, that it is suppressed when the

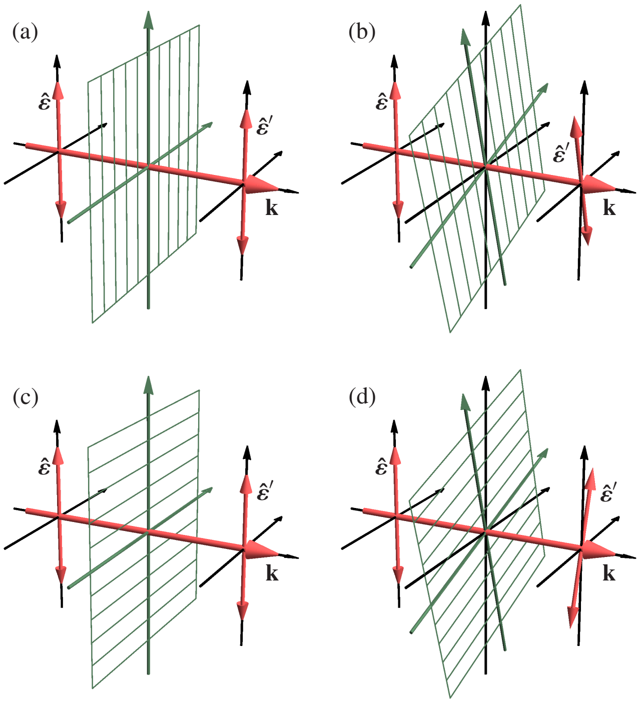

Figure 10.1: Illustration of the rotating polarizer model for optical rotation. (a) Optical pumping on a $F_g = 1 \to F_e = 0$ or $F_g = 1 \to F_e = 1$ transition causes the medium to act as a polarizing filter with transmission axis along the input light polarization $\hat{\varepsilon}$. (b) When the transmission axis rotates due to Larmor precession, the output light polarization $\hat{\varepsilon}'$ follows the transmission axis and so rotates in the same sense as the Larmor precession. (c) If polarization produced by pumping on one transition is probed on the other, the polarization functions as a polarizing filter with transmission axis *perpendicular* to the input light polarization. (Attenuation of the light beam is not indicated.) (d) When the medium polarization rotates, the output light polarization tends to rotate toward the transmission axis, in the opposite sense to the Larmor precession in this case.

excited-state hyperfine splitting goes to zero. Equation (10.3) shows that the two contributions indeed cancel when $\omega_{0,1}$ approaches $\omega_{1,1}$.

Equation (10.3) and the two components of Eq. (10.1) are plotted as a function of light detuning from the $F_g = 1 \to F_e = 1$ transition in Fig. 10.2, for particular values of the ground- and excited-state hyperfine coefficients A_g and A_e. (For $J = I = 1/2$, the hyperfine coefficient A is equal to the splitting between the two hyperfine levels.) Here and below numerical values of frequencies are given in units of Γ. As discussed above, each spectrum consists of two peaks of equal magnitude and opposite sign. For the spectrum of alignment due to depopulation and the spectrum of rotation for a given amount of alignment, the peaks are separated by the excited-state hyperfine splitting, so that they cancel as this splitting goes to zero. For the spectrum of alignment due to repopulation, the peaks are separated by the ground-state hyperfine splitting; they cancel as the ground-state splitting goes to zero.

In this section we are analyzing a Doppler-free system, i.e., we assume that the atoms all have the same velocity, which we take to be zero for simplicity. Then the observed optical rotation signal is found by simply substituting Eq. (10.1) into Eq. (10.3). We first consider the case in which the ground-state hfs is well resolved. The rotation signal is plotted in Fig. 10.3 for large ground-state hyperfine splitting and

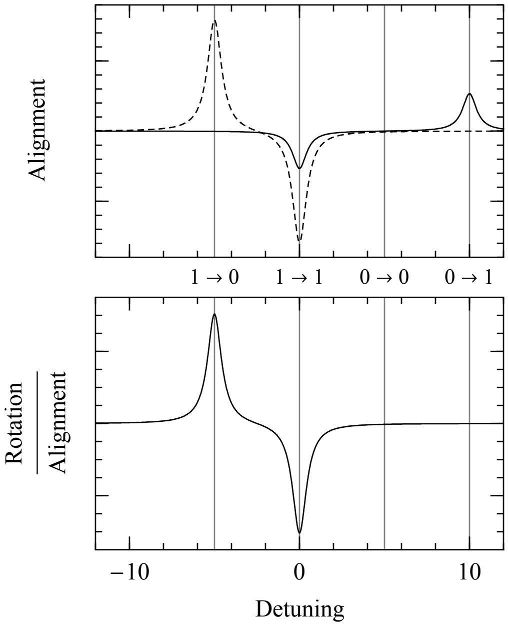

Figure 10.2: Dependence on light detuning from the $F_g = 1 \to F_e = 1$ transition of (top) the components of ground-state alignment due to depopulation (dashed) and repopulation (solid) (Eq. 10.1) and (bottom) optical rotation for a given amount of alignment (Eq. 10.3). Gray vertical lines show $F_g \to F_e$ transition resonance frequencies. Parameter values in units of Γ are $\gamma \ll 1$, $A_g = 10$, $A_e = 5$.

various excited-state splittings A_e. The components of the rotation signal due to depopulation (dashed) and repopulation (solid) are plotted in the left-hand column, and the total signal is plotted on the right. As the previous discussion indicates, the rotation signal decreases as the excited-state hyperfine splitting A_e becomes smaller, with the component due to depopulation decreasing faster than the component due to repopulation. This is also seen in Fig. 10.4, which shows the maximum magnitude of the rotation spectrum as a function of A_e (for each value of A_e, the signal is optimized with respect to detuning). Thus, for small splittings, the component due to repopulation dominates. To lowest order in A_e, the signal is given by

$$\ell_0 \frac{d\alpha}{d\ell} = \frac{A_e \tilde{\kappa}_2 x_1 R (\Gamma/2)^4 \Delta_1}{144 \left[(\Gamma/2)^2 + \Delta_1^2\right]^3}, \tag{10.6}$$

i.e., linear in A_e, with a modified dispersive shape that falls off far from resonance as $1/\Delta_1^5$, where Δ_1 is the detuning from the center of the $F_g = 1 \to F_e$ transition group.

The previous discussion also explains why the two peaks in the component due to depopulation seem to cancel as they overlap, even though they have the same sign: the factors in the signal due to the creation and detection of alignment cancel individually (Fig. 10.2); it is only in their product that the two peaks have the same sign.

We now consider the case in which both the ground- and excited-state hyperfine

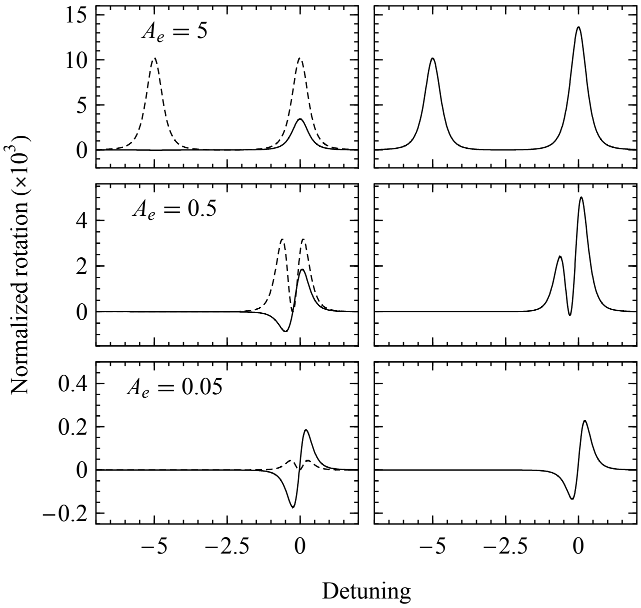

Figure 10.3: Spectra of normalized optical rotation $\ell_0/(\tilde{\kappa}_2 x_1)(d\alpha/d\ell)$ for the Doppler-free transit effect. Left column: components due to polarization produced by depopulation (dashed) and repopulation (solid); right column: total signal. Parameter values in units of Γ are $\gamma \ll 1$, $A_g \gg 1, A_e$.

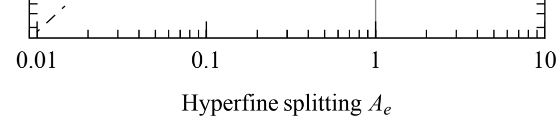

Figure 10.4: Maximum of the spectrum of the Doppler-free nonlinear magneto-optical rotation transit effect as a function of excited-state hyperfine splitting. Plotted are the component due to polarization produced by depopulation (dash-dotted) due to polarization produced by repopulation (dashed) and the total signal (solid). Parameters as in Fig. 10.3.

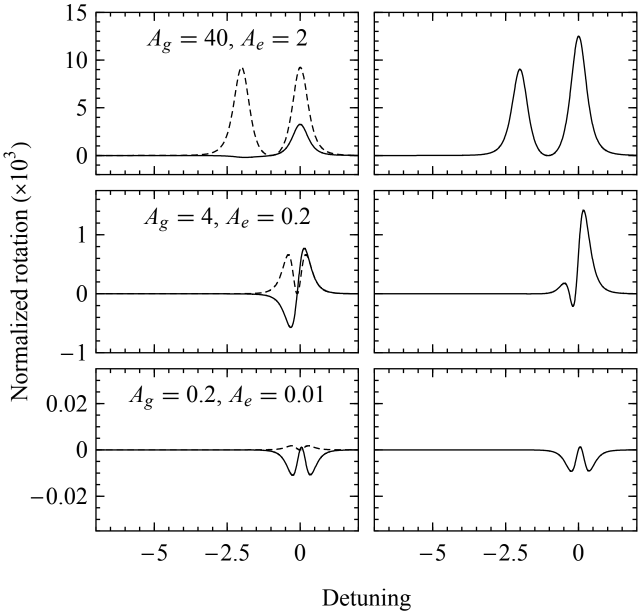

Figure 10.5: As in Fig. 10.3, with A_g and A_e varied simultaneously ($A_g = 20A_e$).

splittings are small, so that all of the hfs is unresolved. To lowest order in A_g and A_e we have

$$\ell_0 \frac{d\alpha}{d\ell} = A_e \left(A_e - \frac{R}{3} A_g \right) \frac{\tilde{\kappa}_2 x_1 (\Gamma/2)^4 \Delta^2}{24 \left[(\Gamma/2)^2 + \Delta^2 \right]^4}, \tag{10.7}$$

where Δ is the light detuning from the line center of the D_1 transition. As we expect, the component of the signal due to polarization produced by repopulation is proportional to A_g for small hyperfine splitting. The component of the signal resulting from depopulation-induced polarization also enters at this order. The optical rotation spectrum in this case is double-peaked, and falls off as $1/\Delta^6$ (Fig. 10.5).

10.2 Doppler-broadened transit effect

We now consider an atomic ensemble with a Maxwellian velocity distribution, but a low rate of velocity-changing collisions, so that the atomic velocities do not change between optical pumping and probing. This is the case for an atomic-beam experiment, or for the "transit effect" in a dilute-vapor cell. Because the atoms have a fixed velocity, the signal from each velocity group can be found individually and then summed to find the total signal. Thus the signal from the Doppler-broadened transit effect is found by multiplying the Doppler-free signal found in the previous section by a Gaussian weighting function representing the Doppler distribution along the light propagation direction and then integrating over atomic velocity. We can perform this integral analytically in different limiting cases.

We first consider the commonly encountered experimental case in which the hyperfine splitting is much greater than the natural linewidth of the excited state (i.e., the Doppler-free spectrum is well resolved). In this case, for a given light frequency and atomic velocity, the light acts on at most one transition between hyperfine levels. Thus the excited-state hyperfine coherences can be neglected, and the cancelation effects due to the overlap of resonance lines do not appear. As found in Eq. (D.21), the Doppler-free rotation spectrum then appears as a collection of peaks, one centered at each optical resonance frequency, each with lineshape function $f(\omega'_{F_eF_g}) = L(\omega'_{F_eF_g})^2$, i.e., the square of a Lorentzian lineshape. (One Lorentzian factor is due to optical pumping, the other to probing.)

In this case, the Doppler-broadened signal is found by making the replacement $f \to f_{DB}$, where the velocity integral for f_{DB} takes the form

$$f_{DB}(\Delta_{F_eF_g}) = \int dv_k f(-\Delta_{F_eF_g} + k_B v_k) G(v_k), \tag{10.8}$$

where

$$G(v_k) = \frac{k_B}{\Gamma_D\sqrt{\pi}} e^{-(k_B v_k/\Gamma_D)^2} \tag{10.9}$$

is the normalized distribution of atomic velocities along the light propagation direction $\hat{\mathbf{k}}$, k_B is the Boltzmann constant, and Γ_D is the Doppler width. This integral can be evaluated in terms of the error function. Under the assumption $\Gamma \ll \Gamma_D$ that we will employ here, the integral can be approximated by replacing f with a properly normalized delta function, resulting in

$$f_{DB}(\Delta_{F_eF_g}) \approx \frac{\sqrt{\pi}}{4}\frac{\Gamma}{\Gamma_D} e^{-(\Delta_{F_eF_g}/\Gamma_D)^2}. \tag{10.10}$$

The Doppler-broadened spectrum, given explicitly by Eq. (D.22), thus consists of a collection of resonances, each with Gaussian lineshape. For the D$_1$ line with $I = 1/2$, we have

$$\ell_0 \frac{d\alpha}{d\ell} = \frac{\tilde{\kappa}_2 x_1}{576}\left((3+R)e^{-(\Delta_{1,1}/\Gamma_D)^2} + 3e^{-(\Delta_{0,1}/\Gamma_D)^2}\right). \tag{10.11}$$

Here ℓ_0 is the absorption length for the Doppler-broadened case, given by

$$\ell_0 = \frac{4\sqrt{\pi}}{Rn\lambda^2}\frac{\Gamma_D}{\Gamma}\frac{(2J_g+1)}{(2J_e+1)}. \tag{10.12}$$

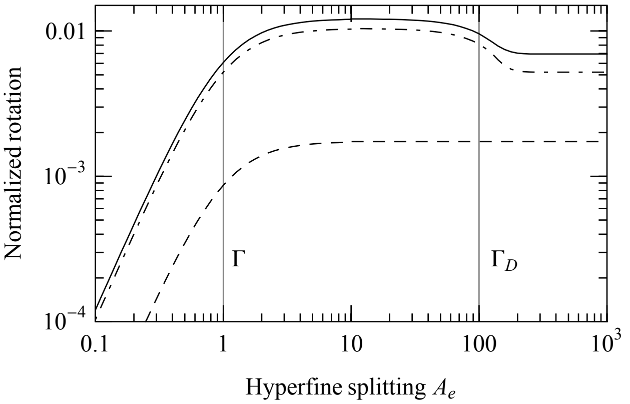

Figure 10.6: Maximum of the spectrum of the Doppler-broadened effect as a function of excited-state hyperfine splitting. Plotted are the component due to polarization produced by depopulation (dash-dotted), due to polarization produced by repopulation (dashed), and the total signal (solid). Equation (10.13) is used for $A_e < 10$, and Eq. (10.11) is used for $A_e > 10$. Parameter values in units of Γ are $\Gamma_D = 100$, $\gamma \ll 1$, $A_g \gg \Gamma_D$.

Equation (10.11) is valid for $A_e, A_g, \Gamma_D \gg \Gamma$. Note that all the terms in this expression have the same sign; thus no cancelation occurs when the resonances overlap. This is because the Doppler-free resonances all have the same sign when the Doppler-free spectrum is well resolved (Fig. 10.3), so when the Doppler-broadened spectrum samples more than one resonance, the contributions from each resonance add.

The same approach can be generalized to describe the case in which some or all of the hyperfine splittings are on the order of or smaller than Γ. In this case, the Doppler-free spectrum is not composed entirely of peaks with a shape given by $f(\omega'_{F_eF_g})$. Nevertheless, as long as each resonance or group of resonances has frequency extent much less than the Doppler width, we can approximate it as a delta function times a coefficient given by the integral of the Doppler-free spectrum over the resonance. For the D_1 line with $I = 1/2$ and $A_e, \Gamma \ll \Gamma_D \ll A_g$, this procedure yields (Eq. D.23)

$$\ell_0 \frac{d\alpha}{d\ell} = \frac{A_e^2 \tilde{\kappa}_2 x_1 (6+R) e^{-\Delta_{1,1}^2/\Gamma_D^2}}{576\,(\Gamma^2 + A_e^2)}. \tag{10.13}$$

The rotation in this case goes as A_e^2 for small A_e; the term linear in A_e (Eq. 10.6) is odd in detuning and consequently cancels in the velocity integral.

Since Eq. (10.11) applies when $A_e \gg \Gamma$ and Eq. (10.13) applies when $A_e \ll \Gamma_D$, we have that—if Γ_D is sufficiently larger than Γ—the two formulas together describe the signal over the entire range of A_e to excellent approximation, as verified by a numerical calculation. Figure 10.6 shows the maximum of the rotation spectrum as a function of the excited-state hyperfine splitting. As discussed above, as A_e is reduced, there is no suppression of the optical rotation signal when the Doppler-broadened hfs becomes unresolved. Only when the Doppler-free spectrum for a particular velocity group becomes unresolved is there suppression, as described in the previous subsection.

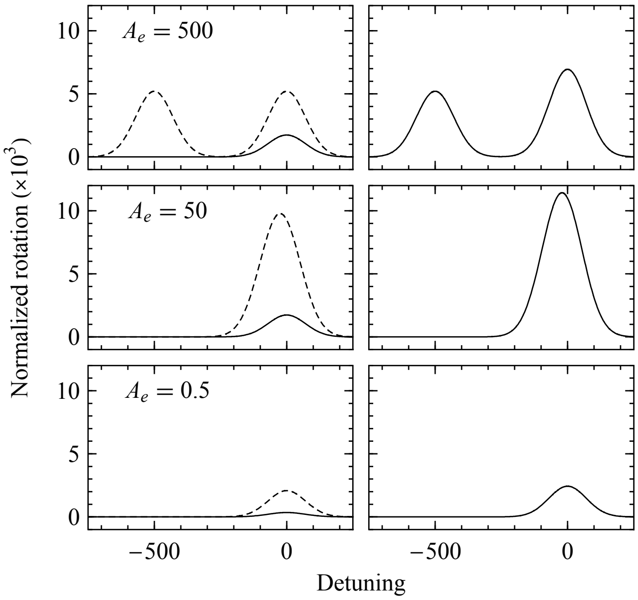

Figure 10.7: Spectra, As in Fig. 10.3, but for the Doppler-broadened transit effect. Parameter values in units of Γ are $\Gamma_D = 100$, $\gamma \ll 1$, $A_g \gg \Gamma_D$.

Spectra for the Doppler-broadened transit effect are shown in Fig. 10.7 for large A_g and various values of A_e, and for A_g and A_e varied together in Fig. 10.8.

In the case in which both A_e and A_g are small, the Doppler-free rotation spectrum is entirely of the same sign [see Eq. (10.7) and the bottom plot of Fig. 10.5]. The Doppler-broadened signal thus behaves similarly to the Doppler-free signal, because no additional cancelation takes place upon integrating over the velocity distribution. The signal for the D_1 line with $I = 1/2$ and $A_g, A_e, \Gamma \ll \Gamma_D$ is given by

$$\ell_0 \frac{d\alpha}{d\ell} = A_e \left(A_e - \frac{R}{3} A_g \right) \frac{\tilde{\kappa}_2 x_1}{96\,\Gamma^2} e^{-\Delta^2/\Gamma_D^2}. \tag{10.14}$$

10.3 Wall effect

We now consider systems in which the atomic velocities change in between optical pumping and probing. This is the case for the "wall effect" in antirelaxation-coated vapor cells: atoms are optically pumped as they pass through the light beam, and then retain their polarization through many collisions with the cell walls before returning to the beam and being probed. A similar situation occurs in vapor cells with buffer gas.

We assume that the atomic velocities are completely randomized after optical pumping. Then the density matrix for each velocity group is the same; to lowest

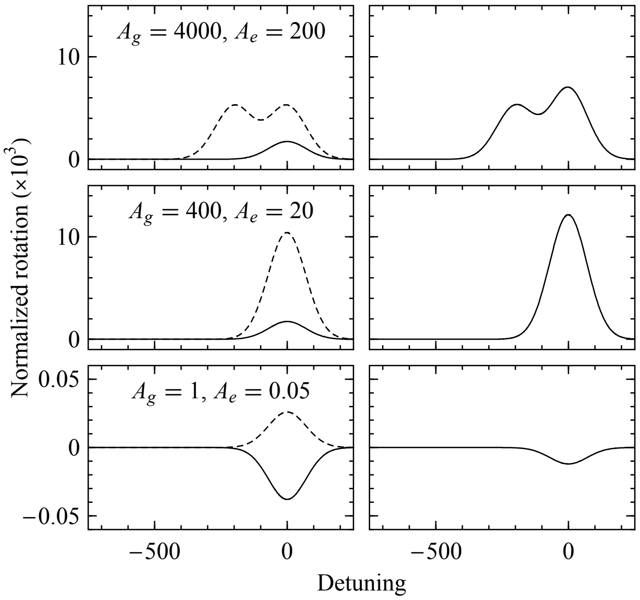

Figure 10.8: As in Fig. 10.7, with A_g and A_e varied simultaneously ($A_g = 20A_e$).

order in light power, we can find the velocity-averaged polarization by integrating the perturbative expression (D.12) over velocity with the Gaussian weighting factor (10.9). Since we are now describing the average over all of the atoms in the cell, and not just the illuminated region of the cell, we take γ to be the average ground-state relaxation rate for an atom in the cell, rather than the transit rate through the light beam. We also multiply the polarization by the illuminated fraction of the cell volume, $V_{\text{illum.}}/V_{\text{cell}}$ (assuming this fraction is small), to account for the fact that the light pumps only some of the atoms at a time.

For the specific case of the D_1 line for an atom with $I = 1/2$, Eq. (D.12) takes the form, given in Eq. (10.1), of a linear combination of Lorentzian functions $L(\omega'_{F_eF_g})$. This simple form arises because, due to the selection rules for this transition, no coherences are formed between excited-state hyperfine levels. For a general system this is not the case; however, if the excited-state hyperfine splitting is greater than Γ, the excited-state hyperfine coherences are suppressed, and all resonances once again have Lorentzian lineshapes. Thus, assuming that $\Gamma \ll \Gamma_D$, the velocity integral can be accomplished by replacing $L(\omega'_{F_eF_g})$ by

$$\int dv_k L(-\Delta_{F_eF_g} + kv_k)G(v_k) \approx \frac{\sqrt{\pi}}{2}\frac{\Gamma}{\Gamma_D}e^{-(\Delta_{F_eF_g}/\Gamma_D)^2}. \tag{10.15}$$

The polarization in this case is given by (Eq. D.24)

$$\begin{aligned}\rho^{(20)}(11) = \frac{\tilde{\kappa}_2\sqrt{\pi}}{24\sqrt{6}}\Big(&\left[e^{-(\Delta_{0,1}/\Gamma_D)^2} - e^{-(\Delta_{1,1}/\Gamma_D)^2}\right] \\ &+ \frac{R}{3}\left[e^{-(\Delta_{1,0}/\Gamma_D)^2} - e^{-(\Delta_{1,1}/\Gamma_D)^2}\right]\Big),\end{aligned} \tag{10.16}$$

where the saturation parameter for the wall effect is defined by

$$\tilde{\kappa}_2 = \frac{\Omega_R^2}{\Gamma\gamma}\frac{\Gamma}{\Gamma_D}\frac{V_{\text{illum.}}}{V_{\text{cell}}}. \tag{10.17}$$

We make this new definition because, in the wall effect, light of a single frequency illuminating just part of the cell effectively pumps all velocity groups in the entire cell.

The signal due to each velocity group is given in terms of $\rho^{(20)}(1)$ by Eq. (10.3); integrating over velocity to find the total signal, we obtain (Eq. D.25)

$$\ell_0\frac{d\alpha}{d\ell} = \frac{1}{4}\sqrt{\frac{3}{2}}\left[e^{-(\Delta_{0,1}/\Gamma_D)^2} - e^{-(\Delta_{1,1}/\Gamma_D)^2}\right]x_1\rho^{(20)}(11). \tag{10.18}$$

The spectrum of the signal due to the wall effect is quite different than the spectrum of the Doppler-broadened transit effect signal, and is in a sense more similar to that of the Doppler-free transit effect (Budker *et al.*, 2000b). Equations (10.16) and (10.18) have the same form as the Doppler-free equations (10.1) and (10.3), with Lorentzians of width Γ replaced by Gaussians of width Γ_D. Thus, the rotation signal produced by the wall effect has similar spectra and dependence on hyperfine splitting as the Doppler-free transit effect, but with scale set by the Doppler width rather than the natural width. This is illustrated in Figs. 10.9 and 10.10 for the case of large ground-state hyperfine splitting. Figure 10.9 shows the spectrum of optical rotation for various values of A_e, and Fig. 10.10 shows the maximum of the rotation spectrum as a function of A_e. These figures can be compared to Figs. 10.3 and 10.4 for the Doppler-free transit effect. In particular, we see the same phenomenon of two resonance peaks of the same sign appearing to cancel as they overlap [observation of this effect in antirelaxation-coated vapor cells is discussed by Budker *et al.* (2000b) and in buffer-gas cells by Novikova *et al.* (2001)]. The explanation for this is the same as in the Doppler-free case.

Also as in the Doppler-free case, the rotation is linear in A_e to lowest order, and this linear term is due to polarization produced by spontaneous emission:

$$\ell_0\frac{d\alpha}{d\ell} = \frac{\sqrt{\pi}}{288}\tilde{\kappa}_2 x_1 R\frac{A_e\Delta_1}{\Gamma_D^2}e^{-2(\Delta_1/\Gamma_D)^2}. \tag{10.19}$$

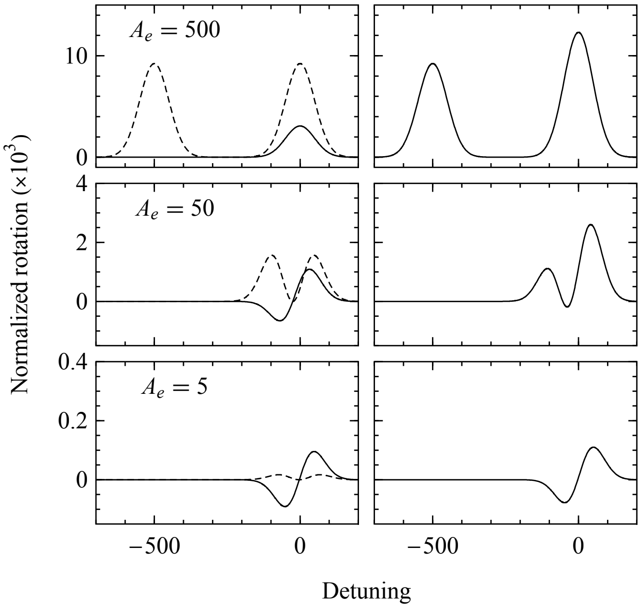

Figure 10.9: Spectra, as in Fig. 10.7, but for the wall effect.

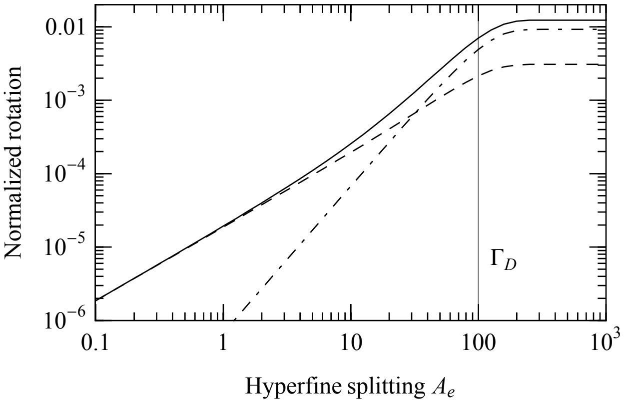

Figure 10.10: As in Fig. 10.4, but for the wall effect. Parameters are the same as in Fig. 10.6.

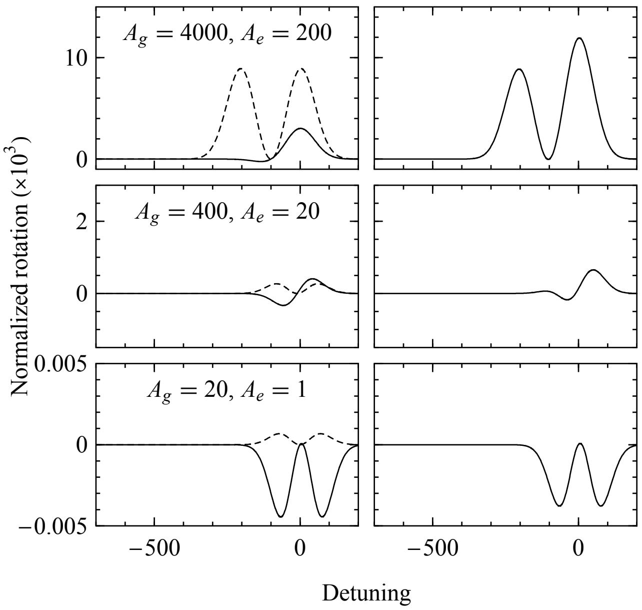

Figure 10.11: As in Fig. 10.8, but for the wall effect.

Spectra for the case in which A_e and A_g are varied together are shown in Fig. 10.11, and are also similar to the Doppler-free transit effect (Fig. 10.5). When both A_e and A_g are small, the signal to lowest order in these quantities is given by

$$\ell_0 \frac{d\alpha}{d\ell} = A_e \left(A_e - \frac{R}{3} A_g \right) \frac{\tilde{\kappa}_2 x_1 \Delta^2}{48\, \Gamma_D^4} e^{-2\Delta^2/\Gamma_D^2}. \tag{10.20}$$

10.4 Higher nuclear spin and the D$_2$ line

When nuclear spins $I \geq 1/2$ are considered, several complications arise. The clearest of these is that the two ground states now have angular momenta $F_g = I \pm \frac{1}{2} \geq 1$, so that they can both support atomic alignment and produce optical rotation. A more subtle difference is that, with higher angular momenta in the excited state, coherences between the excited state hyperfine levels can be created when the excited-state hyperfine splitting is on the order of the natural width or smaller. (Ground-state hyperfine coherences can be neglected as long as the ground-state hyperfine splitting is much larger than the ground-state relaxation rate.) This can change the optical rotation spectrum, and also causes the symmetry between the Doppler-free transit and wall effects discussed above to be partially broken, as we see below.

However, many of the results obtained above for the $I = 1/2$ system are a consequence of the general arguments discussed in Chapter 9, and thus hold for any nuclear spin. In particular, the dependence of the optical rotation signal on the hyperfine splitting for large ground-state and small excited state splitting (Eqs. 10.6, 10.13, and 10.19) and for both ground- and excited-state hyperfine splitting small (Eqs. 10.7, 10.14, and 10.20) remains the same. We have, for large A_g and small A_e, and for a particular transition group, the following three expressions. For the Doppler-free transit effect,

$$\ell_0 \frac{d\alpha}{d\ell} \propto A_e \tilde{\kappa}_2 x_{F_g} R \frac{(\Gamma/2)^4 \Delta_{F_g}}{\left[(\Gamma/2)^2 + \Delta_{F_g}^2\right]^3}; \tag{10.21}$$

for the Doppler-broadened transit effect,

$$\ell_0 \frac{d\alpha}{d\ell} \propto A_e^2 \tilde{\kappa}_2 x_{F_g} \frac{e^{-\Delta_{F_g}^2/\Gamma_D^2}}{(\Gamma^2 + A_e^2)}; \tag{10.22}$$

and for the wall effect,

$$\ell_0 \frac{d\alpha}{d\ell} \propto A_e \tilde{\kappa}_2 x_{F_g} R \frac{\Delta_{F_g} e^{-2(\Delta_{F_g}/\Gamma_D)^2}}{\Gamma_D^2}. \tag{10.23}$$

For A_g and A_e both small, we have, for the Doppler-free transit effect,

$$\ell_0 \frac{d\alpha}{d\ell} \propto A_e \left(A_e - \frac{R}{3} A_g\right) \frac{\tilde{\kappa}_2 (\Gamma/2)^4 \Delta^2}{[(\Gamma/2)^2 + \Delta^2]^4}; \tag{10.24}$$

for the Doppler-broadened effect,

$$\ell_0 \frac{d\alpha}{d\ell} \propto A_e \left(A_e - \frac{R}{3} A_g\right) \frac{\tilde{\kappa}_2}{\Gamma^2} e^{-\Delta^2/\Gamma_D^2}; \tag{10.25}$$

and for the wall effect,

$$\ell_0 \frac{d\alpha}{d\ell} \propto A_e \left(A_e - \frac{R}{3} A_g\right) \frac{\tilde{\kappa}_2 \Delta^2}{\Gamma_D^4} e^{-2\Delta^2/\Gamma_D^2}. \tag{10.26}$$

To illustrate the differences that arise when the nuclear spin is increased, we plot (analogously to Figs. 10.4, 10.6, and 10.10) in Fig. 10.12 the maximum of the rotation spectra for large A_g as a function of A_e for the Doppler-free transit, Doppler-broadened transit, and wall effects. Three values of the nuclear spin are used ($I = 1/2$, $3/2$,

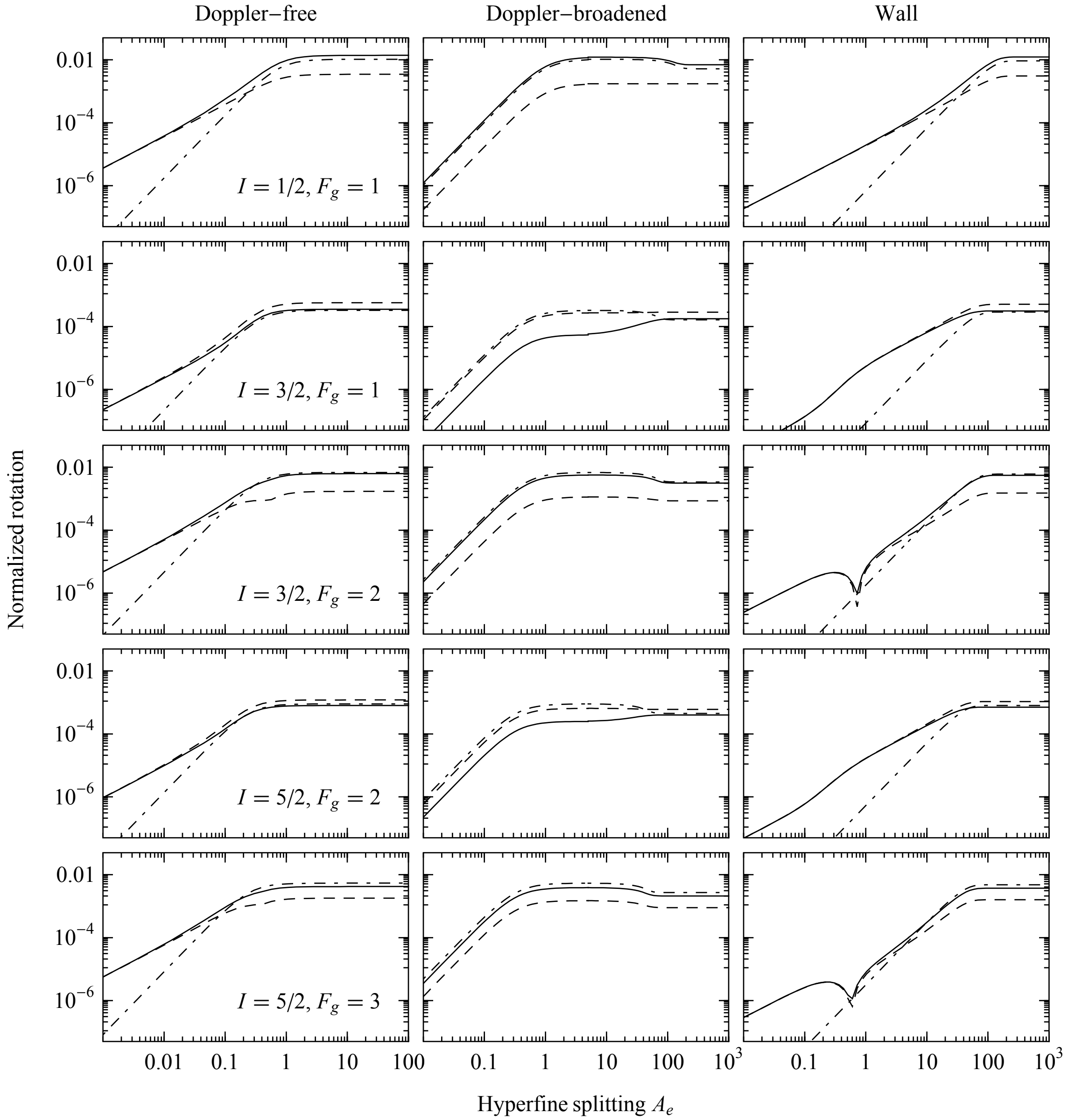

Figure 10.12: Maximum of the normalized optical rotation spectra $\ell_0/(\tilde{\kappa}_2 x_{F_g})d\alpha/d\ell$ for the Doppler-free transit, Doppler-broadened transit, and wall effects on the D_1 line for $I = 1/2$, $3/2$, and $5/2$. We assume $\Gamma_D = 100$, $\gamma \ll 1$, $A_g \gg \Gamma_D$ in units of Γ. The maxima for the $F_g = I \pm 1/2 \rightarrow F_e$ transitions are plotted separately. Each plot shows rotation due to polarization produced by depopulation (dot-dashed line), rotation due to polarization produced by repopulation (dashed line), and total rotation (solid line).

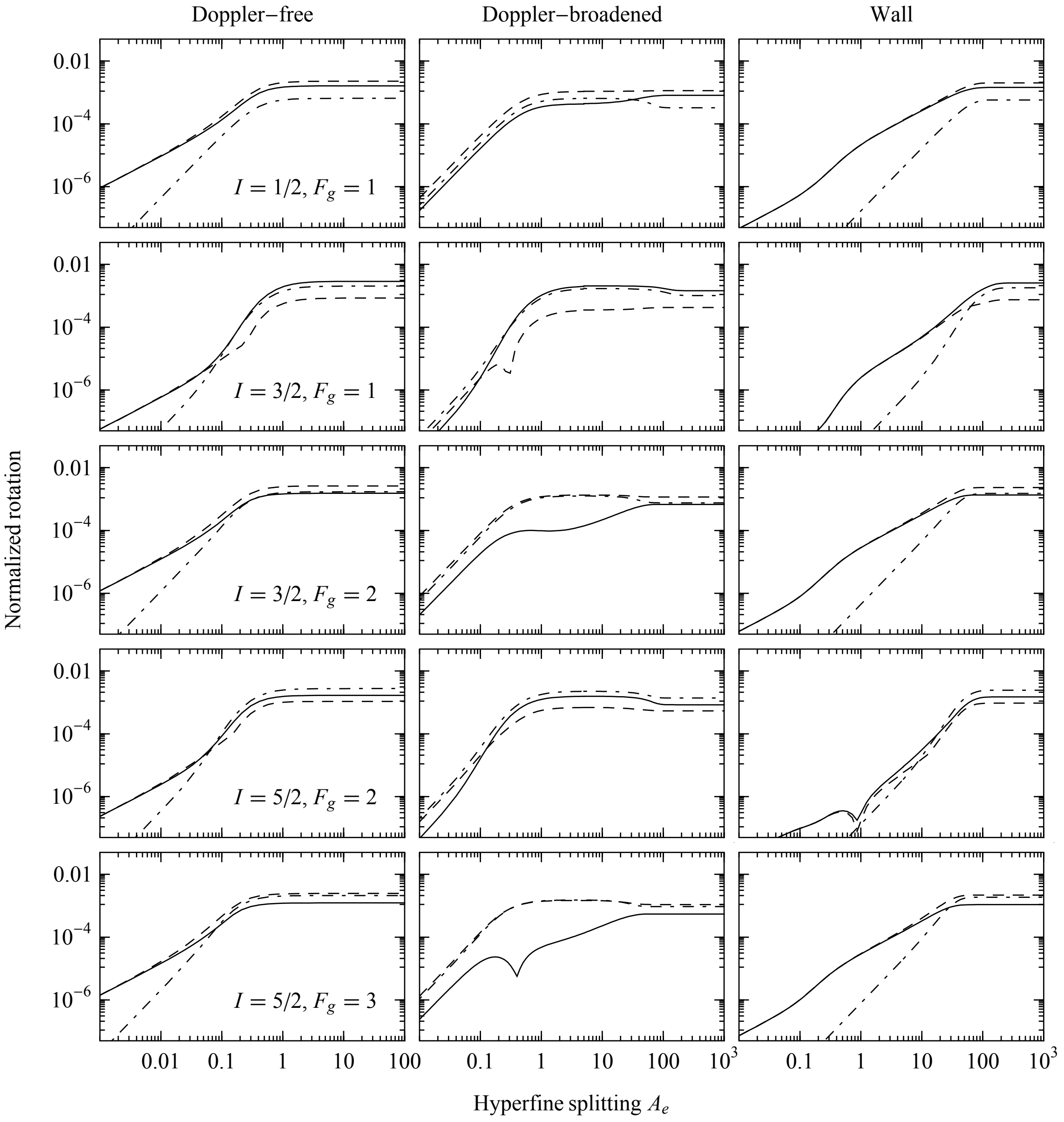

Figure 10.13: Maximum of the normalized optical rotation spectra, as in Fig. 10.12, but for the D_2 line. For the $I = 3/2$, $F_g = 2$ and the $I = 5/2$, $F_g = 3$ systems for the Doppler-broadened transit effect, the two contributions to optical rotation nearly cancel, with the consequence that the approximations used in obtaining the analytic formulas for the total Doppler-broadened signal begin to break down. Numerical convolution is employed in these cases.

and 5/2), and for $I = 3/2$ and 5/2 the rotation on the $F_g = I \pm 1/2 \to F_e$ lines is plotted separately. Rotation due to polarization produced by the depopulation and repopulation mechanisms is plotted, as well as the total rotation signal. In many cases these two contributions are of opposite sign, so the details of the total signal can depend on how closely the two contributions cancel each other. (The cancelation tends to be more complete for the $F_g = I - 1/2$ lines.) However, the qualitative features of these plots follow, in large part, the pattern exhibited in the $I = 1/2$ case. One exception is the behavior of the wall effect plot for A_e in the neighborhood of the natural width. As mentioned above, when $I > 1/2$, excited-state hyperfine coherences can form when the excited-state hyperfine splitting becomes small. This leads to "interference" effects when the Doppler-free resonance lines overlap that do not occur when the Doppler-broadened resonance lines in the wall effect overlap. This breaks the symmetry between the wall effect and the Doppler-free transit effect that is found in the $I = 1/2$ case.

We now discuss the $J_g = 1/2 \to J_e = 3/2$ D_2 transition. The presence of three hyperfine levels in the excited state leads to additional features in the dependence of the signal on the hyperfine splitting (Fig. 10.13). However, the fact that the ground-state electronic momentum is still $J_g = 1/2$ means that the dependence of the signal on the excited-state hyperfine splitting as A_e goes to zero remains the same, for the reasons discussed in Chapter 9. Thus, to lowest order in A_e, the rotation signals on the D_2 line for large A_g are given by Eqs. (10.21)–(10.23). (We set the hyperfine coefficient B_e to zero for simplicity.)

Considering the signals obtained when both the excited- and ground-state hyperfine splittings are small, we expect somewhat different behavior for the contribution due to polarization produced by repopulation pumping than in the D_1 case. This is because the excited-state electronic angular momentum is $J_e = 3/2$, so that production of rank $\kappa = 2 < 2J_e$ atomic alignment in the ground state by spontaneous emission is allowed even when the ground-state hfs is unresolved (Sec. 9.2). The lowest order dependence on hyperfine splitting for the D_2 line is given by

$$\ell_0 \frac{d\alpha}{d\ell} \propto A_e \left[A_e - R \left(2A_e + \frac{1}{3} A_g \right) \right] \tag{10.27}$$

for each of the three effects, with the spectral line shapes remaining as in Eqs. (10.24)–(10.26). Note that there is now a term that depends on polarization due to repopulation that does not go to zero as A_g goes to zero.

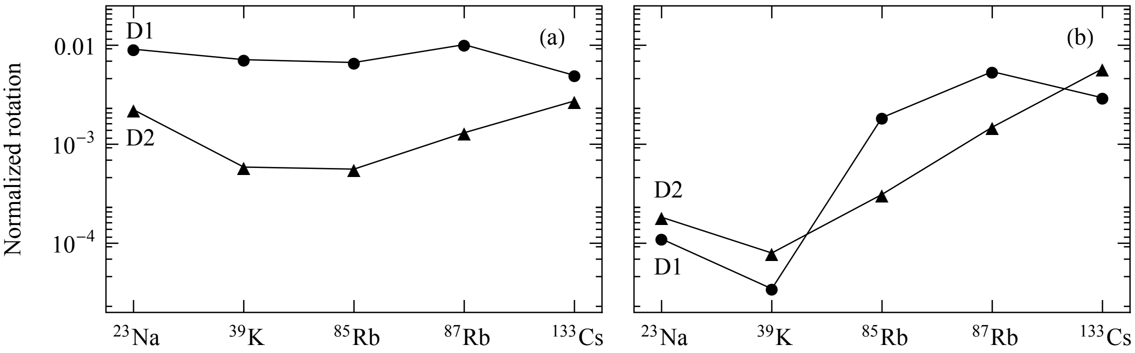

Figure 10.14: Maximum of the spectrum of normalized optical rotation for the (a) Doppler-broadened transit effect and (b) wall effect for various alkali atoms. Circles indicate the D_1 line and triangles indicate the D_2 line. Room-temperature Maxwellian velocity distributions are assumed. Normalized rotation is defined here as $\ell_0/(\tilde{\kappa}_2 x_{I+J_g})(d\alpha/d\ell)$, where ℓ_0 in this case is the unsaturated absorption length at the detuning that gives maximum absorption. The normalized magnitude of unsuppressed optical rotation is nominally on the order of unity; however, this is to some degree dependent on the normalization convention chosen. For example, if the maximum matrix element of d_z is used in the definition of $\tilde{\kappa}_2$, rather than the reduced matrix element, the values in this plot are increased by a factor of ~ 6.

10.5 Comparison of results for alkali atoms

We now examine the consequences of the preceding discussion for the alkali atoms commonly used in nonlinear magneto-optical experiments. In Fig. 10.14 the maximum of the spectrum of optical rotation is plotted for the D_1 and D_2 lines of several alkali atoms. The Doppler-broadened transit effect is shown in Fig. 10.14(a) and the wall effect is shown in Fig. 10.14(b). (Numerical convolution was used to obtain these results, because the alkalis do not all satisfy the conditions under which the analytic formulas were derived.) The nuclear spins, hyperfine splittings, excited-state lifetimes, and Doppler widths all vary between the different alkali atoms. However, focusing our attention on the hyperfine splittings, which have the greatest degree of variation, we can see the correspondence of these results to the preceding discussion. In particular, we have seen that the magnitude of the Doppler-broadened transit effect is largely independent of the hyperfine splitting when the splittings are greater than the natural width of the transition. This is generally the case for the alkalis, leading to the relative constancy of the magnitude of the transit effect among the alkalis. For the wall effect, on the other hand, we have found that the magnitude of the effect diminishes when the hyperfine splitting becomes less than the Doppler width. In the alkalis the excited-state hyperfine splitting is generally on the order of or smaller than the Doppler width, and the general trend is that the ratio of hyperfine splitting to Doppler width increases as the atomic mass number increases. This accounts for the general upward trend in Fig. 10.14(b). The trend is not completely consistent: the hyperfine splitting of K is smaller than that of Na, which is reflected in the plot of the wall effect.

Chapter 11

Laser Guide Stars and Mesospheric Magnetometry

11.1 Modeling laser guide stars

11.1.1 Introduction

Large ground-based telescopes require adaptive optics (AO) to correct for distortions introduced by atmospheric turbulence. In order to function, the AO system must track a bright point source as a reference. Although a natural star may be used, in order to obtain full sky coverage an artificial beacon created with a laser must be employed (Ageorges and Dainty, 2000).

Laser guide stars (LGS) are becoming essential for the next generation of large telescopes. The current generation of 8–10 m class telescopes, such as the Very Large Telescope (VLT) on Cerro Paranal, Chile, or the Keck telescopes on Mauna Kea, have been retrofitted with LGS, although they are still operated in many observing programs with natural guide stars or no AO at all. The upcoming 30+ m telescopes such as the 42-m European Extremely Large Telescope (E-ELT) or the Thirty Meter Telescope (TMT), by contrast, are being designed from the start as adaptive telescopes and will require LGS in nearly all of their science operation.

The most common type of LGS, first proposed by Happer *et al.* (1994), employs the ~10 km thick layer of sodium atoms occurring in the mesosphere at an altitude of about 90 km. A laser at 589 nm excites the Na atoms on the $3\,^2S_{1/2}$–$3\,^2P_{3/2}$ D_2 line and the subsequent fluorescence is observed. Use of the sodium atoms is advantageous because the product of their absorption cross section and column density is large ($\sim 10^{-11}$ cm^2 $\times$ 4×10^{13} m^{-2}) and they have a fluorescence wavelength in the visible.

The high altitude of the sodium layer means that a large fraction of the turbulent atmosphere column above the telescope can be sampled, as opposed to LGS employing Rayleigh scattering, which has a much lower effective altitude (Happer *et al.*, 1994, Table 1). Unfortunately, powerful diffraction-limited laser beams at 589 nm are quite expensive to produce due to the lack of solid-state materials that amplify 589 nm or 1178 nm light.

In order to optimize the laser parameters, numerical simulations are necessary, as the experimental situation so far is unsatisfactory: The sodium layer and atmospheric parameters often fluctuate rapidly (Thomas *et al.*, 2008; Pfrommer *et al.*, 2009), few reliable powerful lasers at 589 nm have been available up to now, and LGS sky experiments lack commonly agreed upon measurement standards. Mesospheric conditions cannot be easily simulated in vapor cells. The work described in this chapter provides optimization rules for the case of continuous wave (cw) lasers over a wide range of laser powers.

The sodium ^{2}S ground state consists of two hyperfine multiplets separated by 1.772 GHz, splitting the D_2 line into the D_2a and D_2b transition groups, corresponding respectively to the $F = 1$ and $F = 2$ Na ground states. The four ^{2}P multiplets ($F = 0 \ldots 3$) are separated by 16, 34, and 60 MHz, respectively. At mesospheric temperatures, near 185 K, the D_2a and D_2b lines are each Doppler broadened to about 1 GHz, giving rise to the characteristic double-hump absorption profile (see for instance Bradley, 1992, Fig. 11, or Fig. 11.1 of this work). When the D_2a transition is excited by circularly polarized light at high intensity, a large fraction of the atoms are pumped into the $F = 2, m = \pm 2$ ground state, and the atoms cycle on the transition to the $F' = 3, m' = \pm 3$ upper state, so that sodium effectively becomes a two-level system. This situation is desirable because both the absorption cross section and the fraction of fluorescence emitted back toward the telescope are increased.

Various processes have the effect of limiting the amount of photon flux returned from a LGS, in particular Larmor precession, atomic recoil (radiation pressure), and transition saturation leading to stimulated emission. Larmor precession is powerful enough to thwart optical pumping if the angle between the beam and the field lines is large (Moussaoui *et al.*, 2009). The average 50-kHz redshift that an atom incurs per spontaneous emission due to atomic recoil can lead to spectral hole burning (depopulation of the respective atoms velocity class) in very bright single-frequency LGS (bandwidth < 10 MHz, Hillman *et al.*, 2008), but it also offers the opportunity of "snowplowing" the sodium population toward higher velocities in the laser-beam direction, requiring continuous chirping of the laser (Kibblewhite, 2009). Ultimately, at high spectral irradiance, stimulated emission becomes relevant, limiting spontaneous emission. Photons from stimulated emission are emitted straight into space, hence becoming useless for LGS.

Another mechanism that limits photon return is the inadvertent optical pumping of atoms from the $F = 2$ ground state to the $F = 1$ state, sometimes known as downpumping. Once an atom is in the $F = 1$ state, it can only be excited if "repump" light is made resonant with the D_2b line (either by allocating 10–20% of the laser power to the D_2b line, or by widening a single laser line to ≥ 2 GHz). Downpumping in the absence of repumping becomes more severe with increasing laser irradiance and reduces the return flux long before the onset of saturation of the excited state. Repumping has already been experimentally demonstrated to be able to boost the LGS return flux by a factor of 1.6 (Denman *et al.*, 2006; Telle *et al.*, 2008), and the work described here indicates that more than a factor of 3 can be achieved. Spin-exchange collisions can also play a role, by exchanging populations between the ground states and within them (transitions between the $F = 1, m = \pm 1$ and $F = 2, m = \pm 2$ ground substates are particularly strong).

Rather than just a high photon return flux, what is really desired when designing AO systems is high luminosity concentrated in a small spot size. Compared to the uplink laser irradiance in the sodium layer, the above mentioned saturation effects spatially broaden the LGS return fluorescence distribution by emphasizing the low-irradiance regions and dimming the peaks. We can show using physical-optics simulations (Holzlöhner *et al.*, 2008) that this effect increases the instantaneous spot sizes on a wavefront sensor by about $0.1''$, which is not negligible.

Understanding the complicated interplay of the above effects and obtaining quantitative values of the fluorescence efficiency requires numerical simulations. A commonly used method is the solution of the Bloch equations for a multilevel atom.

Milonni and Thode (1992) simplified the D_2 scheme to a 2-level Bloch model which they solve in the time domain. Bradley (1992) simulated the full 24-state density matrix, exciting the sodium by a train of short (nanosecond range) laser pulses like Milonni and Thode, using Runge-Kutta integration for one pulse period and exploiting the periodicity. Linear and circular light polarizations were treated. However, both works neglect the geomagnetic field. Morris (1994) studied frequency-modulated pulses over a wide range of pulse durations and line widths up to 3 GHz, hence spanning the entire Doppler broadened D_2 line, employing time-domain integration, for both linearly and circularly polarized light. Morris also neglects the geomagnetic field, although an estimate is given of its impact.

Milonni *et al.* (1998, 1999) have published a detailed Bloch-equation simulation of sodium LGS, later generalized by Telle *et al.* (2006, 2008). Milonni *et al.* (1998) treat the cases of laser pulses that are short, comparable, and long compared to the ^{2}P lifetime of $\tau = 16.24$ ns, using numerical solution methods similar to those of Bradley. Milonni *et al.* (1999) deal with cw excitation only and introduce spin relaxation and Larmor precession into the Bloch equations. The Larmor terms due to the geomagnetic field are shown to counteract optical pumping by redistributing the magnetic sublevel populations. This and all of the above mentioned works solve the Bloch equations separately for a number (100–400) of different sodium velocity classes and then perform a weighted average over the results. All of these works neglect atomic recoil.

An alternative method of simulating atomic fluorescence is to use rate equations, either implemented as a set of differential equations (Pique *et al.*, 2006; Hillman *et al.*, 2008), or by employing Monte Carlo rate-equation techniques.

In this work, we present a Bloch-equation method that can model any alkali atom, taking into account spontaneous and stimulated emission, Larmor precession due to the geomagnetic field, arbitrary elliptical light polarization, recoil, on the order of 100 coupled velocity classes with velocity-changing collisions and spin exchange, finite atomic dwell time in the beam (atom replacement), arbitrary laser bandwidth, and repumping. We neglect nonlinear Zeeman shifts and hyperfine coherences since we found them to have a small effect on the result. In contrast to the above cited Bloch-simulation publications, we directly compute the steady-state solution, which is more efficient than time-domain solutions (a single run takes about 2 s on a modern personal computer). The program is written in Mathematica and based on the *Atomic Density Matrix* package, available at `http://budker.berkeley.edu/ADM/`.

Section 11.1.2 describes the Bloch-equation method, Section 11.1.3 gives details about the simulation parameters, and Section 11.1.4 presents some results. Detailed discussion of LGS parameter optimization is given by Holzlöhner *et al.* (2010).

11.1.2 Bloch equations

In order to calculate the observed fluorescence from mesospheric sodium atoms, the evolution of the atoms is modeled using the optical Bloch equations for the atomic density matrix. The density matrix describes the statistical state of an ensemble of atoms in the state space of the Na D_2 transition. In order to account for atoms with different Doppler shifts, the density matrix is also considered to be a function of atomic velocity along the laser beam propagation direction, as discussed in Chapter 7. (An additional degree of freedom is included to account for laser line broadening, as discussed below.) As described in earlier chapters, a semiclassical calculation is performed. Because the density matrix describes all populations of, and coherences between, the 24 Zeeman sublevels making up the ground and excited states, the calculation describes, in principle, all saturation and mixing effects for essentially arbitrarily large optical and magnetic fields. (In practice, certain coherences in the system are negligible under our experimental conditions and can be neglected in order to increase the computational efficiency.)

In order to perform numerical calculations, the velocity dependence of the density matrix is discretized to describe an appropriate number $n_{v.g.}$ of velocity groups, each with a fixed longitudinal velocity. Because coherences between atoms with different velocities can be neglected, the complete density matrix ρ can be thought of as a collection of $n_{v.g.}$ separate but coupled density matrices, each of dimension 24×24.

The evolution of the density matrix is given by the Liouville equation (Chapter 3), here written as

$$\frac{d}{dt}\rho = \frac{1}{i\hbar}[H, \rho] + \Lambda(\rho) + \beta, \tag{11.1}$$

where $H = H_0 + H_E + H_B$ is the total Hamiltonian, with H_0 the Hamiltonian for the unperturbed energy structure of the atom, $H_E = -\mathbf{d} \cdot \mathbf{E}$ the Hamiltonian for the interaction of the electric dipole $\mathbf{d}$ of the atom with the electric field $\mathbf{E}$ of the light, and $H_B = -\boldsymbol{\mu} \cdot \mathbf{B}$ the Hamiltonian for the interaction of the magnetic moment $\boldsymbol{\mu}$ of the atom with the local magnetic field $\mathbf{B}$. The term Λ in Eq. (11.1) represents phenomenological terms added to account for relaxation processes not described by the Hamiltonian (Sec. 3.2 and Chapter 7). In our case these relaxation processes include spontaneous decay (omitted from the Hamiltonian due to the semiclassical approximation), collisional spin relaxation ("S-damping") proportional to $S^2\rho - S\cdot(\rho S)$ (Sec. 7.3), and the exit of atoms from the light beam due to motion of the atoms and the beam. In addition, there are terms included in Λ to describe changes in atomic velocity due to collisions and light-induced recoil, as well as an effective relaxation rate that describes dithering of the laser phase in order to simulate a finite bandwidth. These terms are described in more detail below. Each relaxation process described by Λ includes a corresponding repopulation process, so that the trace over the density matrix for all velocity groups is conserved, corresponding to conservation of the total number of atoms. The repopulation process describing the entrance of atoms into the beam is independent of ρ and so is written as a separate term β.

Velocity-changing collisions are treated as hard collisions in which the velocity of the colliding atom is rethermalized in a Maxwellian distribution (no speed memory). The internal state of the atom is assumed to be unchanged.

Light-induced recoil is described phenomenologically by causing a fraction $v_r/\Delta v_{v.g.}$ of the excited-state atoms in each velocity group to be transferred upon decay into the next higher velocity group (Sec. 7.5). Here v_r is the recoil velocity and $\Delta v_{v.g.}$ is the width of the bin defining a particular velocity group. This model relies on the fact that $v_r = 2.9461$ cm/s (equivalent to a Doppler shift of 50.004 kHz) is much smaller than the typical minimum value of $\Delta v_{v.g.}$, which is on the order of the natural line width (∼10 MHz).

In order to simulate a finite bandwidth laser, a form of phase dithering is used (frequency or amplitude dithering can also be employed). To avoid resorting to a time-domain calculation, the dithering is implemented in the spatial domain: density matrices are written for two "regions" with light fields that are π out of phase with each other, and relaxation terms are included that transfer the atoms between the regions (this doubles the size of the system of equations). The model is that of a laser beam with very fine "speckles" of different phases. The result is an effective laser spectrum of Lorentzian shape with a width proportional to the transfer rate between the regions. This method has been verified by comparison to a time-domain model (implemented for a nuclear-spinless system) in which the light frequency randomly changes with a Lorentzian distribution. Identical results from the two methods are obtained for the case in which the rate that the light frequency changes is faster than the natural decay rate.

Equation (11.1) supplies a linear system of differential equations for the density-matrix elements, known as the optical Bloch equations. Thinking of ρ as a column vector of $n_{v.g} \times 24^2$ density-matrix elements, the Bloch equations can be written as $\dot{\rho} = A\rho + b$, where A and b are a matrix and vector, respectively, that are independent of ρ. The vector b corresponds to β and A to the rest of the right-hand side of Eq. (11.1).

The laser light field has a frequency component tuned near the D_2 $F = 2 \rightarrow F'$ transition group (D_2a), and may have an additional "repump" component tuned near the $F = 1 \rightarrow F'$ transition group (D_2b). Thus the matrix A has components that oscillate at each of these frequencies. Under the rotating-wave approximation (Sec. 3.3.2), the overall optical frequency is removed from A. However, the beat frequency between the two light-field components remains. This beat frequency can also be removed from the Bloch equations in our case: each frequency component interacts strongly with one transition group and very weakly with the other, so the weak coupling can be neglected for each transition. If, in addition, the small magnetic-field-induced mixing between the two hyperfine ground states is neglected, the beat frequency can be entirely removed from the evolution equations. This makes A time-independent for cw light. To find the steady-state density matrix, we can set $\dot{\rho} = 0$ and solve the linear system $A\rho = -b$. The vectors ρ and b have 322 elements per velocity class (576 if hyperfine states are not neglected), so that the sparse linear equation system has dimension 32,500–65,000 in practice. If the line broadening by phase dithering technique is employed, the dimensions are doubled.

To solve the Bloch equations for a particular set of experimental parameters, we first choose an appropriate set of velocity groups. Since the signal is strongly peaked for atoms whose Doppler-shifted resonance frequency is near the light frequency, we can obtain more accurate results for a given number of velocity groups if narrower bins are used for resonant atoms, and wider for off-resonant. We have two methods for doing this.

The first method is to choose two fixed bin sizes, one narrow and one wide, and the number of narrow bins to cluster near each resonance. The wide bins are then used to take up the rest of the Doppler distribution. This method is useful when we don't know beforehand what the spectrum of the signal in velocity space is.

If we have an estimate of the spectrum (obtained using the first method), we can refine it using the second method, which takes advantage of this knowledge. We create a weighting function consisting of three terms: a constant term, which tends to make equal-sized bins, a term proportional to the spectrum, which makes more bins where the signal is large, and a term proportional to the magnitude of the second derivative of the signal, which makes more bins where the signal changes rapidly as a function of velocity. The bin sizes are then found by dividing the integral of the weighting function evenly into the chosen number of bins.

The linear system is solved using the implementation of the iterative stabilized biconjugate gradient, or BiCGSTAB, method (van der Vorst, 1992) built in to Mathematica. This is a Krylov subspace method in which an initial guess is improved by minimizing the residual over a subspace with dimension much smaller than that of the full system. The rate of convergence of the method is increased by pre-multiplication with a block-diagonal preconditioner (approximate inverse of A), obtained by setting all terms that connect density matrix elements from different velocity groups to zero, and then inverting the block for each velocity group.

The fluorescent photon flux per solid angle emitted in a given direction can be found from the steady-state solution for ρ as the expectation value of a fluorescence operator (Corney, 2006).

11.1.3 Simulation parameters

Table 11.1 lists the various simulation parameters together with their chosen standard values. The launched laser power P equals the laser device output beam power, diminished by optical losses in the beam train and launch telescope (LT). The repumping fraction q is the fraction of the total laser power allocated to the repump beam: the D_2a beam power is $(1-q)P$ and the power in the D_2b beam (tuned Δf_{ab} above the D_2a frequency) is qP.

The geomagnetic-field strength B has a strong impact on the return flux. Its value

Table 11.1: Simulation parameters and their standard nominal values

Variable name	Symbol	Standard value
Laser parameters		
Launched laser power in air	P	20 W
Mesospheric laser irradiance	I	46 W/m^2
Central D$_2$ vacuum wavelength	λ	589.159 nm
Polarization ellipticity angle	ε	$\pm\pi/4$ (circular)
Laser FWHM linewidth	Δf	0
Repumping power fraction	q	0.12
Repumping frequency offset	Δf_{ab}	1.7178 GHz
Atomic, atmospheric, and mesospheric parameters		
Outer turbulence scale	L_0	25 m
Geomagnetic field in mesosphere	B	0.228 G
One-way transmission at λ at zenith	T_a	0.84
Average mesospheric temperature	T_{Na}	185 K
Sodium centroid altitude (a.s.l.)*	H_{Na}	92 km
Sodium column density	C_{Na}	4.0×10^{13} m^{-2}
Na beam dwell velocity	v_γ	38 m/s
Beam atom exchange rate	γ_{ex}	1/(6.0 ms)
Na–N$_2$ v.c.c.† cross section	$\sigma_{\mathrm{Na-N_2}}$	0.71×10^{-14} cm^2
Na–O$_2$ v.c.c.† cross section	$\sigma_{\mathrm{Na-O_2}}$	0.70×10^{-14} cm^2
Weighted v.c.c.† rate	γ_{vcc}	1/(35 µs)
Na–O$_2$ spin exchange cross sect. at T_{Na}	$\sigma^S_{\mathrm{Na-O_2}}$	0.50×10^{-14} cm^2
Weighted spin-exchange rate at T_{Na}	γ_S	1/(490 µs)
Launch telescope (LT) parameters		
Zenith angle	ζ	30°
LT altitude (a.s.l.)*	H_{tele}	2650 m
LT aperture	D	40 cm
LT beam radius ($1/e^2$)	w	$0.36D = 14.4$ cm
Launched beam rms wavefront error	WFE	100 nm $\approx \lambda/6$
Polar angle of **B** (laser $\parallel z$)	θ	$\pi/2$
Azimuth of **B** (laser $\parallel z$)	ϕ	$\pi/2$

*a.s.l. = above sea level; †v.c.c. = velocity-changing collision varies considerably over the world and can be computed for different mesospheric altitudes using the International Geomagnetic Reference Field[1] model. Cerro Paranal in northern Chile, the location of the VLT and the reference site for this work (24.6°S, 70.4°W), has $B \approx 0.23$ G at 92 km altitude, Mauna Kea (Hawaii) has $B \approx 0.35$ G, and the Starfire Optical Range (SOR; Albuquerque, New Mexico) has $B \approx 0.48$ G, about twice the field strength at Paranal.

The mesospheric temperature, as well as partial gas densities, can be derived using the MSISE-90 model.[2] Our values for the sodium layer centroid altitude H_{Na} and column abundance C_{Na} are obtained from studies taking place for over 30 years in São Paulo (Simonich *et al.*, 1979; Moussaoui *et al.*, 2010), a site whose latitude differs only by one degree from the ESO Paranal Observatory. We believe that the sodium layer parameter statistics on the seasonal and daily variations are valid for Paranal.

Atomic collisions have a significant effect on the sodium states and hence on the LGS return flux. Since mesospheric sodium is rarefied (the total mass of global mesospheric sodium is about 600 kg), Na–Na collisions are negligible compared to Na–N_2 and Na–O_2 collisions. Most of these collisions are binary (collision of two molecules). One important effect of collisions is to change the velocity of the atoms, causing diffusion of optically pumped atoms in velocity space (Sec. 7.4). Since the masses of N_2 and O_2 molecules are comparable to that of Na atoms, we assume here that every collision completely randomizes their velocity. (We have also performed calculations using a soft-collision model, Holzlöhner *et al.*, 2010.) The collision rate of a gas of particle mass M_1 with another gas type of particle mass M_2 and number density n_2 is given by (Wright, 2004)

$$\gamma_{12} = n_2 \sigma_{12} \sqrt{\frac{8 k_B T}{\pi} \left(\frac{1}{M_1} + \frac{1}{M_2} \right)}, \tag{11.2}$$

where k_B is Boltzmann's constant and $\sigma_{12} = \pi (r_1 + r_2)^2$ is the collisional cross section with the effective particle radii r_1, r_2. Measuring these radii for velocity-changing collisions is difficult; here we just assume the Van der Waals radii of $r_{\mathrm{Na}} = 227$ pm, $r_{\mathrm{N}_2} = 250$ pm, and $r_{\mathrm{O}_2} = 245$ pm (Fishbane *et al.*, 2005). The effect of other gas species is negligible. With these numbers, we have, for example, $\sigma_{\text{Na-N}_2} = 0.72 \times 10^{-14}$ cm^2 and $\gamma_{\text{Na-N}_2} = 3.98 \times 10^{-10}$ cm^{-3}s^{-1} $\times\, n_{\mathrm{N}_2} = 1/(62.8$ µs) at the sodium centroid ($n_{\mathrm{N}_2} = 4.0 \times 10^{13}$ cm^{-3}).

---

[1] IGRF Release 2005 geomagnetic model online at NOAA website (`http://www.ngdc.noaa.gov/IAGA/vmod/`).

[2] MSISE-90 atmospheric model online at NASA website (`http://ccmc.gsfc.nasa.gov/modelweb/atmos/msise.html`).

The sodium layer has a median FWHM thickness of 11.1 km and its median centroid lies at $H_{\mathrm{Na}} = 92$ km (Moussaoui *et al.*, 2010). The gas pressure decreases exponentially with altitude and the collision rate varies across the layer by about one order of magnitude, as shown by the MSISE-90 atmospheric model. We compute the mean collision rate of Na with N_2 and O_2, based on a table of n_{N_2}, n_{O_2}, and T_{Na} as functions of altitude, weighted by the assumed Gaussian sodium density distribution. The result, which we will use throughout this work, is $\gamma_{\mathrm{vcc}} = \gamma_{\mathrm{Na\text{-}N_2,O_2}} = 1/(35\ \mu\mathrm{s})$, which is three times higher than the assumption of $1/(100\ \mu\mathrm{s})$ used by Milonni *et al.* (1999). Since the sodium abundance, layer thickness, and altitude are highly variable and the layer's profile often deviates significantly from Gaussian, one cannot expect a high accuracy in this parameter.

The other important relaxation mechanism besides velocity-changing collisions is spin-randomization relaxation or S-damping (Sec. 7.3), in particular for Na–O_2 collisions. Spin relaxation time constants have been measured between rubidium and metastable triplet helium (He*, Dmitriev *et al.*, 2008), as well as between rubidium and H_2, O_2, and N_2 (Nagengast *et al.*, 1998), and sodium and various gases (Ramsey and Anderson, 1964; Kartoshkin, 1998). A major difficulty with such measurements is that the overwhelming contribution to S-damping of Na in the mesosphere is due to collisional spin exchange with O_2; however, in gas cells O_2 oxidizes Na quickly and hence this particular cross section is hard to determine experimentally. Theoretical calculations of the cross section involve Born-Oppenheimer molecular potential curves of doublet/quartet surfaces for Na–O_2, analogous to the singlet/triplet curves for Na–Na and have not yet been carried out to our knowledge.

We estimate $\sigma^S_{\mathrm{Na\text{-}O_2}} = 0.5 \times 10^{-14}$ cm^2 at 185 K, based on spin-exchange cross-section measurements of Na-He* and O_2-He. However, only 1/2 of this cross section is effective in our case (Dmitriev *et al.*, 2008, Eq. 3). Setting $\sigma_{12} = \sigma^S_{\mathrm{Na\text{-}O_2}}/2$ in Eq. (11.2), we obtain $\gamma_S = 1/(680\ \mu\mathrm{s})$ at 92 km altitude, which is close to the value $\gamma_S = 1/(640\ \mu\mathrm{s})$ that Milonni *et al.* (1999) find through fitting to experimental data. Note, however, that the initial guess used by Milonni *et al.* was $\sigma^S_{\mathrm{Na-O_2}} = 1.0 \times 10^{-14}$ cm^2, and they do not apply the scaling factor of 1/2. Performing the same sodium-density-weighted averaging over altitude as above, we obtain $\gamma_S = 1/(490\ \mu\mathrm{s})$, which will be used throughout this work. We will discuss the sensitivity of the Na return flux to variations in γ_S and γ_{vcc} in the following section.

The root-mean-square lateral velocity $v_\gamma = d\gamma_{\mathrm{ex}}$ describes the sodium atom exchange into and out of the beam, where $d \approx 23$ cm is the median FWHM mesospheric speckle diameter (see the following section), and γ_{ex} is the atom exchange rate. We take into account four contributions to v_γ that we sum in quadrature since they are in general uncorrelated: gas diffusion orthogonal to the beam, mesospheric wind

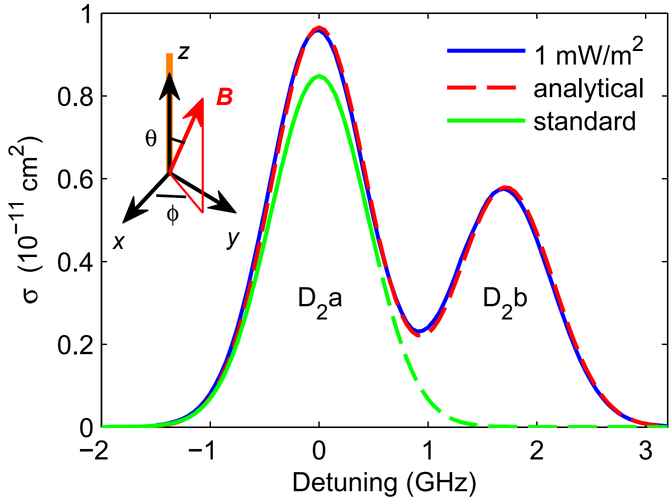

Figure 11.1: Absorption cross section σ vs. detuning from the Na D_2a line center. Solid blue: simulation at $I = 0.001$ W/m^2 ($q = 0$); dashed red: analytical cross section; green: simulation of effective cross section at standard conditions ($I = 46$ W/m^2, $q = 0.12$). Inset: reference coordinate system.

orthogonal to the beam, beam wander caused by atmospheric turbulence, and LGS beam slewing due to star tracking. An estimate of these contributions gives an effective value for the atomic velocity of $v_\gamma = 38$ m/s, and hence $\gamma_{\mathrm{ex}} = 1/(6.0\ \mathrm{ms})$.

11.1.4 Results

We compute the normalized return flux ψ, equal to the number of photons per atom, per unit time, per solid angle, and per unit of light intensity spontaneously emitted in the direction of the launch telescope, using the method and parameters described above. Using the standard conditions of Table 11.1, we obtain $\psi = 258$ ph/s/sr/atom/(W/m^2).

Figure 11.1 plots the effective frequency-dependent absorption cross section $\sigma = h\nu W/I$, where $\nu = c/\lambda$ is the transition frequency and W is the actual rate of spontaneous emissions at irradiance I as a function of detuning of the (main) laser line. The simulated effective cross section as a function of laser detuning obtained at low intensity is shown to agree with the analytical formula obtained under the assumption of linear absorption (Milonni *et al.*, 1998, Eqs. (10,11)) at $T = 185$ K.

The effective cross section for the standard conditions ($I = 46$ W/m^2 and $q = 0.12$) is also plotted; the reduction in σ due to saturation is modest. The tail of this curve toward the D_2b line center at 1.772 GHz is dashed, because the computational simplification of letting the main laser line only excite the D_2a Na transitions, and analogously allowing the repumping line to only excite the D_2b transitions, whenever repumping is used ($q > 0$), breaks down at this point. Once the detuning approaches the D_2b line center, this assumption obviously becomes invalid. By contrast, the

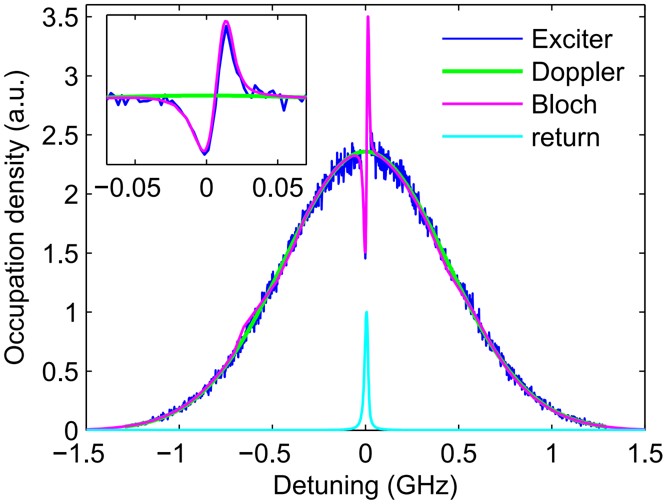

Figure 11.2: Atomic velocity distribution under standard conditions (but $\theta = q = 0$); blue: *Exciter*; green: Doppler profile; magenta: Bloch equations; cyan: return light spectrum in the atomic frame. Inset: zoom on line center.

low-intensity curve was computed for $q = 0$ and without using this simplification, and it is valid for any frequency offset.

The inset in Fig. 11.1 sketches the definition of the spherical angles θ and ϕ of the **B**-vector in a coordinate system where the laser beam is projected along the z-axis. The major axis of the polarization ellipse for noncircular polarization is parallel to x.

Figure 11.2 shows the simulated atomic velocity distribution under standard conditions, except that Larmor precession and repumping are absent ($\theta = q = \gamma_{\text{ex}} = 0$). The abscissa shows relative atomic velocity away from the receiver in frequency units (proportionality constant $1/\lambda$). (Under this convention, velocities directed away from the receiver are labeled with positive frequency shifts, rather than the physically observed negative shifts.) Along with the results of the Bloch simulation, the occupation histogram from the Monte Carlo rate-equation simulation *Exciter* (Holzlöhner *et al.*, 2010) and a Gaussian distribution with FWHM width of 1.033 GHz, representing the thermal equilibrium, are shown. For reference, the simulated return flux spectrum in the atomic frame is also shown (plotted at arbitrary vertical scale), which in the present case of single-frequency excitation is close to the sodium natural line shape of a Lorentzian with a FWHM of $1/(2\pi\tau) = 9.8$ MHz.

The effect of spectral hole burning is quite striking; in fact the occupation at the D_2a line center is depleted to 64% below the green Doppler curve. The atomic population, as seen from the telescope, is shifted within about one velocity class. We observe that spectral hole burning due to recoil is in general exacerbated if repumping is applied, presumably due to the larger number of excitations per time. On the other hand, hole burning is mitigated when the laser bandwidth is extended at constant laser power because of the reduced spectral irradiance.

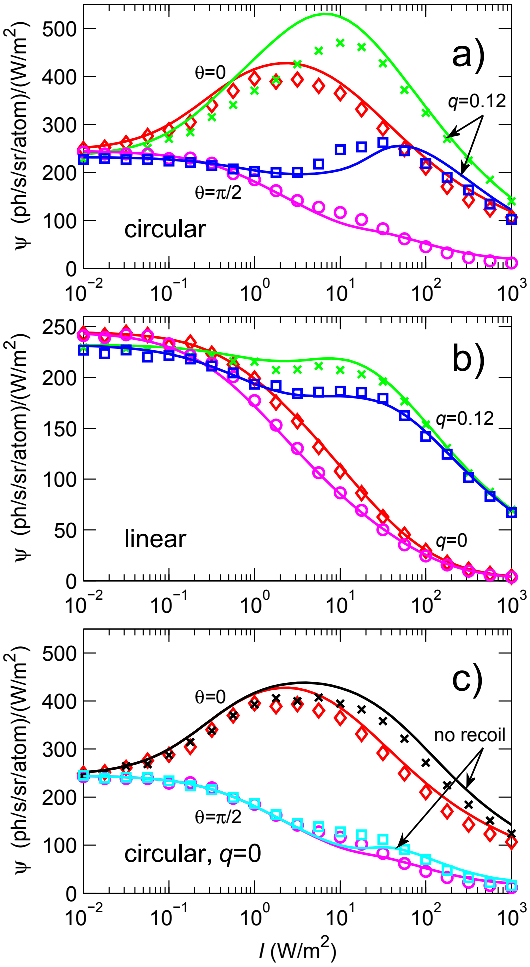

Figure 11.3: Specific return flux $\psi(I)$. Lines: Bloch equations, symbols: Monte Carlo rate-equation simulation *Exciter*. a) Green, crosses: $\theta = 0$, $q = 0.12$; red, diamonds: $\theta = 0$, $q = 0$; blue, squares: $\theta = \pi/2$, $q = 0.12$ (standard conditions); magenta, circles: $\theta = \pi/2$, $q = 0$ (all with circular polarization and $\gamma_{\mathrm{ex}} = 0$). b) Same as a), but for linear polarization. c) Red and magenta lines, diamonds and circles: as in a); black, crosses and cyan, squares: same, respectively, without recoil.

Figure 11.3 shows three semilogarithmic plots of $\psi(I)$ for the standard conditions of Table 11.1 unless noted otherwise, but neglecting exchange with thermal Na atoms outside the beam ($\gamma_{\mathrm{ex}} = 0$). Discrepancies between the Bloch (lines) and the *Exciter* (symbols) results have been attributed to approximations made in the *Exciter* code. Figure 11.3(a) shows the cases of magnetic field along ($\theta = 0$) and orthogonal ($\theta = \pi/2$) to the light beam, with ($q = 0.12$) and without ($q = 0$) repumping. Figure 11.3(a) shows the same for linear polarization (note the difference in vertical scale).

We see that the magnetic field reduces the return flux strongly when it is orthogonal to the light beam, at some irradiances by several times. At very low irradiance ($I = 10^{-2}$ W/m^2), the atom is in thermal equilibrium and all magnetic sublevels are nearly equally populated. Optical pumping sets in with increasing I if using circular

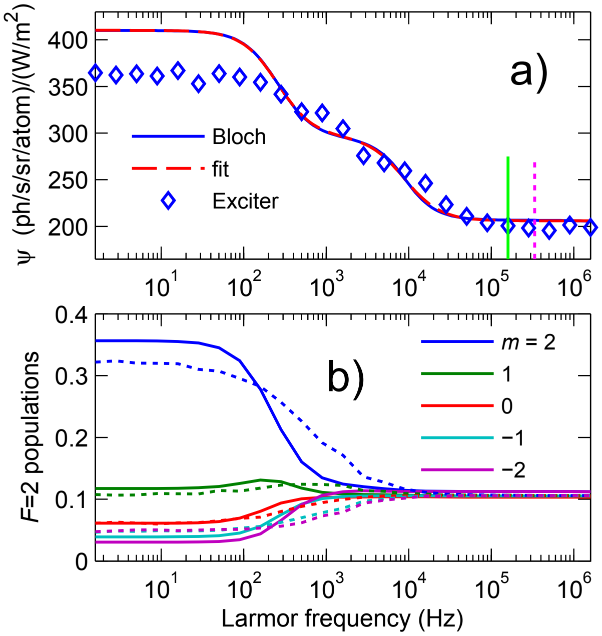

Figure 11.4: Magnetic field impact. a) Blue curve: ψ as a function of the Larmor frequency $1/\tau_L$ at $I = 1$ W/m^2. Red dashed curve (almost obscuring the blue curve): fit (sum of two Lorentzians). Blue diamonds: *Exciter*. Solid green (dashed magenta) lines: $1/\tau_L$ at Paranal (SOR). b) $F = 2$ fractional sublevel populations, solid (dashed) curves: Bloch (*Exciter*) simulation.

polarization, but Larmor precession is powerful enough to completely suppress it at $\theta = \pi/2$, as evident from the monotonically falling magenta curve. Conversely, in the absence of Larmor precession ψ strongly peaks near $I = 2$ W/m^2.

At very low I, repumping is ineffective and even slightly decreases the return flux due to the smaller cross section of the D$_2$b transition, but at high I it is quite beneficial.

Figure 11.3(c) shows the $q = 0$ cases from Fig. 11.3(a), along with the same but neglecting recoil. Recoil leads to a significant reduction in ψ above 2 W/m^2.

Figure 11.4(a) shows ψ as a function of the Larmor frequency $1/\tau_L$ (solid line) at $I = 1$ W/m^2. The dashed line, overlapping the solid line, is a fit function composed of the sum of two Lorentzians of different widths, centered at the origin, plus a constant term. The (half-)width of the narrower Lorentzian (517 Hz $= 0.25\gamma_S$) is determined by the S-damping resonance, and that of the broader Lorentzian (17.9 kHz $= 0.63\gamma_{\rm vcc}$) by the velocity-changing collision rate, and the widths change proportionally when varying γ_S or $\gamma_{\rm vcc}$. However, both resonances are somewhat power-broadened. The geomagnetic field is strong enough at $I = 1$ W/m^2 to place us on the lowest terrace of the curve, as indicated by the vertical lines. The diamonds show the result of *Exciter* for comparison, also exhibiting the terraces.

Figure 11.4(b) shows the corresponding relative populations of the five $F = 2$ ground-state sublevels ($m = -2 \ldots 2$), where the solid lines indicate Bloch equations

Table 11.2: Sensitivity of ψ to a 1% perturbation in some simulation parameters under standard conditions.

Name of perturbed variable	Symbol	ψ change (%)
Mesospheric laser irradiance	I	0.025
Geomagnetic field in mesosphere	B	-0.33
Average mesospheric temperature	T_{Na}	-0.48
Beam atom exchange rate	γ_{ex}	0.0025
Weighted v.c.c.* rate	γ_{vcc}	0.15
Weighted spin-exchange rate at T_{Na}	γ_S	0.013
Recoil frequency (50 kHz)		-0.24

* v.c.c. = velocity-changing collision

and dotted lines *Exciter*. For $1/\tau_L > 300$ Hz, the sublevel populations collapse to the same value due to Larmor-induced sublevel mixing. Conversely, for $1/\tau_L < 300$ Hz, the populations diverge and the laser pumps the $m = 2$ sublevel most strongly. When increasing the irradiance to $I = 46$ W/m^2 (not shown in the plot), the curves in Fig. 11.4(b) would look similar, but the divergence point shifts upward to ~ 1 kHz. Furthermore, when plotting the sublevel populations at $I = 46$ W/m^2 as a function of θ, one observes that the magnetic field at Paranal is just strong enough to collapse the populations for $\theta \to \pi/2$. In other words, by scanning θ across the sky with a narrow-band 20-W-class laser, we can observe sodium excitation all the way from full optical pumping to no pumping at all, leading to a severe return flux penalty, as shown in the following figures.

Table 11.2 lists the sensitivity of ψ with respect to a 1% perturbation in some simulation parameter p, more precisely $\psi(1.01p)/\psi(p) - 1$, where all other parameters are those of Table 11.1. A value of b% in the last table column thus indicates that $\psi(p) \propto p^b$ in some range around the chosen value of p. We have selected only those parameters that we will not study in greater detail in the following subsections (except I). In addition, we have excluded those parameters around which ψ is stationary ($\psi'(p) = 0$), and also those parameters whose influence on the observed return flux is obviously linear, such as C_{Na}.

From Table 11.2, we notice that with the parameters of Table 11.1 the sensitivity to changes in I is small. A comparison with Fig. 11.3(b) shows that $\psi(I)$ is very shallow near $I = 46$ W/m^2 (the slope is actually weakly positive due to the magnetic resonance bump), meaning that $\Psi(I) = \psi I \propto I$ (i.e. the absolute photon return grows linearly with the irradiance). The dependence of ψ on B, however, is strong: Switching from $B = 0.23$ (Paranal) to $B = 0.48$ (SOR, factor 2.11) decreases ψ by a factor of 0.76. The scaling with temperature is fairly high as well since the width of the velocity distribution scales like $T_{\mathrm{Na}}^{1/2}$, and conversely its normalization (the number of Na atoms per velocity class) scales like $T_{\mathrm{Na}}^{-1/2}$. However, increasing T_{Na} from 185 K to 200 K, which may be a typical seasonal variation, reduces ψ by only 3.7%, and hence common temperature variations do not directly influence ψ much (we note that temperature influences the sodium abundance). Both γ_{ex} and γ_S have a small influence on ψ, mainly due to the presence of repumping, as Milonni *et al.* (1999) have also noted (for $q = 0$, the sensitivities are 0.049% and 0.56%, respectively).

We can draw two lessons here: First, there is little point in spending much effort improving the spin-exchange cross section $\sigma^S_{\mathrm{Na-O_2}}$ estimate, and, second, repumping makes ψ more robust toward some parameter variations, leading to higher stability in numerical simulations and possibly also in experiment. The variation of ψ with γ_{vcc} is much larger than with γ_S, and at first sight surprisingly, the derivative is positive. We explain the positivity by the fact that collisions mitigate spectral hole burning due to recoil (neglecting recoil, the derivative is -0.089%). Finally, we have included the average recoil frequency shift in the list, although it depends only on fundamental constants and λ (more precisely $h/(m_{\mathrm{Na}}\lambda^2) = 50.0$ kHz, with the atomic mass of Na $m_{\mathrm{Na}} = 3.819 \times 10^{-26}$ kg), in order to demonstrate the importance of proper recoil modeling at $I > 1$ W/m^2.

Holzlöhner *et al.* (2010) use the Bloch-equation simulation to optimize ψ with respect to light polarization ellipticity angle ε, repumping frequency offset Δf_{ab}, repumping power fraction q, and laser linewidth Δf, showing that the laser parameters of Table 11.1 are close to optimal, given the other conditions of the table. They focus on the case $\theta = \pi/2$ where the laser beam is directed orthogonal to the geomagnetic field (the worst case, for which LGS lasers must be designed to achieve a given return flux requirement).

In this work we have treated only steady-state sodium excitation with cw lasers. Pulsed lasers, with pulse durations close to or shorter than the sodium lifetime of 16 ns, will be dealt with in a forthcoming publication. However, we surmise that our present results are valid for microsecond laser pulses that are useful for mesospheric spot tracking and lidar (light detection and ranging).

11.2 Mesospheric magnetometry

11.2.1 Introduction

Measurements of geomagnetic fields are an important tool for peering into the earth's interior, with measurements at differing spatial scales giving information about sources at corresponding depths. Measurements of fields on the few-meter scale can locate buried ferromagnetic objects (e.g., unexploded ordnance or abandoned vessels containing toxic waste), while maps of magnetic fields on the kilometer scale are used to locate geological formations promising for mineral or oil extraction. On the largest scale, the earth's dipole field gives information about the geodynamo at depths of several thousand kilometers. Magnetic measurements at intermediate length scales, in the range of several tens to several hundreds of kilometers, likewise offer a window into important scientific phenomena, including the behavior of the outer mantle, the solar-quiet dynamo in the ionosphere (Campbell, 1989), and ionic currents as probes of ocean circulation (Tyler *et al.*, 2003), a major actor in models of climate change.

To avoid contamination from local perturbations, magnetic-field measurements on this length scale must typically be made at a significant height above the earth's surface. Though magnetic mapping at high altitude has been realized with satellite-borne magnetic sensors (Friis-Christensen *et al.*, 2006; Slavin *et al.*, 2008; Purucker *et al.*, 2007), the great expense of multi-satellite missions places significant limitations on their deployment and use. In this section we describe a high-sensitivity method of measuring magnetic fields, introduced by Higbie *et al.* (2009), that has 100-km spatial resolution and avoids the cost of spaceborne apparatus, by exploiting the naturally occurring atomic sodium layer in the mesosphere and the significant technological infrastructure developed for astronomical LGS. This method promises to enable creation of global sensor arrays for continuous mapping and monitoring of geomagnetic fields without interference from ground-based sources.

11.2.2 Principle of the method

The measurement we envisage is closely related to the techniques of atomic magnetometry, appropriately adapted to the conditions of the mesosphere. The principle of the method is to measure the magnetic field using spin precession of sodium atoms by creating atomic spin polarization, allowing it to evolve coherently in the magnetic field, and determining the post-evolution spin state. Conceptually, these processes are distinct and sequential, although in practice they may occur simultaneously and at different times for different atoms. Preparation of spin-polarized mesospheric sodium atoms is achieved by optical pumping as for a sodium

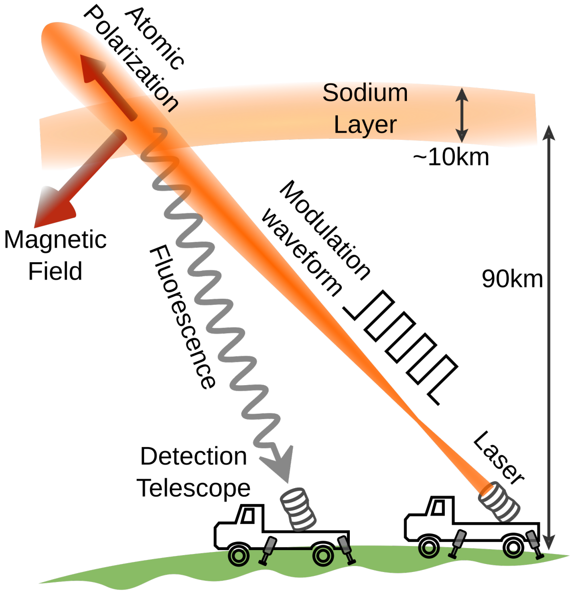

Figure 11.5: Fluorescent detection of magneto-optical resonance of mesospheric sodium (diagram not to scale). Circularly polarized laser light at 589 nm, modulated near the Larmor frequency, pumps atoms in the mesosphere. The resulting spin polarization (pictured as instantaneously oriented along the laser beam propagation direction) precesses around the local magnetic field. Fluorescence collected by a detection telescope exhibits a resonant dependence on the modulation frequency.

LGS discussed in Sec. 11.1. In the simplest realization, the pumping laser beam is circularly polarized and is launched from a telescope at an angle approximately perpendicular to the local magnetic field, as shown in Fig. 11.5. In the presence of the magnetic field, the transverse polarization generated by optical pumping precesses around the magnetic-field direction at the Larmor frequency. In order to avoid "smearing" of the atomic polarization due to this precession, the optical-pumping rate is modulated near the Larmor frequency, as first demonstrated by Bell and Bloom (1961). When the modulation frequency and the Larmor frequency coincide, a resonance results, and a substantial degree of atomic polarization is obtained. The atomic polarization in turn modifies the fluorescence from the sodium atoms, which can be detected by a ground-based telescope. This allows the sodium atoms to serve as a remote sensor of the magnitude of the magnetic field in the mesosphere (i.e. as a scalar magnetometer). By stationing lasers and detectors on a few-hundred-kilometer grid, a simultaneous map of magnetic fields may be obtained; alternatively, the laser and detector can be mounted on a relocatable stable platform such as a ship or truck to facilitate magnetic surveying. In contrast to both ground-based and satellite-based measurements, the platform is not required to be magnetically clean or quiet.

The magneto-optical resonance manifests itself as a sharp increase in the returned fluorescence for the D_2 line of sodium, or a decrease for the D_1 line, as a function of the modulation frequency. The sodium fluorescence may be captured either by a single-channel photodetector or by an imaging array (e.g., a CCD camera); the latter allows additional background discrimination and the possibility of separately analyzing fluorescence signals from different altitudes if the imaging and laser-beam axes are not parallel.

11.2.3 Measurement parameters

The magnetometric sensitivity of this technique is governed by the number of atoms involved in the measurement, the coherence time of the atomic spins, and the fraction of the total fluorescence intercepted by the detector, each of which we seek to maximize. A discussion of mesospheric properties relevant to LGS was given in Sec. 11.1. The Na number density of around 3×10^9 m^{-3} is low by vapor-cell standards, but the interaction volume and hence the atom number can be quite large, limited chiefly by available laser power. The coherence time is limited primarily by collisions with other atmospheric molecules and secondarily by atom loss from the region being probed (e.g., due to diffusion or wind). A velocity-changing collision occurring after an atom is pumped typically removes the atom from the subset of velocity classes which are nearly resonant with the laser light; as a consequence, these collisions result in an effective decay of spin polarization. Moreover, spin-exchange collisions of sodium atoms with unpolarized paramagnetic species in the mesosphere, predominantly O_2, result in a randomization of the electron spin, and therefore also lead to decay of sodium polarization. As discussed in Sec. 11.1.3, the spin-exchange cross section of oxygen with sodium has not been measured, but its magnitude can be estimated from other known spin-exchange cross sections to be on the order of 500 µs. In fact, it is anticipated that measurement of mesospheric coherence times via magnetic-field measurements will more tightly constrain this important LGS parameter. The fraction of intercepted fluorescence is determined by the solid angle subtended by the detection telescope and the angular emission pattern of the fluorescing atoms; for a 1-m^2 telescope and isotropic emission, the fraction is approximately 10^{-11} when the detector is directly below the fluorescing sample.

11.2.4 Results

One expects on intuitive grounds that the optimum laser intensity resonant with a single velocity class should be such that the characteristic rate of optical pumping $\Gamma_p \equiv \gamma_0 I/2I_{\rm sat}$ (where I is the laser intensity and $I_{\rm sat} \approx 60$ W/m^2 is the saturation intensity of the sodium cycling transition) is on the same order as the decay rate of atomic polarization. For higher intensities, optical pumping will "reset" the precession before its coherence time has been fully exploited, while use of lower intensities sacrifices signal without improving the coherence time.

We have performed a detailed density-matrix analysis of spin precession and optical pumping on the D_1 and D_2 transitions of sodium. In this analysis, we employ a circularly polarized pump laser beam oriented at right angles to a magnetic field of 0.5 G, with a spin-exchange collision time of 500 µs and a velocity-changing collision time of 200 µs. Most of the simulations in this section, in contrast to those in Sec. 11.1, are performed using rate equations for the ground state (Sec. 5.2.3) and assuming that the velocity groups are uncoupled. Since we employ optical intensities substantially lower than the saturation intensity, we expect the ground-state method to be accurate; we have also performed calculations of the resonance contrast for selected parameters using the full (ground and excited-state) optical Bloch equations. For a variety of settings of the pump light intensity and of the duty cycle (defined as the duration of a single pumping light pulse divided by the period of the modulation), we calculate resonance spectra as functions of the laser modulation frequency. Sample spectra for the laser tuned to the D_1 $F = 2 \rightarrow F' = 1$ and the D_2 $F = 2 \rightarrow F' = 3$ lines are shown in Fig. 11.6. From the width and peak height of these spectra, as well as the optical shot noise of the detected fluorescence, we calculate the magnetometric sensitivity. We assume that the noise is dominated by the fundamental shot noise and therefore neglect technical noise due to the photometric measurement. Contour plots of the sensitivity are shown as functions of the duty cycle and the laser intensity in Fig. 11.7 for the D_1 and D_2 lines. A fixed number of velocity classes is considered in these calculations (specifically fifteen, or five per excited-state hyperfine component), and the effective laser beam size is adjusted to maintain a constant launched laser power of 20 W (typical of the latest generation of LGS lasers), which results in different numbers of participating atoms for different laser intensities. The optimum sensitivity of $1.2\ \mathrm{nT}/\sqrt{\mathrm{Hz}}$ occurs on the D_1 transition, at a duty cycle of 25% and pump intensity during each pulse of $1.0\ \mathrm{W/m^2}$. The optimum intensity corresponds to an effective laser beam diameter in the mesosphere of around 5 m. This sensitivity is approximately one order of magnitude worse than the limit set by quantum spin-projection noise for the sodium atoms, presumably as a result of hyperfine structure and Doppler broadening. The optimum on the D_1 line offers superior magnetometric sensitivity in part because the D_1 resonances are dark, i.e., they result in a reduction of fluorescence, so that the photon shot noise is smaller and broadening of the resonance is reduced. If technical rather than fundamental noise sources dominate, then the D_2 resonance may be preferable for its larger signal size.

We note also that the time scale of velocity-changing collisions is comparable to the relaxation time of the atomic spins, so that it is likely for a given atom to interact

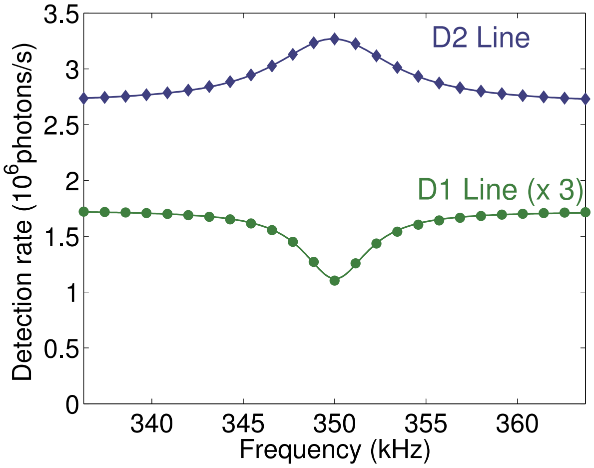

Figure 11.6: Calculated magneto-optical resonance profiles for mesospheric sodium. The resonances shown correspond to the D_2 F=2 → F'=3 (upper curve, blue diamonds) and D_1 F=2 → F'=1 (lower curve, green circles) sodium lines. The D_1 curve has been multiplied by a factor of three to improve visibility. Symbols are the results of numerical calculations, and solid lines are Lorentzian fits to these results. Calculations are for an intensity $I = 1$ W/m^2 and a modulation duty cycle of 20% with a detector collection area of 1 m^2.

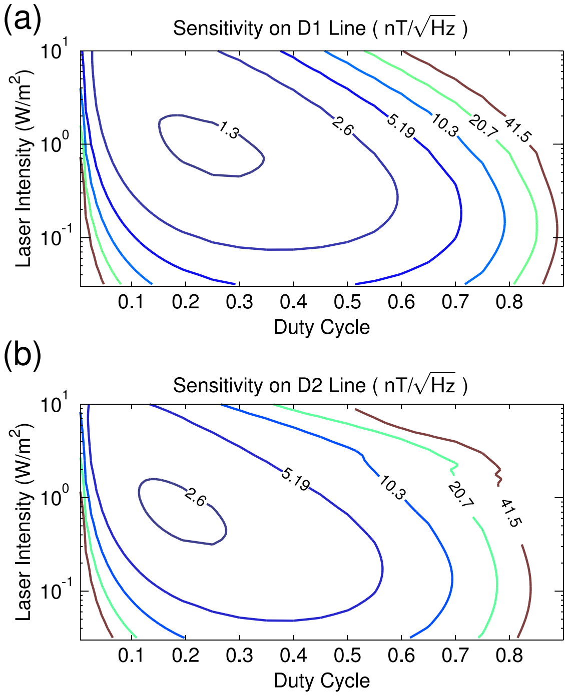

Figure 11.7: Contour plot of calculated magnetometer sensitivity as a function of pumping duty cycle and intensity. Sensitivity is calculated including the hyperfine effect for the D_2 F=2 → F'=3 and D_1 F=2→ F'=1 lines, using a detector area of 1 m^2, a spin-exchange collision time of 500 μs, and a velocity-changing collision time of 200 μs. Contours are logarithmically spaced at intervals of one octave.

more than once with the laser light while remaining in a single velocity class. Thus the excited-state hyperfine structure is resolved throughout the pumping and probing process, and proximity to a given ground-to-excited hyperfine transition can strongly influence the light-atom interaction (Auzinsh *et al.*, 2009a). For the same reason, magneto-optical resonances involving higher polarization multipoles such as alignment (which can be prepared by pumping with linearly polarized light) are expected to be observable in mesospheric sodium.

11.2.5 Additional effects

The magneto-optical resonance linewidth in mesospheric sodium is broader than in typical vapor-cell magnetometers; as a result, several effects important in vapor cells are less significant for mesospheric-sodium measurements. The quadratic Zeeman shift, for instance, leads to a splitting of the resonance into multiple resonances spaced by ∼150 Hz. However, since the width of the resonance at the optimum is around 5 kHz, this splitting will merely result in a small (and calculable) distortion of the lineshape. The natural inhomogeneity of the geomagnetic field will also affect the measurement, since the resonant frequency varies with altitude. Variation of the earth's field over the 10-km height of the sodium layer is on the order[3] of 100 nT, corresponding to about 700 Hz in Larmor frequency. Thus, although the modulation pumping laser cannot perfectly match the resonance frequency throughout the height of the mesosphere, this inhomogeneous broadening is again small compared to the width of the resonance at the sensitivity optimum. Consequently, we expect the effects of both the natural magnetic gradient and the quadratic Zeeman shift to be small. Temporal variations of the magnetic field in the mesosphere are, in principle, merely part of the signal being measured, and not an instrumental limitation. However, large enough fluctuations could make it difficult to track the resonance frequency. We take as a likely upper bound for the magnetic fluctuations on time scales of 1 s to 100 s the typical observed value at the earth's surface under ordinary conditions of around 1 nT. As this is again substantially smaller than the resonance linewidth, we expect that except during magnetic storms, it should not be difficult to keep the laser modulation frequency on resonance. Variations of the height and density of the sodium layer itself are an additional practical concern. A realistic measurement will require reducing sensitivity to such variations through comparison of on-resonant and off-resonant signals, either by temporally dithering the modulation frequency or by employing spatially separated pump beams with different modulation frequencies.

---

[3] National Geophysical Data Center (`http://www.ngdc.noaa.gov/geomagmodels/IGRFWMM.jsp`).

A further deviation of the real experiment from the idealization embodied in the calculations comes from turbulence in the lower atmosphere, which causes random phase shifts in distinct transverse patches of the laser beam. In the typical LGS application, the far-field diffraction (or speckle) pattern in the mesosphere from these low-altitude phase patches consists of elongated filaments whose individual lateral size is set by the numerical aperture of the laser launch telescope, but whose collective extent is governed by the size of the atmospheric patches (Happer *et al.*, 1994). Fluctuation of these filaments in time results in undesirable effects including random changes in pump-laser intensity in the mesosphere, motion of the illuminated column, and variation of the returned fluorescence. The relatively low intensity and large beam area indicated by our magnetometry calculations make such filamentation a lesser concern, however, since the beam diameter may be kept within the Fried length (Fried, 1966) of around 0.1 m in the most turbulent region of the lower atmosphere. Although lensing and beam-steering due to atmospheric variations will prevent precise fine-tuning of laser intensity, we do not anticipate that such variations will strongly affect the sensitivity obtainable with the proposed technique. We plan nevertheless to perform detailed modeling of atmospheric effects using physical optics, as has recently been done with reference to LGS (Holzlöhner *et al.*, 2008).

11.2.6 Conclusions

In conclusion, we have presented a promising alternative to satellite missions for the measurement of geomagnetic fields. The proposed method requires only ground-based apparatus, and is consequently substantially less expensive per sensor than a satellite formation, while still achieving high magnetometric sensitivity. We anticipate that the low cost of deployment will make possible large-scale magnetic mapping and monitoring applications at the 100-km length scale, with temporal and spatial coverage that would be difficult to obtain by current techniques. Furthermore, as satellites cannot be operated as low as 100 km in altitude without excessive drag and heating, remotely detected mesospheric magnetometry promises superior spatial resolution of terrestrial sources. In addition, the technique offers to supplement existing ground-based magnetic observatory data, allowing high-precision magnetic monitoring from a mobile platform without the requirement of a large-area, remote, and magnetically clean observation site on the earth's surface. We are currently constructing a 20-W-class laser projection system and working to implement this technique in proof-of-principle magnetic-field measurements.

Chapter 12

Conclusion

We have discussed methods for density-matrix modeling of nonlinear magneto-optical effects. These effects can be exquisitely sensitive to energy-level shifts, making them useful for applications such as magnetometry and tests of fundamental physics (Budker and Romalis, 2007). Modeling can aid in understanding these effects, and in analyzing and optimizing devices based on them. We have given several examples of this, addressing such topics as polarization dynamics in rf fields, the effect of hyperfine structure on the creation and detection of polarization, and optimization of systems for laser guide stars.

There are many ways in which the techniques described in this work can be extended. More detailed descriptions of relaxation processes can be implemented, and additional effects such as radiation trapping (Molisch and Oehry, 1998) can be accounted for. More efficient numerical methods and optimized code can allow larger systems and systems with more widely separated time scales to be modeled. Calculations of quantum noise can allow predictions of magnetometric sensitivity, including the effects of squeezed atomic and light-polarization states (Matsko *et al.*, 2002; Auzinsh *et al.*, 2004). Inclusion of interatomic interactions and correlations can allow the description of atoms in optical lattices, Bose-Einstein condensates, and applications in quantum information and quantum computing (Anderlini *et al.*, 2007). Finally, it may be possible to adapt models for atoms to describe similar systems, such as interactions between nuclei (Ledbetter *et al.*, 2009) and nitrogen-vacancy centers in diamond (Acosta *et al.*, 2010).

Bibliography

Acosta, V., Ledbetter, M. P., Rochester, S. M., Budker, D., Jackson Kimball, D. F., Hovde, D. C., Gawlik, W., Pustelny, S., Zachorowski, J. and Yashchuk, V. V. (2006). *Phys. Rev. A*, **73**, 053404.

Acosta, V. M., Auzinsh, M., Gawlik, W., Grisins, P., Higbie, J. M., Kimball, D. F. J., Krzemien, L., Ledbetter, M. P., Pustelny, S., Rochester, S. M., Yashchuk, V. V. and Budker, D. (2008). *Opt. Express*, **16**, 11423.

Acosta, V. M., Bauch, E., Jarmola, A., Zipp, L. J., Ledbetter, M. P. and Budker, D. (2010). *Appl. Phys. Lett.*, **97**, 174104.

Ageorges, N. and Dainty, C. (eds.) (2000). *Laser Guide Star Adaptive Optics for Astronomy.* Kluwer Academic Publishers, Boston.

Aleksandrov, E. B., Chaika, M. P. and Khvostenko, G. I. (1993). *Interference of Atomic States.* Springer Series on Atoms and Plasmas; 7, Springer-Verlag, Berlin.

Alexandrov, E. B., Auzinsh, M., Budker, D., Kimball, D. F., Rochester, S. M. and Yashchuk, V. V. (2005). *J. Opt. Soc. Am. B*, **22**, 7.

Alexandrov, E. B., Balabas, M. V., Pasgalev, A. S., Vershovskii, A. K. and Yakobson, N. N. (1996). *Laser Phys.*, **6**, 244.

Alexandrov, E. B. and Bonch-Bruevich, V. A. (1992). *Opt. Eng.*, **31**, 711.

Allegrini, M., Arimondo, E. and Bambini, A. (1977). *Phys. Rev. A*, **15**, 718.

Anderlini, M., Lee, P. J., Brown, B. L., Sebby-Strabley, J., Phillips, W. D. and Porto, J. V. (2007). *Nature*, **448**, 452.

Auzinsh, M. (1997). *Can. J. Phys.*, **75**, 853.

Auzinsh, M., Blushs, K., Ferber, R., Gahbauer, F., Jarmola, A. and Tamanis, M. (2006). *Phys. Rev. Lett.*, **97**, 043002.

Auzinsh, M., Budker, D., Kimball, D. F., Rochester, S. M., Stalnaker, J. E., Sushkov, A. O. and Yashchuk, V. V. (2004). *Phys. Rev. Lett.*, **93**, 173002.

Auzinsh, M., Budker, D. and Rochester, S. M. (2009a). *Phys. Rev. A*, **80**, 053406.

——— (2010). *Optically Polarized Atoms: Understanding Light–Atom Interactions.* Oxford University Press, Oxford.

Auzinsh, M. and Ferber, R. (1992). *Phys. Rev. Lett.*, **69**, 3464.

——— (1995). *Optical Polarization of Molecules.* Cambridge University Press, Cambridge.

Auzinsh, M., Ferber, R., Gahbauer, F., Jarmola, A. and Kalvans, L. (2009b). *Phys. Rev. A*, **79**, 053404.

Auzinsh, M. P. and Ferber, R. S. (1991). *Phys. Rev. A*, **43**, 2374.

Balabas, M. V., Karaulanov, T., Ledbetter, M. P. and Budker, D. (2010). *Phys. Rev. Lett.*, **105**, 070801.

Barrat, J. P. and Cohen-Tannoudji, C. (1961). *J. Phys. Radium*, **22**, 329.

Bell, W. and Bloom, A. (1961). *Phys. Rev. Lett.*, **6**, 280.

Bennett, W. R. (1962). *Phys. Rev.*, **126**, 580.

Bergmann, K., Theuer, H. and Shore, B. W. (1998). *Rev. Mod. Phys.*, **70**, 1003.

Berry, M. V. (1984). *Proc. R. Soc. London, Ser. A*, **392**, 45.

Bison, G., Wynands, R. and Weis, A. (2003). *Appl. Phys. B: Lasers Opt.*, **76**, 325, 10.1007/s00340-003-1120-z.

Blum, K. (1996). *Density Matrix Theory and Applications.* Physics of Atoms and Molecules, Plenum Press, New York, 2nd ed.

Blushs, K. and Auzinsh, M. (2004). *Phys. Rev. A*, **69**, 063806.

Bouchiat, M.-A. (1963a). *J. Phys. France*, **24**, 379.

——— (1963b). *J. Phys. France*, **24**, 611.

Bouchiat, M. A. and Brossel, J. (1966). *Phys. Rev.*, **147**, 41.

Bradley, L. C. (1992). *J. Opt. Soc. Am. B*, **9**, 1931.

Bradley, R., Clarke, J., Kinion, D., Rosenberg, L. J., Bibber, K., Matsuki, S., Muck, M. and Sikivie, P. (2003). *Rev. Mod. Phys.*, **75**, 777.

Brandt, S. (1999). *Data Analysis: Statistical and Computational Methods for Scientists and Engineers*. Springer, New York, 3rd ed.

Brink, D. M. and Satchler, G. R. (1993). *Angular Momentum*. Clarendon Press, Oxford.

Brossel, J. and Bitter, F. (1952). *Phys. Rev.*, **86**, 308.

Budker, D., Gawlik, W., Kimball, D. F., Rochester, S. M., Yashchuk, V. V. and Weis, A. (2002a). *Rev. Mod. Phys.*, **74**, 1153.

Budker, D., Kimball, D. F. and DeMille, D. (2008). *Atomic Physics. An Exploration through Problems and Solutions*. Oxford University Press, Oxford, 2nd ed.

Budker, D., Kimball, D. F., Rochester, S. M. and Urban, J. T. (2003). *Chem. Phys. Lett.*, **378**, 440.

Budker, D., Kimball, D. F., Rochester, S. M. and Yashchuk, V. V. (1999a). *Phys. Rev. Lett.*, **83**, 1767.

——— (2000a). *Phys. Rev. Lett.*, **85**, 2088.

——— (2002b). *Phys. Rev. A*, **65**, 033401.

Budker, D., Kimball, D. F., Rochester, S. M., Yashchuk, V. V. and Zolotorev, M. (2000b). *Phys. Rev. A*, **62**, 043403.

Budker, D., Kimball, D. F., Yashchuk, V. V. and Zolotorev, M. (2002c). *Phys. Rev. A*, **65**, 055403.

Budker, D., Lamoreaux, S. K., Sushkov, A. O. and Sushkov, O. P. (2006). *Phys. Rev. A*, **73**, 022107.

Budker, D., Orlando, D. J. and Yashchuk, V. (1999b). *Am. J. Phys.*, **67**, 584.

Budker, D. and Rochester, S. M. (2004). *Phys. Rev. A*, **70**, 25804.

Budker, D. and Romalis, M. V. (2007). *Nature Phys.*, **3**, 227.

Budker, D., Yashchuk, V. and Zolotorev, M. (1998). *Phys. Rev. Lett.*, **81**, 5788.

Campbell, W. (1989). *Pure Appl. Geophys.*, **131**, 315.

Chakmakjian, S., Koch, K. and C. R. Stroud, J. (1988). *J. Opt. Soc. Am. B*, **5**, 2015.

Chalupczak, W., Josephs-Franks, P., Pustelny, S. and Gawlik, W. (2010). *Phys. Rev. A*, **81**, 013422.

Chin, C., Leiber, V., Vuletic, V., Kerman, A. J. and Chu, S. (2001). *Phys. Rev. A*, **63**, 033401.

Cohen-Tannoudji, C. (1962a). *Ann. Phys. (Paris)*, **7**, 423.

——— (1962b). *Ann. Phys. (Paris)*, **7**, 469.

——— (1994). *Atoms in Electromagnetic Fields.* World Scientific, Singapore.

Corney, A. (2006). *Atomic and Laser Spectroscopy.* Oxford: Clarendon Press, Oxford.

Corwin, K. L., Zheng-Tian, L., Hand, C. F., Epstein, R. J. and Wieman, C. E. (1998). *Appl. Opt.*, **37**, 3295.

Denman, C. A., Drummond, J. D., Eickhoff, M. L., Fugate, R. Q., Hillman, P. D., Novotny, S. J. and Telle, J. M. (2006). B. L. Ellerbroek and D. B. Calia (eds.), *Advances in Adaptive Optics II*, Proc. of SPIE, vol. 6272, p. 62721L.

Di Domenico, G., Bison, G., Groeger, S., Knowles, P., Pazgalev, A. S., Rebetez, M., Saudan, H. and Weis, A. (2006). *Phys. Rev. A*, **74**, 063415.

Dmitriev, S. P., Dovator, N. A. and Kartoshkin, V. A. (2008). *Tech. Phys. Lett.*, **34**, 693.

Dougherty, M. K., Achilleos, N., Andre, N., Arridge, C. S., Balogh, A., Bertucci, C., Burton, M. E., Cowley, S. W. H., Erdos, G., Giampieri, G., Glassmeier, K.-H., Khurana, K. K., Leisner, J., Neubauer, F. M., Russell, C. T., Smith, E. J., Southwood, D. J. and Tsurutani, B. T. (2005). *Science*, **307**, 1266.

Dougherty, M. K., Khurana, K. K., Neubauer, F. M., Russell, C. T., Saur, J., Leisner, J. S. and Burton, M. E. (2006). *Science*, **311**, 1406.

Dowling, J. P., Agarwal, G. S. and Schleich, W. P. (1994). *Phys. Rev. A*, **49**, 4101.

Ducloy, M. (1976). *J. Phys. B*, **9**, 357.

Dyakonov, M. I. (1964). *Zh. Eksp. Teor. Fiz.*, **47**, 2213.

——— (1965). *Sov. Phys. JETP*, **20**, 1484.

Edmonds, A. R. (1996). *Angular momentum in quantum mechanics.* Princeton University, Princeton, N.J.

Fano, U. and Racah, G. (1959). *Irreducible Tensorial Sets.* Academic Press, New York.

Fishbane, P. M., Gasiorowicz, S. G. and Thornton, S. T. (2005). *Physics for scientists and engineers.* Pearson Prentice Hall.

Fleischhauer, M., Imamoglu, A. and Marangos, J. P. (2005). *Rev. Mod. Phys.*, **77**, 633.

Fried, D. L. (1966). *J. Opt. Soc. Am.*, **56**, 1372.

Friedmann, H. and Wilson-Gordon, A. D. (1987). *Phys. Rev. A*, **36**, 1333.

Friis-Christensen, E., Luhr, H. and Hulot, G. (2006). *Earth, Planets and Space*, **58**, 351.

Garroway, A., Buess, M., Miller, J., Suits, B., Hibbs, A., Barrall, G., Matthews, R. and Burnett, L. (2001). *IEEE Trans. Geosci. Remote Sens.*, **39**, 1108 .

Graf, M. T., Kimball, D. F., Rochester, S. M., Kerner, K., Wong, C., Budker, D., Alexandrov, E. B., Balabas, M. V. and Yashchuk, V. V. (2005). *Phys. Rev. A*, **72**, 023401.

Grossetête, F. (1964). *J. Phys. France*, **25**, 383.

——— (1968). *J. Phys. France*, **29**, 456.

Happer, W. (1972). *Rev. Mod. Phys.*, **44**, 169.

Happer, W., Jau, Y.-Y. and Walker, T. (2010). *Optically Pumped Atoms.* John Wiley-VCH.

Happer, W., MacDonald, G. J., Max, C. E. and Dyson, F. J. (1994). *J. Opt. Soc. Am. A*, **11**, 263.

Happer, W. and Mathur, B. (1967). *Phys. Rev.*, **163**, 12.

Happer, W., Miron, E., Schaefer, S., Schreiber, D., van Wijngaarden, W. A. and Zeng, X. (1984). *Phys. Rev. A*, **29**, 3092.

Happer, W. and Van Wijngaarden, W. (1987). *Hyperfine Interact.*, **38**, 435, 10.1007/BF02394855.

Harris, S. E. (1997). *Phys. Today*, **50**, 36.

Higbie, J. M., Rochester, S. M., Patton, B., Holzlöhner, R., Calia, D. B. and Budker, D. (2009). *Magnetometry with mesospheric sodium*, arXiv:0912.4310 [physics.atom-ph].

Hillman, P. D., Drummond, J. D., Denman, C. A. and Fugate, R. Q. (2008). N. Hubin, C. E. Max and P. L. Wizinowich (eds.), *Adaptive Optics Systems*, Proc. of SPIE, vol. 7015, p. 70150L.

Holzlöhner, R., Calia, D. B. and Hackenberg, W. (2008). N. Hubin, C. E. Max and P. L. Wizinowich (eds.), *Adaptive Optics Systems*, Proc. of SPIE, vol. 7015, p. 701521.

Holzlöhner, R., Rochester, S. M., Bonaccini Calia, D., Budker, D., Higbie, J. M. and Hackenberg, W. (2010). *Astron. Astrophys.*, **510**, A20+.

Holzlöhner, R., Rochester, S. M., Pfrommer, T., Calia, D. B., Budker, D., Higbie, J. M. and Hackenberg, W. (2010). B. L. Ellerbroek, M. Hart, N. Hubin and P. L. Wizinowich (eds.), *Adaptive Optics Systems II*, Proc. of SPIE, vol. 7736, p. 77360V.

Jackson Kimball, D. F., Jacome, L. R., Guttikonda, S., Bahr, E. J. and Chan, L. F. (2009). *J. Appl. Phys.*, **106**, 063113.

Jackson Kimball, D. F., Neitzke, O., Bahr, E. J., Guttikonda, S., Rochester, S. M., Ledbetter, M. P., Novikova, I., Coste, B., Rangwala, S. A., Higbie, J. M., Okunevich, A. I., Yashchuk, V. V. and Budker, D. (2010). In preparation.

Judd, B. R. (1998). *Operator Techniques in Atomic Spectroscopy.* Princeton University Press, Princeton, N.J.

Kanorskii, S. I., Weis, A. and Skalla, J. (1995). *Appl. Phys. B: Lasers Opt.*, **60**, S165.

Kanorsky, S. I., Weis, A., Wurster, J. and Hänsch, T. W. (1993). *Phys. Rev. A*, **47**, 1220.

Kartoshkin, V. A. (1998). *Opt. Spectrosc.*, **85**, 177.

Kastler, A. (1950). *J. Phys. Radium*, **11**, 225.

Keilson, J. and Storer, J. (1952). *Q. Appl. Math.*, **10**, 243.

Kibblewhite, E. (2009). *Advanced Maui Optical and Space Surveillance Technologies Conference*, p. E33.

Kleppner, D., Ramsey, N. F. and Fjelstadt, P. (1958). *Phys. Rev. Lett.*, **1**, 232.

Kocharovskaya, O. A. and Khanin Ya, I. (1988). *JETP Lett.*, **48**, 630.

Kominis, I. K., Kornack, T. W., Allred, J. C. and Romalis, M. V. (2003). *Nature*, **422**, 596.

Kornack, T. W., Ghosh, R. K. and Romalis, M. V. (2005). *Phys. Rev. Lett.*, **95**, 230801.

Landau, L. D. and Lifshitz, E. M. (1977). *Quantum Mechanics: Non-Relativistic Theory*. Pergamon Press, Oxford, 3d ed.

Ledbetter, M., Crawford, C., Pines, A., Wemmer, D., Knappe, S., Kitching, J. and Budker, D. (2009). *J. Magn. Reson.*, **199**, 25 .

Ledbetter, M. P., Acosta, V. M., Rochester, S. M., Budker, D., Pustelny, S. and Yashchuk, V. V. (2007). *Phys. Rev. A*, **75**, 023405.

Ledbetter, M. P., Savukov, I. M., Acosta, V. M., Budker, D. and Romalis, M. V. (2008). *Phys. Rev. A*, **77**, 033408.

Lee, S.-K., Sauer, K. L., Seltzer, S. J., Alem, O. and Romalis, M. V. (2006). *Appl. Phys. Lett.*, **89**, 214106.

Lehmann, J. (1967). *Ann. Phys. (Paris)*, **2**, 345.

Lezama, A., Barreiro, S. and Akulshin, A. M. (1999). *Phys. Rev. A*, **59**, 4732.

Macaluso, D. and Corbino, O. M. (1898). *Nuovo Cimento*, **8**, 257.

——— (1899). *Nuovo Cimento*, **9**, 384.

Malakyan, Y. P., Rochester, S. M., Budker, D., Kimball, D. F. and Yashchuk, V. V. (2004). *Phys. Rev. A*, **69**, 013817.

Matsko, A. B., Novikova, I., Welch, G. R., Budker, D., Kimball, D. F. and Rochester, S. M. (2002). *Phys. Rev. A*, **66**, 043815.

Milonni, P. W., Fearn, H., Telle, J. M. and Fugate, R. Q. (1999). *J. Opt. Soc. Am. A*, **16**, 2555.

Milonni, P. W., Fugate, R. Q. and Telle, J. M. (1998). *J. Opt. Soc. Am. A*, **15**, 217.

Milonni, P. W. and Thode, L. E. (1992). *Appl. Opt.*, **31**, 785.

Molisch, A. F. and Oehry, B. P. (1998). *Radiation trapping in atomic vapours*. Clarendon Press, New York.

Morgan, S. W. and Happer, W. (2010). *Phys. Rev. A*, **81**, 042703.

Morris, J. R. (1994). *J. Opt. Soc. Am. A*, **11**, 832.

Moussaoui, N., Clemesha, B. R., Holzlöhner, R., Simonich, D. M., Bonaccini Calia, D., Hackenberg, W. and Batista, P. P. (2010). *Astron. Astrophys.*, **511**, A31.

Moussaoui, N., Holzlöhner, R., Hackenberg, W. and Bonaccini Calia, D. (2009). *Astron. Astrophys.*, **501**, 793.

Nagengast, W., Nass, A., Grosshauser, C., Rith, K. and Schmidt, F. (1998). *J. Appl. Phys.*, **83**, 5626.

Nasyrov, K., Cartaleva, S., Petrov, N., Biancalana, V., Dancheva, Y., Mariotti, E. and Moi, L. (2006). *Phys. Rev. A*, **74**, 13811.

Novikova, I., Matsko, A. B., Velichansky, V. L., Scully, M. O. and Welch, G. R. (2001). *Phys. Rev. A*, **63**, 063802.

Okunevich, A. (2004). *Opt. Spectrosc.*, **97**, 834, 10.1134/1.1843940.

Okunevich, A. I. (1994). *Opt. Spectrosc.*, **77**, 178.

——— (1995). *Opt. Spectrosc.*, **79**, 12.

——— (2005). *J. Opt. Soc. Am. B*, **22**, 29.

Omont, A. (1965). *J. Phys. France*, **26**, 26.

Pfrommer, T., Hickson, P. and She, C.-Y. (2009). *Geophys. Res. Lett.*, **36**, L15831.

Pique, J.-P., Moldovan, I. C. and Fesquet, V. (2006). *J. Opt. Soc. Am. A*, **23**, 2817.

Purucker, M., Sabaka, T., Le, G., Slavin, J. A., Strangeway, R. J. and Busby, C. (2007). *Geophys. Res. Lett.*, **34**, L24306.

Pustelny, S., Gawlik, W., Rochester, S. M., Kimball, D. F. J., Yashchuk, V. V. and Budker, D. (2006a). *Phys. Rev. A*, **74**, 063420.

Pustelny, S., Jackson Kimball, D. F., Rochester, S. M., Yashchuk, V. V., Gawlik, W. and Budker, D. (2006b). *Phys. Rev. A*, **73**, 023817.

Pustelny, S., Wojciechowski, A., Kotyrba, M., Sycz, K., Zachorowski, J., Gawlik, W., Cingoz, A., Leefer, N., Higbie, J. M., Corsini, E., Ledbetter, M. P., Rochester, S. M., Sushkov, A. O. and Budker, D. (2007). P. A. Atanasov, T. N. Dreischuh, S. V. Gateva and L. M. Kovachev (eds.), *14th International School on Quantum Electronics: Laser Physics and Applications*, Proc. of SPIE, vol. 6604, p. 660404.

Ramsey, A. and Anderson, L. (1964). *Il Nuovo Cimento*, **32**, 1151.

Ramsey, N. F. (1990). *Rev. Mod. Phys.*, **62**, 541.

Risken, H. and Vollmer, H. D. (1980). *Z. Phys. B: Condens. Matter Quanta*, **39**, 339.

Robinson, H., Ensberg, E. and Dehmelt, H. (1958). *Bull. Am. Phys. Soc.*, **3**, 9.

Rochester, S. M. and Budker, D. (2001). *Am. J. Phys.*, **69**, 450.

Rochester, S. M., Hsiung, D. S., Budker, D., Chiao, R. Y., Kimball, D. F. and Yashchuk, V. V. (2001). *Phys. Rev. A*, **63**, 043814.

Sakurai, J. J. and Tuan, S. F. (1994). *Modern Quantum Mechanics*. Addison-Wesley, Reading, Mass.

Schuh, B., Kanorsky, S. I., Weis, A. and Hänsch, T. W. (1993). *Opt. Commun.*, **100**, 451.

Scully, M. O., Shi-Yao, Z. and Gavrielides, A. (1989). *Phys. Rev. Lett.*, **62**, 2813.

Shore, B. W. (1990). *The Theory of Coherent Atomic Excitation*. John Wiley, New York.

Simonich, D. M., Clemesha, B. R. and Kirchhoff, V. W. J. H. (1979). *J. Geophys. Res.*, **84**, 1543.

Skalla, J. and Waeckerle, G. (1997). *Appl. Phys. B: Lasers Opt.*, **B64**, 459.

Slavin, J. A., Le, G., Strangeway, R. J., Wang, Y., Boardsen, S. A., Moldwin, M. B. and Spence, H. E. (2008). *Geophys. Res. Lett.*, **35**, L02107.

Sobelman, I. I. (1992). *Atomic Spectra and Radiative Transitions.* Springer, Berlin.

Stenholm, S. (2005). *Foundations of Laser Spectroscopy.* Dover Publications, Mineola, N.Y.

Telle, J., Drummond, J., Denman, C., Hillman, P., Moore, G., Novotny, S. and Fugate, R. (2006). C. Y. Young and G. C. Gilbreath (eds.), *Atmospheric Propagation III*, Proc. of SPIE, vol. 6215, p. 62150K.

Telle, J., Drummond, J., Hillman, P. and Denman, C. (2008). O. Korotkova (ed.), *Atmospheric Propagation of Electromagnetic Waves II*, Proc. of SPIE, vol. 6878, p. 68780G.

Thomas, S. J., Gavel, D., Adkins, S. and Kibrick, B. (2008). N. Hubin, C. E. Max and P. L. Wizinowich (eds.), *Adaptive Optics Systems*, Proc. of SPIE, vol. 7015, p. 70155L.

Tyler, R. H., Maus, S. and Luhr, H. (2003). *Science*, **299**, 239.

Vallés, J. A. and Alvarez, J. M. (1994). *Phys. Rev. A*, **50**, 2490.

——— (1996). *Phys. Rev. A*, **54**, 977.

van der Vorst, H. A. (1992). *SIAM J. Sci. Stat. Comput.*, **13**, 631.

Varshalovich, D. A., Moskalev, A. N. and Khersonskii, V. K. (1988). *Quantum Theory of Angular Momentum: Irreducible Tensors, Spherical Harmonics, Vector Coupling Coefficients, 3j Symbols.* World Scientific, Singapore.

Walker, T. G. and Happer, W. (1997). *Rev. Mod. Phys.*, **69**, 629.

Wasilewski, W., Jensen, K., Krauter, H., Renema, J. J., Balabas, M. V. and Polzik, E. S. (2010). *Phys. Rev. Lett.*, **104**, 133601.

Weis, A., Bison, G. and Pazgalev, A. S. (2006). *Phys. Rev. A*, **74**, 033401.

Wright, M. (2004). *An Introduction to Chemical Kinetics.* Wiley, New York.

Xia, H., Baranga, A. B.-A., Hoffman, D. and Romalis, M. V. (2006). *Appl. Phys. Lett.*, **89**, 211104.

Xu, S., Crawford, C. W., Rochester, S. M., Yashchuk, V. V., Budker, D. and Pines, A. (2008). *Phys. Rev. A*, **78**, 013404.

Xu, S., Rochester, S. M., Yashchuk, V. V., Donaldson, M. H. and Budker, D. (2006a). *Rev. Sci. Instrum.*, **77**, 083106.

Xu, S., Yashchuk, V. V., Donaldson, M. H., Rochester, S. M., Budker, D. and Pines, A. (2006b). *Proc. Natl. Acad. Sci.*, **103**, 12668.

Yashchuk, V., Budker, D. and Davis, J. (2000). *Rev. Sci. Instrum.*, **71**, 341.

Yashchuk, V. V., Budker, D., Gawlik, W., Kimball, D. F., Malakyan, Y. P. and Rochester, S. M. (2003). *Phys. Rev. Lett.*, **90**, 253001.

Yashchuk, V. V., Granwehr, J., Kimball, D. F., Rochester, S. M., Trabesinger, A. H., Urban, J. T., Budker, D. and Pines, A. (2004). *Phys. Rev. Lett.*, **93**, 160801.

Youdin, A. N., Krause, J., D., Jagannathan, K., Hunter, L. R. and Lamoreaux, S. K. (1996). *Phys. Rev. Lett.*, **77**, 2170.

Zare, R. (1988). *Angular Momentum: Understanding Spatial Aspects in Chemistry and Physics.* John Wiley, New York.

Zigdon, T., Wilson-Gordon, A. D., Guttikonda, S., Bahr, E. J., Neitzke, O., Rochester, S. M. and Budker, D. (2010). *Opt. Express*, **18**, 25494.

Appendix A

Classical Rotations

The theory of rotations is very important for the discussion of angular momentum, and consequently atomic physics. In this appendix we discuss classical rotations in the Cartesian and spherical bases, and introduce the concepts of covariance and contravariance.

A.1 Rotations in the Cartesian basis

Suppose we have a vector $\mathbf{v}$ in three-dimensional space and have chosen a Cartesian basis $\hat{\mathbf{x}}_i$, so that we can write $\mathbf{v}$ in terms of its Cartesian components v_i:

$$\mathbf{v} = \hat{\mathbf{x}}_i v_i, \quad \text{with} \quad v_i = \hat{\mathbf{x}}_i \cdot \mathbf{v}, \tag{A.1}$$

where we use the orthonormality of the Cartesian basis: $\hat{\mathbf{x}}_i \cdot \hat{\mathbf{x}}_j = \delta_{ij}$.

Now consider a rotation of $\mathbf{v}$ by an angle θ about a direction $\hat{\mathbf{n}}$ to obtain a rotated vector $\mathbf{v}' = R_{\hat{\mathbf{n}}}(\theta)\mathbf{v}$, where $R_{\hat{\mathbf{n}}}(\theta)$ (abbreviated as R) is the rotation operator. The right-hand rule is used to fix the rotation direction: if the thumb of the right hand points along $\hat{\mathbf{n}}$, the fingers curl in the direction of a positive rotation. We can expand the rotated vector in the Cartesian basis to obtain

$$\mathbf{v}' = R\mathbf{v} = R\hat{\mathbf{x}}_i v_i = \hat{\mathbf{x}}_j \hat{\mathbf{x}}_j \cdot R\hat{\mathbf{x}}_i v_i = \hat{\mathbf{x}}_j \mathsf{R}_{ji} v_i, \tag{A.2}$$

where $\mathsf{R}_{ji} = \hat{\mathbf{x}}_j \cdot R\hat{\mathbf{x}}_i$ is the rotation matrix corresponding to R. If we consider R to act on the components v_i, as indicated in Eq. (A.2), we see that they are transformed to a new set of components v'_i according to $v'_i = \mathsf{R}_{ij} v_j$, and the rotation of $\mathbf{v}$ can be written $\mathbf{v}' = \hat{\mathbf{x}}_i v'_i$. A rotation thought of in this way, in which the basis vectors are held fixed and the vector components are rotated, is called an *active rotation*. An

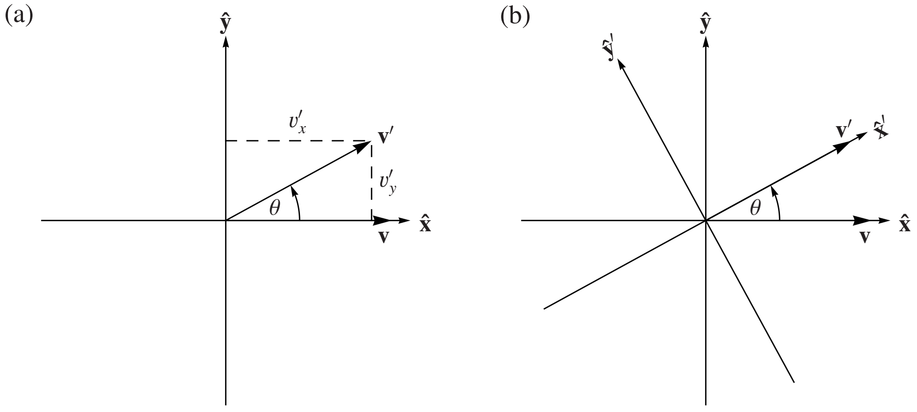

Figure A.1: A rotation of a vector $\mathbf{v}$, originally along the $\hat{\mathbf{x}}$ direction, by an angle θ about the $\hat{\mathbf{z}}$ direction. By inspection, we find that $v'_x = |\mathbf{v}|\cos\theta$ and $v'_y = |\mathbf{v}|\sin\theta$.

example of an active rotation by an angle θ about the $\hat{\mathbf{z}}$ direction shown in Fig. A.1. From trigonometric arguments, we can find that the rotation matrix in this case is given by

$$\mathsf{R}_{\hat{\mathbf{z}}}(\theta) = \begin{pmatrix} \cos\theta & -\sin\theta & 0 \\ \sin\theta & \cos\theta & 0 \\ 0 & 0 & 1 \end{pmatrix}. \tag{A.3}$$

Writing the expressions in matrix notation, and using the case of Fig. A.1(a),

$$\mathbf{v} = \hat{\mathbf{x}} = \begin{pmatrix} \hat{\mathbf{x}} & \hat{\mathbf{y}} & \hat{\mathbf{z}} \end{pmatrix} \begin{pmatrix} 1 \\ 0 \\ 0 \end{pmatrix}, \tag{A.4}$$

as an example, we have for the rotated vector components

$$\begin{pmatrix} v'_x \\ v'_y \\ v'_z \end{pmatrix} = \begin{pmatrix} \cos\theta & -\sin\theta & 0 \\ \sin\theta & \cos\theta & 0 \\ 0 & 0 & 1 \end{pmatrix} \begin{pmatrix} 1 \\ 0 \\ 0 \end{pmatrix} = \begin{pmatrix} \cos\theta \\ \sin\theta \\ 0 \end{pmatrix}, \tag{A.5}$$

and for the vector itself,

$$\mathbf{v}' = \begin{pmatrix} \hat{\mathbf{x}} & \hat{\mathbf{y}} & \hat{\mathbf{z}} \end{pmatrix} \begin{pmatrix} \cos\theta \\ \sin\theta \\ 0 \end{pmatrix} = \hat{\mathbf{x}}\cos\theta + \hat{\mathbf{y}}\sin\theta. \tag{A.6}$$

It is also possible to think of the rotation matrix in Eq. (A.2) as acting on the basis vectors $\hat{\mathbf{x}}_i$. A general property of rotation matrices in the Cartesian basis is that they are *orthogonal*, meaning that their transpose equals their inverse: $\mathsf{R}^t = \mathsf{R}^{-1}$.

> This results from the fact that a rotation preserves the length of the vector, i.e.,
>
> $$\mathbf{v}\cdot\mathbf{v} = \mathbf{v}'\cdot\mathbf{v}' = \mathsf{R}_{ki}v_i\mathsf{R}_{kj}v_j = v_i\mathsf{R}^t_{ik}\mathsf{R}_{kj}v_j, \tag{A.7}$$
>
> so that $v_i\mathsf{R}^t_{ik}\mathsf{R}_{kj}v_j = v_i\delta_{ij}v_j$. Since this is true for any vector $\mathbf{v}$, we have $\mathsf{R}^t\mathsf{R} = \mathbb{1}$, where $\mathbb{1}$ is the identity matrix.

Using this property, we can write Eq. (A.2) as

$$\mathbf{v}' = R\mathbf{v} = \hat{\mathbf{x}}_j\mathsf{R}_{ji}v_i = \mathsf{R}^t_{ij}\hat{\mathbf{x}}_jv_i = \mathsf{R}^{-1}_{ij}\hat{\mathbf{x}}_jv_i. \tag{A.8}$$

In this form, the same rotation is due to a transformation of the basis vectors, rather than the vector components: $\mathbf{v}' = \hat{\mathbf{x}}'_iv_i$, where the rotated basis vectors are given by $\hat{\mathbf{x}}'_i = \mathsf{R}^{-1}_{ij}\hat{\mathbf{x}}_j$. The effect on the vector $\mathbf{v}$ is the same as for the active rotation, but here the basis vectors move along with $\mathbf{v}$, so that the relationship between $\mathbf{v}$ and the basis vectors (represented by the vector components) is unchanged [Fig. A.1(b)]. This type of rotation is not normally given a specific name, but we can call it a *joint rotation* because the vector and the basis vectors are rotated jointly. As the vector does not move in relation to the basis vectors, this kind of rotation is often thought of as leaving the system unchanged—it is equivalent, in a sense, to simply tilting one's head! Thus, two rotations are generally thought of as equivalent if they differ only by a given joint rotation.

Note that applying R to the vector components has the same effect on $\mathbf{v}$ as applying R^{-1} to the basis vectors. This shows that the rotation matrix has the opposite effect on the components as it does on the basis vectors.

By applying a joint rotation to the rotated vector $\mathbf{v}'$, we can find a rotation that is equivalent to the active rotation (A.2), but leaves the vector $\mathbf{v}$ unchanged. In this type of rotation, called a *passive* rotation, we think of the basis being rotated and the vector being held fixed, as opposed to the vector rotating and the basis being held fixed, as for an active rotation. In a passive rotation the basis vectors and the vector components must rotate in a complementary way so that the vector itself does not rotate. This relationship is expressed by saying that the components and the basis vectors are *relatively contravariant.* Applying the inverse rotation R^{-1} to $\mathbf{v}'$ gives back the original vector $\mathbf{v}$ (Fig. A.2). Thus we can write

$$\mathbf{v} = R^{-1}\mathbf{v}' = R^{-1}\hat{\mathbf{x}}_j\mathsf{R}_{ji}v_i = \hat{\mathbf{x}}_k\mathsf{R}^{-1}_{kj}\mathsf{R}_{ji}v_i = \mathsf{R}_{jk}\hat{\mathbf{x}}_k\mathsf{R}_{ji}v_i. \tag{A.9}$$

We can therefore write the passive rotation as $\mathbf{v} = \hat{\mathbf{x}}''_jv''_j$, with $\hat{\mathbf{x}}''_j = \mathsf{R}_{jk}\hat{\mathbf{x}}_k$ and

$v''_j = \mathsf{R}_{ji} v_i = v'_j$. In the example of Figs. A.1 and A.2, we have

$$\begin{pmatrix} \hat{\mathbf{x}}'' \\ \hat{\mathbf{y}}'' \\ \hat{\mathbf{z}}'' \end{pmatrix} = \begin{pmatrix} \cos\theta & -\sin\theta & 0 \\ \sin\theta & \cos\theta & 0 \\ 0 & 0 & 1 \end{pmatrix} \begin{pmatrix} \hat{\mathbf{x}} \\ \hat{\mathbf{y}} \\ \hat{\mathbf{z}} \end{pmatrix} = \begin{pmatrix} \hat{\mathbf{x}}\cos\theta - \hat{\mathbf{y}}\sin\theta \\ \hat{\mathbf{x}}\sin\theta + \hat{\mathbf{y}}\cos\theta \\ 0 \end{pmatrix}, \tag{A.10}$$

and $v''_j = v'_j$ given by Eq. (A.5). Then

$$\mathbf{v} = \begin{pmatrix} \hat{\mathbf{x}}\cos\theta - \hat{\mathbf{y}}\sin\theta & \hat{\mathbf{x}}\sin\theta + \hat{\mathbf{y}}\cos\theta & 0 \end{pmatrix} \begin{pmatrix} \cos\theta \\ \sin\theta \\ 0 \end{pmatrix} = \hat{\mathbf{x}}. \tag{A.11}$$

Here we see that because R has the opposite effect on the basis vectors as it does on the components, applying it to each has the desired effect of leaving $\mathbf{v}$ constant. Thus, even though they are relatively contravariant, in the Cartesian basis the vector components and the basis vectors transform according to the same rule.

We have found this expression by performing an active rotation of the components by an angle θ, and then a joint rotation on the basis vectors by $-\theta$. Accordingly, an active rotation on the vector components by θ is equivalent to a passive rotation of the basis vectors by $-\theta$. In our discussion, we have parameterized the rotation matrix in terms of active rotations: $\mathsf{R}_{\hat{\mathbf{n}}}(\theta)$ rotates the vector by θ when applied to the vector components. We can make a note of this by writing $\mathsf{R}^{(a)}_{\hat{\mathbf{n}}}(\theta)$. However, we normally describe a passive rotation in terms of the rotation of the basis vectors. Since $\mathsf{R}^{(a)}_{\hat{\mathbf{n}}}(\theta)$ rotates the basis vectors by $-\theta$, we can write the rotation matrix for passive rotations as

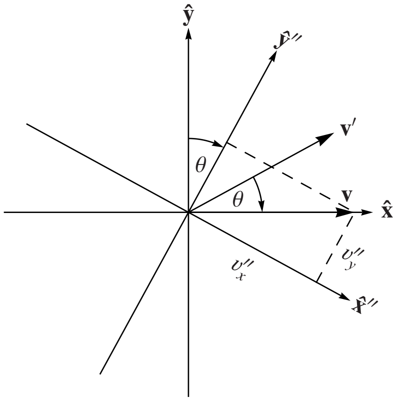

Figure A.2: The inverse rotation to that shown in Fig. A.1, returning the vector $\mathbf{v}'$ back to $\mathbf{v}$. The combination of the two rotations can be written as a passive rotation, with the original vector $\mathbf{v}$ being written in terms of the rotated basis vectors $\hat{\mathbf{x}}''_i$.

$$\mathsf{R}^{(p)}_{\hat{\mathbf{n}}}(\theta) = \mathsf{R}^{(a)}_{\hat{\mathbf{n}}}(-\theta) = \left(\mathsf{R}^{(a)}_{\hat{\mathbf{n}}}(\theta)\right)^{-1}. \tag{A.12}$$

Then an active rotation of $\mathbf{v}$ by an angle θ is given by

$$\mathbf{v}' = \hat{\mathbf{x}}_i \mathsf{R}^{(a)}_{ij}(\theta) v_j, \tag{A.13}$$

a passive rotation of the basis vectors by an angle θ is described by

$$\mathbf{v} = \mathsf{R}^{(p)}_{jk}(\theta)\hat{\mathbf{x}}_k \mathsf{R}^{(p)}_{ji}(\theta) v_i, \tag{A.14}$$

and the active rotation equivalent to this passive rotation is given by

$$\mathbf{v}'' = \hat{\mathbf{x}}_j \mathsf{R}^{(p)}_{ji}(\theta) v_i = \hat{\mathbf{x}}_j \mathsf{R}^{(a)}_{ji}(-\theta) v_i. \tag{A.15}$$

When we omit the superscript label on the rotation operator, we will continue to mean an active rotation.

A.2 The spherical basis

Let us introduce a new set of basis vectors, defined by

$$\hat{\boldsymbol{\epsilon}}_1 = -\frac{1}{\sqrt{2}}(\hat{\mathbf{x}} + i\hat{\mathbf{y}}), \tag{A.16a}$$

$$\hat{\boldsymbol{\epsilon}}_0 = \hat{\mathbf{z}}, \tag{A.16b}$$

$$\hat{\boldsymbol{\epsilon}}_{-1} = \frac{1}{\sqrt{2}}(\hat{\mathbf{x}} - i\hat{\mathbf{y}}). \tag{A.16c}$$

The fact that these unit vectors, describing the *spherical basis*, are complex has consequences for the algebra of rotations.

The transformation between the Cartesian and spherical bases can be written in terms of a matrix U, given by

$$U = \begin{pmatrix} -\frac{1}{\sqrt{2}} & -\frac{i}{\sqrt{2}} & 0 \\ 0 & 0 & 1 \\ \frac{1}{\sqrt{2}} & -\frac{i}{\sqrt{2}} & 0 \end{pmatrix}, \tag{A.17}$$

so that

$$\begin{pmatrix} \hat{\boldsymbol{\epsilon}}_1 \\ \hat{\boldsymbol{\epsilon}}_0 \\ \hat{\boldsymbol{\epsilon}}_{-1} \end{pmatrix} = U \begin{pmatrix} \hat{\mathbf{x}}_1 \\ \hat{\mathbf{x}}_2 \\ \hat{\mathbf{x}}_3 \end{pmatrix}. \tag{A.18}$$

This can also be notated as

$$\hat{\boldsymbol{\epsilon}}_q = U_{qj} \hat{\mathbf{x}}_j, \tag{A.19}$$

keeping track of the fact that q runs from 1 to -1, while j runs from 1 to 3. Here the matrix U is *unitary*, meaning that its inverse is equal to its conjugate transpose:

$$U^{-1} = (U^*)^t = U^\dagger. \tag{A.20}$$

This means that the inverse transformation is given by

$$\hat{\mathbf{x}}_j = U^{-1}_{jq}\hat{\boldsymbol{\epsilon}}_q = U^{\dagger}_{jq}\hat{\boldsymbol{\epsilon}}_q. \tag{A.21}$$

We now consider the components of $\mathbf{v}$ in the spherical basis, v^q, chosen so that they satisfy

$$\mathbf{v} = \hat{\boldsymbol{\epsilon}}_q v^q. \tag{A.22}$$

Here we have written the component index q as a superscript, for reasons to be explained below. We can treat the spherical components using a procedure similar to that used in Eq. (A.1) for the Cartesian components. Note, however, that the tensor $\hat{\boldsymbol{\epsilon}}_{q'} \cdot \hat{\boldsymbol{\epsilon}}_q$ is not equivalent to the identity tensor. Rather,

$$\hat{\boldsymbol{\epsilon}}^*_q \cdot \hat{\boldsymbol{\epsilon}}_{q'} = U^*_{qk}\hat{\mathbf{x}}_k \cdot U_{q'j}\hat{\mathbf{x}}_j = \hat{\mathbf{x}}_k \cdot \hat{\mathbf{x}}_j U^*_{qk} U^t_{jq'} = \left(U_{qj}U^{\dagger}_{jq'}\right)^* = \delta_{qq'}, \tag{A.23}$$

where we have used the fact that $\hat{\mathbf{x}}_j$ is real and U is unitary. This means that we can find the spherical components by taking the dot product between $\hat{\boldsymbol{\epsilon}}^*_{q'}$ and $\mathbf{v}$:

$$\hat{\boldsymbol{\epsilon}}^*_q \cdot \mathbf{v} = \hat{\boldsymbol{\epsilon}}^*_q \cdot \hat{\boldsymbol{\epsilon}}_{q'} v^{q'} = v^q. \tag{A.24}$$

How are the components v^q related to the Cartesian-basis components v_j? We have

$$\mathbf{v} = \hat{\mathbf{x}}_j v_j = U^{\dagger}_{jq}\hat{\boldsymbol{\epsilon}}_q v_j = \left(U^*_{jq}\right)^t \hat{\boldsymbol{\epsilon}}_q v_j = \hat{\boldsymbol{\epsilon}}_q U^*_{qj} v_j. \tag{A.25}$$

Using $\mathbf{v} = \hat{\boldsymbol{\epsilon}}_q v^q$, we find that the components in the new basis are given by

$$v^q = U^*_{qj} v_j, \tag{A.26}$$

or, explicitly,

$$v^1 = -\frac{1}{\sqrt{2}}(v_x - iv_y), \tag{A.27a}$$

$$v^0 = v_z, \tag{A.27b}$$

$$v^{-1} = \frac{1}{\sqrt{2}}(v_x + iv_y). \tag{A.27c}$$

The inverse transformation is given by

$$v_j = U^{\dagger *}_{jq} v^q = U^t_{jq} v^q. \tag{A.28}$$

We see that the transformation that takes the vector components into the spherical basis is the complex conjugate of the one given by Eq. (A.19) that acts on the basis vectors.

Now let us consider rotations in the spherical basis. We first look at passive rotations. Following the procedure of Eq. (A.9), we can write a passive rotation as

$$\mathbf{v} = R^{-1}R\mathbf{v} = \hat{\boldsymbol{\epsilon}}_{q_2}\tilde{\mathsf{R}}^{-1}_{q_2q_1}\tilde{\mathsf{R}}_{q_1q}v^q, \tag{A.29}$$

where $\tilde{\mathsf{R}}$ is the matrix for rotation in the spherical basis. In the Cartesian basis, R is orthogonal. This is not necessarily the case for $\tilde{\mathsf{R}}$, because it may be complex. However, it is guaranteed to be unitary, i.e., $\tilde{\mathsf{R}}^\dagger = \tilde{\mathsf{R}}^{-1}$. Thus, we can write

$$\mathbf{v} = \hat{\boldsymbol{\epsilon}}_{q_2}\tilde{\mathsf{R}}^{-1}_{q_2q_1}\tilde{\mathsf{R}}_{q_1q}v^q = \hat{\boldsymbol{\epsilon}}_{q_2}\tilde{\mathsf{R}}^{\dagger}_{q_2q_1}\tilde{\mathsf{R}}_{q_1q}v^q = \tilde{\mathsf{R}}^{*}_{q_1q_2}\hat{\boldsymbol{\epsilon}}_{q_2}\tilde{\mathsf{R}}_{q_1q}v^q. \tag{A.30}$$

The spherical basis vectors and vector coefficients must be relatively contravariant in order that $\mathbf{v}$ remain unchanged under a passive rotation. In contrast to the Cartesian case, here the relatively contravariant quantities have different transformation properties—the rotation matrix for the basis vectors, $\tilde{\mathsf{R}}^*$, is the complex conjugate of that for the vector components, $\tilde{\mathsf{R}}$.

Note that it is not true that basis vectors always transform one way and vector components another. Taking the complex conjugate of Eq. (A.30), we have

$$\mathbf{v} = \tilde{\mathsf{R}}_{q_1q_2}\hat{\boldsymbol{\epsilon}}^*_{q_2}\tilde{\mathsf{R}}^*_{q_1q}v^{q*}, \tag{A.31}$$

where we have assumed that $\mathbf{v}$ is real for simplicity. This shows that the alternate set of unit vectors $\hat{\boldsymbol{\epsilon}}^*_q$ transforms the same way that v^q does, whereas v^{q*} transforms like $\hat{\boldsymbol{\epsilon}}_q$. In addition, from Eqs. (A.19) and (A.26) we find that $\hat{\boldsymbol{\epsilon}}^*_q$ and v^q transform to the Cartesian basis in the same way as each other, and likewise $\hat{\boldsymbol{\epsilon}}_q$ and v^{q*}. To keep track of these different types of quantities, we will call sets of quantities that transform like $\hat{\boldsymbol{\epsilon}}_q$ *covariant*, and sets that transform like v^q *contravariant*. As may be already clear, this distinction is indicated in the notation by writing the index on contravariant quantities as a superscript. We will discuss the relationship between covariant and contravariant quantities further below.

The matrix $\tilde{\mathsf{R}}_{\hat{\mathbf{n}}}(\theta)$ produces a transformation of the spherical components equivalent to an active rotation by an angle θ about $\hat{\mathbf{n}}$. To find an expression for $\tilde{\mathsf{R}}$, we consider an active rotation in the Cartesian basis:

$$v'_j = \mathsf{R}_{jk}v_k. \tag{A.32}$$

Multiplying on the left by U^* and inserting $(U^{-1}U)^*$ before v_k, we have

$$(v^q)' = U^*_{qj}v'_j = U^*_{qj}\mathsf{R}_{jk}U^{\dagger *}_{kq_1}U^*_{q_1l}v_l = U^*_{qj}\mathsf{R}_{jk}U^{\dagger *}_{kq_1}v^{q_1} = \tilde{\mathsf{R}}_{qq_1}v^{q_1}, \tag{A.33}$$

with $\tilde{\mathsf{R}} = (U\mathsf{R}U^\dagger)^*$. For example, for the rotation by an angle θ about $\hat{\mathbf{z}}$ specified by Eq. (A.3), the corresponding rotation matrix for contravariant quantities in the spherical basis is

$$\begin{aligned} \tilde{\mathsf{R}} &= \begin{pmatrix} -\frac{1}{\sqrt{2}} & \frac{i}{\sqrt{2}} & 0 \\ 0 & 0 & 1 \\ \frac{1}{\sqrt{2}} & \frac{i}{\sqrt{2}} & 0 \end{pmatrix} \begin{pmatrix} \cos\theta & -\sin\theta & 0 \\ \sin\theta & \cos\theta & 0 \\ 0 & 0 & 1 \end{pmatrix} \begin{pmatrix} -\frac{1}{\sqrt{2}} & 0 & \frac{1}{\sqrt{2}} \\ -\frac{i}{\sqrt{2}} & 0 & -\frac{i}{\sqrt{2}} \\ 0 & 1 & 0 \end{pmatrix} \\ &= \begin{pmatrix} e^{-i\theta} & 0 & 0 \\ 0 & 1 & 0 \\ 0 & 0 & e^{i\theta} \end{pmatrix}. \end{aligned} \tag{A.34}$$

This shows that a rotation about the z-axis induces phase shifts in the spherical components, but does not mix them. This is an important feature of the spherical basis.

The matrix $\tilde{\mathsf{R}}$ applies to active rotations of the contravariant components, and can be notated in full as $\tilde{\mathsf{R}}^{(a)}_{\hat{\mathbf{n}}}(\theta)$. In a passive rotation of the basis vectors by an angle θ, the components undergo a transformation equivalent to an active rotation of $-\theta$, as discussed in the previous section. The matrix that describes this equivalent rotation is then given by $\tilde{\mathsf{R}}^{(p)}_{\hat{\mathbf{n}}}(\theta) = \tilde{\mathsf{R}}^{(a)}_{\hat{\mathbf{n}}}(-\theta) = [\tilde{\mathsf{R}}^{(a)}_{\hat{\mathbf{n}}}(\theta)]^{-1}$.

We have seen above that taking the complex conjugate evidently converts covariant quantities into contravariant, and vice versa. Therefore we can define the set of contravariant basis vectors

$$\hat{\boldsymbol{\epsilon}}^q = \hat{\boldsymbol{\epsilon}}_q^* = U^*_{qj}\hat{\mathbf{x}}_j, \tag{A.35}$$

which transform under passive rotations as $(\hat{\boldsymbol{\epsilon}}^q)' = \tilde{\mathsf{R}}^{(p)}_{q'q}\hat{\boldsymbol{\epsilon}}^q$. Note, however, that we have used here the fact that the Cartesian basis vectors $\hat{\mathbf{x}}_j$ are real. If we attempt to use a similar scheme to define a set of covariant vector components, we run into problems if the vector is complex (i.e., if its Cartesian components are complex). Taking the complex conjugate of Eq. (A.22), we have

$$\mathbf{v}^* = \hat{\boldsymbol{\epsilon}}_q^* v^{q*} = \hat{\boldsymbol{\epsilon}}^q v^{q*}. \tag{A.36}$$

This shows that taking the complex conjugate of the contravariant spherical components of $\mathbf{v}$ gives a set of covariant spherical components, but they are the components of $\mathbf{v}^*$, not $\mathbf{v}$. Another problem with the conjugation method is that we will wish to generalize the discussion to include covariant and contravariant components of quantities that do not possess complex conjugates.

There is another, more general, way to convert between covariant and contravariant components. Inspection of the form (A.17) of the transformation matrix U shows that its matrix elements obey the relation

$$U^*_{qj} = (-1)^q U_{-q,j}. \tag{A.37}$$

Consider a rotation applied to a contravariant set y^q, where y could represent either a vector or a basis. Because they are contravariant, the components y^q transform according to

$$(y^q)' = \tilde{\mathsf{R}}_{qq_1} y^{q_1}, \tag{A.38}$$

where the transformation matrix $\tilde{R}$ can be written using Eq. (A.37) as

$$\tilde{\mathsf{R}}_{qq_1} = U^*_{qj}\mathsf{R}_{jk}U^{\dagger *}_{kq_1} = (-1)^q U_{-qj,}\mathsf{R}_{jk}U^{\dagger}_{k,-q_1}(-1)^{q_1} = (-1)^{q+q_1}\tilde{\mathsf{R}}^*_{-q,-q_1}. \tag{A.39}$$

Substituting back into Eq. (A.38) and flipping the signs of the indices, we have

$$\left[(-1)^q y^{-q}\right]' = \tilde{\mathsf{R}}^*_{qq_1}(-1)^{q_1} y^{-q_1}. \tag{A.40}$$

This shows that $(-1)^q y^{-q}$ transforms as a covariant set. Likewise, if y_q is a covariant set of quantities, $(-1)^q y_{-q}$ is contravariant. For the spherical basis vectors, the contravariant set obtained in this way coincides with the above definition of $\hat{\boldsymbol{\epsilon}}^q$:

$$(-1)^q \hat{\boldsymbol{\epsilon}}_{-q} = (-1)^q U_{-q,j}\hat{\mathbf{x}}_j = U^*_{q,j}\hat{\mathbf{x}}_j = \hat{\boldsymbol{\epsilon}}^*_q = \hat{\boldsymbol{\epsilon}}^q. \tag{A.41}$$

For the spherical components, $(-1)^q v^{-q}$ is equal to v^{q*} only if $\mathbf{v}$ is real. It is clear that this set comprises the covariant components corresponding to $\hat{\boldsymbol{\epsilon}}^q$:

$$\mathbf{v} = \hat{\boldsymbol{\epsilon}}_q v^q = (-1)^q \hat{\boldsymbol{\epsilon}}_{-q}(-1)^q v^{-q} = \hat{\boldsymbol{\epsilon}}^q (-1)^q v^{-q}. \tag{A.42}$$

Therefore, we make the definition $v_q = (-1)^q v^{-q}$.

The transformation converting between covariant and contravariant sets can be written in terms of a matrix Y given by

$$Y = \begin{pmatrix} 0 & 0 & -1 \\ 0 & 1 & 0 \\ -1 & 0 & 0 \end{pmatrix}, \tag{A.43}$$

so that $U^* = YU$, $\hat{\boldsymbol{\epsilon}}^q = Y_{qq'}\hat{\boldsymbol{\epsilon}}_{q'}$, and $v_q = Y_{qq'}v^{q'}$. The transformation Y is equivalent up to an overall sign to a rotation by π about the y-axis.

The transformation rules for various quantities in the spherical basis are summarized in Table A.1.

Using the definition of $\hat{\boldsymbol{\epsilon}}^q$, we can write the spherical-basis orthonormality relation (A.23) as

$$\hat{\boldsymbol{\epsilon}}^q \cdot \hat{\boldsymbol{\epsilon}}_{q'} = \delta_{qq'}. \tag{A.44}$$

Table A.1: Various spherical-basis quantities and their transformation properties.

quantity	type	rotation type	transformation
v^q	contravariant components	active	$\tilde{\mathsf{R}}^{(a)}_{q'q} v^q$
		passive	$\tilde{\mathsf{R}}^{(p)}_{q'q} v^q$
$\hat{\boldsymbol{\epsilon}}_q$	covariant basis vectors	passive	$\tilde{\mathsf{R}}^{(p)*}_{q'q} \hat{\boldsymbol{\epsilon}}_q$
v_q	covariant components	active	$\tilde{\mathsf{R}}^{(a)*}_{q'q} v_q$
		passive	$\tilde{\mathsf{R}}^{(p)*}_{q'q} v_q$
$\hat{\boldsymbol{\epsilon}}^q$	contravariant basis vectors	passive	$\tilde{\mathsf{R}}^{(p)}_{q'q} \hat{\boldsymbol{\epsilon}}^q$

The scalar product in this relation is between a covariant and a contravariant vector. This is a general requirement for scalar products—because a scalar is invariant under rotations, the effect of rotating one of the vectors in the scalar product must cancel that of the other. Thus the scalar product must be between relatively contravariant quantities.

To write the scalar product of two vectors $\mathbf{v}$ and $\mathbf{w}$ in terms of their spherical components, we convert from the Cartesian components:

$$\mathbf{v} \cdot \mathbf{w} = v_j w_j = v_j U^t_{jq} w^q = U_{qj} v_j w^q = v_q w^q. \tag{A.45}$$

Employing the transformation between covariant and contravariant components, the scalar product can be written in the alternate forms:

$$\mathbf{v} \cdot \mathbf{w} = v_q w^q = v_q Y_{qq'} w_{q'} = (-1)^q v_q w_{-q} = v^q w_q = (-1)^q v^q w^{-q}. \tag{A.46}$$

A.3 Euler angles

The Cartesian rotation matrices for rotations about $\hat{\mathbf{x}}$, $\hat{\mathbf{y}}$, and $\hat{\mathbf{z}}$ are given by

$$\mathsf{R}_{\hat{\mathbf{x}}}(\theta) = \begin{pmatrix} 1 & 0 & 0 \\ 0 & \cos\theta & -\sin\theta \\ 0 & \sin\theta & \cos\theta \end{pmatrix}, \tag{A.47a}$$

$$\mathsf{R}_{\hat{\mathbf{y}}}(\theta) = \begin{pmatrix} \cos\theta & 0 & \sin\theta \\ 0 & 1 & 0 \\ -\sin\theta & 0 & \cos\theta \end{pmatrix}, \tag{A.47b}$$

$$\mathsf{R}_{\hat{\mathbf{z}}}(\theta) = \begin{pmatrix} \cos\theta & -\sin\theta & 0 \\ \sin\theta & \cos\theta & 0 \\ 0 & 0 & 1 \end{pmatrix}. \tag{A.47c}$$

Rather than attempting to write out the matrix for rotation about an arbitrary axis, we can decompose an arbitrary rotation into a series of rotations about the Cartesian axes. An arbitrary rotation can be described by three successive rotations by the *Euler angles* α, β, and γ. To describe these rotations in the active sense, we make use of *body-fixed* axes, which undergo the same active rotation as the rotating object, so as to remain fixed with respect to it, as opposed to the original set of *space-fixed* axes, which do not change during an active rotation. The sequence of Euler rotations can then be described as follows (Fig. A.3a).

1. A rotation by angle α ($0 \leq \alpha \leq 2\pi$) around the z-axis. (Prior to this rotation, the space-fixed and body-fixed axes coincide.)

2. A rotation by angle β ($0 \leq \beta \leq \pi$) around the body-fixed y-axis (denoted as the y'-axis in the space-fixed coordinate system).

3. A rotation by angle γ ($0 \leq \gamma \leq 2\pi$) around the body-fixed z-axis (the z''-axis in the space-fixed system).

This combination of rotations can produce any desired resultant rotation. In other words, an axis-angle rotation $R_{\hat{\mathbf{n}}}(\phi)$ can be written as

$$R_{\hat{\mathbf{n}}}(\phi) = R_{\hat{\mathbf{z}}''}(\gamma)\, R_{\hat{\mathbf{y}}'}(\beta)\, R_{\hat{\mathbf{z}}}(\alpha) \tag{A.48}$$

for some combination of α, β, and γ.

It is much more convenient, however, to describe rotations with respect to the space-fixed coordinate system. To do this, we use a remarkable relation between space-fixed rotations and body-fixed rotations. Namely, the combination of three active Euler rotations with respect to the body-fixed axes $\hat{\mathbf{z}}$, $\hat{\mathbf{y}}'$, $\hat{\mathbf{z}}''$ is equivalent to the same three active rotations with respect to the space-fixed axes $\hat{\mathbf{z}}$, $\hat{\mathbf{y}}$, $\hat{\mathbf{z}}$, but performed in the opposite order (Fig. A.3b). Denoting a rotation by Euler angles as $R\,(\alpha, \beta, \gamma)$, we have

$$\begin{aligned} R\,(\alpha, \beta, \gamma) &= R_{\hat{\mathbf{z}}''}(\gamma) R_{\hat{\mathbf{y}}'}(\beta) R_{\hat{\mathbf{z}}}(\alpha) \\ &= R_{\hat{\mathbf{z}}}(\alpha) R_{\hat{\mathbf{y}}}(\beta) R_{\hat{\mathbf{z}}}(\gamma). \end{aligned} \tag{A.49}$$

For a proof of this property, see the book by Sakurai and Tuan (1994).

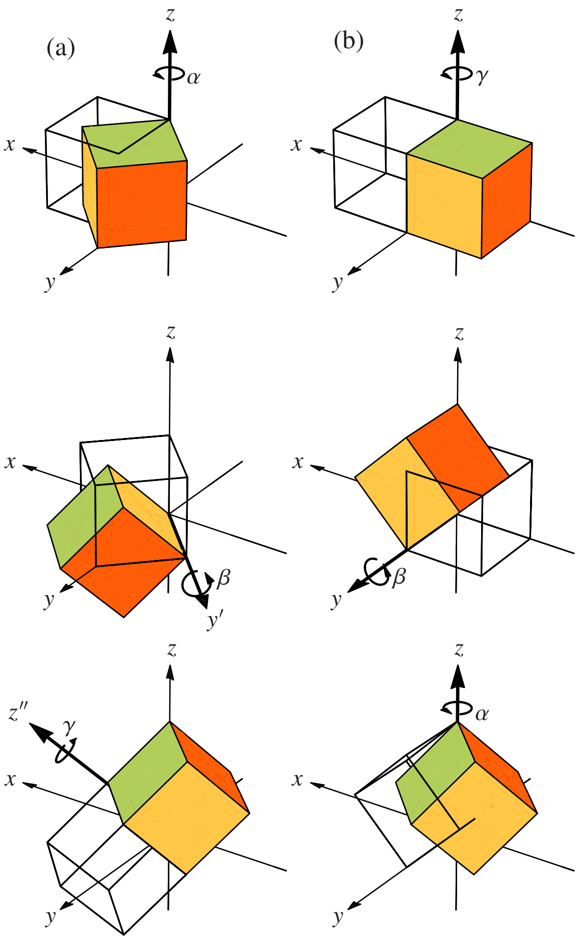

Figure A.3: Rotation of a body by (a) Euler angles α, β, γ with respect to the body-fixed z, y', and z'' axes is equivalent to rotation by (b) the same angles but in the opposite order with respect to the original space-fixed axes z, y, and z. For each step, the rotation direction is indicated by a curved arrow; the initial position of the body is shown as a cubic frame, and the final position is shown as a filled cube.

Using this property and the rotation matrices given above, we can write a general active Euler-angle rotation as

$$R(\alpha,\beta,\gamma) = \begin{pmatrix} \cos\alpha & -\sin\alpha & 0 \\ \sin\alpha & \cos\alpha & 0 \\ 0 & 0 & 1 \end{pmatrix} \begin{pmatrix} \cos\beta & 0 & \sin\beta \\ 0 & 1 & 0 \\ -\sin\beta & 0 & \cos\beta \end{pmatrix} \begin{pmatrix} \cos\gamma & -\sin\gamma & 0 \\ \sin\gamma & \cos\gamma & 0 \\ 0 & 0 & 1 \end{pmatrix}. \tag{A.50}$$

A.4 Commutation relations

Rotations in three-dimensional space, in contrast to the case of two-dimensional rotations, have an important property: the result of a composite transformation consisting of consecutive rotations around different axes generally depends on the

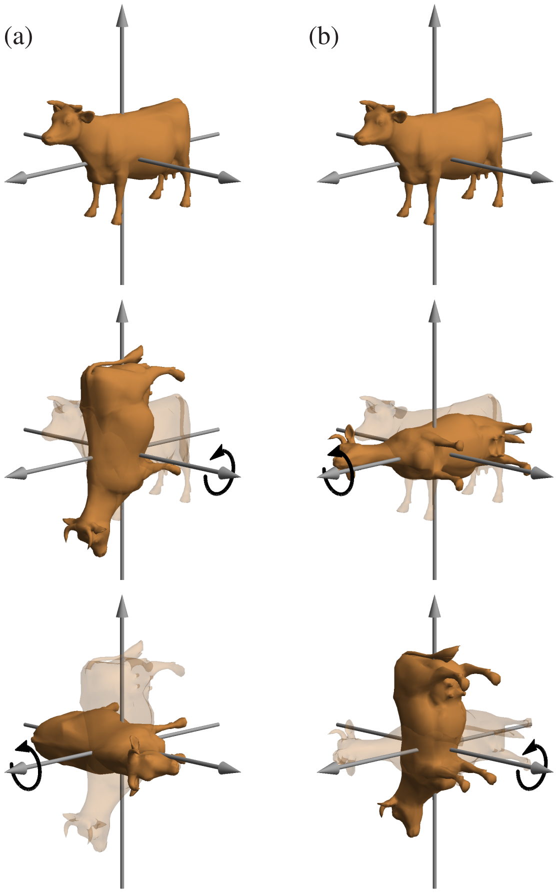

Figure A.4: Two consecutive rotations performed in one order in the left column (a) and the opposite order in the right column (b). The steps proceed from top to bottom—the transparent objects show the starting position for each step, the circular arrows indicate the rotation applied, and the solid objects show the results of the rotation.

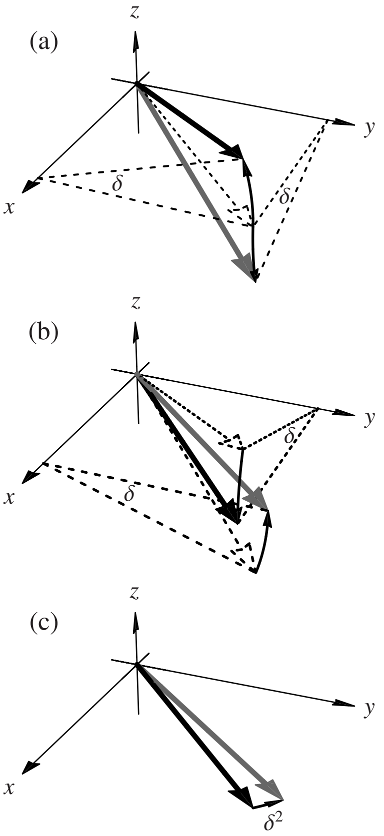

Figure A.5: Classical commutation relation for rotations about the x and y axes (Eq. A.51). Start with two copies of a vector along $\hat{\mathbf{x}} + \hat{\mathbf{y}}$. One copy (black) is rotated by (a) an angle δ about $\hat{\mathbf{x}}$ and then (b) the same angle about $\hat{\mathbf{y}}$, while the other copy (gray) undergoes the same rotations but in the opposite order. The difference in the resultant vectors is approximately the same as (c) the difference between the original vector and a copy rotated by δ^2 about $\hat{\mathbf{z}}$.

order in which these rotations are performed. This *noncommutativity* property for sequential rotations about different axes is illustrated in Figs. A.4 and A.5.

In Fig. A.4 we show the result of two consecutive $\pi/2$ rotations around two orthogonal axes, and the two rotations in the opposite order. It is apparent that the results of these two sequences of rotations are completely different. In order to quantify this difference, however, it is helpful to consider the case of small rotations.

The case of rotations by small angles is shown in Fig. A.5, and can be described by the *commutation relations*

$$[R_i(\delta), R_j(\delta)] = \epsilon_{ijk} \left(R_k(\delta^2) - 1 \right) , \tag{A.51}$$

to second order in a small angle δ. Here $R_i \equiv R_{\hat{\mathbf{x}}_i}$ ($\hat{\mathbf{x}}_{1,2,3}$ are the Cartesian unit vectors), the square brackets designate the *commutator* $[A, B] = AB - BA$, and ϵ_{ijk} is the totally antisymmetric tensor.

Appendix B

Quantum-mechanical Rotations

B.1 General properties

In quantum mechanics, instead of rotating vectors, we wish to rotate wave functions. Under a classical rotation R, a state will transform according to a quantum-mechanical rotation operator $\mathscr{D}(R)$ corresponding to R. In other words, for a given classical rotation that takes a vector $\mathbf{v}$ into a new vector $\mathbf{v}' = R\mathbf{v}$, there is a quantum-mechanical rotation operator $\mathscr{D}(R)$ that takes a wave function $|\psi\rangle$ into a new wave function $|\psi'\rangle = \mathscr{D}(R)|\psi\rangle$. We will evaluate $\mathscr{D}$ explicitly later in this chapter; in this section we examine some of its general properties.

We will assume that the quantum-mechanical rotation operators share some features of their classical counterparts. In particular, as the length of a classical vector is preserved upon rotation, the norm of a wave function should also be preserved. Since wave functions are not real-valued, $\mathscr{D}$ is not necessarily orthogonal, but it is unitary, i.e.,

$$\mathscr{D}^\dagger \mathscr{D} = 1. \tag{B.1}$$

In addition, we assume that the quantum-mechanical rotation operators satisfy the same commutation relations as the classical operators. In other words, for active rotations,

$$[\mathscr{D}_i(\delta), \mathscr{D}_j(\delta)] = \epsilon_{ijk}\big(\mathscr{D}_k(\delta^2) - 1\big), \tag{B.2}$$

where $\mathscr{D}_i(\delta) = \mathscr{D}\left[R_i(\delta)\right]$.

These two requirements can be taken as the definition of the quantum-mechanical rotation operator. In an explicit form, the operator for a rotation $R_{\hat{\mathbf{n}}}(d\phi)$ by a small angle $d\phi$ about an axis $\hat{\mathbf{n}}$ can be written in terms of the angular momentum operator $\mathbf{J}$:

$$\mathscr{D}\left[R_{\hat{\mathbf{n}}}(d\phi)\right] = 1 - i\mathbf{J}\cdot\hat{\mathbf{n}}\, d\phi/\hbar. \tag{B.3}$$

Finite rotations can be found in terms of the angular momentum operator by compounding many infinitesimal rotations:

$$\begin{aligned}\mathscr{D}\left[R_{\hat{\mathbf{n}}}(\phi)\right] &= \lim_{N\to\infty}\left[1 - i\mathbf{J}\cdot\hat{\mathbf{n}}\,\phi/(\hbar N)\right]^N \\ &= \exp\left(-i\mathbf{J}\cdot\hat{\mathbf{n}}\,\phi/\hbar\right).\end{aligned} \tag{B.4}$$

As for classical rotations, an arbitrary quantum-mechanical rotation is conveniently specified in terms of Euler angles (Sec. A.3), so that it takes the form

$$\begin{aligned}\mathscr{D}(\alpha,\beta,\gamma) &= \mathscr{D}_{\hat{\mathbf{z}}}(\alpha)\,\mathscr{D}_{\hat{\mathbf{y}}}(\beta)\,\mathscr{D}_{\hat{\mathbf{z}}}(\gamma) \\ &= \exp\left(-iJ_z\alpha/\hbar\right)\exp\left(-iJ_y\beta/\hbar\right)\exp\left(-iJ_z\gamma/\hbar\right).\end{aligned} \tag{B.5}$$

Thus, explicit matrix representations of the rotation operators can be found in terms of the properties of the angular momentum operator, as discussed in the next section.[1]

B.2 Wigner D-functions

The Wigner D-functions are the matrix elements of the quantum-mechanical rotation operators in the Zeeman (spherical) basis. They are defined in terms of the Euler angles by the formula

$$D^{(J)}_{m'm}(\alpha,\beta,\gamma) = \langle m'|\mathscr{D}_{\hat{\mathbf{z}}}(\alpha)\,\mathscr{D}_{\hat{\mathbf{y}}}(\beta)\,\mathscr{D}_{\hat{\mathbf{z}}}(\gamma)\,|m\rangle. \tag{B.6}$$

They are useful whenever the effect of a specific rotation on a quantum state needs to be found. There are various methods for obtaining a general expression for the Wigner D-functions. The matrix for rotations about the z-axis follows directly from the fact that the basis states are eigenstates of J_z. We have $\langle Jm'|J_z|Jm\rangle = m\hbar\delta_{m'm}$, so

$$\left[\mathscr{D}_{\hat{\mathbf{z}}}(\phi)\right]_{m'm} = \langle Jm'|e^{-iJ_z\phi/\hbar}|Jm\rangle = e^{-im\phi}\delta_{m'm}. \tag{B.7}$$

Thus the D-function can be written

$$\begin{aligned}D^{(J)}_{m'm}(\alpha,\beta,\gamma) &= \langle m'|\mathscr{D}_{\hat{\mathbf{z}}}(\alpha)\,\mathscr{D}_{\hat{\mathbf{y}}}(\beta)\,\mathscr{D}_{\hat{\mathbf{z}}}(\gamma)\,|m\rangle \\ &= \sum_{m'',m'''}\delta_{m'm'''}e^{-im'\alpha}\langle m'''|\mathscr{D}_{\hat{\mathbf{y}}}(\beta)\,|m''\rangle e^{-im\gamma}\delta_{mm''} \\ &= e^{-i(\alpha m'+\gamma m)}d^{(J)}_{m'm}(\beta),\end{aligned} \tag{B.8}$$

---

[1] The reader should be cautioned that, unfortunately, there are a variety of conventions and definitions in use related to angular momentum. For example, there is a difference between Landau and Lifshitz (1977) and Edmonds (1996) in the definitions of the $\mathscr{D}$ operators and the order in which the Euler rotations are applied.

where $d^{(J)}_{m'm}(\beta)$ is the matrix for rotations about the y-axis. One technique for finding a formula for this matrix involves relating angular-momentum eigenstates to states of a system consisting of two uncoupled harmonic oscillators (see Sakurai and Tuan 1994 for details). This approach results in *Wigner's formula* for $d^{(J)}_{m'm}(\beta)$:

$$\begin{aligned} d^{(J)}_{m'm}(\beta) = {} & \sum_k (-1)^{k-m+m'} \frac{\sqrt{(J+m)!\,(J-m)!\,(J+m')!\,(J-m')!}}{(J+m-k)!\,k!\,(J-k-m')!\,(k-m+m')!} \\ & \times \left(\cos\frac{\beta}{2}\right)^{2J-2k+m-m'} \left(\sin\frac{\beta}{2}\right)^{2k-m+m'}, \end{aligned} \tag{B.9}$$

where the sum runs over values of k for which none of the arguments of the factorials are negative. For the $J = 1$ case, for example, this becomes

$$d^{(1)}(\beta) = \begin{pmatrix} \cos^2\frac{\beta}{2} & -\frac{\sin\beta}{\sqrt{2}} & \sin^2\frac{\beta}{2} \\ \frac{\sin\beta}{\sqrt{2}} & \cos\beta & -\frac{\sin\beta}{\sqrt{2}} \\ \sin^2\frac{\beta}{2} & \frac{\sin\beta}{\sqrt{2}} & \cos^2\frac{\beta}{2} \end{pmatrix}, \tag{B.10}$$

resulting in the full rotation matrix

$$D^{(1)}(\alpha,\beta,\gamma) = \begin{pmatrix} e^{-i(\alpha+\gamma)}\cos^2\frac{\beta}{2} & -e^{-i\alpha}\frac{\sin\beta}{\sqrt{2}} & e^{-i(\alpha-\gamma)}\sin^2\frac{\beta}{2} \\ e^{-i\gamma}\frac{\sin\beta}{\sqrt{2}} & \cos\beta & -e^{i\gamma}\frac{\sin\beta}{\sqrt{2}} \\ e^{i(\alpha-\gamma)}\sin^2\frac{\beta}{2} & e^{i\alpha}\frac{\sin\beta}{\sqrt{2}} & e^{i(\alpha+\gamma)}\cos^2\frac{\beta}{2} \end{pmatrix}. \tag{B.11}$$

B.3 Rotations in the Zeeman basis

The issues of active vs. passive rotations and covariant vs. contravariant components discussed in Appendix A also arise for quantum-mechanical rotations. Suppose we have a state ket $|\psi\rangle$ representing the angular degrees of freedom of a state with angular momentum J. We can expand the ket in the basis of eigenstates $|m\rangle$ of the J_z operator:

$$|\psi\rangle = |m\rangle\langle m|\psi\rangle = |m\rangle\psi^m, \tag{B.12}$$

where $\psi^m = \langle m|\psi\rangle$ are the Zeeman components of $|\psi\rangle$.

Consider a rotation applied to $|\psi\rangle$:

$$|\psi'\rangle = \mathscr{D}|\psi\rangle. \tag{B.13}$$

This rotation can be written as an active rotation:

$$|\psi'\rangle = |m_1\rangle\langle m_1|\mathscr{D}|m_2\rangle\langle m_2|\psi\rangle = |m_1\rangle D_{m_1m_2}\psi^{m_2} = |m_1\rangle\psi'^{m_1}, \tag{B.14}$$

where

$$\psi'^{m_1} = D_{m_1 m_2} \psi^{m_2}. \tag{B.15}$$

We can also write a passive rotation:

$$|\psi\rangle = \mathscr{D}^{-1}|\psi'\rangle = \mathscr{D}^{-1}|m_1\rangle D_{m_1 m}\psi^m = |m_2\rangle D^{-1}_{m_2 m_1} D_{m_1 m}\psi^m = |m_1\rangle'\psi'^{m_1}, \tag{B.16}$$

with

$$|m_1\rangle' = D^*_{m_1 m_2}|m_2\rangle. \tag{B.17}$$

Comparing with Eq. (A.30), we see that this is quite similar to the case of vectors in the spherical basis: relatively contravariant quantities transform with rotation operators that are complex conjugates of one another. The parallel goes further, however. Consider the operator $\mathscr{D}_{\hat{\mathbf{z}}}(\theta)$ for rotations about $\hat{\mathbf{z}}$ by an angle θ. In matrix form for a $J = 1$ state, we have in the Zeeman basis

$$\mathscr{D}_{\hat{\mathbf{z}}}(\theta) = e^{-iJ_z\theta} = \begin{pmatrix} e^{-i\theta} & 0 & 0 \\ 0 & 1 & 0 \\ 0 & 0 & e^{i\theta} \end{pmatrix}. \tag{B.18}$$

This matrix is identical to the spherical-basis rotation matrix $\tilde{\mathsf{R}}_{\hat{\mathbf{z}}}(\theta)$ given by Eq. (A.34). In fact, the components ψ^m of a $J = 1$ state $|\psi\rangle$ transform just like the contravariant spherical components v^q of a vector $\mathbf{v}$. Likewise, the basis states $|m\rangle$ transform like the covariant spherical basis vectors $\hat{\boldsymbol{\epsilon}}_q$. Furthermore, taking the Hermitian conjugate of the above expressions, we see that the dual basis states $\langle m|$ transform like contravariant spherical basis vectors $\hat{\boldsymbol{\epsilon}}^q$, and the components ψ_m of $\langle\psi|$ expanded over $\langle m|$ transform like covariant spherical basis components v_q.

The $2J+1$ Zeeman components and basis states for a state with arbitrary angular momentum J also transform according to the rules described in this section, but with different matrix representations of the rotation operators. We therefore generalize the definition of the spherical basis, and call a basis that has the transformation properties of the angular-momentum-J Zeeman basis $|m\rangle$ the spherical basis of rank J. A rank-J basis has $2J + 1$ basis vectors. Thus the spherical basis described in Sec. A.2 has rank 1. Similarly to the definition made for the rank-1 spherical basis, quantities that transform like the Zeeman basis states $|m\rangle$ (Eq. B.17) are defined to be covariant, while those that transform like the coefficients ψ^m (Eq. B.15) are defined to be contravariant.

B.4 The effect of rotations on operators

The effect of rotations on quantum-mechanical operators can be thought of in several different ways. We first examine the effect of a passive rotation corresponding to the active rotation $\mathscr{D}$.

Consider the expectation value of an operator A with respect to a state $|\psi\rangle$: $\langle A\rangle = \langle\psi|A|\psi\rangle$. Suppose that we take the directional dependence of the operator A to be fixed relative to space, rather than to the coordinate system. For example, if A is the J_z operator, we take A to be associated with the angular-momentum projection on a particular axis in space (given by the z-axis in the initial coordinate system). Even if the coordinate system rotates, the axis does not. Then, under a passive rotation, the expectation value of A will not change, because while the coordinate system rotates, the state and the operator both remain fixed. Writing this situation in terms of the equivalent active rotation $|\psi'\rangle = \mathscr{D}|\psi\rangle$, we have

$$\langle A\rangle = \langle A'\rangle = \langle\psi'|A'|\psi'\rangle = \langle\psi|\mathscr{D}^\dagger A'\mathscr{D}|\psi\rangle, \tag{B.19}$$

where A' is the form of the operator after rotation. Comparing with $\langle A\rangle = \langle\psi|A|\psi\rangle$, we have $A' = \mathscr{D}A\mathscr{D}^\dagger$ in this case.

Alternatively, we may consider the operator to be fixed to the coordinate system, so that, for example, A would represent the angular-momentum projection along the z-axis in the rotated coordinate system. In this case, the expectation value should transform exactly as for the equivalent active rotation, under which the operator is unchanged:

$$\langle A'\rangle = \langle\psi'|A|\psi'\rangle. \tag{B.20}$$

Thus $A' = A$ under this assumption.

The active rotation also has another interpretation. Namely, we can write

$$\langle A'\rangle = \langle\psi'|A|\psi'\rangle = \langle\psi|\mathscr{D}^\dagger A\mathscr{D}|\psi\rangle = \langle\psi|A'|\psi\rangle, \tag{B.21}$$

where we have written the effect of the rotation in terms of an effective transformation of the operator, while holding the state fixed. This shows that, rather than rotating the state, we can obtain an equivalent result by instead "rotating the operator," using the formula

$$A' = \mathscr{D}^\dagger A\mathscr{D}. \tag{B.22}$$

We can also relate $\mathscr{D}$ to R by this method. If $\mathbf{A}$ is a vector observable, its expectation value $\langle\mathbf{A}\rangle = \langle\psi|\mathbf{A}|\psi\rangle$ should transform as a classical vector. In other words, under the active rotation R,

$$\langle\mathbf{A}'\rangle = R\langle\mathbf{A}\rangle. \tag{B.23}$$

The expectation value after the rotation can also be written

$$\langle\mathbf{A}'\rangle = \langle\psi'|\mathbf{A}|\psi'\rangle = \langle\psi|\mathscr{D}^\dagger\mathbf{A}\mathscr{D}|\psi\rangle; \tag{B.24}$$

combining Eqs. (B.23) and (B.24), we have

$$\langle\psi|\mathscr{D}^\dagger\mathbf{A}\mathscr{D}|\psi\rangle = R\langle\psi|\mathbf{A}|\psi\rangle, \tag{B.25}$$

or

$$\mathscr{D}^\dagger\mathbf{A}\mathscr{D} = R\mathbf{A}. \tag{B.26}$$

Writing the components of the vector operator $\mathbf{A}$ in Eq. (B.26) in the spherical basis (with covariant components), we have

$$\mathscr{D}^\dagger A_q\mathscr{D} = \tilde{\mathsf{R}}^*_{qq_1}A_{q_1}. \tag{B.27}$$

In terms of the Wigner D-functions this becomes

$$D^{(J)\dagger}A_qD^{(J)} = D^{(1)*}_{qq_1}A_{q_1}. \tag{B.28}$$

Note that this relates the transformation properties of one component of the A_q operator, which rotates according to rank-J D-functions, to the transformation properties of the set of vector components of the operator, which rotate according to rank-1 D-functions. This result places very strong restrictions on the form of a vector operator, and can be extended to operators of higher tensor rank, as discussed in Appendix C.2.

The density matrix transforms differently than other operators. To see the effect of an active rotation on the density matrix ρ, consider the expectation value of an operator A (Eq. 2.5). From Eq. (B.22), we have for the expectation value after a rotation obtained using the rotation operator $\mathscr{D}$:

$$\langle A'\rangle = \mathrm{Tr}\left(\rho A'\right) = \mathrm{Tr}\left(\rho\mathscr{D}^\dagger A\mathscr{D}\right) = \mathrm{Tr}\left(\mathscr{D}\rho\mathscr{D}^\dagger A\right) = \mathrm{Tr}\left(\rho' A\right), \tag{B.29}$$

using the invariance of the trace to cyclic permutation of its arguments, where the rotated density matrix is given by

$$\rho' = \mathscr{D}\rho\mathscr{D}^\dagger. \tag{B.30}$$

This formula can also be obtained by directly rotating the wave functions in the definition (2.6). Note that the formula for rotation of a density matrix differs from that for the rotation of an operator representing an observable, in that the rotation operator is swapped with its Hermitian conjugate.

Appendix C

Irreducible Tensors and the Wigner–Eckart Theorem

C.1 Irreducible tensors and tensor products

We can refer to a set of objects that transform into each other under rotations via a linear transformation a *tensor*. So far, we have seen components of classical vectors (in the spherical or Cartesian bases), components of wave functions, and components of vector operators, and their associated basis sets, as examples of tensors. Another trivial example of a tensor is a scalar, which has only one component, and whose rotation transform is the identity.

Physically, it is clear that any vector can be rotated to point along any other vector, so that for a general rotation R of a vector $\mathbf{v}$, each component v'_i of the rotated vector depends on all three components v_j of the original vector. This means that, for example, there is no basis $(\hat{\mathbf{a}}, \hat{\mathbf{b}}, \hat{\mathbf{c}})$ such that the component of the vector in the $(\hat{\mathbf{a}})$ subspace, $v_a\hat{\mathbf{a}}$, remains in this subspace under all possible rotations, while the component $v_b\hat{\mathbf{b}} + v_c\hat{\mathbf{c}}$ remains in the $(\hat{\mathbf{b}}, \hat{\mathbf{c}})$ subspace. A tensor with this property is called *irreducible*—there is no basis in which it can be written as the sum of two or more tensors, the components of each of which transform only into themselves. All of the tensors that we have discussed so far have this property.

An irreducible tensor defined on a spherical basis of rank κ is called a rank-κ irreducible spherical tensor and has $2\kappa + 1$ components, commonly indexed with the label q. Thus, for example, the three spherical components of a vector comprise an irreducible spherical tensor of rank 1. As another important example, the spherical harmonics $Y_{lm}(\theta, \varphi)$ with $m = -l, \ldots, l$ form an irreducible spherical tensor of rank l. Thus an alternate definition of an irreducible spherical tensor is a collection of

$2l + 1$ quantities that rotate like (have the same rotation matrix as) the spherical harmonics of rank l. The standard notation for the covariant components of a general irreducible tensor A of rank κ is A^{κ}_{q} and for the contravariant components $A^{\kappa q}$.

To find an example of a *reducible* tensor, we consider a rank-2 Cartesian tensor $T = T_{ij}\hat{\mathbf{x}}_i\hat{\mathbf{x}}_j$. (The rank of a Cartesian tensor is given by the number of its indices, and is related to the rank of an irreducible tensor in a manner described below.) Such a tensor has nine components T_{ij} and nine basis tensors $\hat{\mathbf{x}}_i\hat{\mathbf{x}}_j$, and transforms under a spatial rotation by applying the rotation operator R twice:

$$T' = T_{ij}R\hat{\mathbf{x}}_iR\hat{\mathbf{x}}_j = T_{ij}\hat{\mathbf{x}}_m\mathsf{R}_{mi}\hat{\mathbf{x}}_n\mathsf{R}_{nj} = \mathsf{R}_{mi}\mathsf{R}_{nj}T_{ij}\hat{\mathbf{x}}_m\hat{\mathbf{x}}_n. \tag{C.1}$$

It is easy to see that T is reducible. We construct a new basis element

$$\frac{1}{3}\hat{\mathbf{x}}_i\hat{\mathbf{x}}_i = \frac{1}{3}\left(\hat{\mathbf{x}}\hat{\mathbf{x}} + \hat{\mathbf{y}}\hat{\mathbf{y}} + \hat{\mathbf{z}}\hat{\mathbf{z}}\right). \tag{C.2}$$

The component of T with respect to this basis element is $T_{ii}/3$ (i.e., one-third of the trace of T). But the trace of a matrix is invariant under an orthogonal transformation.[1] Thus this component is invariant under rotations and so forms an irreducible subspace of rank zero. Similarly, one can construct three more basis elements that form an irreducible subspace of rank one; the remaining five elements form an irreducible subspace of rank two.

An important case of a rank-two Cartesian tensor is a *dyadic* $T = \mathbf{ab}$ formed out of the direct product of two vectors $\mathbf{a}$ and $\mathbf{b}$. The components $T_{ij} = a_ib_j$ can then be decomposed into terms for each irreducible subspace as

$$T_{ij} = \frac{\mathbf{a}\cdot\mathbf{b}}{3}\delta_{ij} + \frac{a_ib_j - a_jb_i}{2} + \left(\frac{a_ib_j + a_jb_i}{2} - \frac{\mathbf{a}\cdot\mathbf{b}}{3}\delta_{ij}\right). \tag{C.3}$$

The first term is a scalar (invariant under rotations), the second term is directly related to the vector product $\mathbf{a}\times\mathbf{b}$, which behaves as a vector under rotations, and the final term is a symmetric traceless tensor of rank two.

Note that each of the terms, denoted T^{κ}_{ij}, in our decomposition of the dyadic has $2\kappa + 1$ independent components, where κ is the rank of the tensor:

$$T^{0}_{ij} = \frac{\mathbf{a}\cdot\mathbf{b}}{3}\delta_{ij} \tag{C.4}$$

has only one independent component,

$$T^{1}_{ij} = \frac{(a_ib_j - a_jb_i)}{2} \tag{C.5}$$

---

[1] Using the invariance of the trace under cyclic permutation, $\mathrm{Tr}\,(\mathsf{R}^tT\mathsf{R}) = \mathrm{Tr}\,(T\mathsf{R}\mathsf{R}^t) = \mathrm{Tr}\,T$.

has three independent components,[2] corresponding to the components of $\mathbf{a} \times \mathbf{b}$, and

$$T^2_{ij} = \frac{(a_i b_j + a_j b_i)}{2} - \frac{\mathbf{a} \cdot \mathbf{b}}{3} \delta_{ij} \tag{C.6}$$

has five independent components, since it is both symmetric and traceless. That gives $1 + 3 + 5 = 9$ independent components, so we have recovered the original number of independent components of the dyadic.

In order to see what the decomposition of T into irreducible tensors looks like in the spherical basis, we first discuss various types of products of irreducible spherical tensors. There are several different kinds of tensor products that are encountered in practical calculations. We have already considered the scalar product of vectors expressed in the spherical basis:

$$\mathbf{U} \cdot \mathbf{V} = \sum_{i=1}^{3} U_i V_i = \sum_{q=-1}^{1} U^{1q} V^1_q . = \sum_{q=-1}^{1} (-1)^q U^1_q V^1_{-q}. \tag{C.7}$$

In general, the scalar product of any two tensors A^κ and B^κ of the same rank is given by

$$A^\kappa \cdot B^\kappa = \sum_{q=-\kappa}^{\kappa} A^{\kappa q} B^\kappa_q = \sum_{q=-\kappa}^{\kappa} (-1)^q A^\kappa_{-q} B^\kappa_q. \tag{C.8}$$

A generalization of the scalar product is the *tensor product*, which combines two tensors A^{κ_1} and B^{κ_2} into a third tensor of a specific rank κ and index q:

$$(A^{\kappa_1} B^{\kappa_2})^\kappa_q = \sum_{q_1, q_2} \langle \kappa_1 q_1 \kappa_2 q_2 | \kappa q \rangle A^{\kappa_1}_{q_1} B^{\kappa_2}_{q_2}. \tag{C.9}$$

From the Clebsch–Gordan-coefficient triangle rule we can see that the possible values of κ are given by $|\kappa_1 - \kappa_2| < \kappa < \kappa_1 + \kappa_2$. Thus only two tensors of the same rank can combine to form a rank-zero tensor. (It is important to note, however, that the tensor product of rank zero is actually different from the scalar product by a numerical factor dependent on the rank of the tensors being combined.)

As for the Cartesian case, the *direct product* of two tensors, $A^{\kappa_1}_{q_1} B^{\kappa_2}_{q_2}$, is a (generally reducible) tensor of rank $\kappa_1 + \kappa_2$. Using the tensor product, it can be expanded into

---

[2] This can be seen by noting that this formula is antisymmetric in i and j. Hence the diagonal elements of T^1_{ij} are zero, and the matrix elements below the diagonal can be found from those above the diagonal. Thus, specifying the three matrix elements above the diagonal determines the entire matrix.

a sum of irreducible tensors:

$$A^{\kappa_1}_{q_1} B^{\kappa_2}_{q_2} = \sum_{\kappa=|\kappa_1-\kappa_2|}^{\kappa_1+\kappa_2} \sum_{q=-\kappa}^{\kappa} \langle \kappa_1 q_1 \kappa_2 q_2 | \kappa q \rangle \left(A^{\kappa_1} B^{\kappa_2} \right)^{\kappa}_{q} . \tag{C.10}$$

Thus, we can find the irreducible spherical tensor components of the tensor T by performing this expansion on the direct product of the vectors **a**, **b** in the spherical basis, $a_{q_1} b_{q_2}$.

Using Eq. (C.9), we find the relationship between the Cartesian tensor components T^1_{ij}, T^2_{ij} and the irreducible tensor components T^1_q, T^2_q:

$$T^1_0 = i\sqrt{2} T^1_{xy}, \tag{C.11a}$$

$$T^1_{\pm 1} = -T^1_{xz} \mp i T^1_{yz}, \tag{C.11b}$$

$$T^2_0 = \sqrt{\frac{3}{2}} T^2_{zz}, \tag{C.11c}$$

$$T^2_{\pm 1} = \mp T^2_{xz} - i T^2_{yz}, \tag{C.11d}$$

$$T^2_{\pm 2} = \frac{1}{2} \left(T^2_{xx} - T^2_{yy} \pm 2i T^2_{xy} \right) . \tag{C.11e}$$

Note that since these quantities are strictly defined as coefficients of irreducible sets of basis tensors, they depend on a choice of normalization of the basis elements. As a consequence, different versions of these formulas may appear (see, for example, Varshalovich *et al.* 1988).

The decomposition of higher-rank tensors becomes quite complicated: for instance, from the 27 independent Cartesian components of a third-rank tensor, one can construct seven irreducible tensors (one zero rank, three first rank, two second rank, and one third rank)! Also, the decomposition is not unique.

C.2 Irreducible tensor operators and the Wigner–Eckart theorem

The formalism of irreducible spherical tensors can be applied directly to quantum-mechanical operators, in particular to any set of operator components that satisfies the general definition of an irreducible spherical tensor. Generalizing Eq. (B.28), we say that a set of $2\kappa + 1$ operator components T^{κ}_{q} satisfying

$$\mathscr{D}^{\dagger} T^{\kappa}_{q} \mathscr{D} = D^{(\kappa)*}_{q q_1} T^{\kappa}_{q_1} \tag{C.12}$$

is an irreducible spherical tensor operator of rank κ. For example, the spherical-basis components J_q of the vector operator $\mathbf{J}$ form a rank-one irreducible spherical tensor. A complete set of irreducible tensor operators, the polarization operators $\mathcal{T}^{\kappa}_{q}$, are discussed in Sec. 2.3.

Because of the close connection between the angular momentum operator and quantum-mechanical rotations, it can be shown that an irreducible spherical tensor operator also satisfies the commutation relations

$$\left[J_z, T^{\kappa}_{q}\right] = \hbar q T^{\kappa}_{q}, \tag{C.13a}$$

$$\left[J_{\pm}, T^{\kappa}_{q}\right] = \hbar\sqrt{\kappa(\kappa+1) - q(q\pm 1)}\, T^{\kappa}_{q\pm 1}, \tag{C.13b}$$

where $J_{\pm}$ are the raising and lowering operators.[3] This can be regarded as an alternate definition of an irreducible tensor operator. From Eqs. (C.13a) and (C.13b), one can also derive

$$\left[J_i, \left[J_i, T^{\kappa}_{q}\right]\right] = \hbar^2\kappa\,(\kappa+1)\, T^{\kappa}_{q}, \tag{C.14}$$

where summation over the repeated index i is implied.

A ubiquitous feature of atomic physics problems is the necessity to calculate matrix elements of operators between various atomic states. An essential tool for performing such calculations is the *Wigner–Eckart theorem*, which makes explicit the restrictions on the form of an irreducible tensor operator mentioned earlier. The Wigner–Eckart theorem states that the matrix elements of the covariant components of an irreducible tensor operator T^{κ}_{q} between states of a standard (Zeeman) angular-momentum basis are given by the product of a constant independent of magnetic quantum numbers (m, m', q) and an appropriate Clebsch–Gordan coefficient:

$$\langle \xi' J' m' | T^{\kappa}_{q} | \xi J m \rangle = \frac{\langle \xi' J' \| T^{\kappa} \| \xi J \rangle}{\sqrt{2J'+1}} \langle J m \kappa q | J' m' \rangle, \tag{C.15}$$

where the quantity

$$\langle \xi' J' \| T^{\kappa} \| \xi J \rangle \tag{C.16}$$

is the so-called *reduced matrix element*, and we employ the standard general angular momentum basis $|\xi J m\rangle$, with

$$\mathbf{J}^2 |\xi J m\rangle = \hbar^2 J(J+1) |\xi J m\rangle, \tag{C.17a}$$

$$J_z |\xi J m\rangle = \hbar m |\xi J m\rangle, \tag{C.17b}$$

---

[3] Note that the spherical components J_1 and J_{-1} differ from the raising and lowering operators J_+ and J_- by numerical factors.

where ξ accounts for all other quantum numbers. It can be shown that for a Hermitian operator T^{κ}_{q},

$$\langle \xi J \| T^{\kappa} \| \xi' J' \rangle = (-1)^{J-J'} \langle \xi' J' \| T^{\kappa} \| \xi J \rangle^{*}. \tag{C.18}$$

This will be useful for relating amplitudes of direct and inverse processes.

The meaning of the Wigner–Eckart theorem can be understood by realizing that the definition of an irreducible tensor T^{κ}_{q} says that it has properties similar to those of an eigenstate of angular momentum $|J=\kappa, m=q\rangle$. In particular, they rotate in the same manner. From this perspective, taking the matrix element $\langle \xi' J' m' | T^{\kappa}_{q} | \xi J m \rangle$ looks a lot like coupling two angular momentum states $|\kappa q\rangle$ and $|Jm\rangle$ into the final state $|J'm'\rangle$. Thus it is natural to see that the result is proportional to the corresponding Clebsch–Gordan coefficient $\langle J m \kappa q | J' m' \rangle$.

An important example of the application of the Wigner–Eckart theorem is when we calculate the expectation value of the components of a vector operator T^{1}_{q} for a given state $|Jm\rangle$. In this case, the initial and final states coincide, and using the Wigner–Eckart theorem and the fact that $\mathbf{J}$ is a vector operator, we can write $\left\langle T^{1}_{q} \right\rangle = \langle Jm | T^{1}_{q} | Jm \rangle \propto \langle Jm | J_q | Jm \rangle = \langle J_q \rangle$. In other words, the expectation value of any vector observable lies along the expectation value of the total angular momentum. For instance, for a state with a given J, the expectation values of $\mathbf{L}$ and $\mathbf{S}$ (assuming LS-coupling), as well as the magnetic moments $\boldsymbol{\mu}_L$, $\boldsymbol{\mu}_S$, and the total magnetic moment $\boldsymbol{\mu}$, all lie along the expectation value of $\mathbf{J}$.

Expressing the Clebsch–Gordan coefficient in Eq. (C.15) with a $3j$ symbol, one arrives at the following form of the Wigner–Eckart theorem:

$$\langle \xi' J' m' | T^{\kappa}_{q} | \xi J m \rangle = (-1)^{J'-m'} \langle \xi' J' \| T^{\kappa} \| \xi J \rangle \begin{pmatrix} J' & \kappa & J \\ -m' & q & m \end{pmatrix}. \tag{C.19}$$

Proofs of the Wigner–Eckart theorem can be found in most advanced quantum-mechanics texts, for example, that by Sakurai and Tuan (1994).

> The definition of reduced matrix elements that we employ is the definition assumed, for example, by Fano and Racah (1959), Varshalovich *et al.* (1988), Zare (1988), Sobelman (1992), Auzinsh and Ferber (1995), Edmonds (1996), and Budker *et al.* (2008). The reader should be forewarned that there is another, less commonly used, convention for the reduced matrix element in the literature (found, for example, in Brink and Satchler, 1993), in which $\langle \xi' J' \| T^{\kappa} \| \xi J \rangle$ absorbs the factor $\sqrt{2J'+1}$, so that the Wigner–Eckart theorem reads
>
> $$\langle \xi' J' m' | T^{\kappa}_{q} | \xi J m \rangle = \langle \xi' J' \| T^{\kappa} \| \xi J \rangle \langle J m \kappa q | J' m' \rangle.$$
>
> We consistently use the form of Eqs. (C.15) and (C.19).

The significance of the Wigner–Eckart theorem lies in its explicit separation of the matrix element into two factors: the reduced matrix element $\langle\xi' J'\|T^\kappa\|\xi J\rangle$, which is a property of the particular physical observable being considered, and the angular coefficient (Clebsch–Gordan coefficient or a $3j$ symbol), which depends only on the geometry of the problem, i.e., the orientation of the physical observables with respect to the quantization axis. What makes the theorem so useful is that all the dependence of the matrix element on the magnetic quantum numbers is contained in the angular coefficient. This allows one to find ratios between different matrix elements, and to determine matrix elements for all values of q, m, and m' once this has been done for one particular case.

In some problems, the need arises to relate the reduced matrix element for some tensor operator T^κ found in an uncoupled angular momentum basis, for example $|Jm_J\rangle|Im_I\rangle$, where J represents the total electronic angular momentum and I represents the nuclear spin, with the reduced matrix element in a coupled basis, for example $|Fm_F\rangle$, where F is the total angular momentum. If T^κ commutes with I, then the formula relating the reduced matrix elements (derived, for example, in the books by Sobelman, 1992 and Judd, 1998) is found to be

$$\langle J'IF'\|T^\kappa\|JIF\rangle = (-1)^{J'+I+F+\kappa}\sqrt{(2F+1)(2F'+1)}\begin{Bmatrix} J' & F' & I \\ F & J & \kappa \end{Bmatrix}\langle J'\|T^\kappa\|J\rangle. \tag{C.20}$$

For more detailed discussions of tensors and tensor operators, see texts such as those by Fano and Racah (1959), Zare (1988), and Sakurai and Tuan (1994).

Appendix D

Nonlinear Magneto-optical Rotation with Hyperfine Structure

D.1 Perturbation theory in terms of polarization moments

The time evolution of the atomic density matrix ρ subject to the action of a time-independent Hamiltonian H is given by the Liouville equation (Eq. 5.1),

$$\dot{\rho} = \frac{1}{i\hbar}\left[H, \rho\right] - \frac{1}{2}\{\widehat{\Gamma}, \rho\} + \Lambda + \mathrm{Tr}\left(F\rho\right), \tag{D.1}$$

where $\widehat{\Gamma}$ is the relaxation matrix, Λ accounts for repopulation, and F is the spontaneous emission operator (Eq. 3.16). (We neglect other relaxation and repopulation mechanisms, such as spin-exchanging collisions, which may require the inclusion of additional terms.)

We will now rewrite Eq. (D.1) in terms of the polarization moments. To do this, we expand the operators appearing in the Liouville equation in terms of polarization operators. In order to describe coherences between two states, as well as polarization moments of an atomic state with a particular value of F, we must extend the definition of the polarization operators given in Sec. 2.3. Thus we define the generalized polarization operators $\mathcal{T}_q^{(\kappa)}(F_1F_2)$ connecting states F_1 and F_2 via the orthonormality condition

$$\mathrm{Tr}\,\mathcal{T}_q^{\kappa}(F_1F_2)\mathcal{T}_{q'}^{\kappa'}(F_1'F_2')^{\dagger} = \delta_{\kappa\kappa'}\delta_{qq'}\delta_{F_1F_1'}\delta_{F_2F_2'} \tag{D.2}$$

and the phase convention

$$\mathcal{T}_q^{\kappa}(F_1F_2)^{\dagger} = (-1)^{F_1-F_2+q}\mathcal{T}_{-q}^{\kappa}(F_2F_1) = \mathcal{T}^{\kappa q}(F_1F_2). \tag{D.3}$$

Here F is understood to represent the total angular momentum quantum number as well as any additional quantum numbers necessary to distinguish between two states with the same total angular momentum.

The reduced matrix element of $\mathcal{T}^\kappa(F_1'F_2')$ is then given by

$$\langle F_1\|\mathcal{T}^\kappa(F_1'F_2')\|F_2\rangle = \sqrt{2\kappa+1}\,\delta_{F_1F_1'}\delta_{F_2F_2'} \tag{D.4}$$

and the matrix elements of the polarization operators are given by

$$\begin{aligned}\langle F_1m_1|\mathcal{T}_q^\kappa(F_1'F_2')|F_2m_2\rangle &= \sqrt{\frac{2\kappa+1}{2F_1+1}}\langle F_2m_2\kappa q|F_1m_1\rangle\delta_{F_1F_1'}\delta_{F_2F_2'}\\ &= (-1)^{F_2-m_2}\langle F_1m_1F_2,-m_2|\kappa q\rangle\delta_{F_1F_1'}\delta_{F_2F_2'}.\end{aligned} \tag{D.5}$$

An arbitrary operator A can now be expanded according to

$$A = \sum A^{\kappa q}(F_1F_2)T_q^\kappa(F_1F_2), \tag{D.6}$$

where $F_{1,2}$ runs over all pairs of states in the system. Using Eq. (D.5) and the orthonormality condition (D.2), we find the expansion coefficients $A^{\kappa q}(F_1F_2)$ in terms of the Zeeman-basis matrix elements of A:

$$\begin{aligned}A^{\kappa q}(F_1F_2) &= \mathrm{Tr}\left[A\mathcal{T}_q^\kappa(F_1F_2)^\dagger\right]\\ &= \sum_{m_1m_2} A_{F_1m_1,F_2m_2}\left[\mathcal{T}_q^\kappa(F_1F_2)\right]_{F_1m_1F_2m_2}\\ &= \sum_{m_1m_2}(-1)^{F_2-m_2}\langle F_1m_1F_2,-m_2|\kappa q\rangle A_{F_1m_1,F_2m_2}.\end{aligned} \tag{D.7}$$

Performing the expansion of each operator, and using appropriate tensor product and sum rules, the equation of motion for the polarization moments is found from the Liouville equation to be

$$\begin{aligned}\dot\rho^{\kappa q}(F_1F_2) = &-i(-1)^{F_1+F_2+\kappa}\sum\sqrt{[\kappa'][\kappa'']}\langle\kappa'q'\kappa''q''|\kappa q\rangle\begin{Bmatrix}\kappa' & \kappa'' & \kappa\\ F_2 & F_1 & F_3\end{Bmatrix}\\ &\times\Bigg[\left(\frac{1}{\hbar}H^{\kappa'q'}(F_1F_3)-\frac{i}{2}\Gamma^{\kappa'q'}(F_1F_3)\right)\rho^{\kappa''q''}(F_3F_2)\\ &\qquad-\rho^{\kappa'q'}(F_1F_3)\left(\frac{1}{\hbar}H^{\kappa''q''}(F_3F_2)+\frac{i}{2}\widehat{\Gamma}^{\kappa''q''}(F_3F_2)\right)\Bigg]\\ &+\Lambda^{\kappa q}(F_1F_2)\\ &+\frac{4\omega^3}{3\hbar c^3}\sum\langle F_1\|d\|F_e\rangle\rho^{\kappa q}(F_eF_e')\langle F_e'\|d\|F_2\rangle(-1)^{F_e+F_e'+\kappa+1}\begin{Bmatrix}\kappa & F_2 & F_1\\ 1 & F_e & F_e'\end{Bmatrix},\end{aligned} \tag{D.8}$$

where all variables not appearing on the left-hand side are summed over (the variables F_e and F'_e appearing in the last term relate to spontaneous emission and run over only those states of higher energy than $F_{1,2}$). Here the arrays enclosed in curly brackets are the $6j$ symbols, and we use the notation $[x] = 2x + 1$.

We now suppose that the total Hamiltonian is $H = H_0 + \hbar V$, where H_0 is diagonal and V is a time-independent perturbation. We also assume that Γ and Λ are diagonal. More precisely, we assume that only $\Gamma^{00}(FF)$, $\Lambda^{00}(FF)$, and $H^{00}(FF)$ are nonzero (for arbitrary F). Taking the steady-state limit in Eq. (D.8) and expanding to second order in the perturbation V, we find for a ground-state polarization moment

$$\begin{aligned}
\rho^{\kappa q}(F_gF_g) = \frac{\gamma}{i\widetilde{\omega}_{FF}N_g}\Bigg[&\delta_{\kappa 0}\delta_{q0}\sqrt{[F_g]} - (-1)^{2F_g+\kappa'+\kappa''}\sqrt{[\kappa'][\kappa'']} \\
&\quad\times \langle\kappa' q' \kappa'' q''|\kappa q\rangle \begin{Bmatrix} \kappa'' & \kappa' & \kappa \\ F_g & F_g & F' \end{Bmatrix} \frac{\widetilde{\omega}_{F_gF'} + \widetilde{\omega}_{F'F_g}}{\widetilde{\omega}_{F_gF_g}\widetilde{\omega}_{F_gF'}\widetilde{\omega}_{F'F_g}} \\
&\quad\times V^{\kappa' q'}(F'F_g)V^{\kappa'' q''}(F_gF') \\
- i\frac{4\omega^3}{3\hbar c^3}&(-1)^{2F'_1+2F'_2+\kappa+\kappa'+\kappa''}\sqrt{[\kappa'][\kappa'']}\langle\kappa' q' \kappa'' q''|\kappa q\rangle \\
&\quad\times \begin{Bmatrix} \kappa'' & \kappa' & \kappa \\ F'_2 & F'_1 & F' \end{Bmatrix} \begin{Bmatrix} \kappa & F_g & F_g \\ 1 & F'_1 & F'_2 \end{Bmatrix} \langle F'_2\|d\|F_g\rangle\langle F_g\|d\|F'_1\rangle \\
&\quad\times \frac{\widetilde{\omega}_{F'_1F'} + \widetilde{\omega}_{F'F'_2}}{\widetilde{\omega}_{F'_1F'}\widetilde{\omega}_{F'_1F'_2}\widetilde{\omega}_{F'F'}\widetilde{\omega}_{F'F'_2}} V^{\kappa'' q''}(F'_1F')V^{\kappa' q'}(F'F'_2)\Bigg].
\end{aligned} \tag{D.9}$$

Here we have neglected the possibility of cascade decays and assumed that V does not couple a state to itself. We have also assumed that Λ repopulates all ground-state sublevels equally: $\Lambda_{Fm,Fm} = \gamma/N_g$, where γ is the ground-state relaxation rate and N_g is the total number of ground-state sublevels. The complex frequency splitting $\widetilde{\omega}_{F_1F_2}$ is given by

$$\widetilde{\omega}_{F_1F_2} = \frac{1}{\hbar}(E_{F_1} - E_{F_2}) - \frac{i}{2}\left(\Gamma_{F_1} + \Gamma_{F_2}\right), \tag{D.10}$$

where $E_F = (2F+1)^{-1/2}H_0^{00}(FF)$ is the unperturbed energy and

$$\Gamma_F = (2F+1)^{-1/2}\Gamma^{00}(FF) \tag{D.11}$$

is the total relaxation rate of a state F.

D.2 Doppler-free transit effect

We now apply the results obtained in Appendix D.1 to the three-stage calculation described in Sec. 10.1. In stage (a), we consider a z-polarized light field $\boldsymbol{\mathcal{E}} = \mathcal{E}_0 \operatorname{Re}\left(\hat{\boldsymbol{\varepsilon}} e^{i(\mathbf{k}\cdot\mathbf{r}-\omega t)}\right)$ with $\hat{\boldsymbol{\varepsilon}} = \hat{\mathbf{z}}$. We let V represent the electric-dipole Hamiltonian in the rotating-wave approximation: $V' = -\frac{1}{2} d_z \mathcal{E}_0$. (Here the prime refers to the rotating frame.) We assume that the magnetic field is absent in this stage. From Eq. (D.9) we find

$$\begin{aligned}
\rho_a^{(20)}(F_g F_g) = -\sqrt{\frac{2}{3}} \sum_{F_e} (-1)^{F_g - F_e} \tilde{\kappa}_2 \frac{[F_e][F_g]}{[I][J_g]} \\
\times \Bigg((-1)^{2I+2J_g} \begin{Bmatrix} 1 & 1 & 2 \\ F_g & F_g & F_e \end{Bmatrix} \begin{Bmatrix} J_e & F_e & I \\ F_g & J_g & 1 \end{Bmatrix}^2 L(\omega'_{F_e F_g}) \\
+ R \sum_{F'_g F'_e} (-1)^{F'_g - F'_e} [J_e][F'_g][F'_e] \begin{Bmatrix} 1 & 1 & 2 \\ F_e & F'_e & F'_g \end{Bmatrix} \begin{Bmatrix} F_g & F_g & 2 \\ F_e & F'_e & 1 \end{Bmatrix} \begin{Bmatrix} J_e & F_e & I \\ F_g & J_g & 1 \end{Bmatrix} \\
\times \begin{Bmatrix} J_e & F_e & I \\ F'_g & J_g & 1 \end{Bmatrix} \begin{Bmatrix} J_e & F'_e & I \\ F_g & J_g & 1 \end{Bmatrix} \begin{Bmatrix} J_e & F'_e & I \\ F'_g & J_g & 1 \end{Bmatrix} \frac{L(\omega'_{F_e F'_g}) L(\omega'_{F'_e F'_g})}{L\left(\sqrt{\omega'_{F_e F'_g} \omega'_{F'_e F'_g}}\right)} \Bigg),
\end{aligned} \tag{D.12}$$

where all variables are as defined in Sec. 10.1. We have evaluated matrix elements using the Wigner–Eckart theorem and have used the relation (see, for example, Sobelman, 1992)

$$R\,\Gamma = \frac{4\omega^3}{3\hbar c^3} \frac{1}{2J_e + 1} \left| \langle J_g \| d \| J_e \rangle \right|^2 . \tag{D.13}$$

The unperturbed energies can be evaluated with

$$\begin{aligned}
E_{JFM} = E_J + \frac{1}{2} K_{IJF} A_J \\
+ \frac{3}{8} \frac{K_{IJF}(K_{IJF}+1) - \frac{4}{3} I(I+1) J(J+1)}{I(2I-1) J(2J-1)} B_J,
\end{aligned} \tag{D.14}$$

where $K_{IJF} = F(F+1) - I(I+1) - J(J+1)$ and A_J and B_J are the hyperfine coefficients. The last term is zero for $J \leq 1/2$ or $I \leq 1/2$.

In the case in which the excited-state hfs is well resolved in the Doppler-free spectrum ($\omega_{F_eF'_e} \gg \Gamma$), Eq. (D.12) reduces to

$$\begin{aligned}\rho_a^{(20)}(F_gF_g) = &-\sqrt{\frac{2}{3}}\sum_{F_e}(-1)^{F_g-F_e}\tilde{\kappa}_2\frac{[F_e][F_g]}{[I][J_g]}\\ &\times\Bigg((-1)^{2I+2J_g}\begin{Bmatrix}1&1&2\\F_g&F_g&F_e\end{Bmatrix}\begin{Bmatrix}J_e&F_e&I\\F_g&J_g&1\end{Bmatrix}^2 L(\omega'_{F_eF_g})\\ &\quad+\sum_{F'_g}R\,(-1)^{F'_g-F_e}[J_e][F'_g][F_e]\begin{Bmatrix}1&1&2\\F_e&F_e&F'_g\end{Bmatrix}\\ &\qquad\times\begin{Bmatrix}F_g&F_g&2\\F_e&F_e&1\end{Bmatrix}\begin{Bmatrix}J_e&F_e&I\\F_g&J_g&1\end{Bmatrix}^2\begin{Bmatrix}J_e&F_e&I\\F'_g&J_g&1\end{Bmatrix}^2 L(\omega'_{F_eF'_g})\Bigg).\end{aligned} \tag{D.15}$$

In stage (b), the ground-state density matrix, which is initially in the state found in stage (a), evolves under the influence of a magnetic field $B\hat{\mathbf{x}}$. We will require only the value of the polarization moment $\rho_b^{(21)}(F_gF_g)$. Using the Hamiltonian $H_B = -\boldsymbol{\mu}\cdot\mathbf{B}$ in Eq. (D.8) and solving for the steady state, we find

$$\rho_b^{(21)}(F_gF_g) = i\frac{\sqrt{3}}{2\sqrt{2}}x_{F_g}\rho_a^{(20)}(F_gF_g), \tag{D.16}$$

where the magnetic-resonance lineshape parameter x_{F_g} is defined in Eq. (10.4).

In stage (c) the ground-state polarization is probed. The optical rotation for weak linearly polarized probe light is given by (Eq. 5.42)

$$\frac{d\mathcal{O}}{d\ell} = -\frac{2\pi\omega n}{\hbar c}\,\mathrm{Im}\left[\hat{\boldsymbol{\varepsilon}}\cdot\overleftrightarrow{\boldsymbol{\beta}}\cdot(\hat{\mathbf{k}}\times\hat{\boldsymbol{\varepsilon}})\right], \tag{D.17}$$

where $\overleftrightarrow{\boldsymbol{\beta}}$ is a tensor defined in Eq. (5.43) that depends on the ground-state density matrix. Expanding $\overleftrightarrow{\boldsymbol{\beta}}$ in terms of the ground-state polarization moments, we obtain

$$\begin{aligned}\overleftrightarrow{\boldsymbol{\beta}} = &\sum_{F_gF_e\kappa q'q''}\frac{(-1)^{F_g+F_e+\kappa}}{\widetilde{\omega}'_{F_eF_g}}\hat{\boldsymbol{\epsilon}}_{-q'}\hat{\boldsymbol{\epsilon}}_{-q''}\langle 1q'1q''|\kappa,q'+q''\rangle\begin{Bmatrix}1&1&\kappa\\F_g&F_g&F_e\end{Bmatrix}\\ &\times\left|\langle F_g\|d\|F_e\rangle\right|^2\rho^{(\kappa,q'+q'')}(F_gF_g),\end{aligned} \tag{D.18}$$

where $\hat{\boldsymbol{\epsilon}}_q$ are the spherical basis vectors. Evaluating (D.17) for z-polarized light and using Eq. (D.16) gives

$$\begin{aligned}\ell_0\frac{d\alpha}{d\ell} = &-\frac{3\sqrt{3}}{4\sqrt{2}}\sum_{F_gF_e}(-1)^{F_g+F_e}[F_g][F_e][J_g]\begin{Bmatrix}1&1&2\\F_g&F_g&F_e\end{Bmatrix}\begin{Bmatrix}J_e&F_e&I\\F_g&J_g&1\end{Bmatrix}^2\\ &\times L(\omega'_{F_eF_g})x_{F_g}\rho_a^{(20)}(F_gF_g),\end{aligned} \tag{D.19}$$

where the unsaturated absorption length for the $J_g \to J_e$ transition is defined in Eq. (10.5). Substituting in Eq. (D.12) results in the full expression for optical rotation due to the Doppler-free transit effect:

$$\begin{aligned}
\ell_0 \frac{d\alpha}{d\ell} = \frac{3}{4}\tilde{\kappa}_2 \sum_{F_g F_e F_e''} & (-1)^{2F_g+F_e''-F_e} \frac{[F_e][F_e''][F_g]^2}{[I]} \begin{Bmatrix} 1 & 1 & 2 \\ F_g & F_g & F_e'' \end{Bmatrix} \begin{Bmatrix} J_e & F_e'' & I \\ F_g & J_g & 1 \end{Bmatrix}^2 x_{F_g} \\
& \times \left((-1)^{2I+2J_g} \begin{Bmatrix} 1 & 1 & 2 \\ F_g & F_g & F_e \end{Bmatrix} \begin{Bmatrix} J_e & F_e & I \\ F_g & J_g & 1 \end{Bmatrix}^2 L(\omega'_{F_eF_g}) L(\omega'_{F_e''F_g}) \right. \\
& + R \sum_{F_g' F_e'} (-1)^{F_g'-F_e'} [J_e][F_g'][F_e'] \begin{Bmatrix} 1 & 1 & 2 \\ F_e & F_e' & F_g' \end{Bmatrix} \begin{Bmatrix} F_g & F_g & 2 \\ F_e & F_e' & 1 \end{Bmatrix} \begin{Bmatrix} J_e & F_e & I \\ F_g & J_g & 1 \end{Bmatrix} \\
& \left. \times \begin{Bmatrix} J_e & F_e & I \\ F_g' & J_g & 1 \end{Bmatrix} \begin{Bmatrix} J_e & F_e' & I \\ F_g & J_g & 1 \end{Bmatrix} \begin{Bmatrix} J_e & F_e' & I \\ F_g' & J_g & 1 \end{Bmatrix} \frac{L(\omega'_{F_eF_g'}) L(\omega'_{F_e'F_g'}) L(\omega'_{F_e''F_g})}{L\left(\sqrt{\omega'_{F_eF_g'}\omega'_{F_e'F_g'}}\right)} \right).
\end{aligned} \tag{D.20}$$

For completely resolved hfs ($\omega_{F_eF_e'}, \omega_{F_gF_g'} \gg \Gamma$), this reduces to

$$\begin{aligned}
\ell_0 \frac{d\alpha}{d\ell} = \frac{3}{4}\tilde{\kappa}_2 \sum_{F_g F_e} & (-1)^{2F_g} \frac{[F_e]^3[F_g]^3}{[I]} \begin{Bmatrix} 1 & 1 & 2 \\ F_g & F_g & F_e \end{Bmatrix} \begin{Bmatrix} J_e & F_e & I \\ F_g & J_g & 1 \end{Bmatrix}^4 x_{F_g} [L(\omega'_{F_eF_g})]^2 \\
& \times \left(\frac{(-1)^{2I+2J_g}}{[F_e][F_g]} \begin{Bmatrix} 1 & 1 & 2 \\ F_g & F_g & F_e \end{Bmatrix} \right. \\
& \left. + R\,(-1)^{F_g-F_e}(2J_e+1) \begin{Bmatrix} 1 & 1 & 2 \\ F_e & F_e & F_g \end{Bmatrix} \begin{Bmatrix} F_g & F_g & 2 \\ F_e & F_e & 1 \end{Bmatrix} \begin{Bmatrix} J_e & F_e & I \\ F_g & J_g & 1 \end{Bmatrix}^2 \right).
\end{aligned} \tag{D.21}$$

D.3 Doppler-broadened transit effect

The procedure used to obtain the optical rotation signal in the Doppler-broadened case is described in Sec. 10.2. When the ground- and excited-state hyperfine splittings are all much greater than the natural width ($\omega_{F_eF_e'}, \omega_{F_gF_g'}, \Gamma_D \gg \Gamma$) we have, applying the integration procedure to Eq. (D.21),

$$\begin{aligned}\ell_0 \frac{d\alpha}{d\ell} &= \frac{3}{8}\tilde{\kappa}_2 \sum_{F_g F_e} (-1)^{2F_g} \frac{[F_e]^3[F_g]^3}{[I]} \begin{Bmatrix} 1 & 1 & 2 \\ F_g & F_g & F_e \end{Bmatrix} \begin{Bmatrix} J_e & F_e & I \\ F_g & J_g & 1 \end{Bmatrix}^4 e^{-(\Delta_{F_eF_g}/\Gamma_D)^2} x_{F_g} \\ &\times \left(\frac{(-1)^{2I+2J_g}}{[F_e][F_g]} \begin{Bmatrix} 1 & 1 & 2 \\ F_g & F_g & F_e \end{Bmatrix} + R\,(-1)^{F_g-F_e}[J_e] \begin{Bmatrix} 1 & 1 & 2 \\ F_e & F_e & F_g \end{Bmatrix} \begin{Bmatrix} F_g & F_g & 2 \\ F_e & F_e & 1 \end{Bmatrix} \begin{Bmatrix} J_e & F_e & I \\ F_g & J_g & 1 \end{Bmatrix}^2 \right),\end{aligned} \tag{D.22}$$

where the unsaturated absorption length for the Doppler-broadened case is given by Eq. (10.12).

In a different limit in which the ground-state hyperfine splittings are much greater than the natural width and the excited-state splittings are much smaller than the Doppler width ($\omega_{F_eF_e'}, \Gamma \ll \Gamma_D$, $\Gamma \ll \omega_{F_gF_g'}$), we have

$$\begin{aligned}\ell_0 \frac{d\alpha}{d\ell} &= \frac{3}{8}\tilde{\kappa}_2 \sum_{F_g F_e F_e''} (-1)^{2F_g+F_e''-F_e} \frac{[F_e][F_e''][F_g]^2}{[I]} \begin{Bmatrix} 1 & 1 & 2 \\ F_g & F_g & F_e'' \end{Bmatrix} \begin{Bmatrix} J_e & F_e & I \\ F_g & J_g & 1 \end{Bmatrix}^2 \begin{Bmatrix} J_e & F_e'' & I \\ F_g & J_g & 1 \end{Bmatrix}^2 \\ &\times x_{F_g} \left((-1)^{2I+2J_g} \begin{Bmatrix} 1 & 1 & 2 \\ F_g & F_g & F_e \end{Bmatrix} + R \sum_{F_e'} (-1)^{F_g-F_e'} [J_e][F_g][F_e'] \begin{Bmatrix} 1 & 1 & 2 \\ F_e & F_e' & F_g \end{Bmatrix} \right. \\ &\times \left. \begin{Bmatrix} F_g & F_g & 2 \\ F_e & F_e' & 1 \end{Bmatrix} \begin{Bmatrix} J_e & F_e' & I \\ F_g & J_g & 1 \end{Bmatrix}^2 \frac{2\Gamma^4 + (2\Gamma^2 + \omega_{F_eF_e'}^2)\omega_{F_eF_e''}\omega_{F_e'F_e''}}{2(\Gamma^2 + \omega_{F_eF_e'}^2)(\Gamma^2 + \omega_{F_e'F_e''}^2)} \right) \frac{e^{-(\Delta_{F_g}/\Gamma_D)^2}\Gamma^2}{\Gamma^2 + \omega_{F_eF_e''}^2}.\end{aligned} \tag{D.23}$$

D.4 Wall effect

The procedure for obtaining the signal in the wall-effect case is described in Sec. 10.3. For excited-state hyperfine splittings much greater than the natural width ($\Gamma \ll \omega_{F_eF_e'}, \Gamma_D$), we have for the ground-state polarization

$$\begin{aligned}\rho_a^{(20)}(F_gF_g) &= -\sqrt{\frac{\pi}{6}} \sum_{F_e} (-1)^{F_g-F_e} \tilde{\kappa}_2 \frac{[F_e][F_g]}{[I][J_g]} \begin{Bmatrix} J_e & F_e & I \\ F_g & J_g & 1 \end{Bmatrix}^2 \\ &\times \left((-1)^{2I+2J_g} \begin{Bmatrix} 1 & 1 & 2 \\ F_g & F_g & F_e \end{Bmatrix} e^{-(\Delta_{F_eF_g}/\Gamma_D)^2} \right. \\ &\quad \left. + R \sum_{F_g'} (-1)^{F_g'-F_e} [J_e][F_g'][F_e] \begin{Bmatrix} 1 & 1 & 2 \\ F_e & F_e & F_g' \end{Bmatrix} \begin{Bmatrix} F_g & F_g & 2 \\ F_e & F_e & 1 \end{Bmatrix} \begin{Bmatrix} J_e & F_e & I \\ F_g' & J_g & 1 \end{Bmatrix}^2 \right),\end{aligned} \tag{D.24}$$

where the saturation parameter for the wall effect is defined by Eq. (10.17). The optical rotation signal is then given by

$$\begin{aligned}
\ell_0\frac{d\alpha}{d\ell} &= -\frac{3\sqrt{3}}{4\sqrt{2}}\sum_{F_gF'_e}(-1)^{F_g+F'_e}[F_g][F'_e][J_g]\begin{Bmatrix}1 & 1 & 2\\ F_g & F_g & F'_e\end{Bmatrix}\begin{Bmatrix}J_g & F_g & I\\ F'_e & J_e & 1\end{Bmatrix}^2 e^{-(\Delta_{F'_eF_g}/\Gamma_D)^2}\\
&\qquad\times x_{F_g}\rho_a^{(20)}(F_gF_g)\\
&= \frac{3\sqrt{\pi}}{8}\tilde{\kappa}_2\sum_{F_gF_eF'_e}(-1)^{2F_g+F'_e-F_e}\frac{[F_e][F'_e][F_g]^2}{[I]}\begin{Bmatrix}1 & 1 & 2\\ F_g & F_g & F'_e\end{Bmatrix}\begin{Bmatrix}J_e & F_e & I\\ F_g & J_g & 1\end{Bmatrix}^2\begin{Bmatrix}J_e & F'_e & I\\ F_g & J_g & 1\end{Bmatrix}^2\\
&\qquad\times x_{F_g}e^{-(\Delta_{F'_eF_g}/\Gamma_D)^2}\Bigg((-1)^{2I+2J_g}\begin{Bmatrix}1 & 1 & 2\\ F_g & F_g & F_e\end{Bmatrix}e^{-(\Delta_{F_eF_g}/\Gamma_D)^2}\\
&\quad+R\sum_{F'_g}(-1)^{F'_g-F_e}[J_e][F_e][F'_g]\begin{Bmatrix}1 & 1 & 2\\ F_e & F_e & F'_g\end{Bmatrix}\begin{Bmatrix}F_g & F_g & 2\\ F_e & F_e & 1\end{Bmatrix}\begin{Bmatrix}J_e & F_e & I\\ F'_g & J_g & 1\end{Bmatrix}^2 e^{-(\Delta_{F_eF'_g}/\Gamma_D)^2}\Bigg).
\end{aligned}\tag{D.25}$$

Appendix E

The *Atomic Density Matrix* Software Package

A *Mathematica* package has been created to facilitate density-matrix modeling, and it has been used for many of the calculations and figures presented in this work. Those who are familiar with this software system may find the package useful for performing practical calculations and/or working out specific examples. The package is available at `http://budker.berkeley.edu/ADM/`.

In this Appendix, we provide a brief description of the capabilities and the underlying principles behind the *Atomic Density Matrix* (*ADM*) package. A more detailed description is accessible via the documentation supplied with the package.

The package is designed to facilitate analytic and numerical simulations of atoms interacting with light and other external fields. The first step in using the package is to define a list of the atomic states making up the system, with all relevant angular-momentum quantum numbers specified. (The package automatically generates hyperfine and Zeeman sublevels of the specified states.) This list of states is then provided to various functions that generate the atomic density matrix, the Hamiltonian, and the system of Liouville equations. The evolution equations can then be solved using built-in *Mathematica* routines, or specialized methods built into the *ADM* package. Once the density matrix is known, functions can be used to find observed signals in transmitted or fluorescent light.

Calculations can be performed in either the Zeeman basis or the basis of polarization moments, and functions are provided to translate between these two representations. Various aspects of tensor algebra are implemented, including inner (scalar) and outer (direct) products, tensor products, and rotations.

The package includes visualization routines, including a function that draws angular-momentum probability surfaces, and one that automatically draws a level diagram for a specified atomic system.

It is also possible to address more complicated experimental systems, in which experimental conditions vary as a function of position or atomic velocity, and atoms travel between the different regions. A list of experimental regions can be provided to *ADM* functions along with the list of atomic states to generate evolution equations for multiple coupled density matrices describing the entire system. This can be used, for example, to do nonperturbative calculations for antirelaxation-coated vapor cells, in which atoms in the light beam are described by a different density matrix than those in the unilluminated region of the cell, and the density matrices for atoms in different velocity groups are coupled due to velocity-changing collisions.

The package is designed, as much as possible, to avoid the use of specific formulas derived for particular purposes, and to rather make calls to a function that uses the Wigner-Eckart theorem to return matrix elements of an appropriate irreducible tensor operator. This approach has two benefits: it lessens the chance of errors appearing as formulas are entered into the code, and it makes the package more easily extensible. For example, the definition of a new Hamiltonian is largely accomplished simply by specifying the reduced matrix element of the corresponding operator.